**National Technical University of Athens**

**School of Naval Architecture and Marine Engineering**

# Hydroelastic interaction between ocean waves and large floating structures in the inhomogeneous ocean environment

This dissertation is submitted for the degree of
*Doctor of Engineering*

**Angeliki Karperaki**

**Advisory Committee:**
Prof. Konstantinos A. Belibassakis *(supervisor)*
Prof. Gerassimos A. Athanassoulis
Assoc. Prof. Stylianos I. Markolefas

March 2021

**Εθνικό Μετσόβιο Πολυτεχνείο**
**Σχολή Ναυπηγών Μηχανολόγων Μηχανικών**

# Υδροελαστική αλληλεπίδραση θαλάσσιων κυματισμών με μεγάλες πλωτές κατασκευές σε ανομοιογενές περιβάλλον

Διδακτορική Διατριβή της

**Αγγελικής Καρπεράκη**

**Τριμελής Συμβουλευτική Επιτροπή**:

1. Κ. Α. Μπελιμπασάκης, *Καθηγητής ΕΜΠ (Επιβλέπων)*
2. Γ. Α. Αθανασούλης, *Καθηγητής ΕΜΠ*
3. Σ. Ι. Μαρκολέφας, *Επίκουρος Καθ. ΕΚΠΑ*

**Επταμελής Εξεταστική Επιτροπή**:

1. Κ. Α. Μπελιμπασάκης, *Καθηγητής ΕΜΠ (Επιβλέπων)*
2. Γ. Α. Αθανασούλης, *Καθηγητής ΕΜΠ*
3. Σ. Ι. Μαρκολέφας, *Επίκουρος Καθ. ΕΚΠΑ*
4. Ε. Σ. Σαμουηλίδης, *Καθηγητής ΕΜΠ*
5. Ε. Ε. Θεοτόκογλου, *Καθηγητής ΕΜΠ*
6. Θ. Γεροστάθης, *Αναπληρωτής Καθ. ΠΑΔΑ*
7. Β. Κατσαρδή, *Επίκουρος Καθ. ΠΑΘΕ*

Μάρτιος 2021

This doctoral thesis was financially supported by the Special Account for Research Grants (NTUA).

To Theo, family, friends and
everyone who put up with me
over the years ...

# Acknowledgements

To say that the pursuit of doctoral level studies is a daunting task is a massive understatement. It is thus without any exaggeration to state that the present endeavor would not have been feasible without the continuous support and encouragement of several people.

First I would like to express my gratitude towards my academic supervisor and mentor through all these years Prof. Kostas Belibassakis. Apart from introducing me to a new field of scientific exploration, he provided me with a solid compass which I dearly needed more often than not. His support and trust was invaluable to me, as well as a source of motivation. I also extend my gratitude towards Prof. Gerassimos Athanasoulis. His teachings on variational principles and other academic discussions were a source of inspiration and often provided me with a valuable insight into advanced topics that proved highly relevant to the present work.

I would be remiss if I did not express my sincere gratitude to Dr. Theodosios Papathanasiou for his extensive guidance and expert feedback on numerous aspects ranging from numerical computation issues to mechanics and the finite element method. I would also like to acknowledge the support of Assoc. Prof. Stylianos Markolefas who provided useful feedback and engaged into prolific discussions on mixed variational forms.

I would also like to thank my colleague and friend Dr. Evangelos Filippas for his support and a number of interesting discussions and collaborations through the years. Many thanks to my office-mates and friends, Dimitra Anevlavi, Iro Malefaki, Constantinos Mavroeidis and Nikolaos Nikoletatos - Kekatos for the many hours of vivid discussions on academic matters and otherwise. It has been a pleasure working side by side with them as they made even mundane days pleasant.

Finally, I thank my dear friend and graphic designer Evi Panagiwtopoulou for aiding in illustration production and visualization aspects of the present thesis. Special shout out to my family and friends that encouraged my efforts every step of the way and showed their unbounded support.

# Abstract

Ocean wave interaction with flexible floating structures finds numerous applications in marine science and technology as well as in ocean and polar engineering. The adjacent fields focus on the study of wave-structure-seabed interaction, targeting man-made structures and geophysical formations, such as ice shelves and ice floes, respectively. Very Large Floating Structures and ice formations share two distinct hydrodynamic features; their large dimensions compared to the incident wavelengths and their relatively low bending rigidity which renders flexural modes dominant. The foundations of the aforementioned problems in both fields are set in hydroelasticity and are characterised by challenges like the inherently large computational domains and the heterogeneity manifested in both the ocean waveguide and the structure. The treatment of heterogeneity in terms of variable bathymetry for the ocean environment and varying material properties and geometry for the structure remain formidable tasks even in the linear regime.

The thesis focuses on the treatment of hydroelastic interaction between ocean waves and large floating structures in an inhomogeneous setting. While both time and frequency domain analyses were undertaken, the present focuses primarily on the latter. Parts I-III, representing the bulk of the conducted research, are set in the frequency domain, while Part IV outlines developed numerical tools targeting transient phenomena.

In the *frequency domain*, confined in the linear regime potential theory is employed for the hydrodynamic modelling. The floating body is assumed to be thin and within the limits of elastic plate models. Depending on the structure slenderness and the excitation wavelength-to-plate thickness ratio, the elastic body is modelled using either the Classical Thin Plate Theory (CPT) or the higher order Reissner-Mindlin Plate theory accounting for first order shear deformation effects (FSDT).Furthermore, The slenderness of the structure justifies the adopted negligible-draft assumption. An *in vacuo* modal expansion for the plate deflection is employed to partially decouple the hydrodynamics from structural mechanics. The modal decomposition allows for the formulation of a series of component hydrodynamic subproblems in the inhomogeneous setting, posed only on kinematic considerations posed on the upper surface. Furthermore, by considering domain partitioning the typical radiation-type problem is written in terms of the velocity potential restrictions in the plate-covered and free-surface subregions supplemented by transmission conditions on the fictitious cylindrical interface.

For the numerical treatment, a weighted residual approach is subsequently employed to derive a permissive form of the hydrodynamic problems facilitating the construction of a FEM-based scheme. To this end, the typical radiation-type problem is re-cast into a mixed weak form by means of a Lagrange multiplier function defined on the interface between the plate-covered and free surface regions. The two-field formulation aims at the weak satisfaction of the essential continuity requirement across the transmission interface. The latter approach circumvents the complexity of constructing appropriate finite element subspaces that would *ab initio* satisfy the Dirichlet type constraint. Subsequently, the dimensionality reduction of the problems at hand is achieved by the introduction of suitable local-mode vertical representations for the velocity potentials in each subregion that enable the consistent satisfaction of the upper surface and seabed boundary conditions, respectively. The reduction ultimately yields the variational form of coupled-mode systems defined on the horizontal plane. The deduced weak forms permit the development of FEM schemes that employ conventional Lagrange elements, capable of $h-p$ refinement. Moreover, the numerical tool incorporates a Perfectly Matched Layer, featuring an unbounded absorbing function, to achieve the efficient truncation of the computational region. The convergence properties of the proposed PML-FEM scheme are initially investigated by means of the scalar Helmholtz equation and then extended to treat the single-mode vertical expansion for the velocity potential, reducing to the Modified Mild Slope Equation in the frequency domain, and finally to the multi-modal representation.

Finally, numerical results for a number of configurations are presented in both the 2D and 3D ocean waveguide. Extensive verification against 2D results found in the literature illustrate the accuracy of the method and showcasing its capabilities in modelling inhomogeneity.

In the *time domain*, the analysis is restricted to shallow water environment. Considering the 2D ocean strip, the structure is assumed to extend indefinitely in the direction normal to wave incidence, thus performing cylindrical bending under long wave action. The Shallow Water Equations are employed for the hydrodynamic modelling while the floating body response in waves is simulated with both CPT and Gao's beam model (Gao, 1996) in plain strain. The latter is able to account for moderately large deflections and strains. The proposed hydroelastic element able to treat the coupled equations feature $C^1$ interpolation for the strip response and $C^0$ for the velocity potential. Thus, the hydroelastic element incorporates cubic Hermite-shape functions for the approximation of the beam deflection/upper surface elevation and the strip slope, while quadratic Lagrange shape functions are employed for the approximation of the unknown velocity potential. The derived schemes can be employed in a number of applications in (a) ice shelf research and (b) marine technology. Details of the analysis are provided in the included scientific contributions (Part V).

# Εκτεταμένη Περίληψη

Η παρούσα διατριβή πραγματεύεται το πρόβλημα της αλληλεπίδρασης μεγάλων πλωτών κατασκευών με κυματισμούς βαρύτητας στο ανομοιογενές θαλάσσιο περιβάλλον. Αντικείμενο της διδακτορικής διατριβής είναι η μελέτη του προβλήματος με έμφαση στις επιδράσεις της ανομοιογένειας, καθώς και η παραγωγή αποδοτικών εργαλείων για τον υπολογισμό των χαρακτηριστικών του πεδίου σε χωρία μεγάλων διαστάσεων. Επιπλέον, επιδιώκεται η συστηματική εφαρμογή των παραπάνω στην προσομοίωση των κυματικών φαινομένων και στην διερεύνηση των παραμέτρων ιδιαίτερα σε ότι αφορά τις ελαστικές αποκρίσεις σωμάτων με γενικά χαρακτηριστικά και περιοχές μεταβαλλόμενης βαθυμετρίας. Βασικός ερευνητικός στόχος είναι η υποστήριξη της τεχνολογίας κατασκευής Μεγάλων Πλωτών Κατασκευών (Very Large Floating Structures ή VLFS), και η παράλληλη αξιοποίηση των αποτελεσμάτων στην πρόβλεψη των μηχανισμών διέγερσης υδροελαστικών φαινομένων σε ροές πάγου και καταστάσεων απόσχισης πάγου στη συνοριακή ζώνη μεταξύ παγετώνων και θάλασσας (Squire, 2018).

Η μελέτη των VLFS βρίσκει πληθώρα εφαρμογών στην παράκτια μηχανική με κοινά παραδείγματα των παραπάνω να είναι πλωτές εξέδρες ανεφοδιασμού, μαρίνες καθώς και πλωτοί αεροδιάδρομοι και κυματοθραύστες (Wang et al., 2006). Οι μεγάλες οριζόντιες διαστάσεις των κατασκευών ενδιαφέροντος, καθιστά τις ελαστικές παραμορφώσεις υπό κυματική καταπόνηση σημαντικές σε σχέση με τις κινήσεις στερεού σώματος. Επομένως, η μελέτη της απόκρισης των μεγάλων πλωτών κατασκευών εμπίπτει στην επιστημονική περιοχή της υδροελαστικότητας, δηλαδή της συζευγμένης αλληλεπίδρασης του ροϊκού πεδίου με την ελαστική παραμόρφωση του πλωτού σώματος. Επιπροσθέτως, οι Μεγάλες Πλωτές Κατασκευές μοιράζονται κοινά υδροδυναμικά χαρακτηριστικά με γεωφυσικές μορφές όπως τα στρώματα πάγου. Η έντονη κυματική διέγερση στρωμάτων πάγου έχει συνδεθεί με φαινόμενα αποσταθεροποίησης και κατακερματισμού τραπεζών πάγου και παγοκριπίδων. Η παλιρροϊκή δράση και η συνεχής καταπόνηση των γεωφυσικών μορφών, σε συνδυασμό με τις εγγενείς ατέλειες του πάγου οδηγεί σε καμπτική αστοχία και την τελική απόσχιση τμημάτων υλικού με προφανές περιβαλλοντικό κόστος και επίδραση στην τοπική ανθρώπινη δραστηριότητα. Ο καταγεγραμμένος κατακερματισμός των στρωμάτων πάγου στην Ανταρκτική και η σημαντική μείωση του θαλάσσιου πάγου στην Αρκτική, φαίνονται να επηρεάζουν άμεσα τις εμπορικές δραστηριότητες και να επιβεβαιώνουν την αρχή μιας σειράς κλιματικών διαταραχών χρίζοντας επομένως εντατικής μελέτης. Τέλος, τα κοινά

χαρακτηριστικά των δύο φαινομενικά ασύνδετων πεδίων εφαρμογής της υδροελαστικότητας πλωτών σωμάτων οδηγεί στην συχνή απο κοινού αντιμετώπιση στην επιστημονική βιβλιογραφία (Squire, 2008).

Σημειώνεται ότι λόγω έλλειψης χώρου η παρούσα εστιάζει στην ανάπτυξη αριθμητικής μεθοδολογίας για την μελέτη του υδροελαστικού προβλήματος στο πεδίο συχνοτήτων, ενώ στο τελευταίο μέρος του τεύχους παρουσιάζονται περιληπτικά σχήματα πεπερασμένων στοιχείων υψηλής τάξης που αναπτύχθηκαν κατά τη διάρκεια των διδακτορικών σπουδών με στόχο την μελέτη μεταβατικών φαινομένων σε περιβάλλον ρηχών υδάτων. Επισυνάπτονται οι σχετικές δημοσιεύσεις σε επιστημονικά περιοδικά.

Οι φυσικές ανομοιογένειες των συνόρων του θαλάσσιου κυματοδηγού και της γενικής γεωμετρίας του ελαστικού σώματος, καθώς και η ύπαρξη χωρίων μεγάλων διαστάσεων καθιστούν ιδιαίτερα πολύπλοκο τον χειρισμό ακόμα και του γραμμικοποιημένου προβλήματος. Με στόχο την ανάπτυξη αποδοτικών τεχνικών επίλυσης για το τρισδιάστατο πρόβλημα, παρουσιάζεται μια αριθμητική μεθοδολογία βασισμένη σε σχήματα πεπερασμένων στοιχείων σε συνδυασμό με συστήματα συζευγμένων ιδιομορφών που βασίζονται σε κατάλληλες κατακόρυφες αναπαραστάσεις του μιγαδικού δυναμικού.

Πιο συγκεκριμένα, στο πεδίο συχνοτήτων το τρισδιάστατο πρόβλημα διατυπώνεται με χρήση της θεωρίας απειροστού πλάτους για την μοντελοποίηση του υδροδυναμικού πεδίου, ενώ για την απόκριση του ελαστικού σώματος εξετάστηκαν οι θεωρίες λεπτής πλάκας Kirchhoff (CPT) καθώς και θεωρία Mindlin (Mindlin, 1951) για σώματα παραμορφώσιμα σε διάτμηση (FSDT). Υποθέτουμε την ύπαρξη στρώματος νερού με πεπερασμένο τμήμα της πάνω επιφάνειας να δεσμεύεται απο την παρουσία του ελαστικού σώματος. Οι μεγάλες οριζόντιες διαστάσεις της κατασκευής επιτρέπουν επιπροσθέτως την υπόθεση αμελητέας βύθισης, έτσι ώστε η άνω επιφάνεια του ρευστού να ακολουθεί την ουδέτερη γραμμή του πλωτού σώματος στο πεπερασμένο τμήμα της επιφάνειας σύζευξης που οριοθετεί την υδροελαστική περιοχή. Επομένως, η παρουσία του πλωτού σώματος δημιουργεί τις ιδεατές υποπεριοχές ελεύθερης επιφάνειας και υδροελαστικής σύζευξης. Εν συνεχεία, η ελαστική απόκριση αναπτύσσεται στις *in vacuo* ιδιομορφές της κατασκευής με στόχο την μερική αποσύζευξη της υδροδυναμικού πεδίου και του πεδίου παραμορφώσεων. Το συνολικό πεδίο αποσυντίθεται στις συνιστώσες του διαδιδόμενου κυματισμού (χωρίς την παρουσία του σώματος), του πεδίου περίθλασης καθώς και του πεδίου ακτινοβολίας λόγω της κίνησης του ελαστικού κινήσεων σώματος. Επιπροσθέτως, η συνιστώσα της ακτινοβολίας γράφεται ως επαλληλία λύσεων σε προβλήματα που αντιστοιχούν στην μοναδιαία φόρτιση από την εκάστοτε ιδιομορφή του ελαστικού σώματος, επιτρέποντας την διατύπωση μιας σειράς υπο-προβλημάτων ακτινοβολίας. Τα ανωτέρω προβλήματα ικανοποιούν στην ουσία μόνο τις κινηματικές παραδοχές του προβλήματος, συγκεκριμένα την εξίσωση των κάθετων ταχυτήτων για το ρευστό και το σώμα πάνω στην υδροελαστική επιφάνεια. Η σύζευξη που επιτρέπει τη σύνθεση της τελικής λύσης επιτυγχάνεται μέσω της ικανοποίησης της

δυναμικής συνθήκης στην βρεχόμενη επιφάνεια του σώματος που εκφράζει την ισορροπία των πιέσεων.

Σημειώνεται ότι η γενική τρισδιάστατη διατύπωση του υδροελαστικού προβλήματος (3D) εκφυλίζεται στο κατακόρυφο δισδιάστατο πεδίο (2D) με την υπόθεση κυματοδηγού με μη μεταβαλλόμενα χαρακτηριστικά κατά τη μία οριζόντια διεύθυνση ενώ γα την ελαστική πλάκα ισχύει επιπλέον η υπόθεση ότι η διάσταση της κατά την ανωτέρω διεύθυνση είναι σημαντικά μεγαλύτερη οδηγώντας σε κατάσταση κυλινδρικής κάμψης. Στην παρούσα διατριβή εξετάζονται και οι δυο περιπτώσεις 3D και 2D μοντελοποίησης του προβλήματος.

Δεδομένης της παραπάνω διατύπωσης του ολικού προβλήματος σε σειρά υποπροβλημάτων, η προτεινόμενη στρατηγική επίλυσης συνίσταται από διακριτά βήματα. Αρχικά επιζητείται η αριθμητική εύρεση των *in vacuo* ιδιομορφών για την περίπτωση ανομοιογενούς κατασκευής γενικού σχήματος, έπειτα η επίλυση του προβλήματος διάδοσης στον ανομοιογενή κυματοδηγό και στη συνέχεια ο χειρισμός του πεπερασμένου πλήθους προβλημάτων ακτινοβολίας που προκύπτουν από την περικομμένη αναπαράσταση της ελαστικής απόκρισης. Τέλος, για την ολοκλήρωση της σύζευξης επιδιώκεται η ικανοποίηση του ισοζυγίου των πιέσεων στην υδροελαστική επιφάνεια με δεδομένες τις λύσεις των ανωτέρω προβλημάτων. Η επίλυση των υδροδυναμικών προβλημάτων στον ανομοιογενή κυματοδηγό αλλά και του προβλήματος ελεύθερης ταλάντωσης της κατασκευής γενικού σχήματος επιτυγχάνεται αριθμητικά με τη μέθοδο των πεπερασμένων στοιχείων.

Με στόχο την κατασκευή των αριθμητικών σχημάτων υιοθετείται η μέθοδος Σταθμικών Υπολοίπων για την παραγωγή κατάλληλων ασθενών μορφών των επιμέρους υδροδυναμικών προβλημάτων. Για τη σειρά των προβλημάτων ακτινοβολίας απαιτείται επιπροσθέτως η ικανοποίηση συνθηκών συνέχειας για το δυναμικό της ταχύτητας και της κάθετης παραγώγου στην κυλινδρική διεπιφάνεια ανάμεσα στις περιοχές ελεύθερου ρευστού και υδροελαστικής σύζευξης. Για την αποφυγή της *ab initio* ικανοποίησης της ουσιώδους απαίτησης συνέχειας στην διεπιφάνεια, επιλέγεται η ασθενής ικανοποίηση της παραπάνω μέσω μιας συνάρτησης πολλαπλασιαστή Lagrange. Επομένως, το τυπικό πρόβλημα επανατοποθετείται σε μικτή μορφή που επιτρέπει την επιλογή συμβατικών χώρων για τις συναρτήσεις δοκιμής και την κατασκευή ενός ευέλικτου αριθμητικού σχήματος.

Εν συνεχεία, επιχειρείται η μείωση της διάστασης των ασθενών προβλημάτων που παρήχθησαν, υιοθετώντας κατάλληλες κατακόρυφες αναπαραστάσεις για το υδροδυναμικό πεδίο. Οι επιλεγμένες αναπαραστάσεις που καλούνται να ικανοποιούν τις κινηματικές συνθήκες της στήλης του ρευστού διαφέρουν στις δυο υποπεριοχές. Για την περιοχή ελεύθερης επιφάνειας χρησιμοποιείται η κλασσική κατακόρυφη αναπαράσταση που προκύπτει από χωρισμό μεταβλητών στο στρώμα ρευστού. Η φυσική αναπαράσταση ενισχύεται από πρόσθετη μορφή που στοχεύει στην συνεπή ικανοποίησή της κινηματικής συνθήκης στον κεκλιμένο πυθμένα ακολουθώντας την εργασία των Athanassoulis and Belibassakis (1999). Στην υδροελαστική περιοχή επιλέχθηκε εναλλακτικά η βάση του προκύπτει από

το κατακόρυφο πρόβλημα ιδιοτιμών με επιβαλλόμενες ομογενείς Dirichlet συνθήκες. Στην αναπαράσταση, εκτός από τον πρόσθετο όρο για την ικανοποίηση της συνθήκης του πυθμένα προστίθεται και μια μορφή που επιτρέπει την ικανοποίηση της κινηματικής συνθήκης στην άνω επιφάνεια. Η παραπάνω διαδικασία παράγει ασθενή συστήματα συζευγμένων ιδιομορφών, ενώ η γεωμετρικά σύμμορφη διεπιφάνεια επιτρέπει ομοίως την ανάπτυξη των συναρτήσεων Lagrange (που ορίζονται στη διεπιφάνεια) σε οποιαδήποτε απο τις δύο βάσεις οδηγώντας ετσι στη μικτή ασθενή διατύπωση των παραπάνω. Τέλος, έχοντας αποφύγει την πολυπλοκότητα της κατάλληλης κατασκευής υπόχωρων συναρτήσεων δοκιμής με ενσωματωμένες ουσιώδεις συνθήκες, χτίζεται ενα $C^0$ σχήμα πεπερασμένων στοιχείων που χαρακτηρίζεται απο $h-p$ προσαρμοστικότητα.

Για την αριθμητική επίλυση των προβλημάτων ακρινοβολίας εφαρμόστηκε επιπροσθέτως ενα στρώμα απορρόφησης PML με σκοπό την ελαχιστοποίηση των αριθμητικών ανακλάσεων. Στα πλαίσια της παρούσας εργασίας επιλέγεται μια συνάρτηση απορρόφησης με ιδιομορφία για το στρώμα. Οι ιδιότητες του σχήματος πεπερασμένων στοιχείων με PML εξετάζονται αρχικά στο εξωτερικό πρόβλημα Helmholtz με κυκλικό σκεδαστή, ενώ στη συνέχεια επεκτείνεται στην περίπτωση της εξίσωσης Mild Slope στο πεδίο συχνοτήτων και τέλος στην περίπτωση της κατακόρυφης αναπαράστασης του δυναμικού.

Στη συνέχεια, η μέθοδος των πεπερασμένων στοιχειών εφαρμόζεται επίσης για την επίλυση του προβλήματος ελεύθερης ταλάντωσης της ανομοιογενούς κατασκευής με γενική γεωμετρία. Κατα την μοντελοποίηση του δισδιάστατου υδροελαστικού προβλήματος (2D), η θεώρηση ημιάπειρης πλάκας υπό κυλινδρική κάμψη επιτρέπει τη χρήση κλασσικών $C^1$ προσεγγίσεων. Στην περίπτωση ανομοιόμορφης, παραμορφώσιμης σε διάτμηση δοκού, η κατακόρυφη κίνηση εκφράζεται μέσω των συζευγμένων εξισώσεων ισορροπίας δυνάμεων και ροπών που επιδέχεται $C^0$ προσέγγιση υψηλής τάξης. Για τον αριθμητικό υπολογισμό των ιδιομορφών κατασκευών με πεπερασμένες διαστάσεις, χρησιμοποιούνται δισδιάστατα στοιχεία πλακών. Συγκεκριμένα χρησιμοποιούνται τρίγωνα Discrete Kirchhoff (DKT) και Discrete Shear (DST) ($C^0$ προσέγγισης). Η ιδιαιτερότητα των παραπάνω στοιχείων είναι η διακριτή ικανοποίηση των κινηματικών συνθηκών που αντιστοιχούν στις θεωρίες λεπτής πλάκας (CPT) και πλάκας σημαντικού πάχους (FSDT) αντίστοιχα.

Αριθμητικά αποτελέσματα παρουσιάζονται στις δύο και τις τρεις διαστάσεις. Η μεθοδολογία, συγκρινόμενη με πειραματικά δεδομένα και πληθώρα αριθμητικών αποτελεσμάτων από τη βιβλιογραφία κατέγραψε ικανοποιητική ακρίβεια στις δύο διαστάσεις, ενώ καταδεικνύεται το βασικό πλεονέκτημα της που είναι ο χειρισμός ανομοιογενείων στις ιδιότητες του ελαστικού σώματος, του γενικού σχήματος και των μεταβολών της βαθυμετρίας.

# Contents

# List of Figures

# List of Tables

# List of Symbols

Several symbols have a different meaning depending on the context and appear multiple times in the following list.

### Variables and Operators

| | |
|---|---|
| $\partial_{(\cdot)}$ | partial derivative |
| $\mathbf{n}$ | normal vector |
| i | unit imaginary number $\sqrt{-1}$ |
| $\mathbf{x}$ | Horizontal variables $\mathbf{x} = (x_1, x_2)$ |

### Greek Symbols

| | | |
|---|---|---|
| $\eta$ | upper surface elevation, | Chapter 1 |
| $\Gamma_{(\cdot)}$ | boundary partition, | Chapter 1 |
| $\gamma_{x_1}, \gamma_{x_2}$ | shear angles about the $x_1$ and $x_2$ axes respectively, | Chapter 2 |
| $\lambda$ | Lagrange Multiplier function, | Chapter 3 |
| $\boldsymbol{\gamma}$ | Complex absorbing functions, | Chapter 6 |
| $\omega$ | angular frequency, | Chapter 1 |
| $\Omega^1$ | free-surface region, | Chapter 1 |
| $\Omega^2$ | plate-covered region, | Chapter 1 |
| $\Omega^c(x, z)$ | bounded subregion in 2D, | Chapter 3 |
| $\partial\Gamma_{(\cdot)}$ | boundary partition in 2D, | Chapter 3 |
| $\varphi_\ell$ | $\ell^{\text{th}}$ radiation wave field, | Chapter 1 |
| $\tau(\mathbf{x})$ | plate thickness, | Chapter 2 |

| | | |
|---|---|---|
| $\theta$ | angle of wave incidence, | Chapter 3 |
| $\theta_l$ | PML layer thickness, | Chapter 6 |
| $\theta_{x_1}, \theta_{x_2}$ | rotations about the $x_1$ and $x_2$ axes respectively, | Chapter 2 |
| $\lambda$ | wavelength, | Chapter 1 |
| $\varphi(\mathbf{x})$ | time-harmonic velocity potential function, | Chapter 1 |

**Other Symbols**

| | | |
|---|---|---|
| $c_\ell$ | $\ell^{\text{th}}$ complex amplitude coefficients, | Chapter 1 |
| $\mathcal{D}(\mathbf{x}, z)$ | 3D fluid layer, | Chapter 1 |
| $\mathcal{D}^c(x, z)$ | 2D fluid layer, | Chapter 3 |
| $w_\ell(\mathbf{x})$ | $\ell^{\text{th}}$ structural bending mode, | Chapter 1 |
| $g$ | acceleration of gravity $9.81\,\text{ms}^2$, | Chapter 1 |
| $h(\mathbf{x})$ | depth function, | Chapter 1 |
| $k_s$ | shear factor, | Chapter 2 |
| $w(\mathbf{x})$ | plate deflection, | Chapter 1 |

**Acronyms / Abbreviations**

| | |
|---|---|
| BEM | Boundary Element Method |
| FEM | Finite Element Method |
| CPT | Classical Plate Theory |
| PML | Perfectly Matched Layer |
| SDT | Shear Deformation Theory |
| WRM | Weighted Residuals Method |

# Introduction

This introductory chapter explores the problem of floating-body hydroelasticity in the ocean setting. The latter constitutes the theme of the present thesis and is highly relevant to marine engineering applications as well as to the study of ice formations in Polar Regions. A general introduction to the context, research questions and outline of the present thesis are given. Furthermore, a literature review on floating-body hydroelasticity is attempted, followed by the statement of thesis objectives and proposed methodology. Finally, the novelties and original contributions of the present work are summarized at the end of the chapter.

## Context and Aim of the Thesis

In the past decades, in line with advancements in marine engineering and technology, the study of hydroelastic interaction between large floating elastic bodies, commonly referred as Very Large Floating Structures (VLFSs), and ocean waves has received great scientific attention.

VLFSs begun as a futuristic vision, documented as early as the late 1800s, when a man-made island became the centerpiece of the Jules Verne novel *'Floating island'*. The VLFS concept was inspired by population densification in coastal areas and the bitter realization of its detrimental effects on both social and environmental grounds. The numerous socio-economic drives facilitating the conceptual maturity of VLFS is thoroughly explored in Wang et al. (2006). Initially the need for commercial space in congested port areas led to costly land reclamation solutions. Soon however, the use of multi-purpose ballast structures, servicing as operational docks, was proved to be an environmentally-friendly and versatile alternative that gained traction as marine technology evolved. Subsequently, the VLFS idea was extended to fit military applications, civil infrastructure and other facets of industry. Typical project examples include bridges, breakwaters, solar and wind power plants, oil and gas drilling and storage facilities, emergency bases and generic industrial space. VLFS applications also extend to aquaculture and recreational activities. Famous examples of existing VLFS projects include the 1km long floating test runaway known as the Mega-Float deployed in Tokyo Bay, the floating oil storage bases in Shirashima and Kamigoto islands, the floating Washington bridge in Seattle and the floating piers in Ujina port (Wang and Tay, 2011; Watanabe et al.,

**(i)** Mega-Float, Tokyo Bay. **(ii)** Oil storage base, Kamigoto island.

**Figure 1** Notable applications of pontoon type VLFSs. Source: Watanabe et al. (2004)

2004). Notably, VLFS can be classified in numerous ways, the majority of them based on technological features. However, since VLFS technology is outside the scope of this thesis, the following discussion adopts an angle suitable to drive the relevant research points. For a better insight into VLFS technology the interested reader is directed to the informative state-of-the art reviews found in the literature, i.e. Dai et al. (2018), Lamas-Pardo et al. (2015), Wang and Tay (2011), Ohmatsu (2005),Kashiwagi (2000) among others. Following Lamas-Pardo et al. (2015) principal VLFS design concepts are, also to the author's opinion, most conveniently distinguished by deployment location, namely whether the structure is to be deployed *near-shore* or *offshore*. The ocean environment plays a profoundly critical role in the design of floating structures. When deployed in sheltered near-shore regions, like bays or lagoons, floating structure design can assume a shallow draft and structures are commonly referred as pontoon type or 'mat-like' in the literature. The latter design features a ballast substructure with large horizontal dimensions compared to thickness offering stability in calm environments while minimising manufacturing and maintenance costs. The flexibility of such structures is significantly increased which renders the hydroelastic effects dominant over rigid body motions, leading to the given floating structure-wavefield interaction to be suitably treated within the realm of hydroelectricity.

When offshore deployment is considered, the semi-submersible design type is more suitable for open ocean applications, such as oil and gas platforms, as it can sustain large amplitude wave forcing. These structures are significantly thicker and do not reach the same slenderness ratios as their near-shore counterparts. The semi-submersible design type is exemplified in the literature by the Mobile Offshore Base or MOB referring to modular barge-like structures where modules are hinged together to form multi-purpose offshore spaces employed for landing, docking and vessel maintenance. While MOBs are often classified as VLFS in the literature, e.g. Ding et al. (2017), it is not straightforward that they share the same unique hydrodynamic features with near-shore applications of the latter. As the number of modules increases however,

**(i)** Gentz Ice Shelf, West Antarctica, Image Credit: NASA/J. Harbeck.

**(ii)** Saline Ice, Arctic, Image Credit: AWI/M. Hoppmann.

**Figure 2** Images of Gentz Ice Shelf in West Antarctica and saline ice fields in the Arctic.

the response of a homogenised MOB structure can be calculated by the same methodologies founded in floating body hydroelasticity.

In a related note, the same hydrodynamic features are exhibited by geophysical formations such as ice shelves and ice floes floating in Polar Regions Fig. 2. Similarly to VLFS, ice formations feature long horizontal dimensions and undergo oscillatory flexural motions under wave excitation. Despite the inherent similarities the scientific fields of marine engineering and sea-ice modelling progressed in parallel for decades mainly disregarding each other, as illustrated in Squire (2008).

To delve further into the motivation behind sea-ice research it is noted that Polar Regions form a transient terrain, hosting crucial climate regulating mechanisms. The scientific attention received by ice self 'disintegration', referring to sudden ice shelf retreat events, is indicative of the grave importance of the matter (Brunt et al., 2011). Calving of glaciers and ice shelves is a phenomenon endorsed by simultaneous processes, the primary factor being the ice structure itself, along with local temperature. Tidal effects and wave excitation add to the inherent structural imperfections in the ice body, while oscillatory bending caused by the excitation ultimately leads to the break off of ice shelves or the splitting of ice sheets. The detrimental effects of gravity wave forcing on Antarctic ice shelves, are explored in Bromirski and Stephen (2012). Moreover, the adverse effects of climate change are linked to increasingly energetic seas (Young et al., 2011), which pose a major threat for saline ice formations (floes) located at the Marginal Ice Zone (MIZ). The MIZ, located in the periphery of an ice shelf, essentially buttresses the large geophysical formations by attenuating incoming wavetrains. When the MIZ is reduced larger sums of energy ultimately reach the ice shelf increasing the likelihood of its destabilisation and eventual collapse. Apart from the obvious environmental hazard, caused by sea ice depletion, the floating ice formations are also endangering commercial ship-routes and the presence of off-shore structures.

To summarise the above points, floating-body hydroelasticity encapsulates the basic principles involved in the technological advancement and design of Very Large Floating Structures

(VLFS) as well as in sea ice modelling. Wave-induced structural response and its underlying effect on the hydrodynamic field are important for the in-depth understanding of physical processes like ice shelf calving events (Ilyas et al., 2018; Papathanasiou and Belibassakis, 2018; Papathanasiou et al., 2019) and valuable for the robust design of engineering structures operating nearshore (Karperaki et al., 2016; Nguyen et al., 2019). The similarities shared between the aforementioned geophysical and man-made structures are (a) their low bending rigidity, (b) their inherently complex geometries and material inhomogeneity and (c) their deployment over large horizontal dimensions where the inhomogeneous ocean setting must be addressed, i.e. bathymetric variations. The above common ground allows for the development of joint computational tools for the general treatment of the coupled wave-structure-seabed interaction.

The intricacies found in the numerical treatment of the above mentioned problems lay on the very same distinct features. Namely, complexity is raised by the large domains of interest and the inherent geometric and material inhomogeneity found in the both structure and waveguide. It is the aim of the present thesis to address the aforementioned complexities and propose novel methodologies for the treatment of the hydroelastic problem featuring an elastic floating body with large horizontal dimensions in the inhomogeneous ocean setting. To formulate the specific research objectives, an account of the relevant literature follows.

## Background Literature

As already stressed, the foundations of wave-floating structure interaction are set in the field of hydroelasticity which is concerned with the coupled fluid and deformable body motions. There exists an established corpus of relevant work focusing on a number of applications ranging from ship hydroelasticity (Bishop and Price, 1976; Jiao et al., 2019; Kim et al., 2013) to the study of VLFS and floating ice sheet response.

In the literature, in order to treat the coupled problem at hand, potential theory is commonly employed for the hydrodynamics while reduced elasticity theories are adopted for the structural modelling. There are several works that opt for higher fidelity in their physical modelling, as in Huang et al. (2019) where an OpenFOAM based methodology is proposed for the treatment of wave-sea ice coupling. The work features the Navier-Stokes equations for the description of the flow field, while coupled with Volume of Fluid methodologies a simulation of overwash phenomena is achieved. In the same note, Kalyanaraman et al. (2020) employ the linear elasticity equations for the structure coupled with potential theory for the hydrodynamic field. These attempts in higher fidelity modelling are significantly aided by the maturity of modular multi-physics software packages and the availability of open source numerical tools and are valuable in providing an insight into complex physical phenomena. As mentioned in Korobkin et al. (2011) however, CFD and elasticity codes coupling is far from trivial and need rigorous theoretical reasoning. To the author's opinion the above claim is still relevant to this

day which illustrates the merit of theoretical and numerical studies based on lower fidelity physical modelling.

Returning to the bulk of floating-body hydroelasticity research, physical modelling is predominantly based on potential flow theory for the hydrodynamics and structural mechanics theories for the elastic body response. Literature can be most efficiently divided into linear and non-linear approaches, with a viable subsequent separation into time and frequency domain methods. The non-linear approach targets large flexural motions in moderate seas, irregular waves and other transient phenomena crucial to VLFS design like wave drift forces and slamming loads. In Cheng et al. (2017) the 2D non-linear interaction of regular waves with a floating elastic plate over non-uniform topography is examined in a fully non-linear numerical wave tank. Generally, a varying degree of either structural or fluid non-linearity is included in the modelling. Notable examples are the works of Sturova et al. (2009), Xia et al. (2004) and Ertekin and Xia (2014) where the linear plate is directly coupled with Boussinesq-type models, and the Green-Naghdi equations. In Hegarty and Squire (2004, 2008) a perturbation approach is adopted to derive non-linear models for the study of the hydroealastic interaction between large amplitude ocean waves and a thin solitary ice floe. In Belibassakis and Athanassoulis (2006) a weakly non-linear, coupled-mode technique is proposed for the hydroelastic analysis of a thin plate over a general bottom topography. In Chen et al. (2003) the non-linear Von Karman plate is coupled with Airy's theory to account for large deflections and assess the influence of membrane forces. Finally, the relevant literature also focuses on the consideration of a non-linear coupling mechanism, separate from field modelling, leading to the simulation of slamming related phenomena (Sun et al., 2021).

Focusing in the linear regime, the commonly adopted small wave amplitude assumption leads to the exclusion of non-linear and viscous effects, and is further justified by structural slenderness. In conjunction to the above kinematic considerations for the fluid, plate theories like the Classical Thin Plate (Kirchhoff-Love plate) are widely employed for the dynamic response of the floating body (Faltinsen, 2015; Wang et al., 2006; Watanabe et al., 2004). The linearized problem is effectively treated in the frequency domain with the majority of published works in the field employing a modal expansion technique, aiming at the decoupling of the structural response and the hydrodynamics, or proposing a direct solution of the coupled equations (Watanabe et al., 2004). In modal expansion techniques, the structural oscillation is expressed as a series expansion involving a class of basis functions. By means of the underlying linearity assumption, the problem is decomposed into component diffraction and a series of radiation problems corresponding to structural oscillations (Newman, 1994; Taylor and Waite, 1978). For the modal expansion of the floating body response, the 'dry' *in vacuo* modes of the unconstrained structure constitute a natural and common choice (Kashiwagi, 1998; Wu et al., 1995). The hydrodynamics and the elastic response are fully decoupled allowing for the adoption of different analytical or numerical tools, facilitating the emergence of numerous computational schemes in the frequency domain (see Squire (2008); Wang et al. (2006) for a

more thorough literature review). In this decomposed regime, the motion equation of the plate needs to be satisfied in order to complete the fluid-structure coupling.

While in the majority of published works on hydroelasticity, the structure is modelled as a thin plate, attempts have been made to account for the rotary inertia and shear deformation effects under wave forcing by means of Mindlin's shear deformable plate theory (Mindlin, 1951), e.g. Fox and Squire (1991), Zhao et al. (2008) and Praveen et al. (2019). Recently, Praveen and Karmakar (2019) considered the hydroelastic behaviour of a floating Mindlin plate over variable bathymetry. The latter work however, confined in the 2D strip, allows for a stepwise variation of the seabed. Considering general bathymetric profiles, Kyoung et al. (2005) employed a modal expansion of the elastic response in terms of the *in vacuo* bending modes of a rectangular Kirchhoff plate in conjunction with FEM discretization in the 2D fluid region in order to capture the general waveguide boundary. Thus, the bottom boundary condition n the varying seabed is explicitly satisfied. It is noted that extrapolated in the 3D setting, the latter method would require the 3D meshing of the waveguide which raises the computational cost considerably. In Liu et al. (2020), the variable bathymetry is approximated by a series of flat steps while local, multi-modal vertical eigenfunction expansions are employed for the wave potential representation. The aforementioned method employs a discrete modules approach for the structure simulation, which although intuitive for marine structures is not convenient for geophysical formation modelling. Belibassakis and Athanassoulis (2005) proposed a continuous coupled-mode technique for the hydroelastic analysis of a uniform thin, semi-infinite plate with shallow draft, floating over variable bathymetry regions. The bottom boundary condition in the non-separable domain is consistently satisfied by means of an additional 'sloping bottom mode' employed in the potential representation Athanassoulis and Belibassakis (1999). A highly desirable feature of the above work is that it leads to dimensionality reduction with no underlying assumptions with respect to the bottom slope or curvature. The method was later extended for the treatment of the full 3D bathymetric effects in Gerostathis et al. (2016). The latter analysis was restricted however to rectangular, homogeneous plates.

In a related note, single-mode and multi-mode vertical expansions were also employed by Porter and Porter (2004) and Bennetts et al. (2007) respectively in the 2D scattering problem by a thin plate of variable thickness and non-negligible draft. In the aforementioned works a variational principle is appropriately augmented by an auxiliary functional featuring a Lagrange multiplier function in order to weakly satisfy continuity conditions across the fluid-structure interface. Finally, in Belibassakis and Athanassoulis (2009) the continuous coupled-mode formulation, introduced in Belibassakis and Athanassoulis (2005), is extended for the case of an infinite thin plate with variable thickness and non-negligible draft, while in Athanassoulis and Belibassakis (2009) the formulation is further extended to account for an infinite structure of moderate thickness.

# Thesis Overview

## Objectives and Methodology

The present thesis aims at the development of novel methods for the simulation and study of the hydroelastic interaction between linear ocean waves and large, floating bodies in a general inhomogeneous setting. The main objective is the derivation of suitable mathematical formulations for the problem at hand, targeting the development of robust numerical tools based on the FE method. More specifically the proposed methods, constructed to treat both frequency domain and transient hydroelastic problems, account for;

- geometric and material inhomogeneity in the floating, elastic body.
- shear deformation effects, that become significant as the incident wavelength to the structure is comparable to its thickness.
- general bathymetric profiles and the consistent treatment of their effects.

In the *frequency domain*, the general 3D ocean waveguide with a finite section of the upper surface constrained by the presence of a floating elastic body is considered. Subsequently, instead of directly tackling the coupled equations of structural and fluid motion, the modal expansion technique is employed to express the plate response as a series representation. The aforementioned expansion, allows for the formulation of a series of component radiation problems corresponding to the unit-amplitude modal flexure of the inhomogeneous structure (Bishop and Price, 1976; Taylor and Waite, 1978). Such 'component' radiation problems are derived on solely kinematic considerations, which are posed on the hydroelastic surface, thus achieving the decoupling of structural dynamics and fluid flow. Furthermore, the plate modal expansion is prolific in a regime where the unknown velocity potential is decomposed into its radiation and diffraction components (Taylor and Eatock Taylor, 2007), which is a common in seakeeping practices. The combined approach permits the total wavefield solution to be expressed as the summation of component solutions to distinct hydrodynamic subproblems. Such decomposition techniques, as opposed to hydroelastic schemes that consider the coupled equations of motion directly, employ a suitable set of basis functions to represent the elastic body response. The 'dry', *in vacuo* modes of the structure present a natural choice. The basis, as opposed to 'wet' modes, essentially neglects the hydrodynamic pressure field effects which are not known *a priori* (Newman, 1994). The choice implicitly leads to all hydrodynamic loads to be externally applied to the structure (Bishop and Price, 1976).

The benefits of the employed decomposition approach, featuring the 'dry' modes for plate response representation, over hydroelastic schemes are listed below;

- ☐ The *ab initio* satisfaction of the free plate edge conditions. The employment of 'dry' flexural modes in the deflection representation guarantees the satisfaction of zero-moment and zero-shear conditions on the plate edges. Considering finite structures of general

geometry, the explicit satisfaction of free-edge conditions can become computationally cumbersome. Additionally, the 'dry' mode approach bypasses the impediment of reformulating the free edge-conditions when different plate theories are employed for structural modelling, thus enhancing the versatility of the method. Notably, the relevant complexity is transferred to the *in vacuo* basis calculation, i.e. the solution of a free vibration problem for the unconstrained, inhomogeneous structure.

- ☐ The decomposition, apart from the partial decoupling of structural motion from the hydrodynamics, allows for the formulation of a series of significantly 'simpler' subproblems. These subproblems are posed solely on kinematic considerations for the hydrodynamics and straightforwardly assume generalizations in an inhomogeneous setting. Another related benefit is the parallelisation potential of the proposed method since in general the formulated subproblems can be tackled independently.

As mentioned in the prequel, plate response decomposition leads to the formulation of a series of component hydrodynamic problems. The total wavefield is expressed as the summation of component solutions corresponding; to the propagating wavefield, computed over the inhomogeneous waveguide without the presence structure, the diffracted solution due to the body remaining fixed in waves and a series of radiation component solutions corresponding to the unit-amplitude flexural modes of the structure. Notably, all of the component subproblems are treated numerically due to the inherent inhomogeneity. Since the total solution accuracy is heavily dependent on the achieved accuracy in each component solution the approach could be labelled 'inefficient' in terms of computational resources compared to a direct approach. However, mature modular methods developed separately for the treatment of hydrodynamics and reduced elasticity theories serve well the proposed approach. Additionally as the series of problems are essentially decoupled, parallel processing can significantly accelerate the proposed method and make it competitive.

Next, towards the construction of FEM-based schemes a Weighted Residuals approach is adopted for the derivation of suitable permissive weak forms of the component hydrodynamic problems. For the radiation-type subproblems, referring to those that assume radiative solutions at infinity, continuity restrictions must hold on the cylindrical interface between the free-surface and plate-covered subregions. To circumvent the complexity of constructing suitable FEM subspaces that *ab initio* satisfy the essential conditions on the interface, a constrained reformulation of the above typical problem is considered. To this end, a Lagrange multiplier function, defined on the fictitious interface, is employed to derive an alternative mixed-field variational formulation aiming at the weak satisfaction of continuity requirements across the interface.

Subsequently, appropriate multi-modal representations for the unknown velocity potential functions are employed to achieve the dimensionality reduction of the deduced variational forms, valid on the prismatic waveguide. The vertical representations are appropriately

constructed as to explicitly satisfy the kinematic conditions on the fluid column, in both free-surface and plate covered subregions. Moreover, both employed vertical structures are enhanced by an additional mode that aims at the consistent satisfaction of the boundary condition on the sloping seabed, originally introduced in Athanassoulis and Belibassakis (1999).

Concerning the modelling of the floating body, the Kirchhoff-Love thin plate theory (CPT) and the First Order Shear deformation theory (FSDT), able to simulate the dynamics of moderately thick plates by accounting for first order shear deformation effects and rotary inertia, are employed. In the context of the proposed method, structural modelling is essentially reduced to the consideration of a free vibration problem for the unconstrained inhomogeneous body and the satisfaction of pressure equilibrium on the wetted surface. The former is solved numerically by means of the finite element method to account for material and geometric inhomogeneity, while the latter completes the coupling. Enforcing the dynamic condition weakly by a Galerkin scheme deduces the complex amplitude coefficients employed in the plate and radiation wavefield expansions that facilitate the final solution composition.

In the *time domain*, the analysis is restricted to the 2D inhomogeneous ocean waveguide. In this case, the coupled equations of fluid and structural motion are tackled directly. The slender, elastic body is modelled again by means of reduced elasticity theories, while pressure equilibrium is considered as the coupling mechanism. Confined in shallow depth, the Shallow Water Equations are employed for the hydrodynamic modelling. The thin, inhomogeneous elastic strip structure that is assumed to undergo cylindrical bending under wave excitation, is modelled by the CPT and Gao's nonlinear theory under plane strain assumptions (Gao, 1996). The latter, formulated with large deflection but small strains assumption, was chosen as to conduct a preliminary assessment of nonlinear effects in the structural modelling. The Weighted Residuals Method is once again employed for the derivation of an equivalent weak coupled problem for the solution of which a FE scheme is subsequently devised. Special hydroelastic elements are constructed for the spatial discretization of the 1D system of equations. The elements implement a $C^0$ approximation for the unknown velocity potential function and $C^1$ for the beam deflection. The discrete system is subsequently integrated in time by means of a time marching scheme.

It is noted that due to space considerations, the analysis of the transient problem is only briefly delineated at the last part of the thesis, while the corresponding research contributions in scientific journals are also included for the reader's reference.

## Outline

The thesis is divided in five Parts. Parts I-III, contemplate the problem formulation in the frequency domain which is the main focus of the present manuscript. In Part IV, the modelling of transient hydroelastic phenomena in a shallow-water regime is examined. The final part is comprised of Appendices with relevant added content.

Part I, containing Chapters 1–4, focuses on the physical and mathematical modelling of the problem at hand.

In *Chapter 1*, the physical considerations and assumptions employed in the mathematical modelling of the linear hydroelastic problem are explored in detail. The linear problem in the frequency domain is decomposed in its radiation and diffraction components while the plate response in expanded in its *in vacuo* flexural modes. The latter results in a series of hydrodynamic subproblems assuming radiative solutions to infinity, coined under the term 'radiation-type' for simplicity, and a transmission problem in terms of the unknown propagating wavefield solution in the 3D waveguide, neglecting the structure. The employed solution strategy focuses on the numerical treatment of the aforementioned subproblems and is presented at the end of the chapter.

In *Chapter 2*, the basic physical considerations describing the structural motion of the floating body in the adopted regime are discussed. For completion, CPT and FSDT theories, along with the corresponding free vibration problems employed in the thesis context, are briefly presented.

In *Chapter 3*, the decomposed hydrodynamic subproblems are recast in a weak form as a stepping stone towards the construction of a FEM-based numerical scheme. The Weighted Residuals Method is adopted for the weak form derivation. Radiation-type problems assume a mixed, two-field variational formulation by means of a Lagrange multiplier function which is employed for the weak satisfaction of transmission conditions across subdomain interfaces.

*Chapter 4* presents the dimensionality reduction of the deduced weak problems by means of a vertical multi-mode representation for the wave potential.

The next part, Part II (Chapters 5–7) focuses on the implementation of the Finite Element Method for the solution of the reduced weak problems and other computational aspects of the proposed numerical scheme.

In *Chapter 5*, the finite element approximation spaces and domain partitions for the 1D and 2D formulations of the reduced hydrodynamic subproblems are constructed. The discrete weak problems are derived and discussed. Moreover, the adopted $C^1$ and $C^0$ approximations for the 1D and 2D structural eigenvalue problems respectively are briefly presented.

*Chapter 6* focuses on domain truncation techniques. An Optimal Perfectly Matched Layer is implemented in the mixed weak forms. Numerical investigation of the PML-FEM scheme is carried out for the scalar Helmholtz equation in the 2D plane featuring a circular inclusion. Applications in the inhomogeneous ocean waveguide are also examined to assess the robustness of the numerical scheme.

In *Chapter 7*, Galerkin schemes aiming at the satisfaction of the pressure condition on the wetted surface and the calculation of the complex amplitude coefficients is presented.

Part III, summarizes the numerical results obtained in the 2D and 3D ocean wave guide.

In *Chapter 8*, numerical results for a series of configurations are presented in the 2D waveguide, while *Chapter 9*, focuses on results derived in the 3D setting. A series of comparisons

against results obtained in the literature are carried out in 2D, showing the excellent agreement of the present method with established research.

The last part of the thesis, Part IV summarizes the key elements of the proposed methods for time domain analysis of the hydroelastic problem.

All produced algorithms were implemented in MATLAB and the thesis manuscript was compiled in LaTeX.

## Original Contributions

The present thesis introduces FEM-based numerical schemes for the hydroelastic interactions in the inhomogeneous ocean wave guide.

In the *frequency domain*, a novel solution strategy is proposed for the treatment of the hydroelastic interactions between linear waves and floating, elastic bodies of a general geometry in the inhomogeneous ocean environment. Notable contributions in the field are given in the points below,

- A mixed formulation is introduced to recast variational, 'radiation-type' subproblems as saddle-point. The latter is explored in Chapter 3. By considering a mixed weak form of the problem at hand, the complexity of constructing conforming trial function spaces that *ab initio* satisfy the Dirichlet type conditions on the interface between free-surface and plate-covered regions is avoided. The employed Lagrange multiplier function allows for the weak satisfaction of transmission on the interface, while the alternative formulation permits the construction of conventional approximation subspaces for FE implementation. The latter approach leads to flexible FEM-based schemes, susceptible to *h-p* refinement. Moreover, the formulation hold value for the theoretical investigation of stability conditions.

- Towards the dimensionality reduction of the problems defined in the prismatic waveguide, enhanced multi-modal vertical representations for the velocity potential functions are employed following the works of Athanassoulis and Belibassakis (1999), Belibassakis and Athanassoulis (2005) and Gerostathis et al. (2016). The constructed FEM-based scheme targets leads to the relaxation of the $C^2$ smoothness requirement introduced in the latter contributions, thus enabling the treatment of more general bathymetric profiles, while the numerical scheme remains rapidly convergent. The generalised multi-modal Kantorovich approach for the dimensionality reduction of the weak hydrodynamic problems is examined in Chapter 4).

- A PML-FEM scheme is introduced for computational domain truncation. Following the work of Bermúdez et al. (2004) on the exterior Helmholtz problem, an unbounded absorbing function is employed for solution attenuation in the inhomogeneous waveguide.

The scheme is initially adapted to treat the Modified Mild Slope Equation (MMSE) and subsequently for intermediate depth and the multi-modal representation of the unknown velocity potential. In Chapter 6, numerical investigation of the proposed scheme and its convergence properties are discussed.

- Finally, the proposed method is able to treat structural inhomogeneity and capture shear deformation effects while accounting for general geometry in a straight forward manner. Due to the adopted decoupling approach that is employed for the hydrodynamics and structural mechanics, higher-order plate theories can be incorporated for the latter with minor adjustments to the methodology.

It is mentioned that the mixed-formulation proposed for the radiation-type subproblems confined in the 2D setting, is presented in Karperaki and Belibassakis (2021). In the same work, the details of the employed dimensionality reduction are given. Finally, a series of validations and numerical experiments provide an insight into the developed methodology.

Moreover, the optimal PML-FEM scheme for linear water wave (MMSE) and hydroacoustic propagation and scattering in the truncated 2D plane is presented in Karperaki et al. (2019). The convergence characteristics of the method and a range of numerical experiments are included in the aforementioned contribution.

In the *time domain*, special hydroelastic elements were proposed for the treatment and investigation of the coupled problem in the shallow water limit. Notable contributions in the field are given in the points below,

- Novel conforming hydroelastic elements were constructed, featuring different approximations for the velocity potential and the structural deflection. The developed FEM tools, able to account for inhomogeneities, are employed for the study of the underlying physics and provide insight into hydroelastic phenomena.
- The developed numerical tools are employed in the assessment of non-linear effects incorporated by means of the coupled Shallow Water Equations and the non-linear Gao beam (Gao, 1996) accounting for moderately large deflections.

In Papathanasiou et al. (2015b), extending a previous work by Papathanasiou et al. (2015a), the developed numerical schemes are applied in the transient, hydroelastic modelling of ice shelves under long-wave excitation. Motivated by the 2011, Sultzberger Ice Shelf calving event (Brunt et al., 2011), a time-domain analysis was carried out to determine the critical bending moment profiles under excitation. The ice shelf was modelled as a thin, inhomogeneous, cantilever beam and the linearised shallow water equations were employed for the hydrodynamics. Subsequently, the hydroelastic analysis of an inhomogeneous, thin structure, elastically connected to the seabed is presented in Karperaki et al. (2016). In the aforementioned paper, the numerical tools are employed in the study of response mitigation and energy extraction potential of elastic connectors mounted on the edges of elastic, floating bodies.

To summarize the author's contributions, scientific publications produced in the context of the present thesis are listed below,

**(P1):** Karperaki, A. (2015). FEM Hydroelastic Models with Application to the Nonlinear Response of Large Floating Bodies in Shallow Wave Conditions. *Procedia Computer Science*, 66:122–131, https://doi.org/10.1016/j.procs.2015.11.015.

**(P2):** Karperaki, A., Belibassakis, K., and Papathanasiou, T. (2016). Time-domain, shallow-water hydroelastic analysis of VLFS elastically connected to the seabed.*Marine Structures*, 48:33-51, ttps://doi.org/10.1016/j.marstruc.2016.04.002.

**(P3):** Karperaki, A. E., Papathanasiou, T. K., and Belibassakis, K. A. (2019). An optimized, parameter-free PML-FEM for wave scattering problems in the ocean and coastal environment. *Ocean Engineering*, 179:307–324, https://doi.org/10.1016/j.oceaneng.2019.03.036.

**(P4):** Karperaki, A. E. and Belibassakis, K. A. (2021). Hydroelastic analysis of Very Large Floating Structures in variable bathymetry regions by multi-modal expansions and FEM. *Journal of Fluids and Structures*, 102:103236,https://doi.org/10.1016/j.jfluidstructs.2021.103236.

Moreover, the author collaborated in a number of themes, relevant to the broad context of the thesis. The aforementioned collaborations led to the following,

**(CO1):** Papathanasiou, T. K., Karperaki, A. E., Theotokoglou, E. E., and Belibassakis, K. A. (2015b). Hydroelastic analysis of ice shelves under long wave excitation.*Natural Hazards and Earth System Sciences*, 15(8):1851–1857,https://doi.org/10.5194/nhess-15-1851-2015.

**(CO2):** Papathanasiou, T. K., Karperaki, A. E., and Belibassakis, K. A. (2019b). On the resonant hydroelastic behaviour of ice shelves. *Ocean Modelling*, 133:11–26, https://doi.org/10.1016/j.ocemod.2018.10.008.

**(CO3):** Anevlavi, D. E., Filippas, E. S., Karperaki, A. E., and Belibassakis, K. A. (2020). A nonlinear BEM-FEM coupled scheme for the performance of flexible flapping-foil thrusters. *Journal of Marine Science and Engineering*, 8(1), 56, https://doi.org/10.3390/jmse8010056.

**(CO4):** Karathanasi, F., Karperaki, A., Gerostathis, T., and Belibassakis, K. (2020). Offshore-to-Nearshore transformation of wave conditions and directional extremes with application to port resonances in the bay of Sitia-Crete. *Atmosphere* 11(3), 280, https://doi.org/10.3390/atmos11030280.

Finally, the following collaborative works, relevant to the context of the present thesis were published in international conference proceedings,

**(CP1):** Karperaki, A. E., Belibassakis, K. A. and Papathanasiou, T. K. (2015). Propagation of acoustic-gravity waves in inhomogeneous ocean environment generated by sea bottom

deformation, 8th GRACM International Congress on Computational Mechanics, Volos, Greece, July 12-15, 2015.

(**CP2):** Karperaki, A.E., Belibassakis, K. A., Papathanasiou,T. K. Markolefas, S. I. (2015). Higher-order FEM for nonlinear hydroelastic analysis of a floating elastic strip in shallow-water conditions, VI International Conference on Coupled Problems in Science and Engineering (COUPLED PROBLEMS 2015), B. Schrefler, E. Onate and M. Papadrakakis (Eds.), San Servolo, Venice, Italy, May 18-20 2015.

(**CP3):** Karperaki, A. E., Papathanasiou, T. K. and K. A. Belibassakis, K. A. (2016). A coupled-mode system for the near-trapping of water waves in the presence of variable bathymetry, 11th HSTAM International Congress on Mechanics, Athens, Greece, May 27-30, 2016.

# Part I

# Physical and Mathematical Modelling

# Chapter 1

# Mathematical Description

The hydroelastic problem, relevant to floating elastic body applications in the inhomogeneous ocean waveguide, is derived from the coupling of Airy's water wave theory and reduced elasticity models governing the flexural motion of the structure. The present chapter explores the governing equations of the underlying phenomena, as well as the coupling between hydrodynamics and the structural response of the floating body. An insight into the adopted solution strategy is also provided at the end of the chapter.

## 1.1 Statement of the Hydroelastic problem

Modelling wave-structure-seabed interaction dictates the simulation of complex hydrodynamic transformations, such as refraction due to a varying seabed, diffraction due to the presence of the floating body and radiation due to the excitation-induced flexural motion. In a linearised regime, the hydroelastic problem, defined in the inhomogeneous ocean waveguide can be effectively treated in the frequency domain. To this end, the present analysis is restricted to the implementation of small-amplitude wave theory for the hydrodynamic modelling and linear reduced elasticity models for the simulation of the structural response. The floating body is assumed to be slender within the limits of reduced plate models as discussed in the sequel, while slenderness justifies the adopted negligible-draft assumption.

The examined configurations consider the two and three-dimensional ocean waveguide, with a part of the free surface constrained by a thin floating body. Regular waves propagate from the open water region and interact with the seabed and structure. Within the scope of the present thesis, a Cartesian coordinate system $(\mathbf{x}, z)$ is adopted, with $\mathbf{x} \in \mathbb{R}^d$, $d = 1, 2$, denoting the horizontal coordinates vector $(x_1, x_2)$. Moreover, when purely two-dimensional motions are considered, i.e. $d = 1$, $x_2$-dependence is omitted and the notation simplifies to $x_1 \equiv x$. Time dependence is denoted with $t$. Focusing on linear water wave propagation, the unbounded fluid layer in two and three dimensions is considered. An inviscid and incompressible fluid occupies

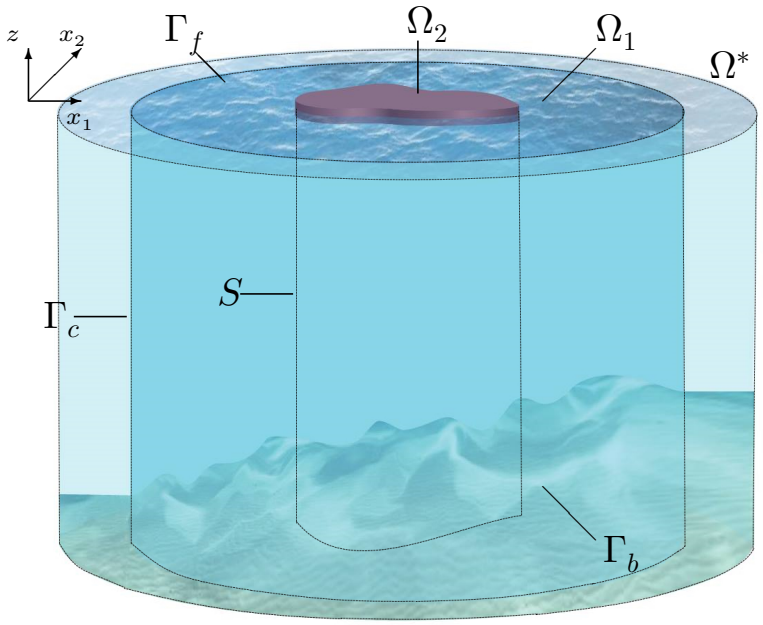


**(i)** Section of the 3D waveguide, supporting the finite structure

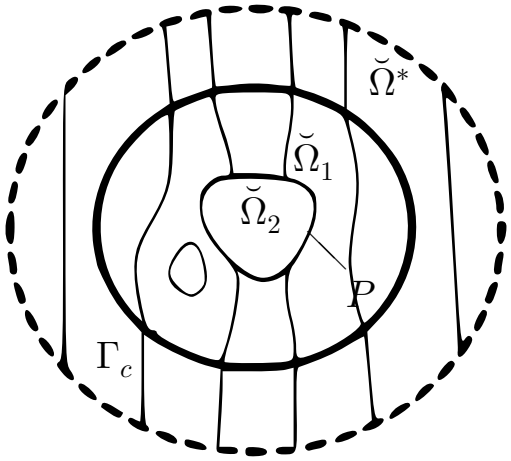


**(ii)** Projection on the 2D plane

**Figure 1.1** Domain Configuration (3D)

the layer, which is confined above by a free material surface and below by a fixed impermeable seabed described by $h(\mathbf{x})$. Towards the reduction of computational efforts, the bathymetry without any loss of generality is considered as a superposition of a background, parallel contour bathymetry $h_i(x)$ and a variable bathymetry containing 3D bathymetric features $h_d(\mathbf{x})$. Thus, it generally holds that $h(\mathbf{x}) = h_i(x) + h_d(\mathbf{x})$. This assumption is not restrictive in any way and will be revisited in the sequel. Following classical conventions, the z-axis is directed vertically upward, while surface $z = 0$ coincides with mean water level. Assuming furthermore that fluid

motion is *irrotational*, velocity $\mathbf{u}$ can be expressed by the scalar potential $\Phi(\mathbf{x}, z; t)$, such as $\mathbf{u} = \nabla\Phi$.

The fluid region of interest is defined as the layer,

$$\mathcal{D}(\mathbf{x}, z) = \{(\mathbf{x}, z) \in \mathbb{R}^{d+1},\ -h(\mathbf{x}) < z < 0\}.$$

Towards the aim of formulating the hydroelastic problem in a general topography setting, the naturally unbounded domain of interest is decomposed into a finite, closed subdomain $\overline{\Omega} \subset \mathcal{D} \subset \mathbb{R}^{d+1}$, with smooth boundary $\Gamma \equiv \partial\Omega$, and its exterior $\Omega^*$. The co-joint, lateral boundary between $\overline{\Omega}$ and $\Omega^*$ is denoted as $\Gamma_c$, such that $\mathcal{D} = (\overline{\Omega}\backslash\Gamma_c) \cup \Omega^*$. Without any loss of generality, inhomogeneity in the form of abrupt seabed variations and the presence of a localised scatterer that is the floating structure, is assumed to be contained within $\overline{\Omega}$. Beyond $\Gamma_c$, the seabed remains generally constant [1]. Moreover, the upper and bottom surface boundaries, restricted in $\overline{\Omega}$ are denoted as $\Gamma_f$ and $\Gamma_b$ respectively (Fig. 1.1(i)). A section of $\Gamma_f$, is occupied by an arbitrarily-shaped, zero-draft floating body. Thus, The mean water level is assumed to coincide with the mid-plane of the body. The boundary of its orthographic projection on the $(x_1, x_2)$ plane is denoted as $P$ (see Fig. 1.1(ii)). The presence of the structure leads to the further decomposition of $\overline{\Omega}$ into two non-overlapping subdomains, $\Omega_1$ and $\Omega_2$. The projector lines constitute a geometrically conforming cylindrical interface between subregions denoted as $S$, such as $S = \partial\Omega_1 \cap \partial\Omega_2$, and $\overline{\Omega} = \left(\overline{\Omega_1} \cup \overline{\Omega_2}\right) \backslash S$. Subregion $\Omega_1$ corresponds to the free fluid surface region of the waveguide, while $\Omega_2$ to the plate-covered enclosed region (Fig. 1.1(i)). An analogous decomposition is adopted for the upper and bottom surface boundaries, hence $\Gamma_f = \Gamma_f^1 \cup \Gamma_f^2$ and $\Gamma_b = \Gamma_b^1 \cup \Gamma_b^2$. Finally, the projections of $\Omega_1$ and $\Omega_2$ on $(x_1, x_2)$ are denoted as $\breve{\Omega}_1$ and $\breve{\Omega}_2$ respectively (Fig. 1.1(ii)).

Under the small-wave amplitude and structural motion assumptions, the time harmonic fluid motion is described by means of $\Phi(\mathbf{x}, z; t) = \mathrm{Re}\left(-\frac{\alpha_0 g}{\omega}\varphi(\mathbf{x}, z)\exp(-\mathrm{i}\omega t)\right)$ for a single radian frequency $\omega$ and amplitude $\alpha_0$. Furthermore, the plane wave excitation is assumed to propagate at an oblique direction $\theta$ with respect to the bottom contours. Similarly, all oscillatory quantities are multiplied by a complex factor to eliminate time-dependence. A pair of functions are employed for the description of the mean upper surface elevation in the two subregions, $\zeta(\mathbf{x}, z; t) = \mathrm{Re}\left(\eta(\mathbf{x}, z)\exp(-\mathrm{i}\omega t)\right), \forall \mathbf{x} \in \Gamma_f^1$ and $W(\mathbf{x}, z; t) = \mathrm{Re}\left(w(\mathbf{x}, z)\exp(-\mathrm{i}\omega t)\right), \forall \mathbf{x} \in \Gamma_f^2$. Throughout this work, the wavenumber of an oscillation is denoted with $k$ and the wavelength as $\lambda = 2\pi k^{-1}$.

Following the above assumptions, the boundary-value problem corresponding to the coupled fluid-structure motion is formulated in $\Omega$. Considering mass conservation in the region of interest, the fluid incompressibility assumption leads to the Laplace equation, with the velocity

[1] The adoption of a PML layer for computaional domain truncation, described in Chapter 6 allows for the relaxation of the constant depth assumption in the exterior region which will be characterised by parallel, straight bathymetric contour lines that span between regions of constant depth

potential function satisfying,

$$\nabla^2\varphi = 0, (\mathbf{x}, z) \in \Omega. \tag{1.1}$$

The above field equation is supplemented by boundary conditions on the unconstrained upper surface and seabed. For the free-surface region, linearised kinematic and dynamic conditions read respectively,

$$\partial_z\varphi + \mathrm{i}\omega\eta = 0, \tag{1.2}$$

$$\mathrm{i}\omega\varphi + g\eta = 0, \text{ on } \Gamma_f^1 \ (z = 0). \tag{1.3}$$

The above Eqs. (1.2) and (1.3) are combined in the following condition valid once again on the free fluid surface,

$$\partial_z\varphi - \mu\varphi = 0, \text{ on } \Gamma_f^1 \ (z = 0), \tag{1.4}$$

with $\mu = \omega^2 g^{-1}$. On the wetted surface of the floating structure, the normal fluid velocity must equal the structural velocity in the same direction. In the linearised regime, the above kinematic condition is applied on the mid-plane (neutral line) of the structure. The equilibrium surface coincides with the section of the upper boundary occupied by the floating body and thus the aforementioned condition is reduced to,

$$\partial_z\varphi = -\mathrm{i}\omega w, \text{ on } \Gamma_f^2 \ (z = 0). \tag{1.5}$$

The wave-structure coupling is completed by means of the pressure equilibrium equation, valid on the constrained section of the free-surface,

$$\mathcal{L}(\mathbf{w}) = \mathrm{i}\rho\omega\varphi - \rho g w, \text{ on } \Gamma_f^2 \ (z = 0), \tag{1.6}$$

where $\rho$ denotes the fluid density. The notation $\mathcal{L}(\cdot)$ is used to imply the reduced elasticity operator governing structural motion, while $\mathbf{w} = (w, \theta_{x_1}, \theta_{x_2})$ is the vector containing the degrees of freedom of the plate, namely the deflection $w$ and the rotations $\theta_{x_d}$, $d = 1, 2$ about the $x_1$ and $x_2$ axes. The employed plate models simulating flexural motion under wave excitation and the final form assumed by $\mathcal{L}(\mathbf{w})$ is the focus of Chapter 2.

Moreover, on the impermeable, variable seabed the kinematic condition reads,

$$\partial_n\varphi = 0, \text{ on } \Gamma_b. \tag{1.7}$$

The above problem is forced by an oblique-incident wave propagating from the exterior region $\Omega^*$, assuming a velocity potential of the form,

$$\varphi^*(\mathbf{x}, z) = \frac{\cosh(k(z+h))}{\cosh(kh)} \exp\{\mathrm{i}k(x_1\cos(a) + x_2\sin(a))\}, (\mathbf{x}, z) \in \Omega^*. \tag{1.8}$$

In Eq. (1.8), the wavenumber $k$ is the real root of the local dispersion relation in the region of incidence $\mu h = kh\tanh(kh)$.

Finally, to ensure the solvability of the above BVP, bounded outgoing solutions at infinity are assumed,

$$\text{thus } |\varphi|, |\nabla_{\mathbf{x}}\varphi| \text{ bounded as } |\mathbf{x}| \to \infty. \tag{1.9}$$

Following Mei et al. (2005) and others, a mathematically rigorous expression of the above condition is formulated by means of the *superelement* exterior region $\Omega^*$. As $\Omega^*$ does not support inhomogeneity, closed form analytic expressions for the wave field that explicitly satisfy radiation conditions at infinity can be written. Subsequently, matching of pressure and velocity conditions at the contour surface $\Gamma_c$ are transformed into approximate termination conditions similar to Dirichlet-to-Neumann ($DtN$) formulations. The above truncation technique involving the super element concept is further discussed in Section 3.2.

## 1.2 Problem Decomposition

The present section focuses on the proposed treatment of the hydroelastic problem defined in the frequency domain. As previously mentioned an incident wavetrain propagating in layer $\mathcal{D}$ undergoes a number of complex transformations. The refracted wave field, due to the varying seabed topography, will be diffracted to produce a scattered wave field and induce the flexural motion of the deformable body which in turn produces a radiating field.

In an attempt, to partially decouple fluid dynamics and structural mechanics the underlying linearity imposed by the modelling assumptions outlined in Section 1.1 is invoked. The plate response is represented by means of its *in vacuo* flexural modes, denoted as $w_\ell$, and complex amplitude coefficients $c_\ell$. The decomposition is conveniently placed in a regime where the wave field solution is decomposed into its radiation and scattered components. Hence, by the superposition principle, the unknown velocity potential is decomposed in a propagating, a diffraction and a radiation component. next To this end, the classical decomposition (Newman, 1994) is followed in Section 1.2.1 and the eigenfunction expansion approach is followed in Section 1.2.2.

### 1.2.1 Decomposition in Radiation and Diffraction Components

By means of the imposed linearity assumptions the velocity potential function $\varphi(\mathbf{x}, z)$ is decomposed into a scattered and a radiation potential as,

$$\varphi = \varphi_S + \varphi_R. \tag{1.10}$$

The scattered solution $\varphi_S$, represents the generated wave field in the presence of the floating body, assumed to remain fixed in waves, while the radiation potential, $\varphi_R$, is generated by the wave-induced flexural motion of the elastic body. The scattered wave field can be further decomposed into a propagating and a diffracted component as,

$$\varphi_S = \varphi_P + \varphi_D. \tag{1.11}$$

In the above, the propagating component solution $\varphi_P$ carries the transformations due to seabed refraction, while the diffracted potential $\varphi_D$, represents the disturbance of the propagating wave field $\varphi_P$ due to the presence of the presumed fixed body.

The propagating wave field $\varphi_P$ is calculated as the solution of a transmission problem, formulated in the region of interest in absence of the elastic body. Potential solution $\varphi_P$ satisfies the Laplace equation Eq. (1.1), and the kinematic bottom boundary condition Eq. (1.7), while in absence of the constrained section of the upper surface boundary, the free-surface condition Eq. (1.4) is enforced on the entire $\Gamma_f$. More details are given in Section 3.3.1.

The diffracted potential $\varphi_D$, also satisfies the field equation Eq. (1.1), the bottom boundary condition Eq. (1.7) and the free-surface boundary condition Eq. (1.4). On $\Gamma_f^2$ the kinematic condition, Eq. (1.5), is substituted with,

$$\partial_z \varphi_D = -\partial_z \varphi_P, \text{ on } \Gamma_f^2 \ (z = 0). \tag{1.12}$$

To ensure a unique solution, $\varphi_D$ must also satisfy radiation conditions at the far field. It is obvious from condition (Eq. (1.12)) that the solution of the reflection-transmission problem in $\Omega$, precedes the treatment of the diffraction problem, as the latter requires the $\varphi_P$ Neumann data on the constrained section of the free-surface modelled as a fully reflective boundary.

Finally, the radiation potential $\varphi_R$ is naturally expected to also satisfy the field equation Eq. (1.1), the bottom boundary condition (1.7), the upper surface kinematic conditions (1.4) and (1.5), and remain bounded at infinity. The kinematic condition Eq. (1.5) is rewritten for the radiation component of the total solution $\varphi_R$,

$$\partial_z \varphi_R = -\mathrm{i}\omega w, \text{ on } \Gamma_f^2 \ (z = 0). \tag{1.13}$$

The satisfaction of the above boundary condition involves the solution of the equation of motion for the structure. Employing a modal expansion for the plate deflection will reformulate

Eq. (1.13) as examined in the sequel and allow and circumvent the complexity of solving the plate equation of motion.

Notably, the dynamic condition Eq. (1.6) on the coupling surface that is valid for the total wave field further binds the decomposed solutions $\varphi_R$ and $\varphi_D$.

### 1.2.2 Modal Expansion for Plate Motion

Next, the following series expansion for the plate deflection in terms of the structural modal functions $\{w_\ell\}$, and the complex amplitudes $\{c_\ell\}$,

$$w(\mathbf{x}) = \sum_{\ell=1}^{\infty} c_\ell w_\ell(\mathbf{x}). \tag{1.14}$$

A natural choice for $\{w_\ell\}$ is the *in vacuo* eigenbasis of the inhomogeneous structure, generated as the solution of the corresponding eigenvalue problem. Thus, it is understood that the synchronous treatment of the coupled equation for vertical motion on the hydroelastic surface is overly avoided. The latter is now substituted with the free vibration problem of an unconstrained inhomogeneous plate. In a general setting the eigenvalue problem can only be treated numerically. To this end, FEM based solutions are considered as examined in a subsequent section of the present thesis (Section 5.2). Furthermore, the employment of expansion Eq. (1.14) allows for the corresponding representation for the radiation potential,

$$\varphi_R(\mathbf{x}, z) = \sum_{\ell=1}^{\infty} c_\ell \varphi_\ell(\mathbf{x}, z). \tag{1.15}$$

where $\varphi_\ell$ denote the unit-amplitude fluid motion generated by the $\ell^{\text{th}}$ modal function $w_\ell$. Since, the kinematic condition Eq. (1.13) must hold for $\varphi_R$ upon substitution of expansions (1.14) and (1.15), as well as for every pair $(\varphi_\ell, w_\ell)$ forming a radiation subproblem, the complex amplitudes $\{c_\ell\}$ employed in the aforementioned representations must be the same. Thus for each radiation wave field $\varphi_\ell$, excited by modal function $w_\ell$, the kinematic condition (1.13) now reads,

$$\partial_z \varphi_\ell = -\mathrm{i}\omega w_\ell, \text{ on } \Gamma_f^2 \ (z = 0), \text{ for } \ell = 1, ...\infty. \tag{1.16}$$

Revisiting the expressions in Eqs. (1.10) and (1.11), the solution of the hydroelastic problem presented in Section 1.1 is expressed based on the above as,

$$\varphi(\mathbf{x}, z) = \varphi_S + \sum_{\ell=1}^{\infty} c_\ell \varphi_\ell(\mathbf{x}, z). \tag{1.17}$$

Notably, the above decomposition (Eq. (1.17)) is a corollary of the underlying linearity assumption. The diffraction and radiation subproblems assume radiative solutions at infinity and will

be referred as *radiation-type* subproblems henceforth. For brevity, the aforementioned problems will be presented in a unified manner implying that $\varphi_0 \equiv \varphi_D$ for ease in presentation. The component, radiation-type hydrodynamic subproblems satisfy a kinematic condition on the coupling surface and are essentially decoupled from the dynamics of the structural response. It is stressed that the wave-structure coupling is completed by the enforcement of the pressure equation Eq. (1.6), involving the total potential.

## 1.3 Solution Strategy

By implementing the total wave field decomposition, expressed in Eq. (1.17) the treatment of the full hydroelastic problem, presented in Section 1.1, is reduced to that of a series of 'simpler' hydrodynamic subproblems which are decoupled from structural dynamics. The aforementioned radiation-type problems are essentially formulated based on the kinematic restrictions imposed on the coupling surface.

As already mentioned, for the 'dry' mode series representation of the plate deflection (Eq. (1.14)) the flexural modes $\{w_\ell\}$ and fundamental frequencies $\{\omega_\ell\}$ need to be calculated as the solutions of an *in-vacuo* eigenvalue problem for the inhomogeneous structure. Subsequently, the eigensolutions $\{w_\ell, \omega_\ell\}$ are employed in the kinematic condition Eq. (1.13), allowing for the formulation of the radiation-type subproblems $\varphi_\ell$ for $\ell = 1, ...\infty$.

Linear water wave propagation in the region of interest, in absence of the floating body is treated independently from the above subproblems. The derived solution $\varphi_P$ is similarly employed in the formulation of the diffraction subproblem $\varphi_\ell$ for $\ell = 0$. After the calculation of $\varphi_\ell, \ell = 0, 1...\infty$ and $\varphi_P$, the only remaining unknowns in Eq. (1.17) are the complex amplitude functions $c_\ell$, which are finally computed by enforcing the pressure Eq. (1.6) and implementing the calculated solutions $\varphi_\ell, (\ell = 0, 1...\infty)$, $\varphi_P$ and $\{w_\ell, \omega_\ell\}$.

Based on the above discussion, a solution strategy with several discrete steps linked with the treatment of formulated subproblems is adopted. The solution strategy is outlined in the mindmap of Fig. 1.2 showing the interrelations between calculation steps. In the scope of the present thesis, each of the steps comprising the strategy are addressed separately.

These solution steps are summarised as,

1. Treatment of the structural eigenvalue problem and the calculation of eigenpairs $\{w_\ell, \omega_\ell\}$.
2. Treatment of the component radiation-type hydrodynamic problems:
    - Propagation subproblem. Calculation of $\varphi_P$.
    - Diffraction subproblem. Calculation of $\varphi_\ell$ for $\ell = 0$, drawing from the calculated $\varphi_P$ Neumann data.
    - Radiation subproblems. Calculation of $\varphi_\ell$ for $\ell = 1, ...\infty$, utilizing computed eigenmodes $w_\ell$.

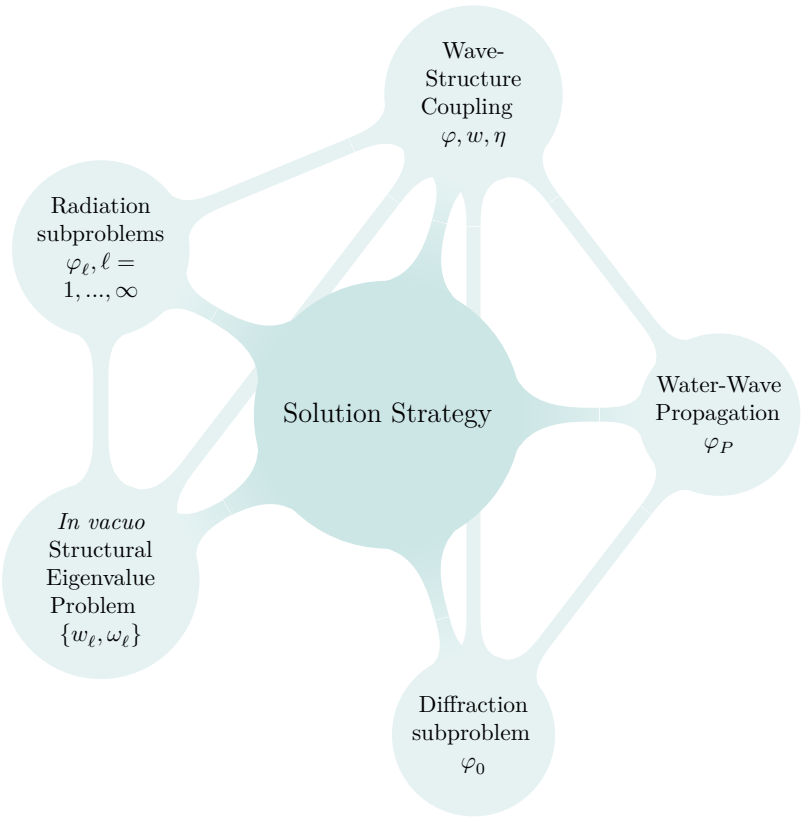


**Figure 1.2** Solution Strategy for the linear hydroelastic problem

3. Satisfaction of the dynamic condition condition (1.6), by means of calculated solutions $\varphi_\ell$, $\varphi_P$ and $\{w_\ell, \omega_\ell\}$

The numerical calculation of the defined subproblems pose several challenges. It is noted that in the field of wave-seabed-structure interaction domains of interest inherently span over large horizontal dimensions, hence capturing the effects of inhomogeneity for a range of excitation wavelengths can become computationally daunting even in the 2D case. In the context of the present work, FEM based schemes are proposed for solving the reduced weak formulations of the hydrodynamic subproblems at hand. Dimensionality reduction is achieved by the employment of a multi-mode vertical expansion for the potential functions in $\Omega_1$ and $\Omega_2$. Finally, closure conditions are achieved by a Cartesian PML featuring unbounded absorbing functions.

# Chapter 2

# Structural Motion

The structural motion of large floating structure is modelled by means of reduced elasticity theories in the context of the present thesis. The following chapter attempts a brief presentation of the employed structural plate theories for pure bending. The corresponding structural eigenvalue problems for both finite plates (2D structure) and elastic strips (1D) under cylindrical bending assumptions are also provided as a reference.

## 2.1 Structural Modelling

Within the scope of the present work the floating, elastic structure is modelled as a *structural plate*. A plate is a flat solid, bounded by two parallel faces, which are considerably larger than its thickness and a cylindrical surface (edge). In hydroelasticity, the aforementioned modelling assumption is justified by the large plan form dimensions compared to the thickness of the assumed floating structure. Homogeneous plates carry lateral loads by bending with zero axial strain, while in-plane motions are completely decoupled by vertical motion in the linear case implying *small deflections*. In the examined regime, the freely floating plate structure undergoes pure bending under ocean wave excitation.

In structural elements modelled as *plates* the thickness-to-principal length ratio is no greater than 1/10 allowing for the reduction of the 3D elasticity equations, since the horizontal dimensions can be considered prevalent. To derive the reduced elasticity theories of plates, a justified assumption is made for the functional form of the vertical displacement field or the stress field. Detailed accounts and investigations of established plate models are provided in Reddy (2006). The present thesis considers the Classical Plate theory (CPT) or Kirchhoff's Thin Plate theory and the First-order shear deformation theory proposed by Mindlin (1951). The two theories differ on the kinematic assumption for the rotation of the transverse normal section to the mid-plane of the structure. The CPT neglects the deformation caused by transverse shear stress and is thus limited to slender plate applications. In the plate model

by Mindlin, the CPT deficiency is remedied by refined kinematic assumptions that allows for the consideration of first-order shear effects, making the model applicable to moderately thick plates. The reader is directed for more details in the works of Fung et al. (2003); Reddy (2006).

## 2.2 Classical Plate Theory-(CPT)

The CPT is formulated under Kirchhoff's hypotheses for plate kinematics. Assuming that the neutral-plane coincides with the structure's mid-line, i.e. is equidistant form the upper and lower faces of the plate, the primary employed assumptions are summarised,

1. Straight transverse normals (perpendicular lines on the neutral mid-plane) remain straight and normal after deformation -*normal orthogonality assumption*.
2. The points on the neutral-line move only vertically.
3. Transverse normals do not elongate after deformation.
4. Normal transverse stresses are assumed negligible -*plane stress assumption*.

The above assumptions allow the expression of all stress components in terms of vertical displacement or deflection $w(\mathbf{x})$ and the derivation of a partial differential equation governing the vertical motion of the plate. Assumptions 1-3 are the kinematic constraints that lead to the definition of the displacement fields, while point 4 simplifies the stress-strain relationship. More specifically, statements 1 renders shear deformation effects negligible. Assumption 4 essentially carries the dimensionality reduction of the formidable 3D case. The geometrical interpretation of the kinematic assumptions is depicted in Fig. 2.1(i). Under the introduced assumptions the rotations $\theta_{x_1}(\mathbf{x}), \theta_{x_2}(\mathbf{x})$ about the $x_1$ and $x_2$ axes respectively, coincide with the transverse normals angles after deformation, restricted to the planes $x_1 z$ and $x_2 z$ respectively. Moreover, due to the orthogonality assumption it holds,

$$\theta_{x_1} = \partial_{x_1} w, \ \theta_{x_2} = \partial_{x_2} w. \tag{2.1}$$

The above kinematic constraints lead to the equations of motion. Horizontal displacements remain uncoupled from vertical motion in linear theory and thus they can be treated separately. The equation governing the vertical motion of a thin plate with variable rigidity $D(\mathbf{x})$ under generalised normal action $q(\mathbf{x}; t)$ is written as,

$$\begin{aligned} &D\nabla^4 W + \nabla^2 D \cdot \nabla^2 W + 2\nabla D \cdot \nabla(\nabla^2 W) \\ -(1-\nu)&\left(\partial^2_{x_1} D \partial^2_{x_2} W - 2\partial_{x_1}\partial_{x_2} D \partial_{x_1}\partial_{x_2} W + \partial^2_{x_2} D \partial^2_{x_1} W\right) + \rho_e \tau \partial_t^2 W = q(\mathbf{x}; t), \end{aligned} \tag{2.2}$$

with $D = E\tau(\mathbf{x})^3/12(1-\nu^2)$ involving plate thickness $\tau(\mathbf{x})$ and the Young's modulus $E$ and Poisson's ratio $\nu$ of the elastic material. The material density is given by $\rho_e$. In Eq. (2.2),

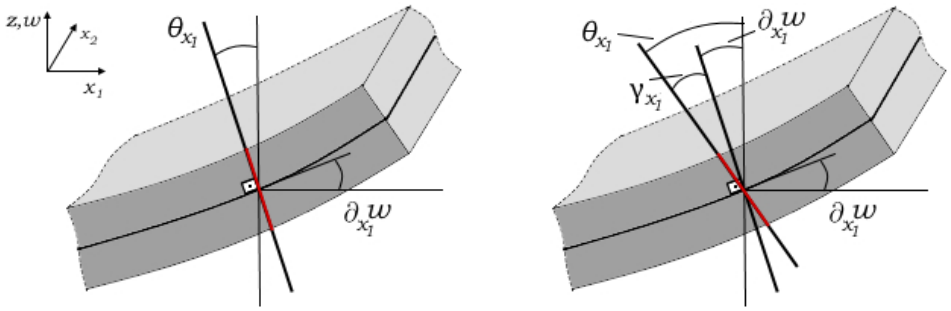


**(i)** Classical Plate Theory **(ii)** 1st Order Shear Deformation Theory

**Figure 2.1** Geometric illustration of kinematic considerations

the flexural rigidity inhomogeneity is attributed to thickness variation. Horizontal variability of the material properties can also be considered without any added complexity.

*Remark* 1. Notably, in the pure bending regime where solely vertical motion is considered thickness and material variations must be smooth enough to validate the expressions for bending and twisting moment resultants employed in the homogeneous case Timoshenko and Woinowsky-Krieger (1959). Consistent treatment of general heterogeneity would invalidate assumption 2, implying that the neutral plane undergoes negligible in-plane deformations, and would require the coupling of bending and membrane forces.

Solving, Eq. (2.2) would retrieve the vertical deflection distribution $w(\mathbf{x})$. The employed kinematic assumptions of CPT, and Hooke's constitutive law for elastic materials leads to well-defined variations through thickness for the stresses. It is convenient to address the stress-state of a plate by means of the thickness integrated stress resultants, namely the bending $M_{x_1}, M_{x_2}$ and twisting $M_{x_1x_2}$ moments and shear forces $Q_{x_1}$, $Q_{x_2}$. Thus, for an isotropic plate with smoothly varying flexural rigidity the bending moments are written in terms of $w(\mathbf{x})$ as,

$$M_{x_1} = -D(\mathbf{x})(\partial^2_{x_1} w + \nu \partial_{x_1x_2} w), \tag{2.3}$$

$$M_{x_2} = -D(\mathbf{x})(\partial_{x_2}\partial_{x_1} w + \nu \partial^2_{x_1} w), \tag{2.4}$$

$$M_{x_1x_2} = -D(\mathbf{x})(\nu - 1)\partial_{x_2}\partial_{x_1} w. \tag{2.5}$$

Additionaly, the shear forces are defined as,

$$Q_{x_1} = -\partial_{x_1}\left[D(\mathbf{x})(\partial^2_{x_1} w + \partial^2_{x_2} w)\right], \tag{2.6}$$

$$Q_{x_2} = -\partial_{x_2}\left[D(\mathbf{x})(\partial^2_{x_2} w + \partial^2_{x_1} w)\right]. \tag{2.7}$$

The solution of the differential equation (2.2) requires the specification of two boundary conditions on the plate edges, which are states for the deflection and slope or moment and shear force or a combination of the two. For a completely free plate (unrestrained), all stress resultants must vanish at the cylindrical surface, forming its edge. Next, considering the

appropriate edge conditions for the completely *free* plate, the unit normal vector on the edge surface $\mathbf{n} = [n_{x_1}, n_{x_2}]^T$, pointing towards the edge exterior is defined. The moment and shear force due to the normal and tangential stresses on the boundary edge are denoted as $M_n, M_{ns}$ and $Q_n$. All of the above stress resultants vanish on a free edge thus the corresponding boundary conditions read,

$$M_n = M_{x_1} n_{x_1}^2 + 2M_{x_1x_2} n_{x_1} n_{x_2} + M_{x_2} n_{x_2}^2 = 0, \tag{2.8}$$

$$M_{ns} = -M_{x_1} n_{x_1} n_{x_2} + M_{x_1x_2}(n_{x_1}^2 - n_{x_2}^2) + M_{x_2} n_{x_1} n_{x_2} = 0, \tag{2.9}$$

$$Q_n = Q_{x_1} n_{x_1} + Q_{x_2} n_{x_2} = 0. \tag{2.10}$$

The incorporation of the three boundary conditions (2.8-2.10) in the differential equation (2.2) can not be carried out in a consistent manner. Kirchhoff showed that in the small-deflection regime, the conditions on on the twisting moment and the shear force are not independent. Employing the effective shear force $V_n$, the conditions on a free edge are written as,

$$M_n = 0, \tag{2.11}$$

$$V_n = Q_n + \partial_s M_{ns} = 0. \tag{2.12}$$

The dynamic response of an elastic, thin structure is also supplemented by prescribed initial conditions for $w$ and $\partial_t w$.

In the frequency domain, which remains the focus of the present work, the pure bending equation (2.2) is reduced to,

$$\begin{aligned} &D\nabla^4 w + \nabla^2 D \cdot \nabla^2 w + 2\nabla D \cdot \nabla(\nabla^2 w) \\ &-(1-\nu)(\partial_{x_1}^2 D \partial_{x_2}^2 w - 2\partial_{x_1}\partial_{x_2} D \partial_{x_1}\partial_{x_2} w + \partial_{x_2}^2 D \partial_{x_1}^2 w) - \omega^2 \rho_e \tau(\mathbf{x}) w = \overline{q}(\mathbf{x};\omega). \end{aligned} \tag{2.13}$$

And finally the free flexural vibration problem of the unrestrained, thin plate is posed by means of the following eigenvalue problem,

$$\begin{aligned} &D\nabla^4 w + \nabla^2 D \cdot \nabla^2 w + 2\nabla D \cdot \nabla(\nabla^2 w) \\ &-(1-\nu)(\partial_{x_1}^2 D \partial_{x_2}^2 w - 2\partial_{x_1}\partial_{x_2} D \partial_{x_1}\partial_{x_2} w + \partial_{x_2}^2 D \partial_{x_1}^2 w) - \omega^2 \rho_e \tau(\mathbf{x}) w = 0. \end{aligned} \tag{2.14}$$

supplemented by free edge conditions Eqs. (2.11) and (2.12). The eigensolutions of Eq. (2.14) $w_\ell(\mathbf{x})$ and $\omega_l(\mathbf{x})$ are the *natural modes* and *naturalfrequencies* of the structure respectively and are functions of the inherent properties of the plate, i.e. elastic material characteristics and geometry. The above eigenvalue problem with variable coefficients can only be treated numerically. To this end, the Finite Element method will be employed for the approximation of the unknown eigenpairs. The latter is explored in Chapter 5.

## 2.3 First-Order Shear Deformation Theory-(FSDT)

The first-order deformation theory by Mindlin relaxes the orthogonality restriction on the straight transverse normals which support constant rotation. Thus, statement 1 is rephrased as,

1. Straight transverse normals (perpendicular lines on the neutral mid-plane) remain straight but *not orthogonal* after deformation.

The rest of the kinematic assumptions introduced in CPT hold. The alleviation of the orthogonality constraint on the transverse normal introduces additional rotation, due to shear deformation $\gamma_{x_1}, \gamma_{x_2}$ referred as the *shear angle*. The geometric illustration of the kinematic assumption is shown in Fig. 2.1(ii). Thus, the rotations $\theta_{x_1}, \theta_{x_2}$ are independent of deflection derivatives and defined as,

$$\theta_{x_1} = \partial_{x_1} w + \gamma_{x_1}, \theta_{x_2} = \partial_{x_2} w + \gamma_{x_2}. \tag{2.15}$$

Notably, the adopted kinematic assumption lead to the formulation of a theory that fails to satisfy the zero shear force condition that the top and bottom plate surfaces. A shear correction factor $\kappa_s$ is introduced to remedy the above and compensate for the constant-through-thickness shear stress assumption. The employed shear correction factor depends on material properties, geometry and also loading and boundary conditions. The kinematic assumption renders three independent degrees of freedom for the Mindlin plate, its deflection $w(\mathbf{x})$ and rotations $\theta_{x_1}, \theta_{x_2}$, that include shear deformations in this case, and thus vertical motion is expressed by three coupled equations expressing forces and moments equilibrium. For the isotropic Mindlin plate with smoothly varying flexural rigidity the bending moments are written in terms of the primary unknown fields,

$$M_{x_1} = D(\mathbf{x})(\partial_{x_1}\theta_{x_1} + \nu\partial_{x_2}\theta_{x_2}), \tag{2.16}$$
$$M_{x_2} = D(\mathbf{x})(\partial_{x_2}\theta_{x_1} + \nu\partial_{x_1}\theta_{x_1}), \tag{2.17}$$
$$M_{x_1x_2} = D(\mathbf{x})\frac{(1-\nu)}{2}(\partial_{x_2}\theta_{x_1} + \partial_{x_1}\theta_{x_2}). \tag{2.18}$$

Similarly, the shear forces are defined as,

$$Q_{x_1} = \kappa_s G\tau(\mathbf{x})\left(\theta_{x_1} + \partial_{x_1} w\right), \tag{2.19}$$
$$Q_{x_2} = \kappa_s G\tau(\mathbf{x})\left(\theta_{x_2} + \partial_{x_2} w\right). \tag{2.20}$$

For free harmonic vertical motion the governing equations equations of an isotropic Mindlin plate including the rotary inertia effects are written as,

$$\partial_{x_1}\left[D(\partial_{x_1}\theta_{x_1}+\nu\partial_{x_2}\theta_{x_2})\right]+\partial_{x_2}\left[D\frac{(1-\nu)}{2}(\partial_{x_2}\theta_{x_1}+\partial_{x_1}\theta_{x_2})\right] -\kappa_s G\tau\left(\theta_{x_1}+\partial_{x_1}w\right)+\omega^2 I_r(\mathbf{x})\theta_{x_1}=0, \tag{2.21}$$

$$\partial_{x_2}\left[D(\partial_{x_2}\theta_{x_2}+\nu\partial_{x_1}\theta_{x_1})\right]+\partial_{x_1}\left[D\frac{(1-\nu)}{2}(\partial_{x_2}\theta_{x_1}+\partial_{x_1}\theta_{x_2})\right] -\kappa_s G\tau\left(\theta_{x_2}+\partial_{x_2}w\right)+\omega^2 I_r(\mathbf{x})\theta_{x_1}=0, \tag{2.22}$$

$$\partial_{x_1}\left[\kappa_s G\tau\left(\theta_{x_1}+\partial_{x_1}w\right)\right]+\partial_{x_2}\left[\kappa_s G\tau\left(\theta_{x_2}+\partial_{x_2}w\right)\right]+\omega^2\rho_e\tau w=0, \tag{2.23}$$

In the above system of equations, $G=E/2(1+\nu)$ is the shear modulus and $I_r=\rho_e\tau(\mathbf{x})^3/12$ is the secondary moment of inertia. The free edge conditions along the cylindrical boundary of the plate read,

$$M_n=D(\mathbf{x})\left(\partial_n\theta_n+\nu\theta_s\right)=0, \tag{2.24}$$

$$M_n s=D(\mathbf{x})\left(\partial_n\theta_n+\nu\theta_s\right)=0, \tag{2.25}$$

$$Q_n=\kappa_s G\tau(\mathbf{x})\left(\theta_n+\partial_n w\right)=0, \tag{2.26}$$

where Eqs. (2.8)–(2.10) for the normal and tangential counterparts for the stress-resultants hold.

## 2.4 Plate Strip theories

The reduced, 2D hydroelastic problem ($d=1$) features an elastic floating structure extending indefinitely in the direction vertical to the page i.e. in $x_2$. In that case, the floating structure is modelled as a *plate strip* undergoing cylindrical bending. The plane strain problem of cylindrical bending under ocean wave action is formulated by means of the CPT and FSDT examined in the previous subsections. In direct analogy the reduced equations are given below.

For a thin strip the governing equation of vertical motion reduces to,

$$\partial_x^2\left(D(x)\partial_x^2 w\right)-\omega^2\rho_e\tau(x)w=0, \tag{2.27}$$

with free edge conditions,

$$M_x=M=-D(x)(\partial_x^2 w)=0, \tag{2.28}$$

$$Q_x=Q=-\partial_x^2\left(D(x)\partial_x^2 w\right)=0. \tag{2.29}$$

For a moderately thick strip, the governing equations of vertical motion reduce to the system corresponding to the Timoshenko beam model in plain strain,

$$\partial_x \left[\kappa_s G\tau(x)(\,\partial_x w - \theta\,)\right] + \omega^2 \rho_e \tau(x) w = 0, \tag{2.30}$$

$$\kappa_s G\tau(x)\,(\partial_x w - \theta) + \partial_x\,(D\partial_x \theta) + \omega^2 \frac{\rho_e \tau(x)^3}{12}\theta = 0, \tag{2.31}$$

The corresponding free-end conditions now read,

$$M_x = M = -D(x)(\partial_x \theta) = 0, \tag{2.32}$$

$$Q_x = Q = \kappa_s G\tau(x)\,(\partial_x w - \theta) = 0. \tag{2.33}$$

# Chapter 3

# Weak Formulation of the Hydrodynamics

The component hydrodynamic problems introduced in Chapter 1 are cast in a more permissive integral form suitable for numerical approximation techniques, i.e. FEM. The weak formulations for both propagating and radiation-type subproblems are produced.

## 3.1 Introduction and some preliminaries

A convenient basis for numerical approximation methods lays in a more permissive integral form of the problem at hand. This integral form, referred as the variational or weak form of the BVP can be recovered by either,

- *variational principles*, obtained in general by means of an energy-type functional for which stationarity is sought,
- or the *Method of Weighted Residuals (WRM)* that handles the differential form directly.

A discussion of the two alternative routes can be found in the works of Finlayson (2013), Brezzi and Fortin (1991), Finlayson and Scriven (1967) and others. The question of optimality when constructing a numerical approximation is heavily problem-dependent and it often becomes a matter of which route is less laboured. Notably, the strong form of a given problem can be linked with several weak forms that give rise to different approximation techniques. The Finite Element Method, which is employed in the present thesis, considers the weak form of a given problem and seeks an approximate solution in a given finite dimensional Hilbert setting. It is important to note that the approximate solution function space and the variational form of the problem are interconnected with the FE approximation. Thus, different variational forms would require solutions to be sought in a particular trial space leading to distinct FEM approximations (Brezzi and Fortin, 1991). In the course of this thesis, the weak formulations of the considered radiation-type problems are written in a mixed form expressing

a saddle-point instead of a stationarity condition for their solution. Such mixed formulations rise naturally in computational physics and engineering when additional constraints need to be satisfied along with field equations, boundary and initial conditions. The latter is based on either (i) modelling grounds or (ii) computational methods.

In the first category, the constraint expresses a physical law that is crucial to the physical modelling of the underlying phenomena. Such examples can be found in fluid mechanics, e.g Stoke's incompressible flow problem. Saddle-point problems also rise in two-field formulations common for example in elasticity and other fields, where the second variable is introduced on the grounds of its natural significance and computational ease in results post-processing. The obtained mixed-formulations, stemming from physical modelling considerations, are either natural as in the case of Stoke's problem or constructed-to-fit a purpose like the stress-displacement formulation in elasticity. Other examples where mixed-formulations rise is when interface problems are considered. Such cases are common in multi-physics modelling where different field equations rise on subdomains of interest while coupling conditions based on physical considerations like mass conservation need to hold on the interface. The reader is referred to the work of Toselli and Widlund (2005) for a thorough review in subdomain methods. The latter mixed-formulations are particularly important when synchronous computational coupling schemes are explored (Peterson et al., 2019). Finally, subdomain partitioning lead to mixed-formulations formed purely for the development of refined computational methods irrespective of the physical problem. For example classical parallelisation schemes by means of FETI-type algorithms in mechanics requires the development of pseudo interface problems and is the cornerstone of subdomain methods.

Returning to the derivation of suitable weak forms for the produced hydrodynamic subproblems the standard Sobolev space notation is followed. For a bounded domain $\Omega \in \mathbb{R}^d$, $d = 1, 2$ , with sufficiently smooth (Lipschitzian) boundary $\partial\Omega$ we initially consider the space od square integrable functions defined in $\Omega$

$$L^2(\Omega) = \left\{ u \,\middle|\, \int_\Omega |u|^2 = \|u\|_{L_2}^2 < +\infty \right\}.$$

Subsequently we define the general Hilbert space for $m > 0$

$$H^m(\Omega) = \{ u \,|\, D^\alpha \in L_2(\Omega) < \infty \}.$$

Next we consider the following trace operators for the sufficiently smooth boundary $\partial\Omega$ and its partition $\Gamma_0 \subset \partial\Omega$,

$$\gamma_0 : H^m(\Omega) \mapsto H^{m-1/2}(\Gamma_0).$$

By means of the above, the restriction of an element $u \in H^m$ is denoted as $\gamma_0 u = u\big|_{\Gamma_0} \in H^{m-1/2}(\Gamma_0)$

## 3.2 Propagating Wave field

The differential form of the linear water wave propagation problem defined in layer $\mathcal{D}$ and in terms of the propagating wave field $\phi_P$ is repeated below,

$$\nabla^2 \phi_P = 0, \text{ for } (\mathbf{x}, z) \in \mathcal{D}, \tag{3.1}$$

$$\partial_z \varphi_P - \mu \varphi_P = 0, \text{ on } \Gamma_f \ (z = 0), \tag{3.2}$$

$$\nabla_{\mathbf{n}_b} \varphi_P = 0, \text{ on } \Gamma_b \ (z = -h(\mathbf{x})), \tag{3.3}$$

$$\text{with } |\varphi_P|, |\nabla \varphi_P| \text{bounded as } |\mathbf{x}| \to \infty. \tag{3.4}$$

The above is formulated by means of the field Eq. (3.1), free surface condition Eq. (3.2) on $\Gamma_f$ and the seabed boundary condition Eq. (3.3) on $\Gamma_b$. As mentioned in 1.1, enforcing conditions Eq. (3.4) ensures the solvability of the problem. A mathematically rigorous version of the above is derived by considering a homogeneous, exterior region to the region of interest $\Omega^*$, referred as the *super-element* in earlier works (Bai, 1972; Mei and Chen, 1976). The assumption of homogeneity at the far-field allows for the implementation of analytical representations for the exterior wave potential, and thus matching conditions can be enforced on the shared boundary between the interior $\Omega$ and exterior $\Omega^*$ regions. By means of the matching, transmission conditions that link solutions $\varphi$ and $\varphi^*$ on $\Gamma_c$ the following transmission problem defined in the bounded subregion $\overline{\Omega}$ is written as,

$$\nabla^2 \phi_P = 0 \text{ for } (x, z) \in \Omega, \tag{3.5}$$

$$\partial_z \phi_P - \mu \phi_P = 0 \text{ on } \Gamma_f \ (z = 0), \tag{3.6}$$

$$\nabla_{\mathbf{n}_b} \phi_P = 0 \text{ on } \Gamma_b, \tag{3.7}$$

$$\phi_\infty^P = \phi^* \text{ and} \tag{3.8 a}$$

$$\partial_x \phi_\infty^P = \partial_x \phi^* \text{ on } \Gamma_c. \tag{3.8 b}$$

The above alternative formulation for the problem at hand allows for the development of numerical procedures that are able to consistently treat inhomogeneity in a bounded subregion of layer $\mathcal{D}$, i.e. $\Omega$. Naturally, the exterior solution $\varphi^*(\mathbf{x}, z) \forall (\mathbf{x}, z) \in \Omega^*$ satisfies field Eq. (3.5) and free-surface Eq. (3.6) condition on $\Gamma_f^*$, while Eq. (3.7) is reduced to,

$$\partial_z \varphi^* = 0 \text{ on } \Gamma_b^*. \tag{3.9}$$

Analytical expressions for $\varphi^*$ are available in either integral or series representation form and satisfy explicitly the radiation conditions at infinity Eq. (1.9)(Mei and Chen, 1976).The enforce-

ment of transmission conditions Eqs. (3.8 a) and (3.8 b) on the artificial termination boundary $\Gamma_c$ is in fact equivalent to a *DtN* mapping (Zienkiewicz and Taylor, 2005).

In the present case, the transmission conditions on $\Gamma_c$ can be satisfied naturally by means of a contrived variational principle (Mei et al., 2005; Zienkiewicz and Taylor, 2005) giving rise to hybrid numerical schemes. Notable works that employ this variational approach, built on contrived principles, for either 2D or 3D radiation, scattering and propagation problems are Aranha et al. (1979), Mei and Chen (1976) and Athanassoulis and Belibassakis (1999).

In the sequel, the contrived variational principle introduced in the works of Bai and Yeung (1974) and Mei and Chen (1976) and the WRM are presented in parallel for the weak formulation of the transmission problem of Eqs. (3.5), (3.8 a) and (3.8 b).

### 3.2.1 Variational formulation

As mentioned in the introductory section of this chapter, the weak form of a differential problem can be derived by means of variational principle. The latter is produced by the theorisation of a functional whose stationarity will yield an integral form of the problem essential to the implementation of an approximate numerical method, i.e. finite differences, least-squares, FEM etc. A variational principle is said to be natural when the derived Euler equations match the governing equations of the problem at hand while the corresponding boundary terms reflect the imposed boundary conditions (Zienkiewicz and Taylor, 2005).

The existence of natural variational principles for self-adjoint, linear operators like the Laplacian with homogeneous or inhomogeneous Dirichlet, Neumann or Robin type conditions valid on sections of the boundary is ensured (Norrie and Vries, 1980). For example, we consider the Laplace equation with an inhomogeneous mixed-type condition valid on the entire boundary $\Gamma \equiv \partial\Omega$,

$$\nabla^2\varphi(\mathbf{x}, z) = 0 \text{ in } \Omega \tag{3.10 a}$$

$$\text{and } \partial_n\varphi + \alpha\varphi + \beta = 0 \text{ on } \Gamma, \tag{3.10 b}$$

for known coefficients $\alpha$ and $\beta$, a variational principle is formulated by the extremisation of the following functional,

$$I(\varphi) = \frac{1}{2}\int_\Omega \nabla\varphi\cdot\nabla\varphi\, d\Omega + \int_\Gamma \left(\frac{1}{2}\alpha\varphi^2 + \beta\varphi\right)\, ds$$

Mikhlin (1964) showed that the function $\varphi$ that renders the above functional stationary (minimum), is also the solution to the BVP described by Eqs. (3.10 a) and (3.10 b) and vice versa. Hence, the variational principle $\delta I = 0$, retrieves Eq. (3.10 a) as the Euler-Lagrange equation and Eq. (3.10 b) as the Robin type natural boundary condition.

A suitable variational principle can be derived for the transmission problem defined by Eqs. (3.5), (3.8 a) and (3.8 b) in a similar manner. The above functional is properly amended

to account for the parts of the boundary $\Gamma_f$ and $\Gamma_c$ where the Robin condition Eq. (3.6) and the non homogeneous Neumann condition Eq. (3.8 b) on $\Gamma_c$ are valid. Hence, the following functional is constructed,

$$J(\varphi_P, \varphi^*) = \frac{1}{2}\int_\Omega \nabla\varphi_P \cdot \nabla\varphi_P \, d\Omega - \frac{1}{2}\mu \int_{\Gamma_f} (\varphi_P)^2 ds - \int_{\Gamma_c} \varphi_P \nabla_{\mathbf{n}_c} \varphi^* ds. \tag{3.11}$$

The solution to Eqs. (3.5), (3.8 a) and (3.8 b) is given by an admissible function $\varphi_P$ that renders $J$ stationary and for which the principal condition $\varphi_P = \varphi^*$ on the lateral interface $\Gamma_c$ holds. The variational form of the problem by means of functional Eq. (3.11) is written as,

$$\begin{aligned} \delta J(\varphi_P, \varphi^*) = &\int_\Omega \nabla\varphi_P \cdot \delta\left(\nabla\varphi_P\right) \, d\Omega - \mu \int_{\Gamma_f} \varphi_P \, \delta\varphi_P \, ds \\ &- \int_{\Gamma_c} \delta\varphi_P \nabla_{\mathbf{n}_c} \varphi^* \, ds = 0, \\ &\text{subject to } \; \varphi_P - \varphi^* = 0 \text{ on } \Gamma_c. \end{aligned} \tag{3.12}$$

Equations (3.8 a) and (3.8 b) express continuity of pressure and velocity between interior and exterior solutions. While, natural conditions are satisfied implicitly by means of the variational principle, any admissible trial function must be *a priori* chosen as to satisfy the inhomogeneous Dirichlet condition Eq. (3.8 a) which introduces the complexity of properly constructing the admissible functions space.

To circumvent the above complexity Mei and Chen (1976) and Bai and Yeung (1974), introduced a contrived *(or restricted)* variational principle based on the following augmented functional,

$$\begin{aligned} \hat{J}(\varphi_P, \varphi^*) = &\frac{1}{2}\int_\Omega \nabla\varphi_P \cdot \nabla\varphi_P \, d\Omega - \frac{1}{2}\mu \int_{\Gamma_f} \varphi_P^2 ds \\ &+ \int_{\Gamma_c} \nabla_n \varphi^* \left(\frac{1}{2}\varphi^* - \varphi_P\right) \, ds. \end{aligned} \tag{3.13}$$

The above functional enables the implicit coupling of interior and exterior solutions through the weak satisfaction of Eqs. (3.8 a) and (3.8 b). Comparing the above functional with the one in Eq. (3.11) it is observed that the final boundary integral term is enhanced. The additional term allows for the natural satisfaction of both transmission conditions. The contrived or restricted variational principle is deduced as,

$$\begin{aligned} \delta\hat{J}(\varphi_P, \varphi^*) = &\int_\Omega \nabla\varphi_P \cdot \delta\left(\nabla\varphi_P\right) \, d\Omega - \mu \int_{\Gamma_f} \varphi_P \, \delta\varphi_P \, ds \\ &- \int_{\Gamma_c} \left(\varphi^* - \varphi_P\right) \, \delta\left(\nabla_n \varphi^*\right) \, ds - \int_{\Gamma_c} \delta\varphi_P \nabla_n \, \varphi^* \, ds = 0 \end{aligned} \tag{3.14}$$

Setting the first variation equal to zero, $\delta J = 0$ and applying the Green-Gauss theorem retrieves Eq. (3.5) as the Euler-Lagrange equation and Eqs. (3.6), (3.7), (3.8 b) and (3.8 a) as the natural boundary conditions. More details on the above calculations can be found in Mei et al. (2005).

Notably, the variational formulation of Eqs. (3.6), (3.7), (3.8 b) and (3.8 a) is equivalent to the implementation of a Lagrange multiplier formulation for the constrained principle. In the latter case an auxiliary function $\lambda$, resembling the Lagrange multiplier is identified as $\lambda = \nabla_n \varphi^*$ (Finlayson, 2013; Zienkiewicz and Taylor, 2005).

The value of such contrived principles is assessed in terms of the numerical tools developed for the approximate solution of the variational form at hand. For instance, Eq. (3.14) restores continuity at the lateral interfaces with the exterior region and allows for consistent domain truncation. However, as stressed in the literature such principles are equivalent to a Weighted Residuals approach Finlayson (2013). Direct handling of the differential equations without the need to construct an appropriately tuned functional and establish a contrived variational principle is more often than not preferable. Apart from the case of linear, self-adjoint operators an example of which was discussed earlier, a WRM for the derivation of finite element formulations is commonly more expeditious and general (Norrie and Vries, 1980; Washizu, 1975).

### 3.2.2 Weighted Residuals Method

Next, the weak form of the transmission problem by Eqs. (3.6), (3.7), (3.8 b) and (3.8 a) is equivalently derived by a weighted residual approach. Initially the space of square integrable functions with square integrable gradient is considered,

$$V = \{H^1(\Omega;\mathbb{C}) : \; v(\mathbf{x},z) \in L^2(\Omega;\mathbb{C}) \text{ and } \nabla v(\mathbf{x},z) \in L^2(\Omega;\mathbb{C})\}. \tag{3.15}$$

The above defined space $V$ is considered throughout the thesis. Multiplying the field Eq. (3.5) by $v(\mathbf{x},z) \in V$ and integrating over the domain results in,

$$\int_\Omega v \nabla^2 \varphi_P \, d\Omega = 0 \tag{3.16}$$

By means of the Green-Gauss theorem the above becomes,

$$\int_\Omega \nabla v \cdot \nabla \varphi_P \, d\Omega - \int_\Gamma v \, \nabla_{\mathbf{n}} \varphi_P = 0. \tag{3.17}$$

Substituting the boundary conditions Eqs. (3.6), (3.7) and (3.8 b) reduces into the above weak form,

$$\begin{aligned} \int_{\Omega} \nabla v \cdot \nabla \varphi_P \, d\Omega - \mu \int_{\Gamma_f} v \, \varphi_P \, ds - \int_{\Gamma_c} v \, \nabla_{\mathbf{n}_c} \varphi^* \, ds = 0, \\ \text{subject to} \int_{\Gamma_c} v \, (\varphi^* - \varphi_P) \, ds = 0. \end{aligned} \tag{3.18}$$

It is clear that the above expression Eq. (3.18) is equivalent to the variational form Eq. (3.12) with the added constraint imposed by the continuity requirement Eq. (3.8 a). Notably, the above weak form is derived by setting $v \equiv \delta\varphi_P$ in Eq. (3.12) and imposing a weak satisfaction of the Dirichlet type condition . Adjusting the trial function space to incorporate the constraint,

$$\overline{V} = \{v \in V, | v - \varphi^* = 0 \text{ on } \Gamma_c\},$$

allows for the following reformulation of Eq. (3.18).

**Weak Problem 3.1.** Find $\varphi_P(\mathbf{x}, z) \in \overline{V}(\Omega)$ such that it holds,

$$\int_{\Omega} \nabla v \cdot \nabla \varphi_P \, d\Omega - \mu \int_{\Gamma_f} v \, \varphi_P \, ds - \int_{\Gamma_c} v \, \nabla_{\mathbf{n}_c} \varphi^* \, ds = 0, \quad \forall v(\mathbf{x}, z) \in \overline{V}.$$

Weak Problem 3.1 is equivalent to the variational form of Eq. (3.12) as well as the weak form Eq. (3.18). The satisfaction of the essential condition Eq. (3.8 a) is achieved through the construction of the affine trial function space $\overline{V}$. Note that $\overline{V}$, unlike $V$, is not a vector space since the sum of two elements is not an element. The above restricts the suitability of conventional trial spaces. A means to tackle the above complexity is to weakly satisfy the essential boundary condition in order to derive a constrained alternative of Weak Problem 3.1 in a similar manner as to the one employed in the derivation of Eq. (3.14). The latter is achieved by the introduction of Lagrange multiplier function $\lambda$, defined on $\Gamma_c$ that allows the satisfaction of continuity requirement naturally.

**Mixed Weak Problem 3.1.** Find $(\varphi_P(\mathbf{x}, z), \lambda(\Gamma_c)) \in V(\Omega) \times (H^{-1/2}(\Gamma_c))$ such that it holds,

$$\begin{cases} \displaystyle\int_{\Omega} \nabla v \cdot \nabla \varphi_P \, d\Omega - \mu \int_{\Gamma_f} v \, \varphi_P \, ds - \int_{\Gamma_c} \lambda v \, ds = 0, \\ \displaystyle\int_{\Gamma_c} \xi \, (\varphi^* - \varphi_P) \, ds = 0, \end{cases} \quad \forall (v(\mathbf{x}, z), \xi(\Gamma_c)) \in V(\Omega) \times (H^{-1/2}(\Gamma_c))$$

It is immediately observed that setting $v \equiv \delta\varphi_P$ and the Lagrange Multiplier function has a clear physical meaning in the present case, i.e. $\lambda = \nabla_{\mathbf{n}_c}\varphi^*$, the above weak problem is equivalent to the variational form Eq. (3.14). It is thus far illustrated that the WRM in conjunction with a Lagrange multiplier function facilitates the derivation of a weak formulation for the transmission problem. Additionally, the WRM is proved more expeditious in this case since the theorisation of a contrived variational principle is avoided. The latter is also employed for the radiation-type problems.

## 3.3 Reduction of the 3D transmission problem

To decrease the computational effort involved in the treatment of the 3D transmission problem described above, a non-restrictive assumption was introduced for the depth function $h(\mathbf{x}) = h_i(x) + h_d(\mathbf{x})$ in Section 1.1. Due to the underlying linearity of the modelled phenomena, the total solution can be decomposed into a part that is refracted due to the parallel contour bathymetry, represented by $\phi_i(\mathbf{x}, z)$ and a diffracted component due to the presence of the 3D morphology of the seabed, $\phi_d(\mathbf{x}, z)$, thus it holds,

$$\varphi_P = \phi_i(\mathbf{x}, z) + \phi_d(\mathbf{x}, z). \tag{3.19}$$

To this end, the 2D vertical cross section of layer $\mathcal{D}$ terminated below by the parallel contour bathymetry $h_i(x)$ is considered,

$$\mathcal{D}^c(x, z) = \{(x, z) \in \mathbb{R}^2,\ -h_i(x) < z < 0\}.$$

In analogy with the 3D case, the bounded subdomain $\Omega^c$ and its exterior $\Omega^{c*}$ are defined (Fig. 3.1). The domain boundaries are projections of the contour boundaries defined earlier on the $(x, z)$ plane and are denoted as $\partial\Gamma$ (as opposed to $\Gamma$ in the 3D regions) to avoid confusion. Thus in accordance to the notation introduced in Section 1.1 it holds $\mathcal{D}^c = (\overline{\Omega^c}\backslash\partial\Gamma_c) \cup \Omega^{c*}$. Furthermore, it is $\partial\Gamma_c = \partial\Gamma^1 \cup \partial\Gamma^2$ for the lateral termination boundaries, and the exterior region is composed of the right and left half-strips as $\Omega^{c*} = \Omega^1_\infty \cup \Omega^2_\infty$ (see Fig. 3.1(i)).

Oblique wave, forming angle $\theta$ with $x_1$ axis, is assumed to propagate from a homogeneous region of incidence, $\Omega^{inc}$ into the region of interest $\Omega$ and transmits in $\Omega^{tr}$ (see Fig. 3.1(ii)). Assuming that the oblique-incident plane wave is $x_2$-periodic, the refracted wave field in $\Omega$ is written as $\phi_i(\mathbf{x}, z) = \hat{\phi}_i(x, z)\exp(\mathrm{i}k_{x_2}x_2)$. The latter is founded on the fact that the considered waveguide is terminated below by the parallel contour bathymetry in essentially $x_2$-independent. This allows for the formulation of a transmission problem in the 2D Cartesian strip $\mathcal{D}^c$, in terms of $\hat{\phi}_i(x, z)$ in $\mathcal{D}^c$. The composition of $\phi_i(\mathbf{x}, z)$ by means of the $x_2$ wavenumber component $k_{x_2}$ is straightforward. Subsequently, obtained incident Cauchy data on the supported 3D morphological features of the seabed are utilised in the formulation of a diffraction

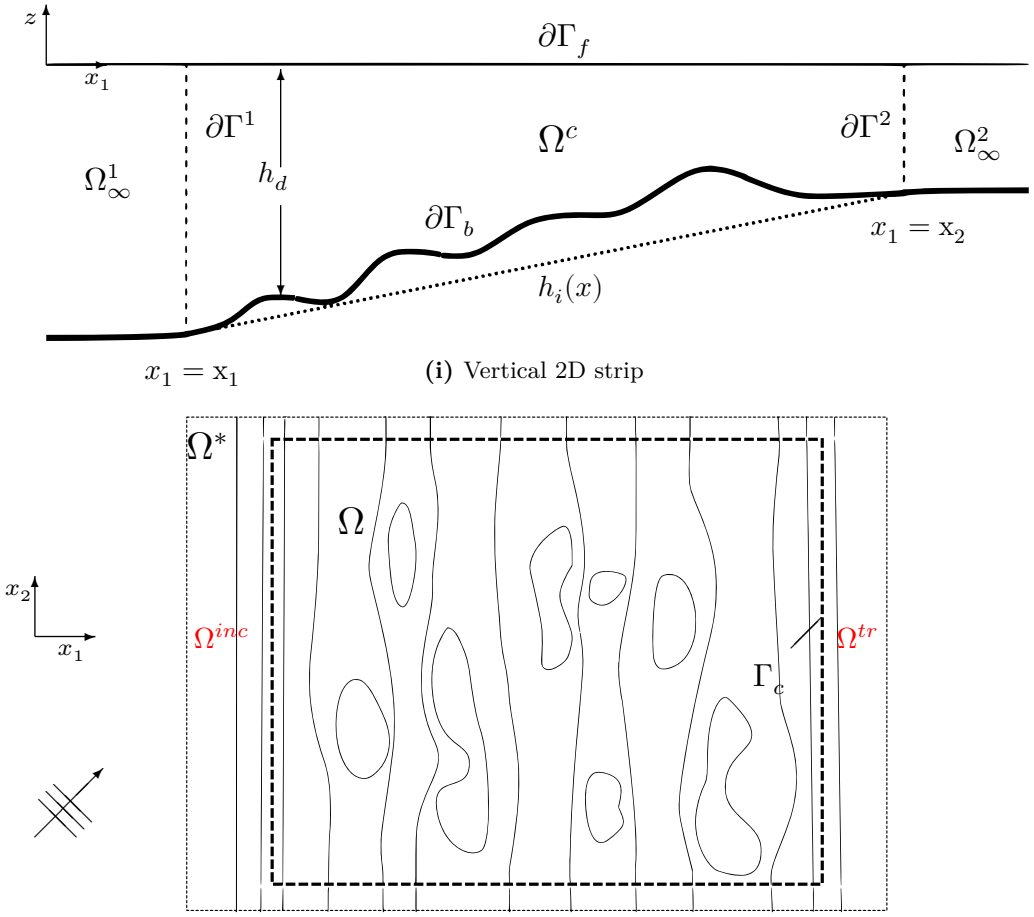


**Figure 3.1** Water wave propagation over a general, mildly sloped bathymetry featuring localised shoals

problem in terms of $\phi_d(\mathbf{x}, z)$ in $\Omega$. The 3D solution is finally composed by means of Eq. (3.19). Appropriate closure conditions for the diffraction problem is derived by means of a Perfectly Matched Layer (PML). The weak forms of the involved transmission (2D) and diffraction (3D) problems are examined in the sequel.

### 3.3.1 Transmission Problem

For ease in presentation the hat notation introduced above is dropped. Henceforth, the 2D and 3D refracted wave field solutions $\phi_i$ will be distinguished by the context and their arguments. The strong form of the 2D transmission problem is straightforwardly derived from Eqs. (3.5)–(3.7). Transmission conditions are expressed on the lateral boundaries of the strip $\partial\Gamma^j$, while

the half-strip potentials are denoted as $\phi^j_\infty, j = 1, 2$.

$$\nabla^2\phi_i = 0 \text{ for } (x, z) \in \Omega^c, \tag{3.20}$$

$$\partial_z\phi_i - \mu\phi_i = 0 \text{ on } \partial\Gamma_f \ (z = 0), \tag{3.21}$$

$$\nabla_{\mathbf{n}_b}\phi_i = 0 \text{ on } \partial\Gamma_b, \tag{3.22}$$

$$\phi^j_\infty = \phi_i \text{ and} \tag{3.23 a}$$

$$\partial_x\phi^j_\infty = \partial_x\phi_i \text{ on } \partial\Gamma^j, j = 1, 2. \tag{3.23 b}$$

A refinement of the conditions on the lateral boundaries requires an *a priori* knowledge of the far-field potential solution behaviour. To this end,the following series representations, obtained by separation of variables in the half-strips, are employed $\phi^j_\infty, j = 1, 2$,

$$\phi^1_\infty(x, z) = \left(A_0 \exp\left(\mathrm{i}\kappa^{(1)}_0 x\right) + A_R \exp\left(-\mathrm{i}\kappa^{(1)}_0 x\right)\right) Z^{(1)}_0(z) + \sum_{n=1}^{\infty} C^{(1)}_n Z^{(1)}_n(z) \exp\left(\kappa^{(1)}_n(x - \mathrm{x}_1)\right), \ (x, z) \in \Omega^1_\infty, \tag{3.24}$$

$$\phi^2_\infty(x, z) = A_T \exp\left(\mathrm{i}\kappa^{(2)}_0 x\right) Z^2_0(z) + \sum_{n=1}^{\infty} C^{(2)}_n Z^{(2)}_n \exp\left(\kappa^{(2)}_n(\mathrm{x}_2 - x)\right), \ (x, z) \in \Omega^2_\infty. \tag{3.25}$$

In the above representations for the wave potential in the half-strips, the terms $\left(A_0 \exp\left(\mathrm{i}\kappa^{(1)}_0 x\right) + A_R \exp\left(-\mathrm{i}\kappa^{(1)}_0 x\right)\right) Z^{(1)}_0(z)$ and $A_T \exp(\mathrm{i}\kappa^{(2)}_0 x) Z^2_0(z)$ are the propagating modes while the remaining terms $n = 1, 2, ...\infty$ correspond to the evanescent modes (Athanassoulis and Belibassakis, 1999; Massel, 1993). The above suggest propagation from a region of incidence , i.e. $\Omega_{inc}$, corresponding to the left half-strip in $\mathcal{D}$ towards a transmission region $\Omega_{tr}$ corresponding to the right half-strip The effective wavenumbers $\kappa^{(j)}_0$, are the $x_1-$component of the local wavenumber $k^{(j)}_0$ in $\Omega^j_\infty, j = 1, 2$. Hence, $\kappa^{(j)}_0 = k^{(j)}_0 \cos(\theta)$ and $\kappa^{(j)}_n = \sqrt{\left(k^{(j)}_n\right)^2 + \left(k^{(j)}_0 \cos(\theta)\right)^2}$. The sets of vertical structures $\{Z^{(j)}_n, n = 0, 1, ...\infty\}$ and wavenumbers $\{\mathrm{i}k^{(j)}_0, k^{(j)}_n, n = 1, ...\infty\}$ are the eigenvalues and eigenvectors of the locally defined Sturm-Liouville problems in $\Omega^j_\infty, j = 1, 2$. The eigenvalues are the roots of the dispersion relation defined at local depth

$$\mu h = -k_n h \tan(k_n h) \tag{3.26}$$

Notably, the representation $\phi^j_\infty, j = 1, 2$ explicitly satisfy the condition for bounded solutions at the farfield. Equations (3.24) and (3.25) can be utilised in the construction of boundary conditions of the form,

$$\partial_n\phi_i - \mathcal{T}_t\phi_i = g \text{ on } \partial\Gamma^j. \tag{3.27}$$

In the above, $\mathcal{T}_t$ represents an appropriate *DtN* mapping constructed determines by the satisfaction of the transmission conditions Revisiting the constrained Weak problem 3.1, and considering the physical interpretation of the identified Lagrange Multiplier functions $\lambda^j \equiv \partial_x \phi^j_\infty(x,z)$ and its variations $\xi$, defined on the lateral boundaries $\partial\Gamma^j$, it is deduced,

**Weak Problem 3.2.** *(2D Transmission)* Find $\phi_i(x,z) \in V(\Omega^c)$ such that it holds,

$$\begin{cases} \displaystyle\int_{\Omega^c} \nabla v \cdot \nabla \phi_i \, d\Omega - \mu \int_{\partial\Gamma_f} v\, \phi_i \, ds - \sum_{j=1}^{2} \int_{\partial\Gamma^j} \partial_x \phi^j_\infty v \, ds = 0, \\ \displaystyle\sum_{j=1}^{2} \int_{\partial\Gamma^j} \delta(\partial_x \phi^j_\infty) \left(\phi^j_\infty - \phi_i\right) \, ds = 0, \end{cases}$$

$$\forall v(x,z) \in V(\Omega^c).$$

The series representations Eqs. (3.24) and (3.25) will be employed for the derivation of explicit boundary conditions of the form of Eq. (3.27) that ensure inflow and outflow on the lateral boundaries. Applying the Green-Gauss theorem on the first equation of Weak Problem 3.2, results in the following lateral boundary terms,

$$\int_{\partial\Gamma^j} \left(\partial_x \phi_i - \partial_x \phi^j_\infty\right) v \, ds \text{ for } j = 1, 2. \tag{3.28}$$

It is noted that the above boundary term expresses the flux continuity requirement across the lateral boundary, while the second equation of Weak Problem 3.2 expresses the continuity requirement on interior and exterior solutions.

### 3.3.2 3D Diffraction Problem

The strong form of the diffraction wave field problem in $\mathcal{D}$ requires the incident wave field $\varphi_P$ Cauchy data on the supported 3D bathymetric features, which are considered known. Thus it must hold,

$$\nabla^2 \phi_d = 0 \text{ for } (\mathbf{x}, z) \in \Omega, \tag{3.29}$$

$$\partial_z \phi_d - \mu \phi_d = 0 \text{ on } \Gamma_f \ (z = 0), \tag{3.30}$$

$$\nabla_{\mathbf{n}_b} \phi_d + f(\mathbf{x}) = 0 \text{ on } \Gamma_b, \tag{3.31}$$

$$\varphi^* = \phi_d \text{ and} \tag{3.32 a}$$

$$\nabla_{\mathbf{n}_c} \varphi^* = \nabla_{\mathbf{n}_c} \phi_d \text{ on } \Gamma_c. \tag{3.32 b}$$

$$\lim_{|r|\to\infty} |r|(\partial_{|r|}\phi^* - \mathrm{i}k\phi^*) = 0. \tag{3.33}$$

In the above $f = \nabla_{\mathbf{n}_b} \phi_P(\mathbf{x}, z)$. Radiation condition at infinity Eq. (3.33) must be satisfied by exterior solution $\varphi^*$ at infinity. As previously discussed, the *a priori* knowledge of the wave

field structure in $\Omega^*$ allows for the derivation of appropriate termination conditions on $\Gamma_c$ It is noted here that when considering the 2D Cartesian strip, refined matching conditions between interior and exterior solutions can be derived by means of the following series representation of out-going solutions at infinity in line with the discussion in Section 3.3.1,

$$\phi^1_\infty(x,z) = C_0 \exp\left(-\mathrm{i}k_0^{(1)}x\right) Z_0^{(1)}(z) + \sum_{n=1}^{\infty} C_n Z_n^{(1)}(z) \exp\left(\mathrm{i}k_n^{(1)}(x-x_1)\right),\ (x,z) \in \Omega^1_\infty, \quad (3.34)$$

$$\phi^2_\infty(x,z) = C_0 \exp\left(\mathrm{i}k_0^{(2)}x\right) Z_0^{2}(z) + \sum_{n=1}^{\infty} C_n Z_n^{(2)}(z) \exp\left(\mathrm{i}k_n^{(2)}(x_2-x)\right),\ (x,z) \in \Omega^2_\infty. \quad (3.35)$$

The sets of vertical structures $\{Z_n^{(j)}, n = 0, 1, ...\infty\}$ and wavenumbers $\{\mathrm{i}k_0^{(j)}, k_n^{(j)}, n = 1, ...\infty\}$ are the eigenvalues and eigenvectors of the locally defined Sturm-Liouville problems in $\Omega^j_\infty, j = 1, 2$. The introduction of a suitable *DtN* mapping, exploiting expansions Eqs. (3.34) and (3.35) can be used to substitute Eqs. (3.33), (3.32 a) and (3.32 b) with the following condition on the truncated boundary,

$$\nabla_{\mathbf{n}}\phi_d - \Im\phi_d = 0 \text{ on } \Gamma_c. \quad (3.36)$$

The latter approach will be adopted when considering 2D diffraction and radiation-type problems. The treatment of radiation condition Eq. (3.33), for the considered 3D problems, assuming radiative conditions at infinity will be the focus of a subsequent chapter exploring PML-FEM formulations for wave scattering problems in the ocean environment. Alternatively, the solvability of the above boundary value problem is ensured by extending the truncated boundaries within the homogenous region (at least a distance of the order of one wavelength) and imposing the Sommerfeld radiation conditions. hence, for the derivation on the weak form, Eq. (3.33) is replaced with,

$$\nabla_{\mathbf{n}}\phi_d - \mathrm{i}k(\mathbf{x})\phi_d = 0 \text{ on } \Gamma_c. \quad (3.37)$$

The Robin type approximate condition Eq. (3.37) is employed for the derivation of a conventional weak form which will be substituted in the sequel by a PML formulation. The present choice of termination condition on the truncated boundary is made towards the simplification of the mathematical treatment of radiation-type problems,

**Weak Problem 3.3.** *(3D Diffraction)* Find $\phi_d(\mathbf{x}, z), \in V(\Omega)$ such that it holds,

$$\int_\Omega \nabla v \cdot \nabla\phi_d \, d\Omega - \mu \int_{\Gamma_f} v\,\phi_d \, ds + \int_{\Gamma_b} v\, f \, ds - \int_{\Gamma_c} \mathrm{i}k(\mathbf{x})\phi_d v \, ds = 0,$$

$$\forall v(\mathbf{x}, z) \in V(\Omega).$$

## 3.4 Radiation-type Wave field

The notions introduced in the previous subsections are transferred to the case of radiation-type problems following the decomposition discussed in Section 1.3. The strong formulation of the $\ell^{\text{th}}$ radiation-type problem is presented along with the corresponding weak form in both 3D and 2D strips. It is reminded that for this type of subproblem the radiative solutions are produced due scattering in the presence of a floating, elastic body supported in the region on inhomogeneity or due to its wave-induced flexural motion. Due to the above, the domain of interest was decomposed into two regions,the free-surface region $\Omega_1$ and the plate-covered region $\Omega_2$, creating the interface $S$ between subregions. Considering the formulation of the given problem in the 2D Cartesian strip, the decomposition of region $\Omega^s$, generates the free-surface regions, $\Omega^s_{1,2}$ the plate-covered region $\Omega^s_3$ and the interfaces $S_{1,2}$

In the 3D strip $\mathcal{D}$ the strong form of the decomposed $\ell^{\text{th}}$ radiation-type problem is written as,

$$\nabla^2 \varphi_\ell^{(j)} = 0, \text{for } (\mathbf{x}, z) \in \Omega_j, \quad j = 1, 2 \tag{3.38}$$

$$\partial_z \varphi_\ell^{(1)} - \mu \varphi_\ell^{(1)} = 0, \text{on } \Gamma_f^1 \ (z = 0), \tag{3.39}$$

$$\partial_z \varphi_\ell^{(2)} + f_\ell = 0, \text{on } \Gamma_f^2 \ (z = 0) \tag{3.40}$$

$$\nabla_{\mathbf{n}_b} \varphi_\ell = 0, \text{on } \Gamma_b, \tag{3.41}$$

$$\varphi_\ell^{(1)} = \varphi_\ell^{(2)}, \text{and} \tag{3.42 a}$$

$$\nabla_{\mathbf{n}_{12}} \varphi_\ell^{(1)} = -\nabla_{\mathbf{n}_{21}} \varphi_\ell^{(2)} \text{on } S, \tag{3.42 b}$$

$$\varphi^* = \varphi_\ell^{(2)} \text{and} \tag{3.43 a}$$

$$\nabla_{\mathbf{n}_c} \varphi^* = \nabla_{\mathbf{n}_c} \varphi_\ell^{(2)} \text{on } \Gamma_c. \tag{3.43 b}$$

For the Neumann condition on $\Gamma_f^2$, it holds that $f_0 = \partial_z \varphi_P$ and $f_\ell = \mathrm{i}\omega w_\ell$ for $\ell = 1, 2, ...\infty$. Regarding the radiation condition Eq. (3.33), the same comments as in Section 3.3.2 can be made. Hence, in the 2D strip, by means of representations Eqs. (3.24) and (3.25), boundary conditions of the form Eq. (3.36) for $\varphi_\ell$ can be derived on $\Gamma$. Employing Eq. (3.37) for now, the following weak formulations are derived. The restrictions of the $\ell^{\text{th}}$ velocity potential solutions in each subregion is denoted as $\varphi_\ell|_{\Omega_j} \equiv \varphi^{(j)}$ for simplicity. The subscript $\ell$ is implied henceforth.

Next, the following tensor product space is defined

$$\mathcal{H} = \{(\varphi^{(1)}, \varphi^{(2)}) \,|\, \varphi^{(j)} \in H^1(\Omega_j; \mathbb{C}) \ j = 1, 2\}.$$

And the affine space,

$$\overline{\mathcal{H}} = \{(\varphi^{(1)}, \varphi^{(2)}) \in \mathcal{H} \,|\, \varphi^{(2)} - \varphi^{(1)} = 0 \text{ on } S\}.$$

Employing the constructed space $\overline{\mathcal{H}}$ that incorporates the essential continuity requirement results is the following weak problem.

**Weak Problem.** *(3D Radiation)* Find $\varphi^{(j)}(\mathbf{x},z) \in \overline{\mathcal{H}}$ such that it holds,

$$\sum_{j=1}^{2}\left(\int_{\Omega}\nabla v^{(j)}\cdot\nabla\varphi^{(j)}\,d\Omega\right)-\mu\int_{\partial\Gamma_f^1}v^{(1)}\,\varphi^{(1)}\,ds+\int_{\partial\Gamma_f^2}v^{(2)}\,f_\ell\,ds$$
$$+\int_S(v^{(2)}-v^{(1)})\nabla_{\mathbf{n}_{12}}\varphi^{(1)}\,ds-\int_{\Gamma_c}\mathrm{i}k(\mathbf{x})\varphi^{(j)}v^{(j)}\,ds=0,$$
$$\forall v^{(j)}(\mathbf{x},z)\in\overline{\mathcal{H}}.$$

The above Problem is per the previous discussion transformed by means of a Lagrange multiplier function leading to the following two-field formulation,

**Mixed Weak Problem 3.2.** *(3D Radiation)* Find $\left(\varphi^{(j)}(\mathbf{x},z),\lambda(S)\right)\in\mathcal{H}\times(H^{-1/2}(S))$ such that it holds,

$$\begin{cases}\displaystyle\sum_{j=1}^{2}\left(\int_{\Omega}\nabla v^{(j)}\cdot\nabla\varphi^{(j)}\,d\Omega\right)-\mu\int_{\Gamma_f^1}v^{(1)}\,\varphi^{(1)}\,ds+\int_{\Gamma_f^2}v^{(2)}\,f_\ell\,ds\\ \qquad+\displaystyle\int_S(v^{(2)}-v^{(1)})\lambda\,ds-\int_{\Gamma_c}\mathrm{i}k(\mathbf{x})\varphi^{(j)}v^{(j)}\,ds=0,\\ \displaystyle\int_S\xi\left(\varphi^{(2)}-\varphi^{(1)}\right)\,ds=0,\end{cases}$$
$$\forall\left(v^{(j)}(\mathbf{x},z),\xi(S)\right)\in\mathcal{H}\times(H^{-1/2}(S)).$$

Next, the corresponding weak form for the typical radiation-type subproblem confined in the 2D plane is derived. Considering again the 2D waveguide $\mathcal{D}^c$, with the addition of a floating strip on a finite subsection of $\partial\Gamma_f$. The presence of the structure facilitates the decomposition of $\Omega^s$, restricted below by the variable seabed $z=h(x)$ (boundary $\partial\Gamma_b$), into the free-surface and plate-covered subregions denoted as $\Omega_j^s, j=1,2$ and $\Omega_3^s$ it is noted that the velocity potential function is now decomposed into the free surface wave fields $\varphi^{(i)},\ j=1,2$ and the plate-covered region solution $\varphi^{(3)}$ (see Fig. 3.2). The subdomains are separated by the geometrically conforming interfaces $S_j,\ j=1,2$. The corresponding tensor product and its affine function space, equipped with the essential conditions on the interfaces $S_j$ are redefined as,

$$\mathcal{H}=\{(\varphi^{(1)},\varphi^{(2)},\varphi^{(3)})\,|\varphi^{(j)}\in H^1(\Omega_j^s;\mathbb{C})\ j=1,2,3\}\text{ and}$$
$$\overline{\mathcal{H}}=\{\varphi^{(j)}\in\mathcal{H}|\varphi^{(j)}-\varphi^{(3)}=0\text{ on }S_j\text{ for }j=1,2\}.$$

By means of the revised $\overline{\mathcal{H}}$ the following weak form is straightforwardly derived for the 2D radiation-type problem,

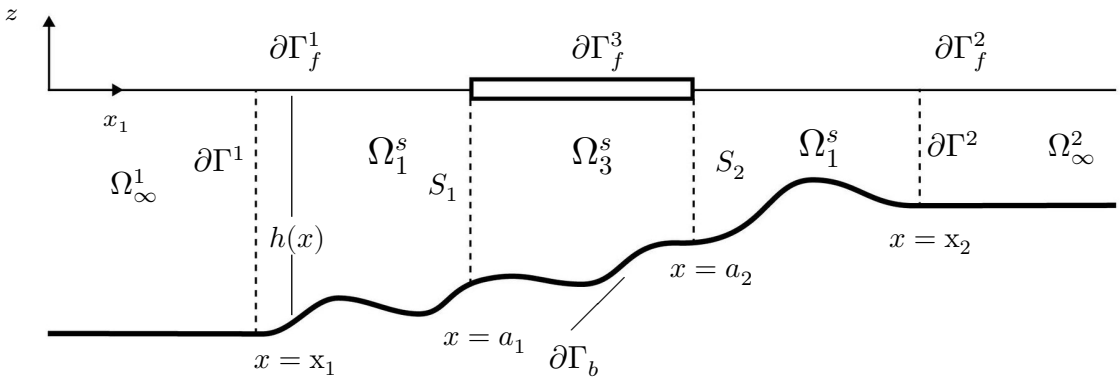


**Figure 3.2** Radiation in the inhomogeneous 2D waveguide due to the floating structure

**Weak Problem.** *(2D Radiation) Find* $\varphi^{(j)}(\mathbf{x}, z) \in \overline{\mathcal{H}}$ *such that it holds,*

$$\sum_{j=1}^{3}\left(\int_{\Omega_j^s}\nabla v^{(j)}\cdot\nabla\varphi^{(j)}\,d\Omega\right)-\sum_{j=1}^{2}\left(\mu\int_{\partial\Gamma_f^j}v^{(j)}\,\varphi^{(j)}\,ds\right)+\int_{\partial\Gamma_f^3}v^{(3)}\,f_\ell\,ds$$
$$+\sum_{j=1}^{2}\left(\int_{S_j}(v^{(3)}-v^{(j)})\nabla_{\mathbf{n}_{js}}\varphi^{(j)}\,ds\right)-\sum_{j=1}^{2}\left(\int_{\partial\Gamma^j}\mathrm{i}k_0^{(j)}(\mathbf{x})\varphi^{(j)}v^{(j)}\,ds\right)=0,$$
$$\forall v(\mathbf{x}, z)\in\overline{\mathcal{H}}.$$

The Lagrange functions that are employed to enable the satisfaction of the continuity requirement in a weak sense across on the interfaces $S_j$ are now denoted with $\lambda^{(j)},\ j=1,2$

**Mixed Weak Problem 3.3.** *(2D Radiation)* Find $\left(\varphi^{(j)}(x,z),\lambda^{(j)}\right)\in V(\Omega_j^s)\times(H^{-1/2}(S_j))$ such that it holds,

$$\begin{cases}\displaystyle\sum_{j=1}^{3}\left(\int_{\Omega_j^s}\nabla v^{(j)}\cdot\nabla\varphi^{(j)}\,d\Omega\right)-\sum_{j=1}^{2}\left(\mu\int_{\partial\Gamma_f^{(j)}}v^{(j)}\,\varphi^{(j)}\,ds\right)+\int_{\partial\Gamma_f^{(3)}}v^{(3)}\,f_\ell\,ds\\ \quad\displaystyle+\sum_{j=1}^{2}\left(\int_{S_j}(v^{(3)}-v^{(j)})\lambda^{(j)}\varphi^{(j)}\,ds\right)-\sum_{j=1}^{2}\left(\int_{\partial\Gamma^j}\mathrm{i}k_0^{(j)}(\mathbf{x})\varphi^{(j)}v^{(j)}\,ds\right)=0,\\ \displaystyle\sum_{j=1}^{2}\int_{S_j}\xi^{(j)}\left(\varphi^{(3)}-\varphi^{(j)}\right)\,ds=0,\end{cases}$$
$$\forall\left(v^{(j)}(\mathbf{x},z),\xi^{(j)}(S_j)\right)\in V(\Omega_j^s)\times(H^{-1/2}(S_j)).$$

In the sequel, the dimensionality reduction of the produced Mixed Weak Problems 3.1–3.3 is sought out by appropriately chosen vertical multi-modal expansions.

# Chapter 4

# Dimensionality reduction

A semi-analytical approach will be employed for the dimensionality reduction of the defined weak problems. The approximate solution in each subregion is sought in a separable form, where the vertical structure of the solution, is chosen a priori. The approach resembles the Kantorovich method for the dimensionality reduction of prismatic problems Kantorovich and Krylov (1960). The application of a multi-term version of Kantorovich's method will allow the reformulation of the previously derived weak forms in horizontal coordinates only.

## 4.1 The Kantorovich Method

The MWR was employed in the previous chapter to derive the weak formulations of the hydrodynamic subproblems following the decomposition introduced in Section 1.3. The MWR presents a powerful tool for the derivation of approximate methods for PDEs. Depending on the choice of the employed weight functions $v(\mathbf{x}, z)$ one can derive approximating methods like the Collocation method, the Subdomain Method the Galerkin Method and others (Finlayson, 2013; Finlayson and Scriven, 1967; Washizu, 1975; Zienkiewicz and Taylor, 2005). Additionally, assuming the trial function in a separable form, ODE-oriented methods are derived. One example is the Ritz method, where the equivalent integral equation, coinciding with a minimisation principle, is reduced to the minimisation of a function of several variables. The trial function assumes a separable form and is represented by a series of products of unknown coefficients and *a priori* chosen functions of principal coordinates. Finally, the associated integral form of the problem is reduced to a function that needs to be minimised in terms of the involved, unknown coefficients. In the sense that no discretisation is required, Ritz is an analytical method. In the work of Kantorovich and Krylov (1960) a method of dimensionality reduction is proposed for prismatic problems that lays between the Ritz and Galerkin methods. The approximate solution is again sought in a separable form, but only a function of one variable is chosen *a priori*, leading to a dimensionality reduction of the problem at hand. The

reduced weak formulation of the problem often needs to be solved numerically, leading to a semi-analytical numerical scheme.

## 4.2 Multi-Mode representation of the wave potential functions

In the following section, a semi-analytical approach will be employed for the approximate solution of the weak hydrodynamic problems defined in Chapter 3. The unknown velocity potential in each subregion is sought in a separable form, where the vertical structure of the solution, is chosen *a priori*. The approach resembles a multi-term Kantorovich method for the dimensionality reduction of boundary value problems, relevant to prismatic domains Kantorovich and Krylov (1960). The approximate solution in each subregion is expanded as a series in terms of the vertical eigenmodes, calculated as solutions to vertical eigenvalue problems. The employed eigenmodes must satisfy the imposed conditions on the vertical water column. In the free-surface region, the employed vertical modes need to satisfy the Robin-type upper surface condition Eq. (1.4), and the homogenous Neumann condition Eq. (1.7) on the seabed. Accounting for the inhomogeneous waveguide, a series of local Sturm-Liouville problems are employed. In essence, the vertical structure of the approximate solution is parametrically defined with horizontal position, and thus features implicit dependence on horizontal coordinates. In a similar manner, the vertical structure employed for the plate-covered region must satisfy Eq. (1.5) along with Eq. (1.7).

The above technique has been employed for the treatment of linear water wave propagation in variable bathymetry regions by Athanassoulis and Belibassakis (1999) and later extended for wave interaction with thin floating elastic plates Belibassakis and Athanassoulis (2005). One advantage of the above choice, is that that the vertical structure of the specific representation is close to the solution of the studied wave problem, as it will be discussed in more detail in the sequel.

In the scope of the present work, the following local-mode series expansion for the unknown wave fields are considered in the free-surface and plate covered subregions respectively,

$$\varphi^{(1)}(\mathbf{x},z) = \sum_{n=0}^{\infty} \varphi_n^{(1)}(\mathbf{x},z) Z_n(z;\mathbf{x}), \text{ for } (\mathbf{x},z) \in \Omega_1 \tag{4.1}$$

$$\varphi^{(2)}(\mathbf{x},z) = \sum_{n=0}^{\infty} \varphi_n^{(2)}(\mathbf{x},z) Y_n(z;\mathbf{x}) + \tilde{\varphi}_0, \text{ for } (\mathbf{x},z) \in \Omega_2. \tag{4.2}$$

*Remark* 2. Considering the field equation is each subregion, there is a $C^0$ continuity requirement for the trial functions Eqs. (4.1) and (4.2) across the common boundary. This is violated by the above choices, but is remedied by the enforcement of the continuity requirement as a constraint.

*Remark* 3. The choice of the above vertical structures $Z_n$ and $Y_n$ are by no means unique. As long as completeness requirements are met to validate the employment of expansions Eqs. (4.1) and (4.2) and the boundary conditions on the upper and lower strip boundaries are satisfied, other families of factions can be considered. The performance of the method heavily relies on the choice of the above functions.

### Vertical Expansion for free-surface region $\Omega_1$

The functions $Z_n(z;\mathbf{x})$, chosen as the vertical structure of the potential in the free-surface regions are obtained as the solutions of the following, locally-defined vertical Sturm-Liouville problem,

$$\partial_z^2 Z_n(z;\mathbf{x}) + k_n^2 Z_n(z;\mathbf{x}) = 0 \text{ for } (\mathbf{x},z) \in \Omega_1, \tag{4.3}$$

$$\partial_z Z_n(z;\mathbf{x}) - \mu Z_n(z;\mathbf{x}) = 0 \text{ on } \Gamma_f^1 \ (z=0), \tag{4.4}$$

$$\partial_z Z_n(z;\mathbf{x}) = 0 \text{ on } \Gamma_b^1 \ (z=-h(\mathbf{x})). \tag{4.5}$$

The eigenfunction solutions of the problem, also briefly discussed in Section 3.3.1 are given as,

$$Z_0(z;\mathbf{x}) = \frac{\cosh\left(k_0(h(\mathbf{x})+z)\right)}{\cos\left(k_0 h(\mathbf{x})\right)}, \ Z_n(z;\mathbf{x}) = \frac{\cos\left(k_n(h(\mathbf{x})+z)\right)}{\cos\left(k_n h(\mathbf{x})\right)} \text{ for } n=1,2,...,\infty \tag{4.6}$$

The eigenvalues $\{\mathrm{i}k_0, k_n\}$ are calculated as the roots of the local dispersion relation defined in the free surface region,

$$\mu h(\mathbf{x}) = -k_n(\mathbf{x})h(\mathbf{x})\tan(k_n(\mathbf{x})(\mathbf{x})) \tag{4.7}$$

*Remark* 4. There is a discrepancy between the kinematic condition Eq. (4.5) satisfied by the employed vertical eigenfunctions and the imposed condition involving the normal derivative of the velocity potential on the variable seabed Eq. (1.7). The above is remedied by the introduction of an additional term in the representation Eq. (4.1) for the treatment of the sloping bottom effects, referred as the *sloping bottom mode* following the work Athanassoulis and Belibassakis (1999). The aforementioned, added mode to the classical representation, denoted as $\varphi_{-1}Z_{-1}$ accounts for the incompatibility of the vertical modes and leads to the consistent satisfaction of the kinematic boundary condition on the sloping seabed. The extra horizontal mode, $\varphi_{-1}$, acts as a set of additional degrees of freedom that account for the non-homogeneity of the vertical derivative on the seabed. It is evident that the choice for $Z_{-1}$ must lead to solutions that satisfy the upper surface condition Eq. (4.4) and render $\varphi_{-1}$ a free variable at the bottom boundary. A convenient, but certainly not unique, choice for the

structure is,

$$Z_{-1}(z;\mathbf{x}) = h(\mathbf{x})\left[\left(\frac{z}{h(\mathbf{x})}\right)^3 + \left(\frac{z}{h(\mathbf{x})}\right)^2\right]. \tag{4.8}$$

The added mode vanishes at constant depth where retrieving the classical standard representation for the wave potential in the homogeneous strip.

### Vertical Expansion for plate-covered region $\Omega_2$

The vertical functions $Y_n(z;\mathbf{x})$ are similarly obtained by addressing the following, locally-defined vertical Sturm-Liouville problem in the plate-covered region,

$$\partial_z^2 Y_n(z;\mathbf{x}) + \vartheta_n^2 Y_n(z;\mathbf{x}) = 0 \text{ for } (\mathbf{x},z) \in \Omega_2, \tag{4.9}$$

$$\partial_z Y_n(z;\mathbf{x}) = 0 \text{ on } \Gamma_f^2 \ (z=0), \tag{4.10}$$

$$\partial_z Y_n(z;\mathbf{x}) = 0 \text{ on } \Gamma_b^2 \ (z=-h(\mathbf{x})),. \tag{4.11}$$

The solutions are given as,

$$Y_n(z;\mathbf{x}) = \cos(\vartheta_n z) \text{ with } \vartheta_n = \frac{n\pi}{h(\mathbf{x})}. \tag{4.12}$$

*Remark* 5. It is observed that the homogeneous Neumann condition Eq. (4.10), satisfied by the vertical modes $Y_n(z;\mathbf{x})$, is incompatible with the imposed kinematic boundary condition of the hydroelastic problem Eq. (1.5). The latter is remedied by the inclusion in the representation Eq. (4.2) of an upper surface mode $\tilde{\varphi}_0 = g(\mathbf{x})q(z;\mathbf{x})$. The additional mode must satisfy the boundary conditions on the entire boundary of the plate-covered region $\Gamma_2$. A judicious choice for the vertical structure of $q(z)$ is,

$$q(z;\mathbf{x}) = \frac{(z+h(\mathbf{x}))^2}{2h(\mathbf{x})}. \tag{4.13}$$

Furthermore, setting $g(\mathbf{x}) = -f_\ell$, for the $\ell^{\text{th}}$ radiation-type problem allows for the consistent satisfaction of the upper surface condition Eq. (1.5) and the homogeneous Neumann conditions on the seabed, by the trial function Eq. (4.12).

*Remark* 6. The addition of the sloping bottom mode in series expansion Eq. (4.12), allows for the consistent satisfaction of Eq. (4.5) as described above.

Based on the above, the representations for the weight functions are,

$$v^{(1)}(\mathbf{x},z)=\sum_{n=0}^{\infty}v_n^{(1)}(\mathbf{x},z)Z_n(z;\mathbf{x}) \tag{4.14}$$

$$v^{(2)}(\mathbf{x},z)=\sum_{n=0}^{\infty}v_n^{(2)}(\mathbf{x},z)Y_n(z;\mathbf{x}) \tag{4.15}$$

The coupling between subdomains is achieved, as previously discussed, by means of the introduced Lagrange multiplier functions that resemble the normal trace of the unknown velocity potential on interface $S$,

$$\lambda(S,z)=\sum_{n=0}^{\infty}\lambda_n(S,z)Z_n(z;S) \tag{4.16}$$

$$\xi(S,z)=\sum_{n=0}^{\infty}\xi_n(S,z)Z_n(z;S) \tag{4.17}$$

*Remark* 7. The geometrical conformity of the interface $S$, allows for the employment of either $Z_n$ or $Y_n$ for the vertical expansion of $\lambda$.

Keeping a finite number of modes $N_m\in\mathbb{N}$ in both expansions and employing the additional sloping bottom mode the truncated series are summarised as,

$$\varphi^{(1)}(\mathbf{x},z)=\sum_{n=-1}^{N_m}\varphi_n^{(1)}(\mathbf{x},z)Z_n(z;\mathbf{x})=\mathbf{Z}^{\mathsf{T}}\boldsymbol{\varphi}^{(1)}\text{ and} \tag{4.18}$$

$$v^{(1)}(\mathbf{x},z)=\sum_{n=-1}^{N_m}v_n^{(1)}(\mathbf{x},z)Z_n(z;\mathbf{x})=\mathbf{Z}^{\mathsf{T}}\mathbf{v}^{(1)},\text{ for }(\mathbf{x},z)\in\Omega_1 \tag{4.19}$$

$$\varphi^{(2)}(\mathbf{x},z)=\sum_{n=-1}^{N_m}\varphi_n^{(2)}(\mathbf{x},z)Y_n(z;\mathbf{x})=\mathbf{Y}^{\mathsf{T}}\boldsymbol{\varphi}^{(2)}\text{ and} \tag{4.20}$$

$$v^{(2)}(\mathbf{x},z)=\sum_{n=-1}^{N_m}v_n^{(2)}(\mathbf{x},z)Y_n(z;\mathbf{x})=\mathbf{Y}^{\mathsf{T}}\mathbf{v}^{(2)},\text{ for }(\mathbf{x},z)\in\Omega_2 \tag{4.21}$$

Similarly for the Lagrange multipliers defined on interface bondary $S$ it holds,

$$\lambda(S,z)=\sum_{n=-1}^{N_m}\lambda_n(S,z)Z_n(z;S)=\mathbf{Z}^{\mathsf{T}}\boldsymbol{\lambda}\text{ and} \tag{4.22}$$

$$\xi(S,z)=\sum_{n=-1}^{N_m}\xi_n(S,z)Z_n(z;S)=\mathbf{Z}^{\mathsf{T}}\boldsymbol{\xi}\text{ for }(\mathbf{x},z)\in S. \tag{4.23}$$

## 4.3 Reduction of the 2D Transmission Problem

The representations Eqs. (4.18) and (4.19) are straight forwardly defined in the 2D strip $\Omega^c$ and the transmission problem, defined in terms of the velocity potential $\phi_i$ in Section 3.3.1.

Particularly, representations for the 2D transmission subproblem are adapted as,

$$\phi_i(x,z) = \sum_{n=-1}^{N_m} \phi_n(x) Z_n(z;x) = \mathbf{Z}^{\mathsf{T}}\boldsymbol{\phi} \text{ and} \tag{4.24}$$

$$v(x,z) = \sum_{n=-1}^{N_m} v_n(x) Z_n(z;x) = \mathbf{Z}^{\mathsf{T}}\mathbf{v}, \text{ for } (x,z) \in \Omega^c. \tag{4.25}$$

### 4.3.1 Boundary conditions at the lateral boundaries

Revisiting Weak Problem 3.2, the Green-Gauss theorem was employed in the first equation, resulting in the lateral boundary terms Eq. (3.28). Exploiting the above representation of the free surface potential and the exterior solution representations Eqs. (3.24) and (3.25), boundary terms Eq. (3.28) become,

at $x = \mathrm{x}_1$

$$\sum_{m=0}^{N_m} v_m(\mathrm{x}_1) \int_{z=-h(\mathrm{x}_1)}^{z=0} \Big\{ \partial_x\phi_0(\mathrm{x}_1) Z_0 - (\mathrm{i}\kappa_0^{(1)} A_0 \exp(\mathrm{i}\kappa_0^{(1)}\mathrm{x}_1) + \mathrm{i}\kappa_0 A_R \exp(\mathrm{i}\kappa_0^{(1)}\mathrm{x}_1)) Z_0^{(1)} + (\partial_x\phi_n(x_1) Z_n - \kappa_n^{(1)} C_n^{(1)} Z_n^{(1)}) \Big\} Z_m(z;\mathrm{x}_1) = 0, \tag{4.26}$$

at $x = \mathrm{x}_2$

$$\sum_{m=0}^{N_m} v_m(\mathrm{x}_2) \int_{z=-h(\mathrm{x}_2)}^{z=0} \Big\{ \partial_x\phi_0(\mathrm{x}_2) Z_0 - \mathrm{i}\kappa_0^{(2)} A_T \exp(\mathrm{i}\kappa_0^{(2)}\mathrm{x}_2) Z_0^{(2)} + (\partial_x\phi_n(\mathrm{x}_2) Z_n - \kappa_n^{(2)} C_n Z_n)) \Big\} Z_m(z;\mathrm{x}_2) = 0. \tag{4.27}$$

Following the same line of thought, the continuity constraints on the lateral boundaries read,

at $x = \mathrm{x}_1$

$$\sum_{m=0}^{N_m} \int_{z=-h(\mathrm{x}_1)}^{z=0} \Big\{ (A_0 \exp(\mathrm{i}\kappa_0^{(1)}\mathrm{x}_1) + A_R \exp(\mathrm{i}\kappa_0^{(1)}\mathrm{x}_1)) Z_0^{(1)} - \phi_0(\mathrm{x}_1) Z_0 + (C_n^{(1)} Z_n^{(1)} - \phi_n(\mathrm{x}_1) Z_n) \Big\} \delta(\partial_x \phi_\infty^1) = 0, \tag{4.28}$$

at $x = \mathrm{x}_2$

$$\sum_{m=0}^{N_m} \int_{z=-h(\mathrm{x}_2)}^{z=0} \Big\{ (A_T \exp(\mathrm{i}\kappa_0^{(2)} \mathrm{x}_2)) Z_0^{(2)} - \phi_0(\mathrm{x}_2) Z_0 + (C_n^{(2)} Z_n^{(2)} - \phi_n(\mathrm{x}_2) Z_n) \Big\} \delta(\partial_x \phi_\infty^2) = 0. \tag{4.29}$$

Noting that the local basis, $Z_n$ and $Z_n^{(j)}$ converge on the lateral boundaries as $x \to \mathrm{x_j}$ and taking into account the arbitrariness of $v_m(\mathrm{x_j})$ and $\delta(\partial_x \phi_\infty^j)$ for $j = 1, 2$.

$$\mathbf{I}_{(N_m+2)}\, \partial_x \boldsymbol{\phi} - \mathbf{T}_t^j \boldsymbol{\phi} = \mathbf{g}^j \text{ on } \partial\Gamma^j. \tag{4.30}$$

with $\mathbf{T}_t^1 = \mathrm{diag}(-\mathrm{i}\kappa_0^{(1)}, \kappa_1^{(1)}, \kappa_2^{(1)}, \cdots, \kappa_{N_m}^{(1)})$ and $\mathbf{T}_t^2 = \mathrm{diag}(\mathrm{i}\kappa_0^{(2)}, -\kappa_1^{(2)}, -\kappa_2^{(2)}, \cdots, -\kappa_{N_m}^{(2)})$ and vectors $\mathbf{g}^1 = (2A_0 \mathrm{i}\kappa_0^{(1)}, 0, \cdots, 0)$, $\mathbf{g}^2 = (0, 0, \cdots, 0)$.

### 4.3.2 Reduced Weak Form

The derived boundary conditions Eq. (4.30) in terms of the unknown modal amplitude functions $\phi_n(x)$ at the lateral boundaries ensure the continuity of pressure and momentum between exterior solutions and solutions in the region of interest. The former allows for a reformulation of Weak Problem 3.2 defined in $\Omega^c$ to the following,

**Weak Problem 4.1.** *(2D Transmission)* Find $\phi_i(x, z) \in V(\Omega^c)$ such that it holds,

$$\int_{\Omega^c} \nabla v \cdot \nabla \phi_i \, d\Omega - \mu \int_{\partial\Gamma_f} v\, \phi_i \, ds - \sum_{j=1}^{2} \int_{\partial\Gamma^j} \partial_x \phi_i v \, ds = 0, \quad \forall v(x, z) \in V(\Omega^c).$$

The last boundary terms defined on $\partial\Gamma^j$ are to be substituted with the derived matching conditions Eq. (4.30).

Next, by substituting the representations Eqs. (4.24) and (4.25) in Weak Problem 4.1 results in the following reduced form in interval $I = [\mathrm{x}_1, \mathrm{x}_2]$,

$$\int_{x_1}^{x_2} \left( \partial_x \mathbf{v}^\mathsf{T} \mathbf{A} \partial_x \boldsymbol{\phi} + \mathbf{v}^\mathsf{T} \mathbf{B_1} \partial_x \boldsymbol{\phi} + \partial_x \mathbf{v}^\mathsf{T} \mathbf{B_2} \boldsymbol{\phi} + \mathbf{v}^\mathsf{T} \mathbf{C} \boldsymbol{\phi} \right) dx - \sum_{j=1}^{2} \left[ \partial_x \mathbf{v}^\mathsf{T} \mathbf{A} \partial_x \boldsymbol{\phi} \right]_{x=\mathrm{x_j}} = 0 \tag{4.31}$$

with matrix coefficients,

$$\begin{aligned} \mathbf{A}(x) = \int_{-h}^{0} \mathbf{Z}\mathbf{Z}^\mathsf{T} dz, \mathbf{B_1}(x) = \int_{-h}^{0} (\partial_x \mathbf{Z}) \mathbf{Z}^\mathsf{T} dz, \mathbf{B_2}(x) = \int_{-h}^{0} \mathbf{Z} (\partial_x \mathbf{Z})^\mathsf{T} dz, \text{ and} \\ \mathbf{C}(x) = \int_{-h}^{0} ((\partial_x \mathbf{Z})(\partial_x \mathbf{Z})^\mathsf{T} + \partial_z \mathbf{Z} (\partial_z \mathbf{Z})^\mathsf{T}) dz - \mu [\mathbf{Z}\mathbf{Z}^\mathsf{T}]_{z=0}. \end{aligned} \tag{4.32}$$

The above $x$-dependent matrix coefficients, with size $(N_m+2)\times(N_m+2)$, are defined parametrically along $I=[\mathrm{x}_1,\mathrm{x}_2]$. Coefficients involve the basis functions $\{\mathrm{Z}_n\}$ and their first derivative $\{\partial_x \mathrm{Z}_n\}$ suggesting a $C^1$ continuity requirement for the depth function $h(x)$. The new reduced integral form, now defined over the interval $I$, is supplemented with conditions Eq. (4.30) at the lateral boundaries $x=\mathrm{x_j}, j=1,2$. The employed vertical representations lead to the reduction of Weak Problem 3.2 into a weak system of coupled equations in $I$, written in terms of the unknown $x$-dependent modal amplitude functions .

*Remark* 8. The reformulation of Weak Problem 4.1, in light of the reduced integral form Eq. (4.31) requires the definition of the compound vector space $V^n=\underbrace{V\times V\times\cdots\times V}_{n}$. Thus, the weak problem is now posed as: Find $\boldsymbol{\phi}\in V(I)^{N_m+2}$ such that Eqs. (4.31) and (4.32) hold $\forall\mathbf{v}\in V(I)^{N_m+2}$.

## 4.4 Reduction of the weak 3D Diffraction Problem

Following the same process, the representations Eqs. (4.18) and (4.19) are employed for the diffracted velocity potential $\phi_d(\mathbf{x},z)$ and the weight function $v(\mathbf{x},z)$ defined in $\Omega$ and are subsequently substituted Weak Problem 3.3, resulting in the following integral form over the projected area $\breve{\Omega}$ on the horizontal 2D plane,

$$\int_{\breve{\Omega}}\Big\{\sum_{j=1}^{2}\Big(\partial_{x_j}\mathbf{v}^{\mathsf{T}}\mathbf{A}\partial_{x_j}\boldsymbol{\phi}_d+\mathbf{v}^{\mathsf{T}}\mathbf{B}_{\mathbf{1}}^{j}\partial_{x_j}\boldsymbol{\phi}_d+\partial_x\mathbf{v}^{\mathsf{T}}\mathbf{B}_{\mathbf{2}}^{j}\boldsymbol{\phi}_d\Big)+\mathbf{v}^{\mathsf{T}}\mathbf{C}\boldsymbol{\phi}_d\Big\}\,d\mathbf{x}=-\int_{\Gamma_b}\partial_n\phi_i\mathbf{v}^{\mathsf{T}}\mathbf{Z}|_{-h}\,ds, \tag{4.33}$$

with matrix coefficients in accordance with Eq. (4.32) for $j=1,2$,

$$\begin{aligned}\mathbf{A}(\mathbf{x})=\int_{-h}^{0}\mathbf{Z}\mathbf{Z}^{\mathsf{T}}dz,\mathbf{B}_{\mathbf{1}}^{j}(\mathbf{x})=\int_{-h}^{0}(\partial_{x_j}\mathbf{Z})\mathbf{Z}^{\mathsf{T}}dz,\mathbf{B}_{\mathbf{2}}^{j}(\mathbf{x})=\int_{-h}^{0}\mathbf{Z}(\partial_{x_j}\mathbf{Z})^{\mathsf{T}}dz\ \text{and}\\ \mathbf{C}(\mathbf{x})=\int_{-h}^{0}\Big(\textstyle\sum_{j=1}^{2}\Big((\partial_{x_j}\mathbf{Z})(\partial_{x_j}\mathbf{Z})^{\mathsf{T}}\Big)+\partial_z\mathbf{Z}(\partial_z\mathbf{Z})^{\mathsf{T}}\Big)\,dz-\mu[\mathbf{Z}\mathbf{Z}^{\mathsf{T}}]_{z=0}.\end{aligned} \tag{4.34}$$

The *rhs* of Eq. (4.33) is essentially known as the *a priori* calculated incident $\phi_i$ Cauchy data on the seabed surface. The reduced integral form of Eq. (4.33) and matrix coefficients Eq. (4.34) are defined in $\breve{\Omega}(x_1,x_2)$.

## 4.5 Reduction of the weak Radiation-type Problem

### 4.5.1 3D Formulation

Next, revisiting the radiation-type subproblem defined in the 3D waveguide a reduced expression on the projected region $\breve{\Omega}$ is sought. The reader is referred to Fig. 1.1(ii) Considering once

again Mixed Weak Problem 3.2, the boundary term on $\Gamma_c$ is ignored at this point, as numerical truncation of the computational region is the subject of a following chapter. Upon substitution of series Eqs. (4.18) and (4.19) the integral terms corresponding to the free-surface region $\Omega_1$ read,

$$\int_{\breve{\Omega}_1} \Big\{ \sum_{j=1}^{2} \Big( (\partial_{x_j} \mathbf{v}^{(1)})^{\mathsf{T}} \mathbf{A} (\partial_{x_j} \boldsymbol{\varphi}^{(1)}) + (\mathbf{v}^{(1)})^{\mathsf{T}} \mathbf{B}_{\mathbf{1}}^{j} (\partial_{x_j} \boldsymbol{\varphi}^{(1)}) + (\partial_x \mathbf{v}^{(1)})^{\mathsf{T}} \mathbf{B}_{\mathbf{2}}^{j} \boldsymbol{\varphi}^{(1)} \Big) + (\mathbf{v}^{(1)})^{\mathsf{T}} \mathbf{C} \boldsymbol{\varphi}^{(1)} \Big\} \, d\mathbf{x} \tag{4.35}$$

The matrix coefficients $\mathbf{A}, \mathbf{B}_{\mathbf{1}}^{j}, \mathbf{B}_{\mathbf{2}}^{j}$ and $\mathbf{C}$ are defined in Eq. (4.34). Similarly, in the plate-covered region the integral terms become,

$$\int_{\breve{\Omega}_2} \Big\{ \sum_{j=1}^{2} \Big( (\partial_{x_j} \mathbf{v}^{(2)})^{\mathsf{T}} \breve{\mathbf{A}} (\partial_{x_j} \boldsymbol{\varphi}^{(2)}) + (\mathbf{v}^{(2)})^{\mathsf{T}} \breve{\mathbf{B}}_{\mathbf{1}}^{j} (\partial_j \boldsymbol{\varphi}^{(2)}) + (\partial_x \mathbf{v}^{(2)})^{\mathsf{T}} \breve{\mathbf{B}}_{\mathbf{2}}^{j} \boldsymbol{\varphi}^{(2)} \Big) + (\mathbf{v}^{(2)})^{\mathsf{T}} \breve{\mathbf{C}} \boldsymbol{\varphi}^{(2)} + \sum_{j=1}^{2} \Big( \partial_{x_j} \mathbf{v}^{(2)\mathsf{T}} \mathbf{G}_{\mathbf{1}}^{j} + (\mathbf{v}^{(2)})^{\mathsf{T}} \mathbf{G}_{\mathbf{2}}^{j} \Big) \Big\} \, d\mathbf{x} \tag{4.36}$$

The matrix coefficients employed above for $j = 1, 2$ are,

$$\begin{gathered}
\breve{\mathbf{A}}(\mathbf{x}) = \int_{-h}^{0} \mathbf{Y}\mathbf{Y}^{\mathsf{T}} dz, \breve{\mathbf{B}}_{\mathbf{1}}^{j}(\mathbf{x}) = \int_{-h}^{0} (\partial_{x_j} \mathbf{Y}) \mathbf{Y}^{\mathsf{T}} dz, \breve{\mathbf{B}}_{\mathbf{2}}^{j}(\mathbf{x}) = \int_{-h}^{0} \mathbf{Y} (\partial_{x_j} \mathbf{Y})^{\mathsf{T}} dz, \\
\breve{\mathbf{C}}(\mathbf{x}) = \int_{-h}^{0} \Big( \sum_{j=1}^{2} \Big( (\partial_{x_j} \mathbf{Z})(\partial_{x_j} \mathbf{Y})^{\mathsf{T}} \Big) + \partial_z \mathbf{Y} (\partial_z \mathbf{Y})^{\mathsf{T}} \Big) \, dz \\
\mathbf{G}_{\mathbf{1}}^{j}(\mathbf{x}) = \partial_{x_j} f_\ell \int_{-h}^{0} q \mathbf{Y} dz + f_\ell \int_{-h}^{0} (\partial_{x_j} q) \mathbf{Y} dz \text{ and} \\
\mathbf{G}_{\mathbf{2}}^{j}(\mathbf{x}) = \partial_{x_j} f_\ell \int_{-h}^{0} q (\partial_{x_j} \mathbf{Y}) dz + f_\ell \int_{-h}^{0} (\partial_{x_j} q)(\partial_{x_j} \mathbf{Y}) dz + f_\ell \int_{-h}^{0} (\partial_z q)(\partial_z \mathbf{Y}) dz + [\partial_z q \mathbf{Y}]_{z=0}.
\end{gathered} \tag{4.37}$$

*Remark* 9. The terms in Eq. (4.36) including the vectors $\mathbf{G}_{\mathbf{i}}^{j}, i, j = 1, 2$ carry no unknowns and will be moved in the *rhs* of the final system.

Next, the interface term found in Mixed Weak Problem 3.2 involving the Lagrange multiplier function is considered next,

$$\int_S (v^{(2)} - v^{(1)}) \lambda \, ds \tag{4.38}$$

Following the familiar process the above term is reduced in,

$$\int_P \Big( (\mathbf{v}^{(2)})^{\mathsf{T}} \mathbf{P} - (\mathbf{v}^{(3)})^{\mathsf{T}} \mathbf{A} \Big) \boldsymbol{\lambda} \, d\mathbf{x} \tag{4.39}$$

with matrix coefficient $\mathbf{A}(\mathbf{x})$ matching the above definition and

$$\mathbf{P}(\mathbf{x}) = \int_{-h}^{0} \mathbf{Y}\mathbf{Z}^{\mathsf{T}} dz. \tag{4.40}$$

The second equation, expressing the constraint on the interface, in Problem 3.2 becomes,

$$\int_{P} (\boldsymbol{\xi})^{\mathsf{T}} \Big( \mathbf{P}^{\mathsf{T}}(\boldsymbol{\varphi}^{(2)}) - \mathbf{A}(\boldsymbol{\varphi}^{(3)}) \Big) \, d\mathbf{x} = \mathbf{F}, \tag{4.41}$$

with,

$$\mathbf{F} = \int_{P} \left( f_{\ell}(P) \int_{-h}^{0} q\mathbf{Z} \, dz \right) \, d\mathbf{x}. \tag{4.42}$$

Adding expressions Eqs. (4.35), (4.36), (4.39) and (4.41) results to a reduced system of integral equations on the horizontal plane. The new weak problem reads,

Find $(\boldsymbol{\varphi}, \boldsymbol{\lambda}) \in \mathcal{H}(\breve{\Omega})^{N_m+2} \times H^{-1/2}(P)^{N_m+2}$ such that,

$$\begin{cases} \displaystyle\int_{\breve{\Omega}_1} \Big\{ \sum_{j=1}^{2} \Big( (\partial_{x_j} \mathbf{v}^{(1)})^{\mathsf{T}} \mathbf{A} (\partial_{x_j} \boldsymbol{\varphi}^{(1)}) + (\mathbf{v}^{(1)})^{\mathsf{T}} \mathbf{B}_{\mathbf{1}}^{j} (\partial_{x_j} \boldsymbol{\varphi}^{(1)}) + (\partial_x \mathbf{v}^{(1)})^{\mathsf{T}} \mathbf{B}_{\mathbf{2}}^{j} \boldsymbol{\varphi}^{(1)} \Big) \\ \quad + (\mathbf{v}^{(1)})^{\mathsf{T}} \mathbf{C} \boldsymbol{\varphi}^{(1)} \Big\} \, d\mathbf{x} + \displaystyle\int_{\breve{\Omega}_2} \Big\{ \sum_{j=1}^{2} \Big( (\partial_{x_j} \mathbf{v}^{(2)})^{\mathsf{T}} \breve{\mathbf{A}} (\partial_{x_j} \boldsymbol{\varphi}^{(2)}) + (\mathbf{v}^{(2)})^{\mathsf{T}} \breve{\mathbf{B}}_{\mathbf{1}}^{x_j} (\partial_{x_j} \boldsymbol{\varphi}^{(2)}) \\ \quad + (\partial_x \mathbf{v}^{(2)})^{\mathsf{T}} \breve{\mathbf{B}}_{\mathbf{2}}^{x_j} \boldsymbol{\varphi}^{(2)} \Big) + (\mathbf{v}^{(2)})^{\mathsf{T}} \breve{\mathbf{C}} \boldsymbol{\varphi}^{(2)} + \displaystyle\sum_{j=1}^{2} \Big( \partial_{x_j} \mathbf{v}^{(2)\mathsf{T}} \mathbf{G}_{\mathbf{1}}^{x_j} + (\mathbf{v}^{(2)})^{\mathsf{T}} \mathbf{G}_{\mathbf{2}}^{x_j} \Big) \Big\} \, d\mathbf{x} \\ \qquad + \displaystyle\int_{P} \Big( \mathbf{P}(\mathbf{v}^{(2)})^{\mathsf{T}} - \mathbf{A}(\mathbf{v}^{(3)})^{\mathsf{T}} \Big) \boldsymbol{\lambda} \, d\mathbf{x} = 0 \\ \displaystyle\int_{P} (\boldsymbol{\xi})^{\mathsf{T}} \Big( \mathbf{P}^{\mathsf{T}}(\boldsymbol{\varphi}^{(2)}) - \mathbf{A}(\boldsymbol{\varphi}^{(3)}) \Big) \, d\mathbf{x} = \mathbf{F} \\ \qquad \forall (\mathbf{v}, \boldsymbol{\xi}) \in \mathcal{H}(\breve{\Omega})^{N_m+2} \times H^{-1/2}(P)^{N_m+2} \, . \end{cases} \tag{4.43}$$

### 4.5.2 2D Formulation

In this subsection, focusing on the 2D radiation-type subproblem, the Mixed Weak Problem 3.3 is similarly reduced by means of the multi modal representations. In reference with Section 3.4 and Fig. 3.2 the projected 1D intervals $I_1 = [\mathrm{x}_1, \mathrm{a}_1]$, $I_2 = [\mathrm{a}_2, \mathrm{x}_2]$ and $I_3 = [\mathrm{a}_1, \mathrm{a}_2]$ are devised. With $I_j, j = 1, 2$ corresponding to free-surface regions $\Omega_j^s$ and $I_3$ to $\Omega_3^s$ the representations reduce to,

$$\varphi^{(j)}(x,z) = \sum_{n=-1}^{N_m} \varphi_n(x) Z_n(z;x) = \mathbf{Z}^{\mathsf{T}} \boldsymbol{\varphi}^{(j)} \text{ and} \tag{4.44}$$

$$v^{(j)}(x,z) = \sum_{n=-1}^{N_m} v_n(x) Z_n(z;x) = \mathbf{Z}^{\mathsf{T}} \mathbf{v}^{(j)}, \text{ for } (x,z) \in \Omega_j^s, \ j = 1,2. \tag{4.45}$$

$$\varphi^{(3)}(x,z) = \sum_{n=-1}^{N_m} \varphi_n(x) \Upsilon_n(z;x) = \mathbf{Y}^{\mathsf{T}} \boldsymbol{\varphi}^{(3)} \text{ and} \tag{4.46}$$

$$v^{(3)}(x,z) = \sum_{n=-1}^{N_m} v_n(x) \Upsilon_n(z;x) = \mathbf{Y}^{\mathsf{T}} \mathbf{v}^{(3)}, \text{ for } (x,z) \in \Omega_j^s, \ j = 1,2. \tag{4.47}$$

with the Lagrange multiplier functions $\lambda^j$, corresponding to $S_j$ and $x = a_j, j = 1,2$ given as,

$$\lambda^{(j)}(x,z) = \sum_{n=-1}^{N_m} \lambda_n^{(j)}(a_j) Z_n(z;a_j) = \mathbf{Z}^{\mathsf{T}} \boldsymbol{\lambda}^{(j)} \text{ and} \tag{4.48}$$

$$\xi^{(j)}(x,z) = \sum_{n=-1}^{N_m} \xi_n^{(j)}(a_j) Z_n(z;a_j) = \mathbf{Z}^{\mathsf{T}} \boldsymbol{\xi}^{(j)}, \text{ for } (x,z) \in S_j, \ j = 1,2. \tag{4.49}$$

The reduced system of integral equations and the refined weak problem is given below,

Find $(\boldsymbol{\varphi}^{(j)}, \boldsymbol{\lambda}^{(j)}) \in V(I_j)^{N_m+2} \times H^{-1/2}(I_3)^{N_m+2}$ such that it holds,

$$\begin{cases} \sum_{j=1}^{2} \int_{I_j} \Big\{ (\partial_x \mathbf{v}^{(j)})^{\mathsf{T}} \mathbf{A} (\partial_x \boldsymbol{\varphi}^{(j)}) + (\mathbf{v}^{(j)})^{\mathsf{T}} \mathbf{B_1} (\partial_x \boldsymbol{\varphi}^{(j)}) + (\partial_x \mathbf{v}^{(j)})^{\mathsf{T}} \mathbf{B_2} \boldsymbol{\varphi}^{(j)} \\ + (\mathbf{v}^{(j)})^{\mathsf{T}} \mathbf{C} \boldsymbol{\varphi}^{(j)} \Big\} \, dx + \int_{I_3} \Big\{ (\partial_x \mathbf{v}^{(3)})^{\mathsf{T}} \breve{\mathbf{A}} (\partial_x \boldsymbol{\varphi}^{(3)}) + (\mathbf{v}^{(3)})^{\mathsf{T}} \breve{\mathbf{B}}_{\mathbf{1}} (\partial_x \boldsymbol{\varphi}^{(3)}) \\ + (\partial_x \mathbf{v}^{(3)})^{\mathsf{T}} \breve{\mathbf{B}}_{\mathbf{2}} \boldsymbol{\varphi}^{(2)} + (\mathbf{v}^{(3)})^{\mathsf{T}} \breve{\mathbf{C}} \boldsymbol{\varphi}^{(3)} + \partial_x \mathbf{v}^{(3)\mathsf{T}} \mathbf{G_1} + (\mathbf{v}^{(2)})^{\mathsf{T}} \mathbf{G_2} \Big\} \, dx \\ + \sum_{j=1}^{2} \Big[ \mathbf{P} (\mathbf{v}^{(j)})^{\mathsf{T}} - \mathbf{A} (\mathbf{v}^{(3)})^{\mathsf{T}} \Big]_{x=a_j} \boldsymbol{\lambda}^{(j)} \, d\mathbf{x} = 0 \\ \sum_{j=1}^{2} \boldsymbol{\xi}^{(j)\mathsf{T}} \Big[ \mathbf{P}^{\mathsf{T}} (\boldsymbol{\varphi}^{(j)}) - \mathbf{A} (\boldsymbol{\varphi}^{(3)}) \Big]_{x=a_j} = \mathbf{F}^j. \\ \forall (\mathbf{v}^{(j)}, \boldsymbol{\xi}^{(j)}) \in V(I_j)^{N_m+2} \times H^{-1/2}(\mathrm{I}_3)^{N_m+2} \, . \end{cases} \tag{4.50}$$

with,

$$\mathbf{F}^j(\mathbf{x}) = f_\ell(a_j) \int_{-h}^{0} q \mathbf{Z} \, dz. \tag{4.51}$$

For the 1D discretization case ($d = 1$), the interface is reduced to single nodes ($d-1$), located at $x = a_j,\ j = 1, 2$.

# Part II

# FEM Implementation and Computational Aspects

# Chapter 5

# Finite Element Implementation

The Finite Element Method is employed for the solution of the hydrodynamics and the structural eigenvalue problems. A conforming approach is followed for the construction of versatile FEM schemes for the approximate solution of the reduced weak problems defined in Chapter 3.

## 5.1 Hydrodynamic Subproblems

In the following sections, the FEM is applied for the treatment of the reduced weak formulations presented in Chapter 4. Discrete FE schemes for the approximate solution of the posed weak hydrodynamic problems will be considered. Employing a conforming approach, the approximate solution is sought in a finite dimensional subspace of $V$ and $\mathcal{H}$, corresponding to reduced weak problems in Eqs. (4.31) and (4.33) and Eqs. (4.43) and (4.50) respectively. It is reminded that the reduced problems of Eqs. (4.31) and (4.50) are defined in one horizontal dimension (1D), while Eqs. (4.33) and (4.43) are defined on the horizontal plane (2D).

The principle idea is to devise appropriate 1D and 2D partitions of the domain of interest and construct the approximate solution subspaces $V^h \subset V$ and $\mathcal{H}^h \subset \mathcal{H}$ composed of piecewise polynomials defined on each element of the partition. For the solution of the aforementioned weak hydodynamic problems, the classical Bubnov-Galerkin FEM approach is followed (see Zienkiewicz and Taylor (2005)). In a conforming approach, the interpolation functions employed by the FEM need to chosen on the grounds of permitting natural embedding into the solution function space dictated by the weak form. For the problems at hand, the finite element spaces need to be embedded in $H^1$, thus $C^0$ continuity is required. Based on their conformity, $C^0$ Lagrange Elements are employed. The continuity requirement is expressed by sharing the degrees of freedom across element boundaries.

### 5.1.1 1D FEM Implementation

A partition $\mathfrak{I}_h$ of the 1D domain of interest $I[\mathrm{x}_1, \mathrm{x}_2] \subset \mathbb{R}$ into $N_e$ subintervals of size $h$ is considered, leading to a number of discrete nodes $N_t$. Hence, $\mathfrak{I}_h : \mathrm{x}_1 = x_0 < x_1 < \cdots < x_{N_t} = \mathrm{x}_2$ and each subinterval is $\mathfrak{I}_h^e = (x_i, x_{i+N-1}),\ i = 1, 2, \cdots, N_e$. The 1D Lagrange element in exploits the space of polynomial functions of degree $\kappa = N-1$, as the finite dimensional approximation space,

$$\mathbb{P}_k = \left\{ p(x) = \sum_{i=0}^{\kappa} a_i x^i, a_i \in \mathbb{R}, x \in \mathfrak{I}_h^e \right\}$$

Notably, $dim(\mathbb{P}_k) = N$, corresponding to the element nodes. The finite element subspace $V^h \subset V$ is the space of globally continuous $C^0$ affine functions in each subinterval,

$$V^h = \{u^h : u^h \in C^0(I; \mathbb{C}), u^h|_e \in \mathbb{P}_k\}.$$

The nodal basis of $\mathbb{P}_k$, $L_k = \{L_1, \cdots, L_N\}$ for which $L_i(x_j) = \delta_{ij},\ i, j = 1, \cdots, N$ is proved to span the element subspace thus,

$$V^h = \{u^h : u^h \in C^0(I; \mathbb{C}), u^h|_e = \sum_{r=1}^{N} L_r u_r\}.$$

Functions $L_r$ are the $r^{\text{th}}$, $N-1$ order Lagrangian Shape function supported in $K_j$.

*Remark* 10. As the element number increases, i.e. $N_e \to \infty, h \to 0$ convergence is achieved, i.e. $u^h \to u$. Similarly, increasing the order of employed interpolation within each element $k$ leads to convergence without increasing the number of elements. The above strategies in constructing proper finite element subspaces are refered as $h$- and $p$ version respectively The presented conforming FE approximation is $h$-$p$ adaptive.

In the following section suitable finite element subspaces are defined and the corresponding discrete weak forms of reduced 1D problems Eqs. (4.31) and (4.50) are considered.

#### Transmission Problem

Returning to the treatment of the weak transmission problem Eq. (4.31), the restriction of the approximate modal amplitude solutions in the $k^{\text{th}}$ element $\phi_n^h|_e \equiv \phi_n^h$ for $n = -1, 0, \cdots, N_m$ is written as,

$$\phi_n^h(x) = \sum_{r=1}^{N} L_r(x) \phi_n^r \ \in V^h \ \forall n = -1, 0, \cdots, N_m. \tag{5.1}$$

Thus, $\boldsymbol{\varphi} \in V^h(I)^{N_m+2}$. The nodal unknowns at the $r^{\text{th}}$ node of the $k^{\text{th}}$ element contains the $N_m+2$ unknown x-dependent modal amplitudes arranged in the following vector (see Fig. 5.1),

$$\mathbf{U}_r = \begin{bmatrix} \phi^r_{-1} & \phi^r_0 & \cdots & \phi^r_{N_m} \end{bmatrix}^{\mathsf{T}}$$

Moreover, the compound vector of the $k^{\text{th}}$ element unknowns is written as

$$\underset{N(N_m+2)\times 1}{\mathbf{U}_k} = \begin{bmatrix} \mathbf{U}_1 & \mathbf{U}_2 & \cdots & \mathbf{U}_N \end{bmatrix}^{\mathsf{T}}$$

while the approximate solution restriction is re written as,

$$U^h_k(x) = \mathbf{N}\mathbf{U}_k \tag{5.2}$$

by means of the array $\underset{(N_m+2)\times N(N_m+2)}{\mathbf{N}} = \begin{bmatrix} L_1\mathbf{I}_{N_m+2} & L_2\mathbf{I}_{N_m+2} & \cdots & L_N\mathbf{I}_{N_m+2} \end{bmatrix}$.

Allowing the weight functions $\mathbf{v}$ to coincide with the Lagrangian Shape functions, i.e. $\mathbf{v} \equiv \mathbf{N}$, and substituting Eq. (5.2) in the integral form Eq. (4.31) results in the following element stiffness matrix of size $d \times d$, with $d = N(N_m + 2)$

$$\underset{d\times d}{\mathbf{k}_e} = \int_K (\partial_x\mathbf{N})^{\mathsf{T}}\mathbf{A}(\partial_x\mathbf{N}) + \mathbf{N}^{\mathsf{T}}\mathbf{B}_1(\partial_x\mathbf{N}) + (\partial_x\mathbf{N})^{\mathsf{T}}\mathbf{B}_2\mathbf{N} + \mathbf{N}^{\mathsf{T}}\mathbf{C}\mathbf{N}\, dx \tag{5.3}$$

After the assembly of local matrices, following discrete system of nodal equations of size $p = N_t \times (N_m + 2)$ is derived,

$$\underset{p\times p}{\mathbb{K}}\ \underset{p\times 1}{\mathbf{u}} = \mathbb{F} \tag{5.4}$$

where vector $\mathbf{u}$ contains the global unknowns. The above system is sparse and diagonally dominant.

*Remark* 11. The only non-zero element of the forcing vector $\mathbb{F}$ is the first node entry which springs form the imposition of the Robin-type conditions Eq. (4.30). Denoting $l = N_m + 2$, the local forcing vector of the first element is,

$$\mathbb{F}_e = \begin{Bmatrix} \mathbf{g}^1 & \underset{l\times l}{\mathbf{0}} & \cdots & \underset{l\times l}{\mathbf{0}} \end{Bmatrix}^{\mathsf{T}}.$$

The solution of the discrete system Eq. (5.16) recovers the unknown complex modal amplitudes $\phi_n$. Subsequently, exploiting the known vertical structure of the mode the total wave field is constructed by means of Eq. (4.18)

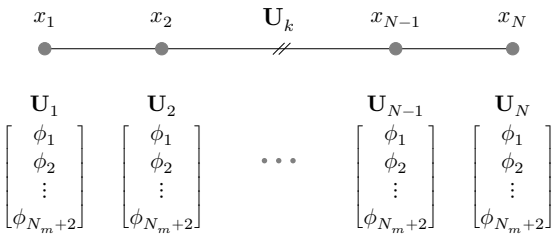


**Figure 5.1** Nodal unknowns-dofs- for $k^{\text{th}}$ element

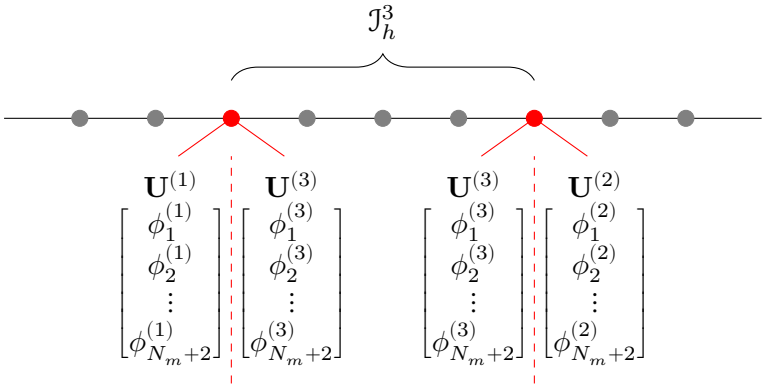


**Figure 5.2** Augmented interface *dofs*

## Radiation-Type Problem

Distinct partitions $\mathcal{I}_h^j$ are employed for the decomposed subregions $I_j$ for $j = 1, 2, 3$. A different number of elements can be employed in each subregion, leading to a total number of discrete nodes $N_t = \sum_{j=1}^{3} N_j$.

As already mentioned, in the 1D discretization case ($d = 1$), the interface boundaries between subregions is reduced to single points ($d - 1$), corresponding to nodes located at $x = a_j$, $j = 1, 2$. The meshes are chosen as to match at the interface, thus adjacent subregions share a common inter-facial node. Thus, the intersections $d_{ij} = \mathcal{I}_h^i \cup \mathcal{I}_h^j$ for $i = 1, 2$ and $j = 3$ contain a single node.

The two inter-facial nodes carry degrees of freedom from both adjacent regions (Fig. 5.2) so element interconnectivity is violated. The interfacial *dofs* are connected through the additional discrete constraints that enforce the appropriate jump conditions.

Revisiting the reduced, two-field weak problem of Eq. (4.50), appropriate approximation spaces for the pair $\boldsymbol{\varphi}$ and $\boldsymbol{\lambda}$, $\mathcal{H}^h$ and $\Lambda^h$ need to be constructed. For $\mathcal{H}^h$ the Lagrangian interpolation of the approximate solution within each element in the corresponding subregions is considered,

$$\mathcal{H}^h = \{u \in \mathcal{H} : u^h|_e = \sum_{r=1}^{N} L_r u_r\}.$$

Thus employing Eq. (5.2) in the expressions Eqs. (4.35) and (4.36), results in the corresponding element matrices,

$$\mathbf{k}_e^{(j)} = \int_K (\partial_x \mathbf{N})^\mathsf{T} \mathbf{A} (\partial_x \mathbf{N}) + \mathbf{N}^\mathsf{T} \mathbf{B}_1 (\partial_x \mathbf{N}) + (\partial_x \mathbf{N})^\mathsf{T} \mathbf{B}_2 \mathbf{N} + \mathbf{N}^\mathsf{T} \mathbf{C} \mathbf{N} \, dx, \text{ for} j = 1, 2. \tag{5.5}$$

$$\mathbf{k}_e^{(3)} = \int_K (\partial_x \mathbf{N})^\mathsf{T} \breve{\mathbf{A}} (\partial_x \mathbf{N}) + \mathbf{N}^\mathsf{T} \breve{\mathbf{B}}_1 (\partial_x \mathbf{N}) + (\partial_x \mathbf{N})^\mathsf{T} \breve{\mathbf{B}}_2 \mathbf{N} + \mathbf{N}^\mathsf{T} \breve{\mathbf{C}} \mathbf{N} \, dx. \tag{5.6}$$

The corresponding force vector, valid in the plate covered region,

$$\mathbf{F}_e^{(j)} = - \int_K (\partial_x \mathbf{N})^\mathsf{T} \mathbf{G_1} + \mathbf{N}^\mathsf{T} \mathbf{G_2} \, dx, \tag{5.7}$$

The discrete trace space $\Lambda^h$ for which it generally holds,

$$\Lambda^h = \{ u \in \Lambda : u^h|_{x=a_j} = \sum_{r=1}^{N} L_r(x) u_r, \; x \in K_i \cap K_j, \; j = 1, 2 \; i = 3 \}.$$

*Remark* 12. The above choice for the multiplier interpolation space essentially allows for the identification of employed shape functions $L_r$ with Dirac functions $\delta(x - a_j)$. Thus, node collocation is performed resulting in $N_m + 2$ discrete multipliers at $x = a_j, \; j = 1, 2$.

At the 'interfacial' nodes, located at $x = a_j$, the discrete multipliers are contained in the vectors $\boldsymbol{\lambda}^{(j)}, \; j = 1, 2$. The total additional *dofs* associated with discrete Lagrange multipliers are contained in vector $\boldsymbol{\lambda} = (\boldsymbol{\lambda}^{(1)}, \boldsymbol{\lambda}^{(2)})^\mathsf{T}$. Next, we distinguish between the dofs in each of the subregions as $\mathbf{u}^{(j)}, j = 1, 2, 3$, contained in the vector of global unknowns $\mathbf{u} = (\mathbf{u}^{(1)}, \mathbf{u}^{(3)}, \mathbf{u}^{(2)})^\mathsf{T}$.

After the assembly of local matrices, the following discrete saddle point problem with respect to $\mathbf{u}$ and $\boldsymbol{\lambda}$ is derived. Denoting once again, $p = N_t \times (N_m + 2)$ and $l = N_m + 2$ leads to,

$$\begin{cases} \underset{p \times p}{\mathbb{K}} \; \underset{p \times 1}{\mathbf{u}} + \underset{p \times 2l}{\mathbb{B}}^\mathsf{T} \; \underset{2l \times 1}{\boldsymbol{\lambda}} = \underset{p \times 1}{\mathbb{F}} \\ \underset{2l \times p}{\mathbb{B}} \; \underset{p \times 1}{\mathbf{u}} = \underset{2l \times 1}{\mathbb{g}} \end{cases} \tag{5.8}$$

The above discrete system retains its symmetric form as seen by the blocked structure in Fig. 5.3. Symmetry is preserved due to the employment of the Bubnov-Galerkin method and the the geometric conformity of the interface boundaries.

### 5.1.2 2D FEM Implementation

For the 2D FEM implementation, triangular partitions denoted as $\{T^h\}$ are considered for $\breve{\Omega} \subset \mathbb{R}^2$. Triangular elements, $K_j$ are chosen for their ability to fit curved boundaries. For an admissible partition, it must hold that the intersection of any two elements of $\{T^h\}$ must be either zero or reduce to a single vertex or a single side. Following the same trail of thought we

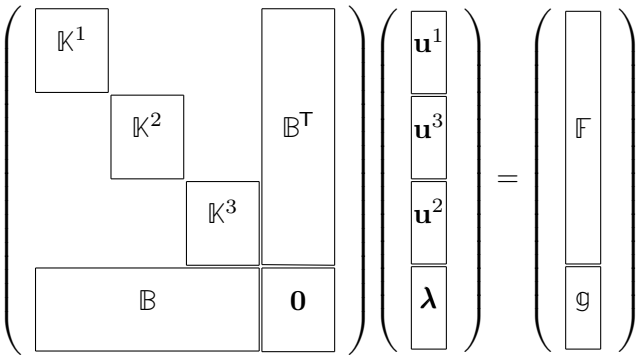


**Figure 5.3** Symmetric form of the discrete saddle point problem

consider the space of polynomial functions of order $k$ in two variables,

$$\mathbb{P}_k = \left\{ p(x_1, x_2) = \sum_{0 \leq i+j \leq k} a_{ij} x_1^i x_2^j \in \mathbb{R}, x \in K_j \right\}$$

The conforming triangle $K_j$, features $k+1$ nodes along each edge. Throughout the present thesis linear Lagrange triangles are considered for the FE approximation of hydrodynamic problems. The corresponding finite element subspace $V^h \subset V$ is the space of globally continuous $C^0$ affine functions in each subinterval,

$$V^h = \{u^h : u^h \in C^0(\Omega; \mathbb{C}), u^h|_e \in \mathbb{P}_1\}.$$

The nodal basis of $\mathbb{P}_1$, $L_k = \{L_1(x_1, x_2), L_2(x_1, x_2), L_3(x_1, x_2)\}$ is proved to span the element subspace thus,

$$V^h = \{u^h : u^h \in C^0(\Omega; \mathbb{C}), u^h|_e = \sum_{r=1}^{3} L_r u_r\}.$$

Linear Lagrange elements feature three nodes on each vertex, $dim(\mathbb{P}_1) = 3$. Next, the FEM approximation of the reduced weak diffraction and radiation-type problems Eqs. (4.33) and (4.43) on the horizontal plane is presented. As in the 1D case, each problem is treated separately.

### Diffraction Problem

In light of the above, the treatment of the diffraction problem Eq. (4.33), the restriction of the approximate modal amplitude solutions in the $k^{\text{th}}$ element $\phi_n^h|_e \equiv \phi_n^h$ for $n = -1, 0, \cdots, N_m$ is written as,

$$\phi_n^h(x_1, x_2) = \sum_{r=1}^{3} L_r(x_1, x_2)\phi_n^r \ \in V^h \ \forall n = -1, 0, \cdots, N_m. \tag{5.9}$$

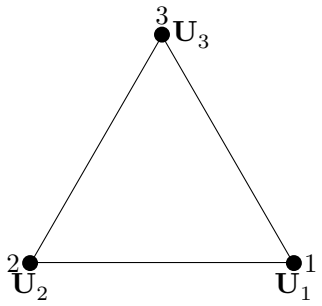


**Figure 5.4** Linear Lagrange Triangle

Thus, $\boldsymbol{\phi} \in V^h(\Omega)^{N_m+2}$. As previously noted, the nodal unknowns at the $r^{\text{th}}$ node of the $k^{\text{th}}$ element contains the $N_m + 2$ unknowns,

$$\mathbf{U}_r = \begin{bmatrix} \phi^r_{-1} & \phi^r_0 & \cdots & \phi^r_{N_m} \end{bmatrix}^{\mathsf{T}}$$

The compound vector of the $k^{\text{th}}$ triangle is now reduced to

$$\underset{3(N_m+2)\times 1}{\mathbf{U}_k} = \begin{bmatrix} \mathbf{U}_1 & \mathbf{U}_2 & \mathbf{U}_3 \end{bmatrix}^{\mathsf{T}}$$

while the approximate solution restriction is re written as,

$$U^h_k(x) = \mathbf{N}\mathbf{U}_k \tag{5.10}$$

by means of the array $\underset{(N_m+2)\times 3(N_m+2)}{\mathbf{N}} = \begin{bmatrix} L_1\mathbf{I}_{N_m+2} & L_2\mathbf{I}_{N_m+2} & L_3\mathbf{I}_{N_m+2} \end{bmatrix}$.

Allowing the weight functions $\mathbf{v}$ to coincide with the Lagrangian Shape functions, and substituting the approximate solution Eq. (5.10) in the integral equation Eq. (4.33) results in the following element stiffness matrix of size $\tilde{d} \times \tilde{d}$, with $\tilde{d} = 3(N_m + 2)$

$$\underset{\tilde{d}\times\tilde{d}}{\mathbf{k}_e} = \underset{\tilde{d}\times\tilde{d}}{\mathbf{k}^1_e} + \underset{\tilde{d}\times\tilde{d}}{\mathbf{k}^2_e}, \tag{5.11}$$

while,

$$\mathbf{k}^j_e = \int_K (\partial_{x_j}\mathbf{N})^{\mathsf{T}}\mathbf{A}(\partial_{x_j}\mathbf{N}) + \mathbf{N}^{\mathsf{T}}\mathbf{B}^j_{\mathbf{1}}(\partial_{x_j}\mathbf{N}) + (\partial_{x_j}\mathbf{N})^{\mathsf{T}}\mathbf{B}^j_{\mathbf{2}}\mathbf{N} + \mathbf{N}^{\mathsf{T}}\mathbf{C}\mathbf{N}\, d\mathbf{x},\ j = 1, 2. \tag{5.12}$$

After the assembly of local matrices, following discrete system of nodal equations of size $p = N_t \times (N_m + 2)$ is derived,

$$\underset{p\times p}{\mathbb{K}}\ \underset{p\times 1}{\mathbf{u}} = \mathbb{F} \tag{5.13}$$

where vector $\mathbf{u}$ contains the global unknowns. The above system remains sparse through the diagonal dominance and of matrix $\mathbb{K}$.

### Radiation-Type problem

In accordance to 1D schemes, Distinct triangular partitions $\mathcal{T}_h^j$ are employed for the decomposed subregions $\breve{\Omega}^j$ for $j = 1, 2$. The interface boundary between subregions is now a closed curve composed of discrete nodes. The triangular meshes are chosen as to match at the interface, thus adjacent subregions share common inter-facial node. Thus, the intersection of the trace meshes on $P$, $\mathcal{T}_h^1 \cup \mathcal{T}_h^2$ contains a finite set of interfacial nodes referred as $P_i$.

As in the 1D case, the interfacial nodes carry degrees of freedom from both adjacent regions (Fig. 5.2) so as to violate element interconnectivity. The interfacial *dofs* are connected through the additional discrete constraints that enforce the appropriate jump conditions.

Revisiting the reduced, two-field weak problem of Eq. (4.43), appropriate approximation spaces for the pair $\boldsymbol{\varphi}$ and $\boldsymbol{\lambda}$, $\mathcal{H}^h$ and $\Lambda^h$ need to be constructed. For $\mathcal{H}^h$ the Lagrangian interpolation of the approximate solution within each element in the corresponding subregions is considered,

$$\mathcal{H}^h = \{u \in \mathcal{H} : u^h|_e = \sum_{r=1}^{3} L_r(x_1, x_2) u_r\}.$$

Thus employing Eq. (5.10) in the expressions Eqs. (4.35) and (4.36), results in the corresponding element matrices $\mathbf{k}_e^{(j)}$ in subregions $\breve{\Omega}^j$,

$$\mathbf{k}_e^{(1)} = \int_K \sum_{j=1}^{2} (\partial_{x_j}\mathbf{N})^\mathsf{T} \mathbf{A} (\partial_{x_j}\mathbf{N}) + \mathbf{N}^\mathsf{T} \mathbf{B}_1^j (\partial_{x_j}\mathbf{N}) + (\partial_{x_j}\mathbf{N})^\mathsf{T} \mathbf{B}_2^j \mathbf{N} + \mathbf{N}^\mathsf{T} \mathbf{C} \mathbf{N} \, d\mathbf{x}, \tag{5.14}$$

$$\mathbf{k}_e^{(2)} = \int_K \sum_{j=1}^{2} (\partial_{x_j}\mathbf{N})^\mathsf{T} \breve{\mathbf{A}} (\partial_{x_j}\mathbf{N}) + \mathbf{N}^\mathsf{T} \breve{\mathbf{B}}_1^j (\partial_{x_j}\mathbf{N}) + (\partial_{x_j}\mathbf{N})^\mathsf{T} \breve{\mathbf{B}}_2^j \mathbf{N} + \mathbf{N}^\mathsf{T} \breve{\mathbf{C}} \mathbf{N} \, d\mathbf{x}. \tag{5.15}$$

The corresponding force vector, valid in the plate covered region,

$$\mathbf{F}_e = -\int_K \sum_{j=1}^{2} (\partial_{x_1}\mathbf{N})^\mathsf{T} \mathbf{G_1} + \mathbf{N}^\mathsf{T} \mathbf{G_2} \, dx, \tag{5.16}$$

The discrete trace space $\Lambda^h$ for which it generally holds,

$$\Lambda^h = \{u \in \Lambda : u^h|_P = \sum_{r=1}^{N} L_r(x_1, x_2) u_r, \; x \in P\}.$$

*Remark* 13. Again node collocation is performed resulting in $N_m + 2$ discrete multipliers at each interfacial node in set $d$

The discrete multipliers are contained in the vector $\mathbf{\Lambda}$.

After the assembly of local matrices, the following discrete saddle point problem with respect to $\mathbf{u}$ and $\boldsymbol{\lambda}$ is derived. Denoting once again, $p = N_t \times (N_m + 2)$ and $l = N_m + 2$ leads to,

$$\begin{cases} \underset{p\times p}{\mathbb{K}}\ \underset{p\times 1}{\mathbf{u}} + \underset{p\times 2l}{\mathbb{B}}^{\mathsf{T}}\ \underset{2l\times 1}{\boldsymbol{\lambda}} = \underset{p\times 1}{\mathbb{F}} \\ \underset{2l\times p}{\mathbb{B}}\ \underset{p\times 1}{\mathbf{u}} = \underset{2l\times 1}{\mathbb{g}} \end{cases} \tag{5.17}$$

The above discrete system retains its symmetric form as seen by the blocked structure in Fig. 5.3. Symmetry is preserved due to the employment of the Bubnov-Galerkin method and the the geometric conformity of the interface boundaries.

## 5.2 Structural Vibration

In Chapter 2, the Kirchoff-Love and Reissner-Mindlin equations describing the vertical motion of thin and moderately thick plates respectively were briefly presented. In the context of the proposed methodology, the focus is placed in the free flexural vibration problems of both finite plates and plate-strips as previously discussed. The solutions to the inhomogenous eigenvalue problems will be sought by means of the FE method.

Following the previous discussion on hydrodynamics, the numerical treatment of the structural eigenvalue problems by the FEM dictates the formulation of a variational problem. The formulation in question is similarly derived by means of either a weighted residual approach or a variational principle. In structural mechanics, the employment of classical principles, like the minimisation of potential energy and the principle of least action has dominated the literature when it comes to the development of numerical schemes. It must be noted that the two approaches are equivalent, and the popularity of variational principles is understood as the involved PDEs are high-order, thus their direct tackling associated with the weighted-residuals approach becomes more involved. The fourth-order PDE, linked with the motion of a thin plate as seen in Chapter 2, presents a $C^1$ variational problem, suggesting that shape functions need to satisfy $C^1$ continuity requirements across element edges. The Reissner-Mindlin theory on the other hand, in its two-field form, poses a $C^0$ problem and is relieved of the above complexity. As the process of constructing conforming approximation spaces for thin plates is an involved process, several approaches have been proposed historically. The interested reader is directed to the works of Oñate (2010) and Zienkiewicz and Taylor (2005). These ideas range from suitable mixed-formulations to 'non-conforming' elements that violate inter-element continuity.

The question of optimality between available techniques for the structural modelling of plates is not trivial. The choice is made on the grounds of versatility, as in whether the formu-

lation is able to account for both 'thick' and 'thin' plates or a variety of support conditions, simplicity in implementation and the total computational cost. As the focus of the present thesis is the development of a monolithic strategy for the treatment of wave-floating structure with emphasis on geometric and material inhomogeneity, triangular elements with a minimal number of nodes and *dofs* per element, able to account for both thin and moderately thick plates were considered.

### 5.2.1 $C^0$ approximation for plate bending

There are several strategies to bypass the complexity introduced by the $C^1$ requirement inherent to the irreducible thin plate model. The majority of methods however falls into two categories. The first considers the reducible, two-field Reissner-Mindlin theory as a starting point and subsequently imposes discrete constraints on the strain definition that are satisfied on given points. The second category introduces pseudo-variables to derive a convenient two-field formulation that would allow $C^0$ interpolation. Both of the above approaches assume 'mixed' formulations and admit different interpolations for the deflection and rotations.

In the present work emphasis is placed in discrete triangular elements, namely the Discrete Kirchhoff Triangle (DKT), and its extension the Discrete Shear Triangle (DKT) intoduced for the treatment of thin and moderately thick plates respectively introduced in the works of Batoz (1980) and Batoz and Lardeur (1989). Both non-conforming triangles employ,

- quadratic $C^0$ interpolation for the unknown rotations $\beta_{x_j}$ within the elements. Linear variation of rotation $\beta_n$ along the tangential direction is assumed along the edges of the triangle.
- cubic $C^1$ interpolation for the unknown displacement $w$ along the element edges.

To satisfy the kinematic assumptions, the following discrete constraints are imposed at the vertices and the edge midnodes,

$$(\partial_s w)|_k + (\partial_s \beta)|_k = F(\beta_{x_1}, \beta_{x_2}),\ \kappa = 4, 5, 6. \tag{5.18}$$

$$(\partial_{x_j} w)|_k + (\partial_{x_j} \beta)|_k = S(\beta_{x_1}, \beta_{x_2}),\ \kappa = 1, 2, 3. \tag{5.19}$$

Implementing the above assumptions and imposing the constraints results in 9 elemental unknowns. The DST (Fig. 5.5) triangle essentially reduces to DKT as element thickness diminishes, i.e. $\tau \to 0$ the expressions for discrete shear strain $F(\beta_{x_1}, \beta_{x_2}), F(\beta_{x_1}, \beta_{x_2}) \to 0$ in Eqs. (5.18) and (5.19) vanish revealing Kirchhoff's kinematic assumption. The above considerations result in the following expressions involving the unknown *dofs* contained in vector $\mathbf{U}$,

$$\begin{aligned} \beta_{x_1} &= \mathbf{H_1 U} \\ \beta_{x_2} &= \mathbf{H_2 U} \end{aligned} \tag{5.20}$$

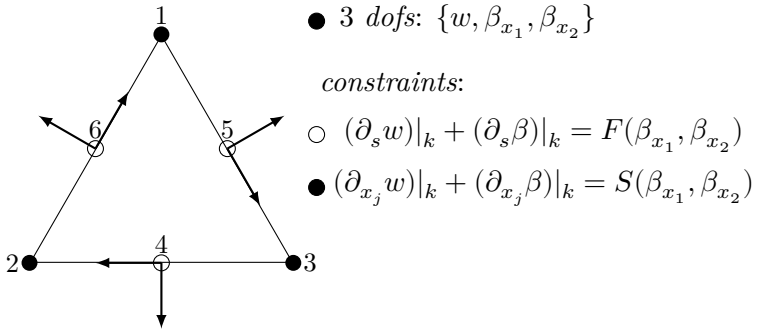


**Figure 5.5** Discrete Shear Triangle-DST (Batoz and Lardeur, 1989)

The shape functions $\mathbf{H_1}$, $\mathbf{H_2}$ are given in Appendix A . Next, the potential energy, expressed as the sum of bending and shear energy in the general case, is written in terms of the curvatures $\boldsymbol{\chi}^{\mathsf{T}} = \begin{bmatrix} \partial_{x_1}\beta_{x_1} & \partial_{x_2}\beta_{x_2} & \partial_{x_1}\beta_{x_2} + \partial_{x_2}\beta_{x_1} \end{bmatrix}$ . and shear strains $\boldsymbol{\gamma}^{\mathsf{T}} = \begin{bmatrix} \partial_{x_1} w + \beta_{x_1} & \partial_{x_2} w + \beta_{x_2} \end{bmatrix}$,

$$\Pi = \frac{1}{2} \int_{\tilde{\Omega}_2} \left( \boldsymbol{\chi}^{\mathsf{T}} \mathbf{D_b} \boldsymbol{\chi} + \boldsymbol{\gamma}^{\mathsf{T}} \mathbf{D_s} \boldsymbol{\gamma} \right) \, d\mathbf{x}. \tag{5.21}$$

In terms of the element unknowns $\mathbf{U}$ the latter are written as,

$$\boldsymbol{\chi} = \underset{3\times 9}{\mathbf{b}_b} \; \underset{9\times 1}{\mathbf{U}} \, , \; \boldsymbol{\gamma} = \underset{2\times 9}{\mathbf{b_s}} \; \underset{9\times 1}{\mathbf{U}} \, . \tag{5.22}$$

By means of Eqs. (5.21) and (5.22), the minimisation principle involving the potential energy functional, $\delta\Pi = 0$ is employed in the following finite element model of static equilibrium,

$$(\mathbf{K_b} + \mathbf{K_s})\mathbf{U} = 0 \tag{5.23}$$

with the element stiffness matrices defined,

$$\mathbf{K_b} = \int_K \mathbf{b}_b^{\mathsf{T}} \mathbf{D_b} \mathbf{b}_b \, dA = 0, \; \mathbf{K_s} = \int_K \mathbf{b}_s^{\mathsf{T}} \mathbf{D_s} \mathbf{b}_s \, dA = 0. \tag{5.24}$$

and for the isotropic case,

$$\mathbf{D_b} = \frac{E\tau^3}{12(1-\nu^2)} \begin{bmatrix} 1 & \nu & 0 \\ \nu & 1 & 0 \\ 0 & 0 & \frac{1-\nu}{2} \end{bmatrix}, \; \mathbf{D_s} = \frac{5E\tau}{12(1+\nu)} \begin{bmatrix} 1 & 0 \\ 0 & 1 \end{bmatrix} \tag{5.25}$$

With the problem of free vibration in mind the inertial effects must be taken into account.

*Remark* 14. Since the deflection $w$ is only defined on the edges of the DKT and the DST, a mass matrix cannot be defined consistently. Following the analysis in Sydenstricker et al. (1995), a pseudo-consistent approach is followed. A cubic Lagrange interpolation $w$ is adopted

for the interior of the triangle in order to match the adopted Hermite interpolation along the edges. Furthermore, by preserving expressions Eq. (5.20) for the rotations pseudo consistent expressions for the element mass matrix can be derived.

$$\mathbf{M} = \int_K \mathbf{b}_b^{\mathsf{T}} \mathbf{D}_\mathbf{b} \mathbf{b}_b \, dA = 0, \tag{5.26}$$

Upon global assembly the free vibration problem is written as,

$$\tilde{\mathbf{K}}\mathbf{u} - \omega_\ell^2 \tilde{\mathbf{M}}\mathbf{u} = 0, \tag{5.27}$$

in terms of the global unknowns vector $\mathbf{u}$ and the natural frequencies $\omega_\ell$.

### Evaluation for discrete elements (DKT/DST)-Eigenvalue problem

Considering the structural eigenvalue problem, the deviation of the numerically calculated eigenvalues to the analytical or semi-analytical solutions are examined for the thick and thin limit cases. To this end, the cases of a free-circular and rectangular plates are considered. First, the DKT and DST elements are compared against semi-analytical solutions and other numerical results obtained for the FFFF rectangular plate. Subsequently, the range of applicability of the DKT and DST elements is tested for the case of a free circular plate.

In an attempt to establish the accuracy of the discrete elements, the simple free vibration problem of a completely free, homogeneous rectangular plate is considered. It is noted here that even for such reduced example as the case of a homogeneous rectangular plate, closed-form solutions can be produced only for the scenarios where the opposite sides of the plate are simply-supported. These are 6 out of the 21 classic scenarios where each edge is considered to be either simply supported, clamped or free. The remaining 15 cases, including the one of a completely free case FFFF, assume semi-analytical solutions (Leissa, 1973). Here, comparisons are mande against the semi-analytical solutions presented in Leissa (1973). Additionally, the natural frequencies are also compared against the calculated values obtained by means of the elasticity toolbox available in MATLAB R2016a, the Rayleigh-Ritz method employing the *in-vacuo* thin beam modes as trial functions and finally the SHELL181 legacy element available in ANSYS Workbench. The considered case is a $10 \times 10 \times 0.1$m square plate and the computed frequencies are tabulated below, while the produced eigenmodes are illustrated in Fig. 5.6. Notably, the first three modes in the FFFF case are corresponding to rigid body modes linked with zero eigenvalues. It is immediately observed in Table 5.1 that the calculated deviations from the natural frequencies documented in Leissa (1973) are kept under 1% in all cases except for the Rayleigh-Ritz method. The use of the *in-vacuo* beam modes as trial functions for an R-R formulation, although straightforward yields slow conversion rates. This is attributed to the inability of the beam mode products to satisfy the free edge conditions on the plate edges

| $\omega_\ell/2\pi$, (=0.3) | | | | | | |
|---|---|---|---|---|---|---|
| $\tau$/a = 0.01 | **4** | **5** | **6** | **7** | **8** | **9** |
| **Leissa (1973)** | **3.289** | **4.826** | **5.958** | **8.542** | **8.542** | **15.005** |
| **DKT** | 3.285 | 4.78 | 5.919 | 8.488 | 8.4882 | 14.902 |
| Dev.(%) | *0.15* | *0.971* | *0.657* | *0.627* | *0.626* | *0.687* |
| **DST** | 3.285 | 4.78 | 5.92 | 8.488 | 8.488 | 14.9016 |
| Dev.(%) | *0.155* | *0.974* | *0.658* | *0.631* | *0.63* | *0.689* |
| **Matlab R2016a** | 3.278 | 4.779 | 5.920 | 8.479 | 8.479 | 14.918 |
| Dev.(%) | *0.341* | *0.974* | *0.645* | *0.735* | *0.731* | *0.577* |
| **R-R** | 3.369 | 4.921 | 6.087 | 8.728 | 8.7282 | 15.328 |
| Dev.(%) | *2.403* | *1.963* | *2.154* | *2.173* | *2.173* | *2.154* |
| **ANSYS**, SHELL181 | 3.274 | 4.78 | 5.92 | 8.46 | 8.46 | 14.889 |
| Dev.(%) | *0.465* | *1.002* | *0.694* | *0.955* | *0.955* | *0.773* |

**Table 5.1** Frequency parameters $\omega_\ell/2\pi$, plate aspect ratio a/b=1

and corners. More efficient R-R schemes employ orthogonal polynomials or other appropriately chosen bases (Bhat, 1985; Oosterhout et al., 1995). From a computational standpoint, R-R formulations for general geometries accounting for inhomogeneity are not trivial to implement which makes the latter inconvenient to use in the context of the present work. MATLAB R2016a linear elasticity toolbox solutions by means of quadratic tetrahedral elements are found in excellent agreement. However as the thickness-to-primary length ratio diminishes, apart from the computational cost that increases dramatically in the numerical treatment of 3D linear elasticity, ill-conditioning issues rise (Zienkiewicz and Taylor, 2005). This is the essentially the reasoning behind the employment of reduced elasticity theories and the popularity of shell and plate elements for the modelling of relatively slender structures. ANSYS SHELL181 element accounts for fist order shear deformation effects. Although a large number of elements was employed in all FEM runs to ensure convergence, ANSYS vibration analysis was carried out in the APDL environment employing a different mesh by default. Additionally the lumped mass method was employed instead of the pseudo-consistent approach for the simulation of inertial effects. The latter facts could explain the slight deviations between the discrete elements and SHELL181.

It is illustrated how the *in-vacuo* vibration analysis of an elastic plate can be carried out numerically, with an abundance of numerical tools available. For the scope of the present work however, the discrete elements were opted due to their robustness which is well documented in the literature and validated in a series of example cases where analytical solutions are available.

Next, the range of applicability for the DST and DKT elements is examined for the case of an unconstrained circular plate. Results are tabulated in Table 5.2

| $\Omega = \omega r^2\sqrt{\rho\tau/r}$ | | | | | | |
|---|---|---|---|---|---|---|
| $\tau$/r = 0.001 | **4** | **5** | **6** | **7** | **8** | **9** |
| **Senjanović et al. (2014)** | **5.358** | **9.003** | **12.439** | **20.474** | **21.835** | **33.495** |
| *DKT* | 5.359 | 9.004 | 12.411 | 20.426 | 21.832 | 33.459 |
| Dev.(%) | *0.015* | *0.010* | *0.228* | *0.237* | *0.013* | *0.107* |
| *DST* | 5.359 | 9.004 | 12.440 | 20.474 | 21.835 | 33.49 |
| Dev.(%) | *0.009* | *0.006* | *0.005* | *0.008* | *0.092* | *0.012* |
| $\tau$/r = 0.1 | **4** | **5** | **6** | **7** | **8** | **9** |
| **Senjanović et al. (2014)** | **5.318** | **8.869** | **12.227** | **19.771** | **21.188** | **31.994** |
| *DKT* | 5.358 | 9.008 | 12.439 | 20.475 | 21.836 | 33.4977 |
| Dev.(%) | *0.0759* | *1.571* | *1.736* | *3.562* | *3.058* | *4.699* |
| *DST* | 5.334 | 8.934 | 12.336 | 20.183 | 21.553 | 32.879 |
| Dev.(%) | *0.305* | *0.735* | *0.892* | *2.085* | *1.722* | *2.767* |
| $\tau$/r = 0.2 | **4** | **5** | **6** | **7** | **8** | **9** |
| **Senjanović et al. (2014)** | **5.203** | **8.508** | **11.671** | **18.087** | **19.635** | **28.719** |
| *DKT* | 5.358 | 9.003 | 12.439 | 20.475 | 21.836 | 33.4978 |
| Dev.(%) | *2.922* | *5.585* | *6.284* | *12.07* | *10.388* | *14.937* |
| *DST* | 5.261 | 8.735 | 12.0355 | 19.373 | 20.755 | 31.193 |
| Dev.(%) | *1.115* | *2.667* | *3.123* | *7.112* | *5.707* | *8.613* |

**Table 5.2** Frequency parameter $\Omega$ and $\kappa_s = 5/6$

### 5.2.2 $C^1$ approximation for thin plate strips

A finite element approach is again adopted for the numerical treatment of the vibration problems plate strip introduced in Section 2.4 employed models under cylindrical bending of a plate.

For the thin,inhomogeneous plate standard Euler-Bernoulli beam elements, featuring $C^1$ Hermite interpolation are employed (Hughes, 2000; Oñate, 2010; Zienkiewicz and Taylor, 2005). The weighted residual approach is followed and Eq. (2.27) is tackled directly. The following analysis assumes a strip extending in $I_p = [-L/2, L/2]$. Introducing weight function $v(x) \in H^1(I_p)$ multiplying each term and then integrating over the domain it is derived,

$$\int_{-L/2}^{L/2} v\,\partial_x^2\left(D(x)\partial_w^x\right)dx - \int_{-L/2}^{L/2} \omega^2\rho_e\tau(x)\,v\,w\,dx = 0. \tag{5.28}$$

Integration by parts yields,

$$\begin{aligned}&\int_{-L/2}^{L/2} \partial_v^x\ \left(D(x)\partial_w^x\right)dx - \int_{-L/2}^{L/2} \omega^2\rho_e\tau(x)\,v\,w\,dx\\ &+\left[v\,\partial_x\left(D(x)\partial_x^2 w\right)\right]_{-L/2}^{L/2} - \left[\partial_x v\ \left(D(x)\partial_x^2 w\right)\right]_{-L/2}^{L/2} = 0.\end{aligned} \tag{5.29}$$

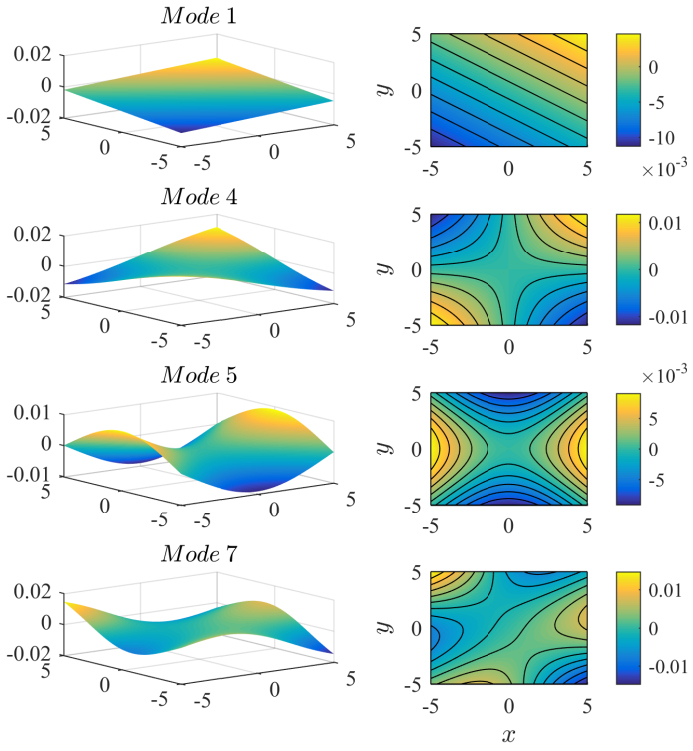


**Figure 5.6** Calculated *in-vacuo* modes for the FFFF rectangular plate by the DKT.

The boundary terms vanish in the unconstrained case due to the zero shear force and bending moment conditions Eqs. (2.28) and (2.29). Subsequently, as already mentioned in order to satisfy the $C^1$ conformity condition 1D Hermite elements are employed.

In general, $k^{th}$ Hermite interpolation in the given reference interval $[-L/2, L/2]$ achieves $C^l$ continuity by means of polynomial functions $p \in (\mathbb{P}_{2k+1})$. The derivatives up to $l^{th}$ of $p(x)$ exist at the interval edges and become zero or unity at the edge nodes for $0 \leq l \leq k$. For $C^1$ requirement cubic Hermite interpolation ($k = 1$) is employed in the derivation of the simplest element. By means of Hermite shape functions, $w$ is interpolated using Hermite shape functions as,

$$w(x) = \sum_{r=1}^{N} H_r w_r + H_{r+N} \partial_x w_r = \mathbf{HU}, \tag{5.30}$$

where $\mathbf{U}^\mathsf{T} = \begin{bmatrix} w_1 & \partial_x w_1 & \cdots & w_N & \partial_x w_N \end{bmatrix}$ and $\mathbf{H} = \begin{bmatrix} H_1 & H_{N+1} & \cdots & H_N & H_{2N+1} \end{bmatrix}$. Next, substituting Eq. (5.30) in Eq. (5.29) results in the following local stiffness and mass matrices,

$$\mathbf{K_b} = \int_K \mathbf{L}^\mathsf{T} D(x) \mathbf{L} \, dx, \quad \mathbf{M} = \int_K \mathbf{L}^\mathsf{T} \rho_e \tau(x) \mathbf{L} \, dx. \tag{5.31}$$

Hence, once again upon global assembly the free vibration problem for the thin plate strip is written as,

$$\tilde{\mathbf{K}}_{\mathbf{b}}\mathbf{u} - \omega_{\ell}^{2}\tilde{\mathbf{M}}\mathbf{u} = 0 \tag{5.32}$$

### 5.2.3 $C^0$ approximation for thick plate strips

The two-field formulation of the FSDT theory allows the employment of $C^0$ Lagrange elements similarly to the 1D hydrodynamic problems that were discussed in Section 5.1.1. Thus, considering again the finite element subspaces $V^h$ the weight functions $v_1, v_2 \in V^h(I_p)$, each multiplying Eqs. (2.30) and (2.31) are introduced. Integrating in the domain of interest $I_p$ yields,

$$\int_{-L/2}^{L/2} v_1\, \partial_x \left[\kappa_s G\tau(\, \partial_x w - \theta\,)\right]\, dx + \int_{-L/2}^{L/2} \omega^2 \rho_e \tau v_1\, w\, dx = 0, \tag{5.33}$$

$$\int_{-L/2}^{L/2} v_2\, \kappa_s G\tau\, (\partial_x w - \theta) + \int_{-L/2}^{L/2} v_2\, \partial_x\, (D\partial_x\theta)\, dx + \int_{-L/2}^{L/2} \omega^2 \frac{\rho_e \tau^3}{12} v_2\, \theta\, dx = 0. \tag{5.34}$$

Performing integration by parts yields,

$$-\int_{-L/2}^{L/2} \partial_x v_1\, \left[\kappa_s G\tau(x)(\, \partial_x w - \theta\,)\right]\, dx + \int_{-L/2}^{L/2} \omega^2 \rho_e \tau(x) v_1\, w\, dx + \left[v_1\, \kappa_s G\tau(\, \partial_x w - \theta\,)\right]_{-L/2}^{L/2} = 0, \tag{5.35}$$

$$\int_{-L/2}^{L/2} v_2\, \kappa_s G\tau\, (\partial_x w - \theta) - \int_{-L/2}^{L/2} \partial_x v_2\, \left(D\partial_x\theta\right)\, dx + \int_{-L/2}^{L/2} \omega^2 \frac{\rho_e \tau^3}{12} v_2\, \theta + \left[v_2\, \left(D\partial_x\theta\right)\right]_{-L/2}^{L/2}\, dx = 0, \tag{5.36}$$

The boundary terms vanish once again since Eqs. (2.32) and (2.33) hold at the free ends. The restrictions of the approximated solutions $w^h, \theta^h$ in the $k^{\text{th}}$ element are written as,

$$w^h(x) = \sum_{r=1}^{N} L_r(x) w^r \in V^h, \tag{5.37}$$

$$\theta^h(x) = \sum_{r=1}^{N} L_r(x) \theta^r \in V^h. \tag{5.38}$$

Arranging the unknowns as $\mathbf{U}^{\mathsf{T}} = \begin{bmatrix} w_1 & \theta_1 & \cdots & w_N & \theta_N \end{bmatrix}$ allows for the above to be written in matrix notation as,

$$w^h(x) = \begin{bmatrix} L_1 & 0 & L_2 & \cdots & L_N & 0 \end{bmatrix}\, \mathbf{U} = \mathbf{N_1}\, \mathbf{U} \tag{5.39}$$

$$\theta^h(x) = \begin{bmatrix} 0 & L_1 & 0 & \cdots & 0 & L_N \end{bmatrix}\, \mathbf{U} = \mathbf{N_2}\, \mathbf{U}. \tag{5.40}$$

Substituting the expressions Eqs. (5.39) and (5.40) in Eqs. (5.35) and (5.36)results in the following local stiffness and mass matrices,

$$\mathbf{K_b} = -\int_K \partial_x \mathbf{N_2}^\mathsf{T} D(x) \mathbf{N_2}\, dx$$

$$\mathbf{K_s} = \int_K \partial_x \mathbf{N_1}^\mathsf{T} \kappa_s G\tau \mathbf{N_2}\, dx - \int_K \partial_x \mathbf{N_1}^\mathsf{T} \kappa_s G\tau \mathbf{N_1}\, dx$$
$$- \int_K \partial_x \mathbf{N_2}^\mathsf{T} \kappa_s G\tau \mathbf{N_1}\, dx + \int_K \partial_x \mathbf{N_2}^\mathsf{T} \kappa_s G\tau \mathbf{N_2}\, dx$$

$$\mathbf{M} = \int_K \mathbf{N_1}^\mathsf{T} \rho_e \tau(x) \mathbf{N_1}\, dx + \int_K \mathbf{N_2}^\mathsf{T} \frac{\rho_e \tau(x)^3}{12} \mathbf{N_2}\, dx.$$

Hence, once again upon global assembly the free vibration problem for the thin plate strip is written as,

$$(\tilde{\mathbf{K_b}} + \tilde{\mathbf{K_s}})\mathbf{u} + \omega_\ell^2 \tilde{\mathbf{M}}\mathbf{u} = 0 \tag{5.41}$$

The solution of the above system reduces the modal functions $\{w_\ell, \theta_l\}$ and natural frequencies $\omega_\ell \ell$.

# Chapter 6

# Computational Domain Truncation

The truncation of the inherently unbounded domain of interest, along with the efficient implementation of closure conditions at the fictitious boundary of the computational region is the focus of the present chapter. The Optimal PML introduced by Bermúdez et al. (2007) to treat the exterior Helmholtz problem is investigated, in conjunction with the Finite Element Method (PML-FEM scheme), focusing on water-wave and hydroacoustic scattering problems in the ocean and coastal environment. Under simplifying assumptions the physical phenomena are modelled by the Mild-Slope (MS) and the Helmholtz equation with variable coefficients, respectively. Furthermore, the PML-FEM scheme is extended to treat the vertical multi-modal expansion of the velocity potential employed for dimensionality reduction in the context of the thesis.

## 6.1 Wave scattering in the Ocean Environment

The accurate prediction of wave fields in nearshore and coastal areas is crucial for several applications, including the design and safe operation of marine structures and harbours, as well as the stability of the coastal zone. In many cases, ranging from pile breakwaters to offshore wind farms, the interaction of free-surface gravity waves with uneven bottom topography and surface-piercing obstacles, like vertical cylinder arrays, is of great significance for engineering studies; see, e.g., Guo et al. (2017). To facilitate the analysis in variable bathymetry regions the assumption of moderate bottom slopes is usually adopted,and hence the wave conditions are determined by means of reduced refraction-diffraction, mild-slope models; see, e.g., Mei et al. (2005) and Dingenmanns (1997). Such models, typically involving only the horizontal spatial variables, allow for the study of water wave diffraction in the presence of obstacles, while accounting for refraction effects due to a mildly sloping bottom. In the work of Booij (1983) (1983) it is shown that the applicability of the classical mild slope by Berkhoff (1972) is limited to bottom slopes up to 1:3. Enhancements of the classical model, in order to account

for stronger bottom variations, led to modified versions presented by various authors, e.g., Radder and Dingemans (1985), Massel (1993), Chamberlain and Porter (1995). Additional effects concerning dissipation due to bottom friction and wave breaking, as well as wave-current interaction, have also been presented in the works of , Tsay and Liu (1983) and Kirby and Dalrymple (1984); see also Belibassakis et al. (2011). Notably, the elliptic mild slope models are reduced to the Helmholtz equation with variable coefficients (see e.g., Mei et al. (2005)). The above fact underlines the similarity between the combined refraction-diffraction problem for water-waves on the horizontal plane and hydroacoustic wave propagation and scattering in the inhomogeneous ocean and coastal waveguides (Jensen et al., 2011), and thus supporting the development of common methods and techniques for numerical treatment; see also Chai et al. (2016). Apart from being governed by the same equation, the above problems also share the characteristic of being inherently formulated in unbounded or partially unbounded domains. This class of problems is further complicated by the fact that the physical properties of the medium (the propagation speed or the index of refraction) are variable at infinity, as approached from different directions.

Next, a unified presentation is followed for problems of linear water-wave propagation in nearshore regions, including the case of wave interaction with bottom founded obstacles, and hydroacoustic wave propagation in the inhomogeneous ocean waveguide in the presence of scatterers. Under specific simplifying assumptions, in the former case, water wave propagation is manifested on the horizontal plane, while in the latter it takes place on the vertical plane.

### 6.1.1 Combined Reffraction-Diffraction

Assuming only a mildly sloping seabed, the Mild Slope Equation (MSE) is a classic model, obtained by integration over the water depth leading a dimensionality reduction of the 3D water wave problem; see e.g., Dingenmanns (1997). An enhanced version of the above classical model, is the Modified Mild Slope equation (MMS), presented by Chamberlain and Porter (1995); Massel (1993), able to account for higher-order effects involving the gradients of the depth function. The latter elliptic model, supplemented by appropriate conditions at fixed boundaries and the description of the incident wave field and/or radiation conditions at open boundaries, is commonly applied to the study of wave transformations in coastal regions as well as in harbor design. The considered marine environment is composed of a layer of inviscid and irrotational fluid bounded above by a free surface and below by a rigid, impermeable bottom. The latter are in agreement with the mathematical assumptions introduced previously and the 3D transmission problem reduction approach discussed in Section 3.3, the decomposition Eq. (3.19) is once again employed. Thus the total wave field solution is decomposed into an unknown incident field $\phi_i$, carrying the imposed wave transformations due to the presence of the parallel contour bathymetry $h_i(x)$ and an unknown, diffracted field $\phi_d$ due the presence of the localized scatterer corresponding to the depth function perturbation $h_d(\mathbf{x})$ .

The MMS equation is employed for each of the reduced problems.Thus, the propagating-refracted wave field over the parallel contour bathymetric profile satisfies the following one-dimensional ($x$-dependent) MMS equation,

$$\partial_x \left( cc_g \, \partial_x \phi_i \right) + cc_g \left( k_0^2 + \psi - k_{x_2}^2 \right) \phi_i = 0, \; x \in \Omega^c \tag{6.1}$$

The above is formulated as a transmission problem with appropriate inflow and outflow conditions as described in Section 3.3.1. In Eq. (6.1), $c(x) = \omega / k_0(x)$ is the phase velocity and $c_g(x) = \partial_k \omega$ is the group velocity. The function $\psi$ involves the terms of bottom slope and curvature of the depth function $h_i(x)$ (Massel, 1993; Miles and Chamberlain, 1998). The diffraction problem on $\phi_d$, over the composed bathymetry $h(\mathbf{x}) = h_i(x) + h_d(\mathbf{x})$ behaves like a radiating solution as discussed in Chapter 3, and it satisfies the MMSE in the horizontal plane $(x_1, x_2)$,

$$\nabla \left( cc_g \, \nabla \phi_d \right) + cc_g \left( k_0^2 + \psi - k_{x_2}^2 \right) \phi_d = f(\mathbf{x}), \; \mathbf{x} \in \breve{\Omega} \tag{6.2}$$

The forcing term $f(\mathbf{x})$ in the right-hand side is obtained from the solution of the incident-refracted wave field $\phi_i$ , as follows $f(\mathbf{x}) = -\left( \nabla \left( cc_g \, \nabla \phi_i \right) + cc_g \left( k_0^2 + \psi - k_{x_2}^2 \right) \phi_i \right)$ , and has support on the projection of the depth inhomogeneity $h_d$. The substitutions $\Phi_d = \sqrt{cc_g \phi_d}$ and $\Phi_i = \sqrt{cc_g \phi_i}$ reduce Eqs. (6.1) and (6.2) to the Helmholtz equation with horizontally varying coefficient $\kappa$, corresponding to an effective wavenumber in 1D and 2D respectively.Thus focusing in the diffraction problem, it is written as,

$$\nabla \Phi_d + \kappa^2 \Phi_d = \frac{f(\mathbf{x})}{\sqrt{cc_g}}, \; \mathbf{x} \in \breve{\Omega}. \tag{6.3}$$

with $\kappa^2 = k^2 + \psi - \frac{\sqrt[2]{cc_g}}{\sqrt{cc_g}}$.

As mentioned above the total solution for the refracted-diffracted wavefield in the presented formulation is derived by the superposition of the incident-refracted wavefield $\Phi_i$ and the diffracted wavefield $\Phi_d$. Next, the case of wavefield diffraction over a single or multiple scatterers, which are assumed to be vertical cylinder(s) of general cross section, extending over the whole length of the water column (from the seabed to the free surface) is considered. These localised scatterers, denoted as $S_i$ , lay in the interior of the computational domain. The union of the disjoint scatterer boundaries is given as $\Gamma_S \cup \Gamma_{si}$.The harmonic water wave diffraction problem over the parallel contour bathymetry in the presence of the scatterers $S_i$, is again governed by the MMS model on the horizontal plane which is now given by,

$$\nabla \Phi_d + \kappa^2 \Phi_d = 0, \; \mathbf{x} \in \Omega \quad S_i. \tag{6.4}$$

supplemented by a suitable boundary condition on the body surfaces,

$$\alpha\partial_n\Phi_d + \beta\Phi_d = -\left(\alpha\partial_n\Phi_i + \beta\Phi_i\right), \text{ on } \Gamma_S, \tag{6.5}$$

where $\alpha$ and $\beta$ are constants and in general dependent on the body properties. In the case of rigid structures the selection $\alpha = 1$, $\beta = 0$ reduces to the standard Neumann condition. The known Cauchy incident data on $\Gamma_S$, employed in Eq. (6.5) are provided again by the solution of the incident-refracted wavefield problem $\Phi_i$, over the parallel contour bathymetry $h_i$ in the absence of the inclusions as in the prequel. The key difference between the above two problems, posed by Eqs. (6.3)–(6.5), is that in the former case, wave diffraction is caused by the assumed depth inhomogeneity $h_d(\mathbf{x})$, superimposed over the variable bathymetry, while in the latter case wave scattering takes place because of the presence of the surface piercing bodies in the region of interest. Notably, the present method is capable to treat the combined effects.

### 6.1.2 Hydroacoustic wave propagation and scattering in the ocean waveguide

In the sequel, the problem of hydroacoustic wave propagation in the inhomogeneous ocean waveguide is considered. Propagation and scattering problems in underwater acoustics, and more specifically in range-dependent domains relevant to coastal applications, are frequently formulated by using a point source (see e.g. Jensen et al. (2011) for field excitation. However, as frequency increases, the problem becomes computationally demanding, and thus, for many practical problems, as well as for inter-model comparisons, it is useful to work with a line source in plane geometry. Assuming constant medium properties along the transverse $x_2$ direction, the line source can be visualised as a distribution of monopole sources along the $x_2$ axis. In this case, underwater acoustic wave propagation is governed by the Helmholtz equation on the vertical plane, while the acoustic waveguide is formed by the free upper surface and seabed boundaries. The domain of interest is thus the inhomogeneous strip $\Omega_c$ matching the 2D vertical strip introduced in Section 3.3.1, featuring an acoustically hard seabed of varying slope. Additionally, these areas are considered to be range independent, hence the acoustic medium properties are assumed to exhibit only vertical variation. In the considered case, the mathematical problem of hydroacoustic propagation in a range-dependent waveguide, excited by a line source, is described by,

$$\nabla^2\Phi_c + \kappa^2\Phi_c = \delta(x - x_0, z - z_0), \ (x, z) \in \Omega^c \backslash S. \tag{6.6}$$

with $\Phi_c$ denoting the acoustic wavefield and $k = \omega/c(x, z)$ the acoustic parameter in the waveguide with a variable index of refraction. The line source location on the $(x, z)$ plane is denoted by $(x_0, z_0)$. The field Eq. (6.6) is supplemented with the following conditions on the

upper and bottom boundaries,

$$\Phi_c(x,0) = 0 \text{ and } \partial_n \Phi_c(x,0) = 0. \tag{6.7}$$

In the present work, the seabed is modeled as an acoustically hard boundary, however, extension to treat a multilayered bottom is possible (Jensen et al., 2011). The total wavefield can be once again split into a solution that carries the field transformations due to the variable index of refraction of the medium, in the absence of the finite body(ies), and a scattered solution due to the presence of the body (ies) in the waveguide. The total wavefield is decomposed to the incident and scattered acoustic wavefields as, $\Phi_c = \Phi_{ci} + \Phi_{cs}$. The former can be calculated by several methods, as e.g., the coupled-mode method where the solution is represented as,

$$\Phi_{ci}(x,z) = \sum_{n=0}^{\infty} \varphi_n(x) \tilde{Z}_n(z;x) \tag{6.8}$$

while $\varphi_n(x)$ are the modal amplitudes and $\tilde{Z}_n(z;x) = Z_n(z;x)/\|Z_n\|$ are the normalised local vertical eigenmodes satisfying the boundary conditions Eq. (6.7). For a range independent environment featuring a flat seabed $h$ , the expansion is reduced to

$$\Phi_{ci}(x,z) = 2\sum_{n=0}^{\infty} \tilde{Z}_n(z;x)\tilde{Z}_n(z_0;x)\frac{\exp\left(\mathrm{i}k_{xn}x - x_0\right)}{k_{xn}} \tag{6.9}$$

where $Z_n(z) = \sin k_{zn}$, $k_{zn} = (n-0.5)\pi/h$ and $k_{xn} = \sqrt{k^2 - k_{zn}^2}$ are the horizontal wavenumbers. Additional details can be found in Appendix B .

The scattering problem in the waveguide containing the scatterer(s) $S_i$ is described by the homogeneous Helmholtz equation,

$$\nabla^2 \Phi_{cs} + k^2 \Phi_{cs} = 0, \ (x,z) \in \Omega_c / S_i. \tag{6.10}$$

supplemented with the Robin-type condition Eq. (6.5) on $\Gamma_S$. Similarities between the examined refraction-diffraction problems for water-wave propagation on the horizontal plane, Eq. (6.3) ,and hydroacoustic scattering on the vertical plane, Eq. (6.10), are profound. In both cases the resulting Helmholtz-type problems with varying coefficients, defined in unbounded domains and supplemented with appropriate conditions on the enclosed scatterer boundaries, allow for the development and implementation of similar computational methods. A major challenge in devising a numerical scheme for problems in (partially of totally) bounded domains, governed by PDEs with variable coefficients, is to ensure energy absorption at the open boundaries with minimum backscattering. An extended discussion of appropriate conditions for the elliptic mild-slope equation can be found in the work of Oliveira (2004). In this direction, Collino and Monk (1998) studied the PML model proposed by Berenger (1994) for the numerical closure of the Helmholtz equation in acoustics and electromagnetics. Modesto

et al. (2016, 2015) employed the same PML model for the case of the MSE in harbor agitation studies.The effectiveness of the above PML is strongly dependent on the layer parameters (thickness, absorbing function form). In the next section the parameter-free PML model by Bermúdez et al. (2007) is applied, in conjunction with the FE method, for the optimal solution of the present diffraction/scattering problems in the coastal environment.

## 6.2 Domain Truncation Techniques

This class of problems is further complicated by the fact that the physical properties of the medium (the propagation speed or the index of refraction) are variable at infinity, as approached from different directions. In this case, the far-field wave pattern is not known a priori, and a standard radiation condition (e.g., Sommerfeld condition) is not available. The truncation of the unbounded domain, in conjunction with efficient implementation of closure conditions at the truncated boundary, is hence required. To this purpose, a number of strategies have been developed in the literature, across disciplines. Absorbing Boundary Conditions (ABCs), approximate DtN operators, infinite elements and boundary element methods have been widely used to truncate problems that are naturally defined in infinite domains; see, e.g., Givoli (1991, 1992). ABC techniques are concerned with the development of radiation condition variants that are able to model the effects of the exterior domain on the open boundary. Since the artificial boundary conditions are constructed to approximately minimize spurious reflections, important issues concerning the order of accuracy and its computational cost rise. Moreover, knowledge of the solution characteristics in the far-field is frequently required for an effective implementation. Additionally, the efficiency of lower order ABCs increases as the open boundary is positioned further away from the scatterer, which makes accuracy a trade-off for computational labour. On the other hand, the employment of the above models involving higher-order derivatives can prove computationally tedious. Higher-order ABCs, able to achieve enhanced accuracy without excessive computational cost, are reviewed in Givoli (2004). A commonly cited advantage of ABCs is the ease of their implementation in FE solvers, since the produced sparse matrices are preferable to the dense matrices produced by non-local DtN strategies.

Opposed to ABCs and DtN methods, perfectly-matched layer (PML) models do not introduce approximate conditions at the external fictitious boundary but a layer with damping qualities, enclosing the computational domain. The complex medium is constructed in such a way that the solution at the interface between the absorber and the domain of interest are perfectly matched, suppressing thus spurious reflections. The classical PML model by Berenger (1994) imposed matching conditions between the incident wavefield and the attenuated solutions for the time-dependent Maxwell equations. The initial split field approach employed is equivalent to complex coordinate stretching as indicated in the works of Rappaport (1995) and others. The rate of solution attenuation within the layer is dictated by the use of a suitable absorbing function; see Abarbanel and Gottlieb (1997), Turkel and Yefet (1998). A unique and

rather desirable quality of PML-based methods over most boundary termination techniques is that their effectiveness is independent of the angle of incidence to the fictitious boundary and the wave frequency. Since the original application by Berenger (1994) to the solution of the Maxwell equations, PML models have been successfully implemented in the treatment of several problems which are naturally defined in infinite domains, such as acoustic scattering (e.g., Qi and Geers (1998)), elasticity (e.g.,Harari and Albocher (2006)) and water waves (e.g., Belibassakis et al. (2001); Modesto et al. (2015); Navon et al. (2004).

The exponential convergence of the PML to the exact solution of the reduced wave equation as the layer thickness tends to infinity is shown by Lassas and Somersalo (1998). However, the numerical treatment requires a truncated layer, thus introducing error due to reflection at the exterior, termination boundary. Even so, the dissipative properties of a finite PML are ensured by allowing for sufficient layer thickness or by the employment of an appropriate absorbing function. Such a function should perform the complex coordinate stretching and minimize the reflection at the outer boundary to eliminate contamination of the numerical solution. However, in real applications numerical reflections do rise due to discretization. Collino and Monk (1998) suggested that the numerical error is effectively contained by optimizing the absorbing function controlling layer. In the same work, it was shown that the choice of the absorbing function and the discretization within the layer affects the reflection coefficient in a non-trivial manner, raising the question of an optimal or parameter-dependent PML at the discretized level. The parameters for optimization are the employed mesh, the layer thickness and the functional form of the absorbing function. Regarding the latter, constant and polynomial functions of a varying degree have been proposed Berenger (1994); Collino and Monk (1998); Singer and Turkel (2004). Recently, a novel PML formulation is proposed by Bermúdez et al. (2007) featuring an unbounded absorbing function; see also Bermúdez et al. (2010) and references cited there. It is shown that the latter singular PML model is able to recover the exact solution for the unbounded Helmholtz equation. The formulation retains the desirable qualities of classical PML approaches without the need to further optimize the parameters of the absorbing function according to the employed mesh and problem data. Hence, by introducing an unbounded absorbing function, PML thickness is the only parameter to be optimized as noted by Cimpeanu et al. (2015), who also studied the thickness-error behaviour of the optimal PML Bermúdez et al. (2007). Most interestingly they note the existence of an optimal normalised thickness range where the numerical error remains insensitive to change, suggesting that within this range the model is rendered parameter-free. Notably, the suggested thickness ranges are very small reducing the computational cost and making the method further appealing. Finally, in the work of Rabinovich et al. (2010) a comprehensive comparison between ABCs and PML models is carried out, showing that the effectiveness of the singular PML is similar to higher-order ABC. While the latter is insensitive to the employed discretization and requires no-tuning, they remain considerably more complex in implementation than the singular PML, which is straightforward to incorporate in a FEM solver.

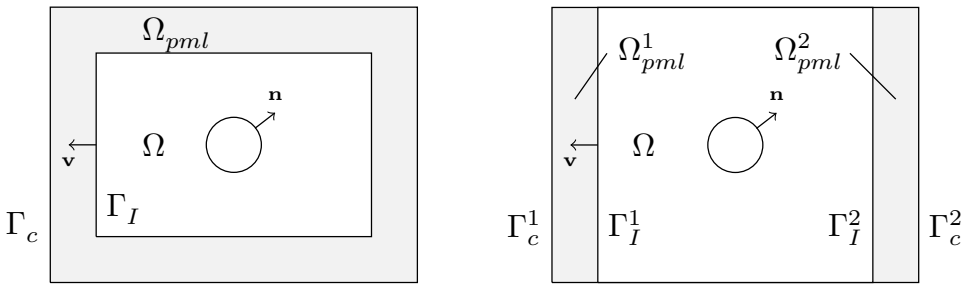


**(i)** Scattering on the horizontal plane **(ii)** Scattering in a waveguide

**Figure 6.1** Configuration of the computational domain including the PML regions for the cases of (ii) the MMS on the horizontal plane (left). (ii) the Helmholtz equation in the acoustic waveguide on the vertical plane (right).

### 6.2.1 Optimal PML and FEM

The considered diffraction problems, in the framework of linear water wave and hydroacoustic wave propagation, are examined in the 2D horizontal space and the 2D vertical strip, respectively. In this section, a unified approach in the truncation of the physical domains and the application of a Perfectly Matched Layer (PML) is pursued first. Subsequently, the weak forms of the truncated problems will be examined from the convergence and accuracy point of view. The water-wave diffraction problem, governed by the Helmholtz equation with variable coefficients formulated in a truncated domain by means of a PML of finite thickness $\theta_l$. The introduced 2D layer is confined in the region denoted as, $\Omega_{pml} = [-X_1 - \theta_l, X_1 + \theta_l] \times [-X_2 - \theta_l, X_2 + \theta_l] \cap [-X_1, X_1] \times [-X_2, X_2]$. The inner region $\Omega_r = [-X_1, X_1] \times [-X_2, X_2]$ enclosing the scatterer constitutes the region of computational interest (Fig. 6.1(i)). The fictitious, outer termination boundary is denoted by $\Gamma_c$ while the interface between the computational region and the PML is $\Gamma_I$. The outward normal vector on the interface is denoted by $\mathbf{v}$. For the hydroacoustic scattering problem, governed by the Helmholtz equation in the infinite strip is similarly treated. The computational waveguide of thickness h is confined in the strip $\Omega_s = [-X_1, X_1] \times [-\mathrm{h}/2, \mathrm{h}/2]$ contained within two layers of thickness $\theta_l$, thus $\Omega_{pml} = \Omega^1_{pml} \cup \Omega^2_{pml}$ with $\Omega^1_{pml} = [-X_1 - \theta_l, -X_1] \times [-\mathrm{h}/2, \mathrm{h}/2]$ and $\Omega^2_{pml} = [X_1, X_1 + \theta_l] \times [-\mathrm{h}/2, \mathrm{h}/2]$. A similar notation is employed for the boundaries (Fig. 6.1(ii)). In PML-based methods, perfect matching of the solution on the absorber layer interface with the computational region is guaranteed by the complex coordinate stretching in the layer (Bermúdez et al., 2007; Collino and Monk, 1998). The notion behind the latter approach is the analytic continuation of a real function into the complex plane. In the physical, unbounded domain, the analytically continuous, wave-like solutions are stretched in a complex contour which allows for oscillating solutions to be turned into decaying waves outside the region of computational interest. The following complex coordinate transformation is

introduced, supported in both vertical and horizontal PML regions,

$$\tilde{x}_j = X_j + \int_{|X_j|}^{|x_j|} \gamma_j(s)\, ds,\ \forall \mathbf{x} \in \Omega_{pml} \text{ for } j = 1, 2. \tag{6.11}$$

The complex functions $\gamma_j(x_j)$ are of the general form,

$$\gamma_j(x_j) = \begin{cases} 1, & \mathbf{x} \in \Omega, \\ 1 + \mathrm{i}\frac{1}{k(x_j)}\sigma_j(x_j), & \mathbf{x} \in \Omega_{pml}. \end{cases} \tag{6.12}$$

where $\Omega$ refers to either $\Omega_s$ or $\Omega_r$. The combined region is denoted as $\tilde{\Omega} = \Omega \cup \Omega_{pml}$ Within the computational region $\gamma_j(x_j)$ reduces to unity, leaving the solution unchanged. Thus, attenuation only takes place within the layer. The rate of decay is determined by the absorbing functions $\sigma_j(x_j)$. The choice of absorbing functions is independent of the presented analysis and will be addressed in a following subsection. It is evident however that in order to ensure decaying solutions within the perfectly matched layer, non-negative absorbing functions must be considered. After performing the following change of variables in the layer,

$$\partial_{\tilde{x}_j} \to \frac{1}{\gamma_j(x_j)}\partial_{x_j},\ j = 1, 2. \tag{6.13}$$

The Helmholtz equation in $\tilde{\Omega}$ reduces to,

$$\nabla \cdot (\boldsymbol{\gamma} \nabla \varphi) + k^2 |\gamma_+| = 0,\ \forall \mathbf{x} \in \tilde{\Omega}, \tag{6.14}$$

with,

$$\boldsymbol{\gamma} = \boldsymbol{\gamma}_+ \boldsymbol{\gamma}_- = \begin{bmatrix} \gamma_2^q & 0 \\ 0 & \gamma_1^r \end{bmatrix} \begin{bmatrix} \gamma_1^{-r} & 0 \\ 0 & \gamma_2^{-q} \end{bmatrix} = \begin{bmatrix} \gamma_2^q \gamma_1^{-r} & 0 \\ 0 & \gamma_1^r \gamma_2^{-q} \end{bmatrix}.$$

The constants $q, r$ are employed for compact notation. It holds,

- $q = 1,\ r = 1$, for the problem formulation in the 2D plane,
- $q = 1,\ r = 0$, for the problem formulation the waveguide spanning along $x_1$,
- $q = 0,\ r = 1$, for the problem formulation the waveguide spanning along $x_2$.

When the truncated waveguide is considered, Eq. (6.14) is supplemented by appropriate conditions at the upper and lower boundaries, $x_2 = \pm X_2$. These are commonly homogeneous Neumann conditions in ocean acoustic applications.

On the scatterer boundary, a general mixed-type condition is given by,

$$\alpha \nabla_{\mathbf{n}} \varphi + \beta \varphi = -(\alpha \nabla_{\mathbf{n}} \varphi_I + \beta \varphi_I) \equiv f,\ \text{on } \Gamma_s. \tag{6.15}$$

In the above, $\varphi$ denotes the known incident data on the scatterer. Setting the coefficients $\alpha = 1, \beta = 0$ and $\alpha = 0, \beta = 1$ reduces to Neumann and Dirichlet conditions respectively. On the internal boundary between the PML and the computational domain, continuity requirement poses on the solution and its normal derivative across the interface is required. Denoting the PML solution as $\varphi_-$ and the interior solution as $\varphi_+$, the following transmission conditions are derived,

$$\varphi_- = \varphi_+ \text{ and} \tag{6.16}$$

$$\frac{1}{\gamma_1}\partial_{v_1}\varphi_- + \frac{1}{\gamma_2}\partial_{v_2}\varphi_- = \partial_{v_1}\varphi_+ + \partial_{v_2}\varphi_+ \text{ on } \Gamma_I. \tag{6.17}$$

The above conditions are *a priori* satisfied by functions $\gamma_j$.

*Remark* 15. As the present work focuses on problems that are governed by the Helmholtz equation with spatially varying coefficients, the analytic continuation of the solution on the interface boundary between the computational region and the PML must be ensured in order for the latter to maintain its reflectionless properties. Hence, arbitrary variation of the effective wavenumber is not technically allowed within the layer region. However, the PML is shown to be reflectionless for inhomogeneous media as long as they remain range independent within the layer along the direction perpendicular to the interface boundary Oskooi et al. (2008). In the present study the above restrictions are easily met without any loss of generality.

Considering a the weight function $u(x_1, x_2) \in H_0^1(\tilde{\Omega}; \mathbb{C})$, the weak form of problem posed by Eq. (6.14) is straightforwardly derived as,

$$\int_{\tilde{\Omega}} u\,\boldsymbol{\gamma}\nabla^2\varphi + k^2 u|\gamma_+|\varphi\; d\tilde{\Omega} = 0 \tag{6.18}$$

A decomposition into subregions and the Green-Gauss theorem application yields,

$$\begin{aligned} &-\left(\int_{\Omega} \nabla u\cdot(\nabla\varphi_+) - k^2 u\varphi_+\; d\Omega\right) + \int_{\Gamma_s} u\nabla_{\mathbf{n}}\varphi_+\; ds + \int_{\Gamma_I} u\nabla_{\mathbf{v}}\varphi_+\; ds \\ &-\left(\int_{\Omega_{pml}} \nabla u\cdot(\boldsymbol{\gamma}\nabla\varphi_-) - k^2 u|\gamma_+|\varphi_-\; d\Omega_{pml}\right) - \int_{\Gamma_I} u\boldsymbol{\gamma}\nabla_{\mathbf{v}}\varphi_-\; ds + \int_{\Gamma_c} u\boldsymbol{\gamma}\nabla_{\mathbf{n}}\varphi_-\; ds = 0 \end{aligned} \tag{6.19}$$

The terms on the interface $\Gamma_I$ vanish due to the explicit satisfaction of Eq. (6.17). The term on the termination boundary $\Gamma_c$ vanishes due to the imposition of homogeneous Dirichlet condition. Finally, the boundary integral on the scatterer is computed using the known incident

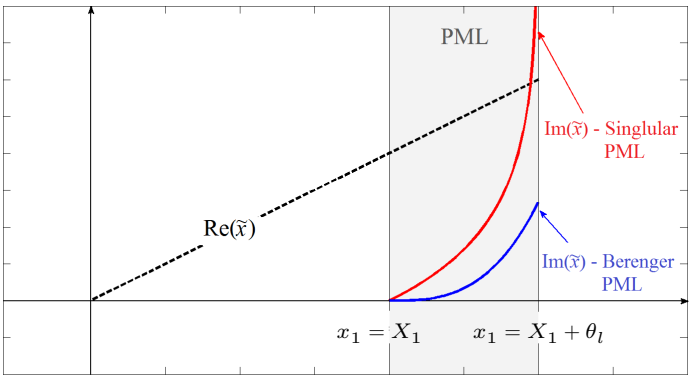


**Figure 6.2** Complex co-ordinate stretching in 1D

wave field data, and hence the weak formulation of the considered problems is reduced to,

$$\text{Find } (\varphi_+, \varphi_-) \in \mathcal{V} \text{ such that,}$$

$$\left(\int_\Omega \nabla u \cdot (\nabla \varphi_+) - k^2 u \varphi_+ \, d\Omega\right) ds + \left(\int_{\Omega_{pml}} \nabla u \cdot (\boldsymbol{\gamma} \nabla \varphi_-) - k^2 u |\gamma_+| \varphi_- \, d\Omega_{pml}\right) = \int_{\Gamma_s} uf \, ds, \quad \forall \, (u_+, u_-) \in \mathcal{V}. \tag{6.20}$$

The classical choices for the functional form of the non-negative absorbing functions $\sigma_j(x_j)$ are polynomials of a varying degree with respect to a normalized coordinate within the layer, i.e. $\sigma_j(x_j) = \frac{1}{k}\sigma\left(\frac{X_j - x_j}{\theta_l}\right)^n$, $j = 1, 2$ with constant $\sigma_j > 0$ and $n \geq 0$. Increasing the value of $\sigma$ and/or the degree $n$ ensures a faster absorption within a given layer. However, increasing $\sigma$ and/or $n$ excessively results in an abrupt solution decay, increasing artificial numerical reflections in the discrete form of the PML medium. Moreover, enhancing the layer thickness is a means to achieve attenuation while keeping a slower decay rate, but would also result in large computational domain and therefore enhanced computational cost. Collino and Monk (1998) note the dependency of the optimal absorbing parameters on the employed mesh and the problem data. Hence, the application of effective PML-based techniques for truncating the computational domain, requires *a priori* tuning of those parameters. The criteria for establishing optimal PML parameters are not trivial and even then, the optimisation problem needs to be solved again after re-meshing Bermúdez et al. (2007). In the present work, the optimal PML model for the scalar, reduced wave equation proposed by Bermúdez et al. (2007)

is adopted. The given model employs non-integrable absorbing functions of the form,

$$\sigma_j(x_j) = \frac{1}{k}\left(\frac{1}{|X_j + \theta_l - x_j|}\right), \; x_j \in \Omega_{pml}, \; j = 1, 2. \tag{6.21}$$

Instead of a bounded imaginary part, the absorbing function of Eq. (6.21) results to an infinite integral in the complex coordinate stretching Eq. (6.13) as seen in the comparative sketch in Fig. 6.2. The above has been proved to be optimal for the attenuation of plane wave solutions for the Helmholtz equation in infinite resolution Bermúdez et al. (2006), and also compares favorably against widely used polynomial functional forms; see Bermúdez et al. (2004, 2006, 2007, 2010, 2001). Naturally, the absence of tunable parameters in Eq. (6.21) overcomes a major drawback of other PML methods. In Cimpeanu et al. (2015) the investigation of the above singular PML model studied the effect of layer thickness, as the only remaining parameter controlling the performance of the layer. A rather interesting finding of their work is the existence of an optimal range of layer thickness values, within which the solution error becomes independent of the chosen thickness, thus rendering the singular PML model parameter-free for the scalar Helmholtz equation. In the present work the parameter-free, unbounded PML model will be implemented in a FEM strategy for the solution of the linear elliptic problems rising in the fields of water-wave propagation and hydroacoustics.

### 6.2.2 Adaptation for the multi-modal vertical representation of the wave potential

In the previous section the PML-FEM formulation for the Helmholtz equation is explored in detail. With the ease in implementation being particularly discernible, an adaptation is attempted for the case of wave propagation in intermediate water depth targeting the radiation-type problems defined in Chapters 3 and 4. To this end, the Cartesian PML defined in a bounded subregion of $\mathbb{R}^2$, as seen Fig. 6.1(i) is considered. Returning to the complex coordinate stretching whithin the layer Eq. (6.13) introducing wave attenuation on the horizontal directions and considering the Laplace equation results in the following field equation valid in the PML region,

$$\frac{1}{\gamma_1}\partial_{x_1}\left(\frac{1}{\gamma_1}\partial_{x_1}\varphi\right) + \frac{1}{\gamma_2}\partial_{x_2}\left(\frac{1}{\gamma_2}\partial_{x_1}\varphi\right) + \partial_z^2\varphi = 0 \;\in \Omega_{pml}. \tag{6.22}$$

A similar manipulation as in the prequel allows recasting Eq. (6.22) in a divergence form, convenient for FEM implementation. Thus, by multiplying Eq. (6.22) with $\gamma_1\gamma_2$ and assuming the notation $\varphi^*$ for the potential function with support within the layer results in,

$$\nabla \cdot (\tilde{\boldsymbol{\gamma}} \nabla \varphi^*) = 0 \tag{6.23}$$

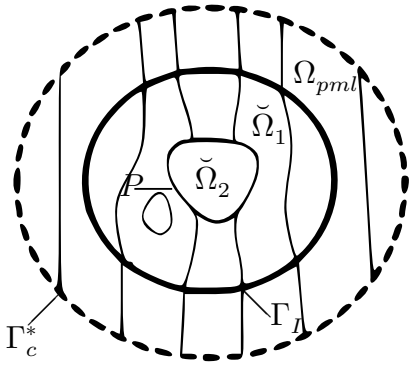


**Figure 6.3** Projection on the 2D plane

with $\tilde{\boldsymbol{\gamma}} = \begin{bmatrix} \frac{\gamma_2}{\gamma_1} & 0 & 0 \\ 0 & \frac{\gamma_1}{\gamma_2} & 0 \\ 0 & 0 & \gamma_1\gamma_2 \end{bmatrix}$.

Revisiting the projection of the general domain of interest on the 2D plane $(x_1, x_2)$ in light of the employed layer formulation, the relevant notation is refined in Fig. 6.3. Equation (6.23) is straightforwardly implemented in Mixed Weak Problem 3.2. In the first equation of the mixed weak form, the term on the numerical truncation boundary is substituted with an interfacial term on $\Gamma_I$,while the field Eq. (6.23) valid in the PML region $\Omega_{pml}$. The revised integral form reads ,

$$\begin{aligned} \sum_{j=1}^{2}\left(\int_{\Omega}\nabla v^{(j)}\cdot\nabla\varphi^{(j)}\,d\Omega\right) - \mu\int_{\Gamma_f^1} v^{(1)}\,\varphi^{(1)}\,ds + \int_{\Gamma_f^2} v^{(2)}\,f_\ell\,ds + \int_S (v^{(2)}-v^{(1)})\lambda\,ds \\ - \int_{\Gamma_I}\partial_n\varphi^{(j)}v^{(j)} + \int_{\Gamma_I}\tilde{\boldsymbol{\gamma}}\partial_n\varphi^{*}v^{(1)}\,ds + \int_{\Omega_{pml}}\nabla v^{(j)}\cdot\tilde{\boldsymbol{\gamma}}\nabla\varphi^{*}\,d\Omega \\ + \int_{\Gamma_f^*}\tilde{\boldsymbol{\gamma}}v^{(1)}\,\partial_n\varphi^{*}\,ds + \int_{\Gamma_b^*}\tilde{\boldsymbol{\gamma}}v^{(1)}\,\partial_n\varphi^{*}\,ds + \int_{\Gamma_c^*}\tilde{\boldsymbol{\gamma}}v^{(1)}\,\partial_n\varphi^{*} = 0. \end{aligned} \tag{6.24}$$

The terms on the interface $\Gamma_I$ vanish once again due to the matching property of the layer. On the fictitious termination boundary $\Gamma_c^*$ the solutions vanish due the enforcement of homogeneous Dirichlet conditions. Finally, the boundary term on the seabed in $\Omega_{pml}$ is dropped since the Neumann conditions are met by the multi-modal representations. Subsequently, the multi-modal expansions are substituted in Eq. (6.24) as described in Chapter 4. Upon FEM discretization the stiffness matrices Eq. (5.14) valid in the PML region are modified accordingly as in,

$$\begin{aligned} \mathbf{k}_e = \int_K \sum_{j=1}^{2} (\partial_{x_j}\mathbf{N})^{\mathsf{T}}(\boldsymbol{g}_j\odot\mathbf{A})(\partial_{x_j}\mathbf{N}) + \mathbf{N}^{\mathsf{T}}(\boldsymbol{g}_j\odot\mathbf{B}_{\mathbf{1}}^{j})(\partial_{x_j}\mathbf{N}) \\ +(\partial_{x_j}\mathbf{N})^{\mathsf{T}}(\boldsymbol{g}_j\odot\mathbf{B}_{\mathbf{2}}^{j})\mathbf{N} + \mathbf{N}^{\mathsf{T}}(\boldsymbol{g}_3\odot\mathbf{C})\mathbf{N}\,d\mathbf{x} \end{aligned} \tag{6.25}$$

with $\boldsymbol{g}_i,\ i=1,2,3$, being $(N_m+1)\times(N_m+1)$ matrices containing the complex functions $\gamma_1,\gamma_2$ and $\odot$ denoting Hadamard elementwise multiplication.

*Remark* 16. Since, the primary concern is the attenuation of the propagating mode. The evanescent mode contributions can be left unaltered. Hence,

$$\boldsymbol{g}_1=\begin{bmatrix}\frac{\gamma_2}{\gamma_1} & 1 & \dots\\ \vdots & \ddots & \\ 1 & & 1\end{bmatrix},\ \boldsymbol{g}_2=\begin{bmatrix}\frac{\gamma_1}{\gamma_2} & 1 & \dots\\ \vdots & \ddots & \\ 1 & & 1\end{bmatrix},\ \boldsymbol{g}_3=\begin{bmatrix}\gamma_1\gamma_2 & 1 & \dots\\ \vdots & \ddots & \\ 1 & & 1\end{bmatrix}.$$

### 6.2.3 Numerical Investigation of Optimal PML-FEM

In this subsection we investigate the performance of the singular PML-FEM for the Helmholtz equation governing the problems under consideration. A series of numerical tests are conducted to determine the effectiveness of the method in simple configurations where analytical solutions are available. The analysis aims at establishing the robustness and limitations of the given methodology before its employment in the following applications of coastal engineering interest, *(a)* linear water wave refraction over mildly sloping bathymetries and in the presence of cylindrical bodies extending over the water column, and *(b)* acoustic wave propagation in the inhomogeneous ocean waveguide. Standard conforming linear triangular elements ($p=1$) are used in all examined cases. The method is clearly not restrictive of $p$-refinement, however the latter is outside the scope of the present study. We define the family of triangular partitions $\{T^h\}$ in domain $\tilde{\Omega}$ and $\phi^h$ denotes the restriction of the approximate solution The approximate solution, restricted in the $k^{\text{th}}$ 3-node triangular element is,

$$\phi^h|_e=\mathbf{L}^{\mathsf{T}}\boldsymbol{\phi} \tag{6.26}$$

where $\boldsymbol{\phi}$ denotes the vector of nodal unknowns $\boldsymbol{\phi}=\left[\phi^1\ \phi^2\ \phi^3\right]^{\mathsf{T}}$ and $\mathbf{L}=\left[L_1\ L_2\ L_3\right]^{\mathsf{T}}$ is a vector containing the linear Lagrange shape functions at the element. The discretised weak formulation of Eq. (6.20) is given by,

$$\int_K\left((\nabla\mathbf{L})^{\mathsf{T}}\boldsymbol{\gamma}(\nabla\mathbf{L})-k^2(\mathbf{L})^{\mathsf{T}}\gamma_2^q\gamma_1^r\right)\boldsymbol{\varphi}\,dx_1dx_2=\mathbf{f}, \tag{6.27}$$

where $\mathbf{f}$ assumes non-zero values when a element edge lays on the scatterer boundary $\Gamma_s$ as per the enforced condition Eq. (6.15). A Delaunay mesh is used for the discretisation of the computational region while a regular triangular grid is employed within the layer. The discretisation of the computational region is assessed by the number of employed elements per wavelength $\tilde{N}_e=N_e/\lambda$, in order to associate maximum element size with examined frequency. For the regular triangular mesh, the number of discrete segments, $N_{x_j}$, employed along the transverse direction of the layer boundary, is used to denote the refinement inside the PML. A single

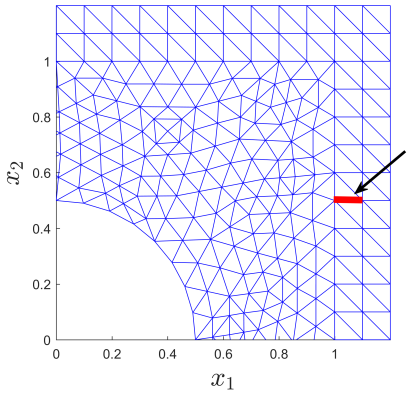


**Figure 6.4** Hybrid triangular Mesh with PML

segment, as seen in Fig. 6.4, results in two triangle faces with a common edge, corresponding to a diagonally divided quadrilateral partition.

The element matrices, in both the PML and the computational region, are computed numerically. The former contain the absorbing functions $\sigma_j(x_j)$ that become unbounded at the outer boundary, and the corresponding integrals involving the elements with an edge or a vertex on the outer boundary become singular. However, as shown in Bermúdez et al. (2007), these integrals are either rendered finite due to the qualities of the Langragian shape functions which diminish at the outer boundary or become zero due to the imposed homogeneous Dirichlet condition at the external boundary $\Gamma_c$ , which is proven necessary for the well-posedness of the discrete problem. Since the singularity is reached at the outer PML boundary the Gauss-Legendre quadrature rule within the edge elements is applicable. A minimum of three integration points per element is employed to ensure that the presented analysis will not be polluted by numerical integration error. In order to assess the performance of the FEM/optimal PML the relative $L_2$ error norm of the approximation with respect to an available analytic solution, is defined as,

$$\text{Error} = \frac{\|\varphi^h - \varphi\|}{\|\varphi\|}$$

In order to establish the robustness of the presented method, a series of numerical experiments is carried out. First, the exterior scalar Helmholtz problem in $\Omega_r \subset \mathbb{R}^2$ , featuring a circular inclusion is considered. The investigation is carried out in the truncated domain $\Omega_r = [-5, 5] \times [-5, 5]$, featuring a circular scatterer with radius $a$ centered at the axes origin. Two cases of incident wave field data on $\Gamma_s$ are considered. The first is the case of parallel plane wave incidence, i.e. $\Phi_I = \exp(\mathrm{i}k\mathbf{x})$, for which the singular PML is shown to be optimal, and the second is the incidence of a wavefield generated by a monopole, i.e. $\Phi_I = \mathrm{H}_0^{(1)}(k|\mathbf{x} - \mathbf{x_s}|)$ positioned at $\mathbf{x_s}/a = (-3, 0)$. Assuming a uniform medium, i.e. $k =$*constant*,the solutions for

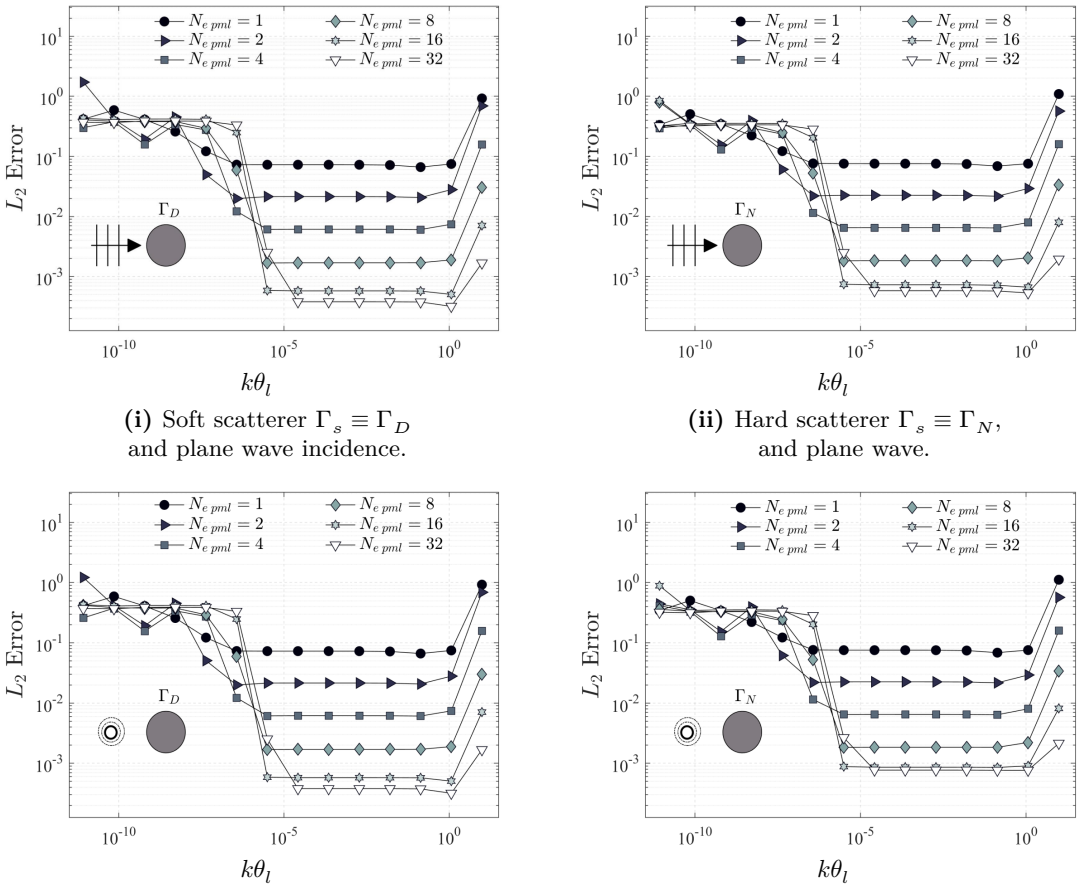


**(i)** Soft scatterer $\Gamma_s \equiv \Gamma_D$ and plane wave incidence.

**(ii)** Hard scatterer $\Gamma_s \equiv \Gamma_N$, and plane wave.

**(iii)** Soft scatterer $\Gamma_s \equiv \Gamma_D$ and source excitation.

**(iv)** Hard scatterer $\Gamma_s \equiv \Gamma_N$, and source excitation.

**Figure 6.5** Calculated error of the scattered field by circular body, $ka = 1$, in the case of incident plane waves. Results for various normalised PML thickness values and increasing PML discretisation

the two incident wave cases are calculated analytically and used for validation of the employed PML-FEM. Analytical solutions are documented in Appendix B .

The effect of normalized absorbing layer thickness is initially considered. The relative errors for solutions with a fixed discretization in the computational region are plotted against a range of layer thickness values, $10^{-12} \leqslant k\theta_l \leqslant 10^{1}$. Different curves correspond to an increasing number of triangular elements in the PML region.Generally, the non-dimensionalised with respect to scatterer radius is examined, namely the values $ka = 1$ and $ka = 3$ are considerd. In all-examined cases the discretization of the internal computational region, $\tilde{N}_e$ is kept constant. It is observed that foe the given discretization in both the internal region and in the PML, there exists an optimal range of thickness values for which the error is independent of further increase of layer thickness. The above result, which is in agreement with similar findings in Cimpeanu et al. (2015), suggests that the singular PML is highly effective for rather small thicknesses that are orders of magnitude smaller than the excited wavelength in this monochromatic case.

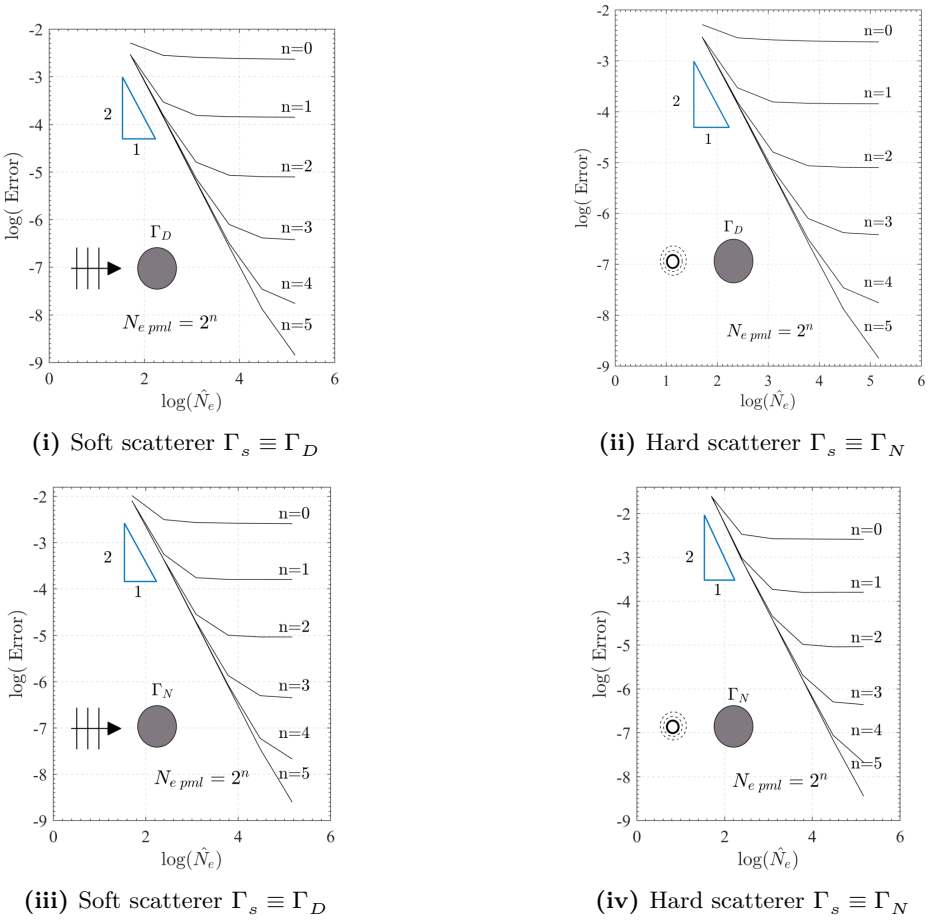


**(i)** Soft scatterer $\Gamma_s \equiv \Gamma_D$

**(ii)** Hard scatterer $\Gamma_s \equiv \Gamma_N$

**(iii)** Soft scatterer $\Gamma_s \equiv \Gamma_D$

**(iv)** Hard scatterer $\Gamma_s \equiv \Gamma_N$

**Figure 6.6** Calculated error of the scattered field by circular body, $ka = 1$, in the case of incident plane waves. Results for various normalised PML thickness values and increasing PML discretisation

The significance of the above result lays in its immediate translation in reduced degrees if freedom for a given level of accuracy. The present results in Fig. 6.5 show optimal thickness values within the range $10^{-4} \leqslant k\theta_l \leqslant 10^{-1}$, depending on the discretization employed in the layer, i.e. $N_{e\,pml}$ . The error increases dramatically as becomes large (order 1 or higher) in the given examples. This is attributed to the crude discretization in the layer, indicating that the restriction on the upper boundary of accepted PML thickness values for a given $k$ is posed by the number of employed elements in the layer. In fact, increasing the number of elements in the layer resulted in enhanced optimal value ranges as seen in Fig. 6.6. Additionally, the rapidly increasing error after the lower limit of the optimal value range is attributed to the error associated with numerical integration. Furthermore, increasing the discretization within the layer appears to improve the calculated error plateau for both plane wave and source excitation cases. However, in finer meshes within the layer, employing $N_{e\,pml} = 16$ and $N_{e\,pml} = 32$, the consistent reduction in the calculated error plateau reaches a halt, suggesting that the error introduced by the discretization in the computational region becomes increasingly dominant.

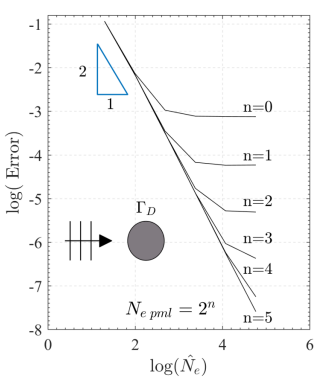


**(i)** Soft scatterer $\Gamma_s \equiv \Gamma_D$

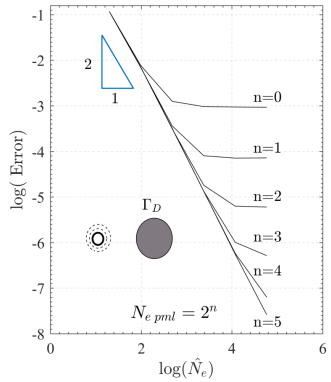


**(ii)** Hard scatterer $\Gamma_s \equiv \Gamma_N$

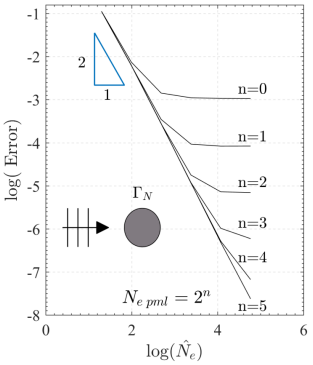


**(iii)** Soft scatterer $\Gamma_s \equiv \Gamma_D$

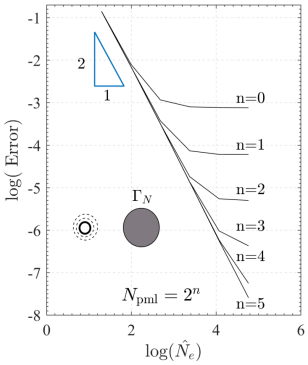


**(iv)** Hard scatterer $\Gamma_s \equiv \Gamma_N$

**Figure 6.7** Calculated error of the scattered field by circular body, $ka = 3$, in the case of incident plane waves. Results for various normalised PML thickness values and increasing PML discretisation

The above observation is verified by the convergence of the method. For the previous cases, log-log plots of the $L_2$ relative error norm, against an increasing number of elements per wavelength are shown in Figs. 6.6 and 6.7 for $ka = 1$ and $ka = 3$, respectively, for PML thickness $k\theta_l = 10^{-4}$ within the established optimal range. Notably, the chosen value of normalised thickness corresponds to an extremely thin layer compared to wavelength as it holds $\theta_l = \lambda/62800$ $[m]$. It is seen that, by refining the mesh in the computational region, the error introduced by the PML discretisation becomes dominant. However, increasing the number of elements within the layer further reduces the error and recovers the theoretically expected convergence rate, which for linear elements is $\|\varphi^h - \varphi\| < C(\tilde{N}_e)^{-2}$ . The verified theoretical convergence is depicted by the slope slope 2:1 is shown in Figs. 6.6 and 6.7. The convergence rate depends on both the computational region discretisation and the refinement within the layer. The fact that the effectiveness of the singular PML is independent of the employed mesh structure and requires no *a priori* tuning, as opposed to polynomial choices for the absorbing function, in conjunction with the above results, suggests that a required level of accuracy can be achieved with little effort. Additionally, the calculated optimal range allows

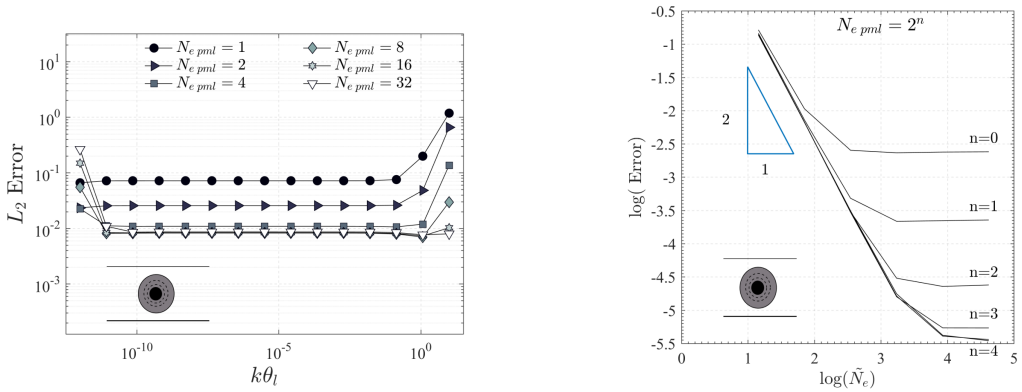


**(i)** Parametric PML thickness study $\Gamma_s \equiv \Gamma_D$ **(ii)** Convergence $\Gamma_s \equiv \Gamma_D$

**Figure 6.8** Radiating field outside a circular scatterer in a planar waveguide, for $ka = 1$. (i) Parametric study of the calculated error for a range of normalised PML thickness values and increasing PML discretisation in the waveguide environment. (ii) Calculated error of the scattered field by circular body, against the number of elements per wavelength, and for increasing number of elements employed in the PML.

for a layer thickness value that is orders of magnitude smaller than the examined wavelength, and thus, the present method does not result in an excessive augmentation of global FEM matrices.

Next, the radiating field from a point source in a waveguide is considered. In absence of analytical solutions for the scattering problem in simple waveguides featuring an inclusion, we employ a radiating solution produced by a line source to compute the Dirichlet data on the boundary of a fictitious scatterer enclosing the source. We consider the unbounded homogeneous waveguide with width h = 10 in $\Omega = [-\infty, \infty] \times [-5, 5]$ with imposed homogeneous Neumann conditions on the top and bottom planar boundaries. The analytical solution of the incident wave field is expressed by normal mode series, and the vertical structure of the modes corresponding to the eigenvalues $k_n$ is chosen as $Z_n(z) = \cos(k_n(z + \mathrm{h}/2))$ in order to satisfy the Neumann conditions on the planar boundaries. Details are provided in Appendix B .The employed series can be truncated, keeping the propagating and a number of evanescent modes sufficient for rapid convergence in the whole region outside a small ball in the vicinity of the line source, i.e. $kr = \sqrt{(x_1 - x_0)^2 + (x_2 - y_0)^2}$. Assuming the presence of a circular scatterer with center $(x_0, y_0)$ enclosing the line source, boundary data are calculated at $r = a$, the scatterer boundary. The computed PML-FEM solution for the waveguide with imposed Dirichlet condition is compared with a seni-analytical solution (see Appendix B ). Results are obtained in the truncated domain $\Omega_s = [-\infty, \infty] \times [-5, 5]$ for $ka = 1$, and the effect of normalized PML thickness is initially examined in Fig. 6.6. Again, a range of optimal layer thickness values is observed, which is now $10^{-10} \leqslant k\theta_l \leqslant 10^{-1}$. Similar to the previous example, the theoretical rate of convergence is revealed by increasing the number of elements in the PML region.

## 6.3 PML-FEM Applications

The presented PML-FEM strategy will be initially implemented in the study of linear water wave propagation phenomena in a mildly sloping ocean environment. The modified-mild slope equation (MMSE), as presented will be employed for the formulation of the combined refraction-diffraction water wave problem in the truncated region of interest. The numerical solution will be compared against a well-known benchmark case of diffraction by an elliptic shoal superimposed over a sloping bottom. Next, the capabilities of the computational tool will be demonstrated for the case of a single as well as multiple bottom founded cylinders. Subsequently the numerical solution of the acoustic scattering problem by an elliptic obstacle in the complex ocean waveguide will be considered.

### 6.3.1 Combined Refraction-diffraction of Linear Water waves

#### Propagation over an elliptic shoal

Assuming only a mildly sloping seabed, the Mild Slope Equation (MSE) is a classical model, obtained by integration over the water depth leading to a dimensionality reduction of the 3D water wave problem; see e.g., Ding et al. (2019). An enhanced version of the above model is the Modified Mild Slope equation (MMS), presented by Massel (1993) and Chamberlain and Porter (1995). This model is able to account for higher-order effects involving the gradients of the depth function. The latter elliptic model, supplemented by appropriate conditions at fixed boundaries and the description of the incident wave field and/or radiation conditions at open boundaries, is commonly applied to study wave transformations in coastal regions and in harbour design. In this case, the considered marine environment is composed of a layer of inviscid and irrotational fluid bounded above by a free surface and below by a rigid, impermeable bottom.

The MMS model featuring the unbounded PML will be tested against the laboratory data concerning monochromatic wave propagation over a submerged elliptic shoal superimposed over a sloping seabed, presented in Berkhoff et al. (1982) (see also Dingenmanns (1997)). The elliptic shoal presents a standard benchmark problem for the validation of numerical schemes aiming in the accurate prediction of combined refraction-diffraction phenomena. We follow the analysis presented in Sections 6.1.1 and 6.2.1 for the case of a mildly sloping bathymetry supporting a localised, submerged scatterer. A monochromatic wave with period $T = 1\,\mathrm{s}$, and initial wave amplitude $a_0 = 2.32\,\mathrm{cm}$ is allowed to propagate parallel to the x-axis in angle $\theta = 20^\circ$ with respect to the minor axis of the elliptic shoal. The underlying plane slope is given

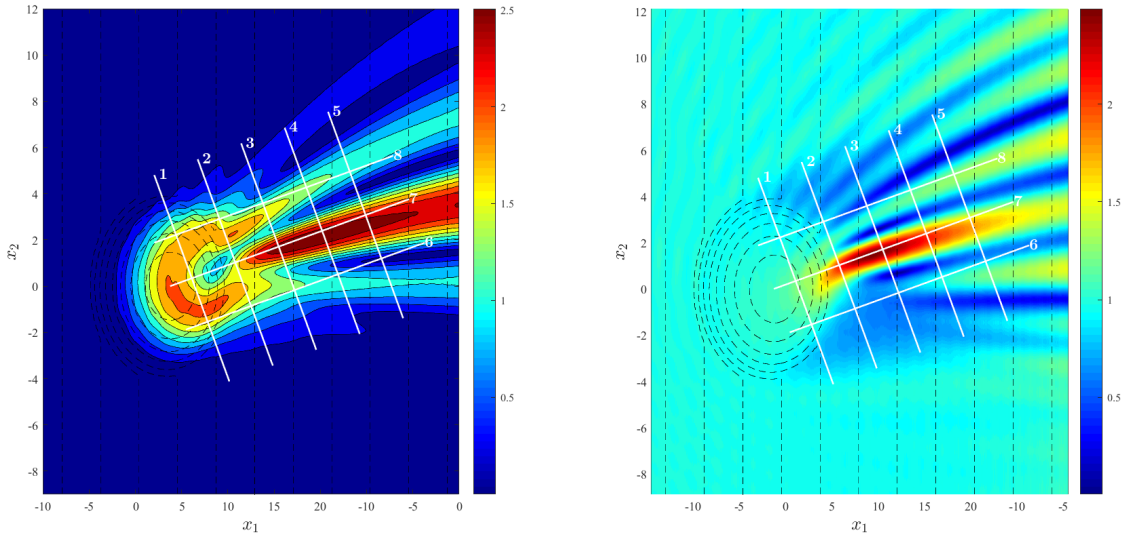


**(i)** Modulus of the diffracted wave field. **(ii)** Modulus of the diffracted wave field.

**Figure 6.9** Calculated solutions by means of the PML-FEM scheme. The sections corresponding to the experimental setup in Berkhoff et al. (1982) are indicated by solid lines

by,

$$h_i(x_1) = \begin{cases} 0.45\,\mathrm{m}, & x_1 < -5.85\,\mathrm{m}, \\ 0.45 - 0.02(5.85 + x_1)\mathrm{m}, & -5.85 \leq x_1 \leq 14.15\,\mathrm{m}, \\ 0.45\,\mathrm{m}, & x_1 > 14.15\,\mathrm{m}. \end{cases} \tag{6.28}$$

The localised elliptic shoal, seen as a disturbance on the background bathymetry is described as,

$$h_d(\mathbf{x}) = \begin{cases} 0\,\mathrm{m}, & (x_1/3)^2 + (x_2/4)^2 > 1, \\ 0.3 - 0.5\sqrt{1 - (x_1/3.75)^2 - (x_2/5)^2}\mathrm{m}, & (x_1/3)^2 + (x_2/4)^2 > 1. \end{cases} \tag{6.29}$$

It is reminded that the MMS Eq. (6.2) is a quasi linear elliptic equation with the effective wavenumber dependent on the depth function through the dispersion relation. The bathymetric profile, defined as the superposition of Eqs. (6.28) and (6.29), satisfies the restrictions imposed on the coefficients of the MMS in order to preserve solution analyticity within the PML. The layer is used to truncate the computational region at and hence the depth function is kept constant in the vertical PML regions. In the horizontal PML regions the depth function exhibits variation only along the coordinate, remaining constant in the direction perpendicular to the horizontal boundaries. The employment of the modified mild slope equation for modelling combined refraction-diffraction phenomena subscribes to the limitations of small amplitude

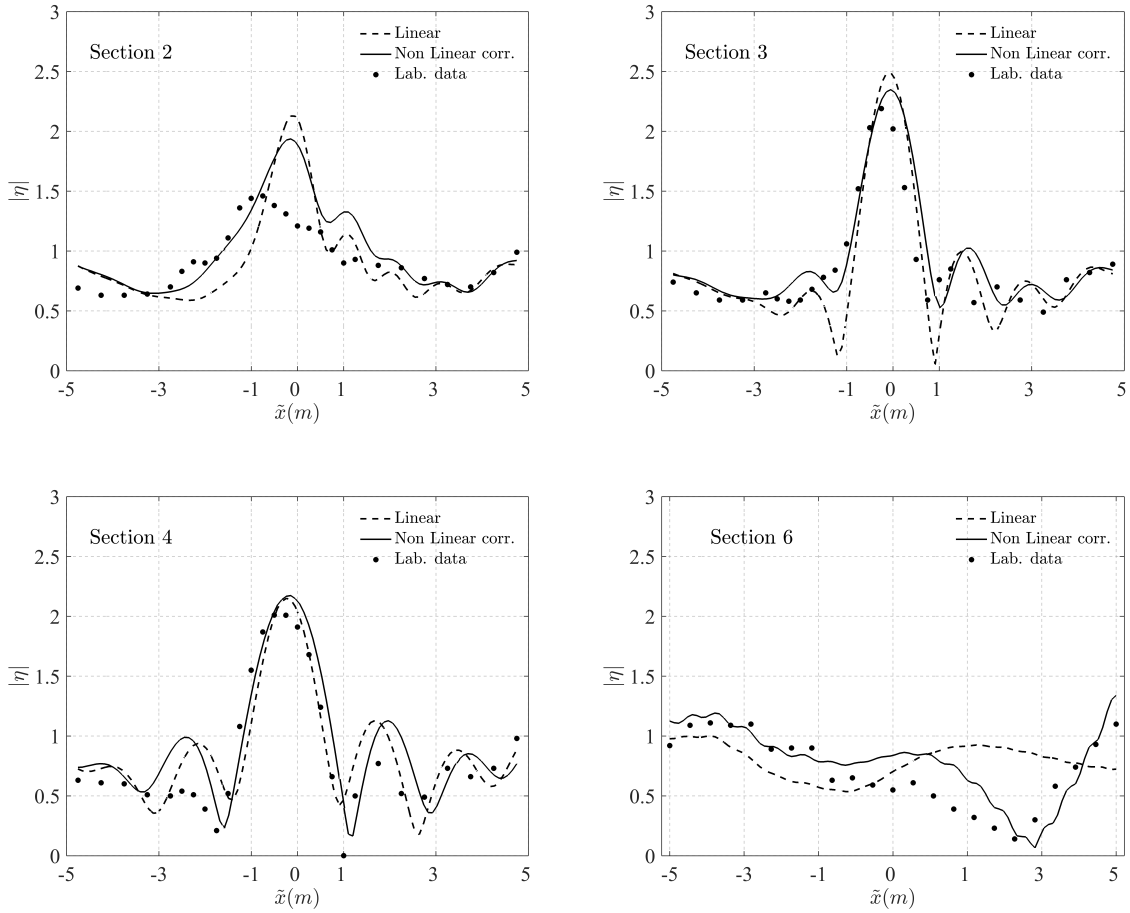


**Figure 6.10** Normalised amplitude on selected sections over the elliptic shoal. Comparison of the present PML-FEM solution, shown by dashed line, against the experimental data denoted by dots. In the same plots the solution featuring the amplitude corrected dispersion relation are shown by using a solid line

water wave theory, which struggles to capture the complex diffraction pattern behind the elliptic shoal. For the numerical experiment a PML thickness $k\theta_l = 4.210^{-4}$, corresponding to the established optimal range is used and 16 line segments were employed for the discretisation of the absorbing layer, while A total of $1.2 \times 10^6$ degrees of freedom were used to ensure the convergence of the present numerical solution in this example.

The diffracted and total wave potential moduli, for the case of the wavenumber determined by the dispersion relation of linearized water waves are plotted in Fig. 6.9. In particular, in Fig. Fig. 6.9(i), the diffracted wavefield solution is illustrated which compares well with similar solutions from the literature (e.g.,Panchang et al. (1991), Belibassakis et al. (2001)), exhibiting smooth isolines for the modulus, suggesting that outgoing solutions are properly attenuated by the present PML model. As expected, due to its inability to account for non-linear processes such as energy dissipation mechanisms the MMS model overestimates the wave amplitude

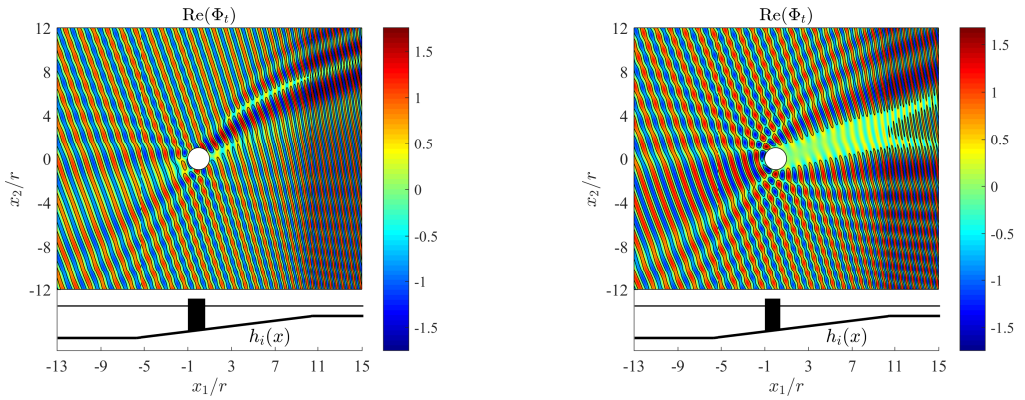


**(i)** Neumann boundary condition on $\Gamma_D$ **(ii)** Dirichlet boundary condition on $\Gamma_D$

**Figure 6.11** A single vertical cylinder with rigid walls over a linear bottom slope for the case of an incoming, incident wave of nondimensional frequency $\omega^2 h g^{-1} = 1.81$ and angle of incidence $\theta = 20°$.

behind the shoal (sections 2, 3 and 4) while it attenuates the solution faster as we move away from the shoal. Next, the computed wave amplitude for various sections is compared against the experimental data in Fig. 6.10, for sections 2-4 and 6. Although present results corresponding to linear solution shown by dashed lines reproduce fairly well the experimental measurements, an updated prediction is also shown in Fig. 6.10 based on the work of Kirby and Dalrymple (1986) who proposed a correction of the wavenumber-parameter of the mild-slope equation in order to also take into account amplitude effects at first-order, as follows,

$$\omega^2 = gk(1 + (kA)^2 f_1 \tanh^5(kh)) \tanh(kh + kA)\, f_2, \tag{6.30}$$

where $f_1 = (\cosh(4kh) + 8 - 2\tanh^2(kh))(8\sinh^4(kh))^{-1}$ and $f_2 = (kh/\sinh(kh))^4$ The above amplitude-dependent dispersion relation generates results that compare more favourably with measured data as shown in Fig. 6.10 by using solid lines. In particular, a number of 5 consecutive iterations were performed updating the predicted wave amplitude and the wavenumber parameter; see also Panchang et al. (1991)). The nonlinear correction provides better matching of the results with experimental data, particularly concerning the peak amplitude values for sections 2, 3 and 4 and a marked improvement on the solution at section 6.

### 3D Scattering over an elliptic shoal - multi-modal vertical expansion

As discussed in Section 6.2.2, the unbounded PML is adapted to accommodate the proposed intermediate depth analysis featuring the multi-modal vertical expansion for the velocity potential.

To this end, the Berkhoff shoal case is once again considered. Revisiting the weak problem Eq. (4.33), it is reminded that the calculation of the incident $\phi_i$ wavefield over the background bathymetry $h_i$ Eq. (6.28) precedes the 3D diffraction problem. The computational domain is

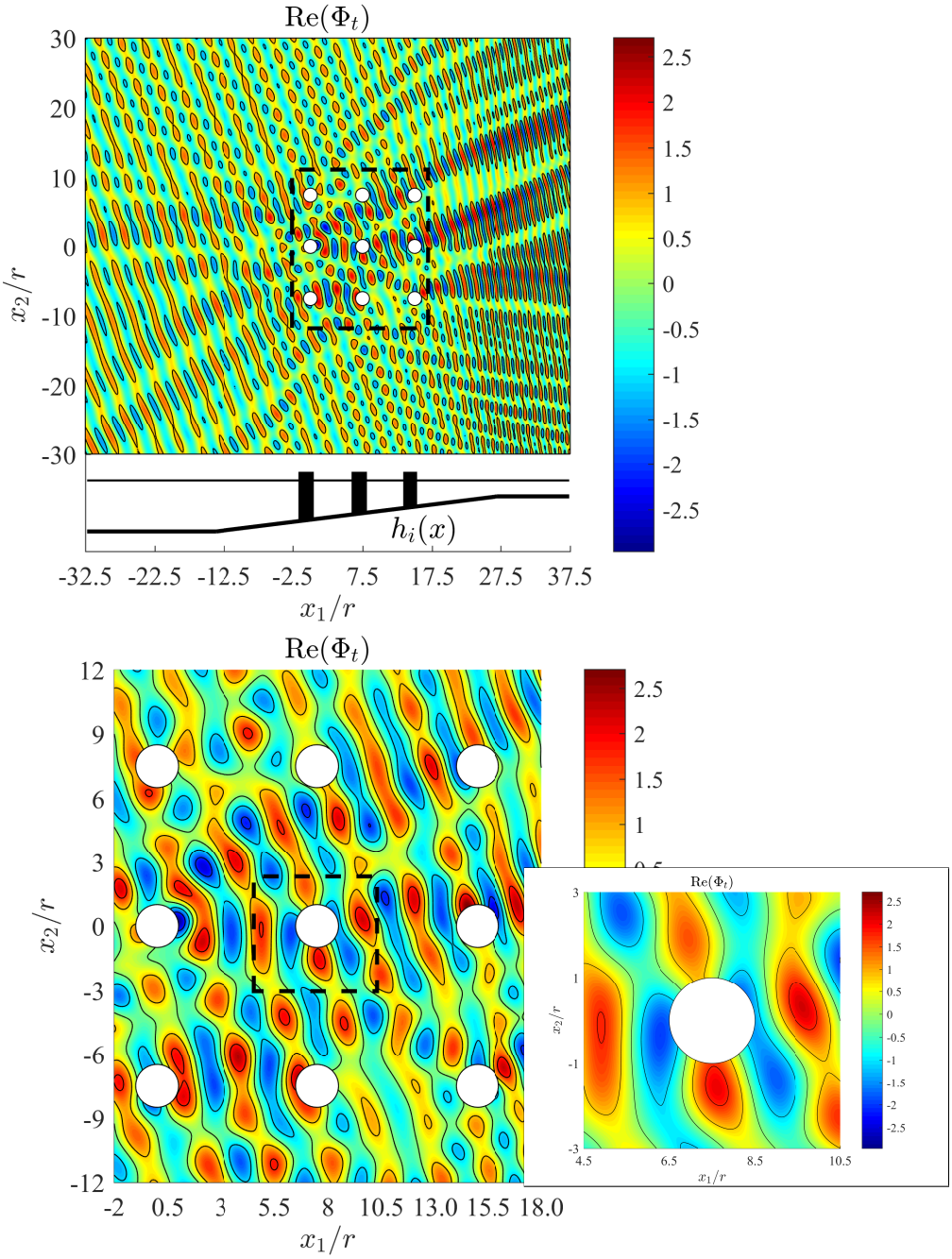


**Figure 6.12** Array of vertical cylinders with rigid walls over a linear bottom slope for the case of an incoming, incident wave of nondimensional frequency $\omega^2 h g^{-1} = 1.81$ and angle of incidence $\theta = 20°$.

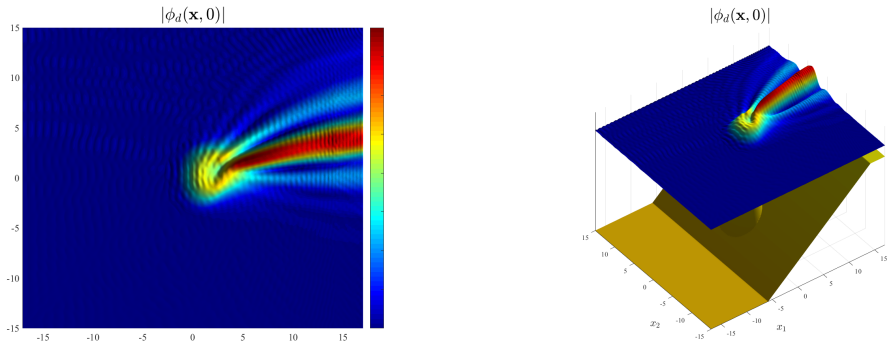


**(i)** Modulus of diffracted solution $\phi_d$. **(ii)** 3D representation of the solution.

**Figure 6.13** Calculated diffracted solution by an elliptic shoal and $N_f = 8$

discretised with elements Eq. (5.14), while in the PML region matrices Eq. (6.25) are employed. In Fig. 6.13 the diffracted solution over the elliptic shoal, with $N_f = 8$ modes in the vertical expansion is found is excellent agreement. For the above results, a layer of thickness $\theta_\ell = 10^{-5}$ and 8 segments is employed.

### Diffraction by an array of vertical cylinders over variable bathymetry

The accurate prediction of wave transformations and induced loads in the presence of man-made structures or physical formations finds several engineering applications. In this subsection, the multiple scattering of an array of bottom-founded cylinders over a mildly sloping seabed is considered. The bodies extend along the water column. For the following analysis, the same bathymetric profile, defined by Eq. (6.28), i.e. a seabed with constant slope 2% is used. An oblique incident wavefield with nondimensional frequency $\omega^2 h g^{-1} = 1.81$, propagating from the deeper water region, is refracted over the sloping seabed topography and interacts with a single bottom founded cylinder with circular cross section. As in the prequel, the numerical solution for the diffracted wavefield $\varphi_d$ is derived by means of the reduced MMSE Eq. (6.3). Use is made of condition Eq. (6.5) on the scatterer surface boundary and the propagating wavefield $\Phi_i$ over Eq. (6.28). Again, a PML enclosing the region of interest, defined in Eq. (6.14), models the absorption of wave energy reaching the exterior termination boundary. Figure 6.11, depicts the real part of the total wave potential field for the cases of imposed Neumann and Dirichlet conditions on the scatterer boundary. As in previous case, a Delaunay-uniform triangular hybrid mesh is employed and as before, the thickness of the employed PML is set to $k\theta_l = 4.210^{-4}$, with 16 line segments in the direction normal to the layer boundary. In this case, a total of 90163 *dofs* were employed for convergence. The drawn axes are normalized with respect to the cylindrical scatterer (pillar) radius. The plotted solutions show no contamination from spurious numerical reflections, suggesting once again the effectiveness of the employed singular PML. The total wavefield is refracted as it propagates

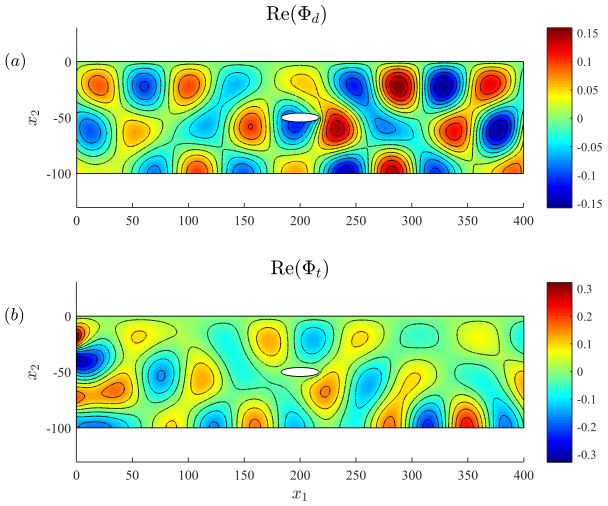


**Figure 6.14** Real part of the scattered field and total wavefield solution in the case of an acoustically soft body (Dirichlet boundary condition) with elliptic boundary, for $kA = 1.7$

towards shallower regions, with the wavelength decreasing up to the constant shallow depth limit. Next, the robustness of the present model in multiple scattering problems within variable bathymetry regions is demonstrated. Figure 6.12 depicts the complex total wavefield, resulting from the interaction of the same oblique, incident wave as in the previous example with the same sloping bathymetry and an array of nine bottom founded cylindrical scatterers with circular cross section. The layer thickness remains the same as in the previous example. The entire domain is shown in the top of Fig. 6.12 , excluding the attenuating layer. The complex amplified wavefield patterns that appear in the vicinity of the array, is shown at the bottom of the figure with a separate focus illustrating the satisfaction of the imposed zero Neumann conditions on the central scatterer boundary.

### 6.3.2 Ocean acoustics

Here, a homogeneous waveguide with planar boundaries $\Omega_s = [0, 400\text{m}] \times [100m, 0]$ is considered excited by a line source located at $(0, 10m)$. The acoustic medium in this example is water and the phase speed is $c = 1500\,\text{m}\,\text{s}^{-1}$. The scattering field from an elliptic body with major and minor axis $A = 16\,\text{m}$ and $B = 4\,\text{m}$ respectively in the middle of waveguide is considered Figs. 6.14 and 6.15. The elliptic geometry of the acoustic scatterer was chosen to both illustrate the capability of the finite element mesh to capture curved boundaries and to simulate common ocean underwater vehicle shapes. Solving the Helmholtz equation, Eq. (6.10), defined on the vertical plane, and forced by a monochromatic point source yields the scattered field solution s. Moreover, the conditions Eq. (6.7) and the PML Eq. (6.14) modelling absorption of wave energy reaching the termination boundaries at the lateral edges of the domain, $x = 0\,\text{m}$and $x = 400\,\text{m}$ are employed. The boundary conditions, supplementing the hydroacoustic problem in the

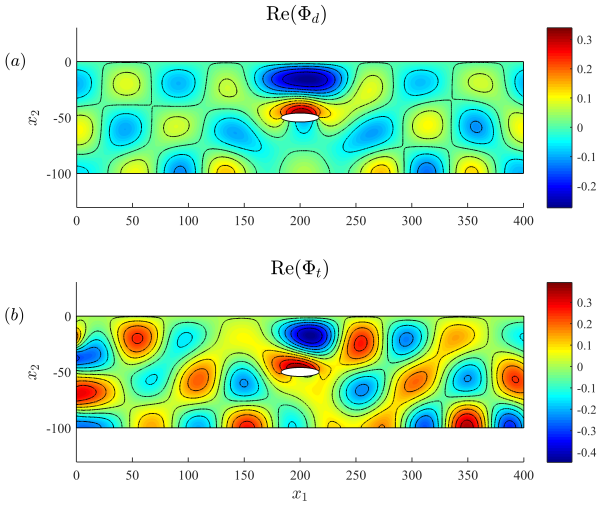


**Figure 6.15** Real part of the scattered field and total wavefield solution in the case of an acoustically hard body (Neumann boundary condition) with elliptic boundary, for $kA = 1.7$

waveguide correspond to a free upper surface boundary and an acoustically hard, impermeable sea bottom. The real parts of the diffracted and total acoustic wavefields for the cases of an acoustically hard and soft scatterer boundary, are shown in Figs. 6.14 and 6.15, for $kA = 1.7$. PML regions with thickness $k\theta_l = 10^-6$ are positioned at the lateral domain boundaries, while 16 line segments along each region are employed. A total of 133856 *dofs* are employed for this example. It is illustrated that the present PML-FEM strategy is able to handle arbitrary scatterer shapes, with the tradeoff being the required h-refinement to handle complex geometries. Moreover, it is clearly observed with the aid of the contour plots of the diffracted wavefield in Figs. 6.14 and 6.15 that the boundary conditions on the surface of the body are satisfied, and although this test case is a rather simplified example, the present method is directly applicable to more realistic cases in general stratified environments and mixed–type boundary conditions on the surface of the scatterer(s).

# Chapter 7

# Wave-Structure coupling

Wave-floating structure coupling is completed via the satisfaction of the pressure equilibrium condition on the restriction of the upper surface in the hydroelastic region. The satisfaction of the latter equilibrium condition leads to the calculation of the complex amplitude functions $c_\ell$ which is achieved by a Galerkin scheme.

## 7.1 Satisfaction of pressure equilibrium

The proposed monolithic approach in wave-structure coupling is completed with the satisfaction of pressure equilibrium condition on the restriction of upper-surface on the hydroelastic region Eq. (1.6). As presented in Chapter 1, the core of the present work is on the decoupling of hydrodynamics and structural motion. The decomposed series of radiation-type problems are posed as to satisfy the kinematic considerations. The final coupling however is completed by calculating the complex amplitudes $c_\ell$

Revisiting the Eq. (1.6), and substituting the expansions for the total velocity potential Eq. (1.17) and Eq. (1.15) results in,

$$\mathcal{L}(\mathbf{w}_\ell, c_\ell) = \mathrm{i}\rho\omega\left(\varphi_S + \sum_{\ell=1}^{\infty} c_\ell \varphi_\ell(\mathbf{x}, z)\right) - \rho g \sum_{\ell=1}^{\infty} c_\ell w_\ell(\mathbf{x}),\ \text{on}\ \Gamma_f^2\ , \tag{7.1}$$

Substituting the reduced elasticity operator $\mathcal{L}(\mathbf{w}_\ell, c_\ell)$ to express the vertical motion of either Kirchhoff (CPT) or Reissner-Mindlin (FSDT) plates accordingly, as presented in Chapter 2, would reduce to the system of equations for equilibrium. In the latter, amplitudes $c_\ell$ are the only remaining unknowns, since the velocity potential functions are calculated as the solutions of the radiation-type subproblems examined in previous chapters and $\mathbf{w}_\ell$ are the eigensolutions of the free structural vibration problems. The satisfaction of Eq. (7.1) leads to the calculation of the complex amplitude functions $c_\ell$ which is finally achieved by a Galerkin scheme. The two theories will be considered separately in the following sections.

### 7.1.1 Pressure equilibrium for CPT

Substituting the irreducible form Eq. (2.14) in Eq. (7.1) straight forwardly results in an expression that involves higher order derivatives of the deflection function. Already computed from the treatment of the inhomogeneous thin plates vibration, the higher-order derivatives are obtained from processing. A more convenient form is derived however by considering that,

$$\begin{gathered} D\nabla^4 w_\ell + \nabla^2 D \cdot \nabla^2 w_\ell + 2\nabla D \cdot \nabla(\nabla^2 w_\ell) \\ -(1-\nu)(\partial_{x_1x_1} D \partial_{x_2x_2} w_\ell - 2\partial_{x_1x_2} D \partial_{x_1x_2} w_\ell + \partial_{x_2x_2} D \partial_{x_1x_1} w_\ell) = \omega_\ell^2 \rho_e \tau(\mathbf{x}) w_\ell. \end{gathered} \tag{7.2}$$

The above holds for every computed eigenpair $\{w_\ell, \omega_\ell\}$ for $\ell = 1, 2, \cdots, N_f$. Exploiting Eq. (7.2) results in the following convenient form,

$$\sum_{\ell=1}^{N_f} c_\ell \left[ (\rho_e \tau(\mathbf{x})(\omega_\ell^2 - \omega^2) + \rho g)\, w_\ell - \mathrm{i}\omega\rho\varphi_\ell(\mathbf{x}, 0) \right] = \mathrm{i}\rho\omega\varphi_S(\mathbf{x}, 0). \tag{7.3}$$

Employing the computed eigenbasis as trial functions and integrating over the plate surface $P$ leads to the following system of equations in terms of the unknown $c_\ell$,

$$\begin{gathered} \sum_{m=1}^{N_f} \sum_{\ell=1}^{N_f} c_\ell \left[ (\omega_\ell^2 - \omega^2) \int_P \rho_e \tau(\mathbf{x}) w_\ell w_m \, dA + \int_P \rho g w_\ell w_m \, dA - \mathrm{i}\omega\rho \int_P \varphi_\ell(\mathbf{x}, 0) w_m \, dA \right] \\ - \int_P \mathrm{i}\rho\omega\varphi_S(\mathbf{x}, 0) w_m \, dA = 0 \end{gathered} \tag{7.4}$$

In matrix notation the above system of $N_f$ equations are re-written as,

$$(\mathbf{A}^{\mathbf{K}} + \mathbf{B}^{\mathbf{K}})\mathbf{c}_\ell = \mathbf{F}^{\mathbf{K}} \tag{7.5}$$

with the matrix coefficients given,

$$\begin{gathered} {\mathbf{A}^{\mathbf{K}}}_{ml} = \int_P (\omega_\ell^2 - \omega^2) \rho_e \tau(\mathbf{x}) w_\ell w_m \, dA, {\mathbf{B}^{\mathbf{K}}}_{ml} = \rho g \int_P w_\ell w_m \, dA - \mathrm{i}\omega\rho \int_P \varphi_\ell(\mathbf{x}, 0) w_m \, dA, \\ {\mathbf{F}^{\mathbf{K}}}_m = \int_P \mathrm{i}\rho\omega\varphi_S(\mathbf{x}, 0) w_m \, dA. \end{gathered} \tag{7.6}$$

The above system is solved to derive the complex amplitude vector $\mathbf{c}_\ell$. Most conveniently, the equation of vertical motion for a thin floating plate Eq. (7.3) and in turn the system Eq. (7.5) are straightforwardly transferred to the 2D case and the motion of a thin plate strip. It is easily noticed that in the 2D case, where the structural motion is described as Eq. (2.27), the corresponding $N_f$ system of equations would involve integrals defined over a single horizontal coordinate, while thickness variations in considered again along a single dimension.

### 7.1.2 Pressure equilibrium for FSDT

The satisfaction of pressure equilibrium condition when a moderately thick plate is considered is slightly more involved that the CPT case, due to the two-field formulation of the Reissner-Minlin model. It is deemed appropriate to address the 2D case, corresponding to the motion of the plate strip first and then present the 3D case.

Considering again the dynamic condition Eq. (2.14) and substituting the reduced elasticity operator with the coupled equations of flexural motion for the strip on $\Gamma_f^2$ Eqs. (2.30) and (2.31) results in the following,

$$-\partial_x \left[\kappa_s G\tau(x)(\,\partial_x w - \theta\,)\right] - \omega^2 \rho_e \tau(x) w = \mathrm{i}\rho\omega\varphi(x,0) - \rho g w, \tag{7.7}$$

$$\kappa_s G\tau(x)\,(\partial_x w - \theta) + \partial_x\,(D\partial_x\theta) + \omega^2 \frac{\rho_e \tau(x)^3}{12}\theta = 0. \tag{7.8}$$

In the above system, Eq. (7.7) expresses the pressure equilibrium while Eq. (7.8) corresponds once again to moment balance on the upper surface of the hydroelastic region. In the inhomogeneous setting the above equations cannot be uncoupled and need to be satisfied simultaneously. To that end the following expansion for the unknown rotation in terms of the computed modal functions $\theta_\ell$ is also employed,

$$\theta(x) = \sum_{\ell=1}^{N_f} d_\ell \theta_\ell(x). \tag{7.9}$$

Thus, substituting the field expansions Eq. (7.8) is written as,

$$\sum_{\ell=1}^{N_f} \left[\kappa_s G\tau(x)\,(c_\ell \partial_x w_\ell - d_\ell\theta_\ell) + \partial_x\,(D d_\ell \partial_x \theta_\ell) + \omega^2 \frac{\rho_e \tau(x)^3}{12} d_\ell \theta_\ell\right] = 0 \tag{7.10}$$

Testing the above equation with the modal functions $\theta_\ell$, reduces the following system of $N_f$ equations,

$$\begin{aligned}\sum_{m=1}^{N_f}\sum_{\ell=1}^{N_f}\Bigg[&-\int_{-L/2}^{L/2} \kappa_s G\tau(x)\,(c_\ell\theta_m\partial_x w_\ell - d_\ell\theta_m\theta_\ell)\;dx - \int_{-L/2}^{L/2}\theta_m\partial_x\,(D d_\ell\partial_x\theta_\ell)\;dx \\ &-\omega^2\int_{-L/2}^{L/2}\frac{\rho_e\tau(x)^3}{12} d_\ell\theta_m\theta_\ell\;dx\Bigg] = 0\end{aligned} \tag{7.11}$$

Performing integration by parts will result in,

$$\sum_{m=1}^{N_f}\sum_{\ell=1}^{N_f}\left[-\int_{-L/2}^{L/2}\kappa_s G\tau(x)\left(c_\ell\theta_m\partial_x w_\ell - d_\ell\theta_m\theta_\ell\right)\,dx + \int_{-L/2}^{L/2}\partial_x\theta_m\left(Dd_\ell\partial_x\theta_\ell\right)\,dx \right.$$
$$\left. + \left[\theta_m d_\ell\left(D\partial_x\theta_\ell\right)\right]_{-L/2}^{L/2} - \omega^2\int_{-L/2}^{L/2}\frac{\rho_e\tau(x)^3}{12}d_\ell\theta_m\theta_\ell\,dx\right] = 0, \tag{7.12}$$

The boundary terms vanish since the computed eigen basis functions $\theta_\ell$ satisfy the free edge condition Eq. (2.32) *a priori*. The remaining terms in the system of equations can be manipulated to derive an expression linking the complex amplitudes $d_\ell, c_\ell$,

$$(\mathbf{B}^M - \omega^2\mathbf{C}^M)\mathbf{d}_\ell = \mathbf{A}^M\mathbf{c}_\ell \tag{7.13}$$

The matrix coefficients are given as,

$$\mathbf{A}^M_{ml} = \textstyle\int_{-L/2}^{L/2}\kappa_s G\tau(x)\theta_m\partial_x w_\ell\,dx, \mathbf{B}^M_{ml} = \int_{-L/2}^{L/2}\left(\kappa_s G\tau(x)\theta_m\theta_\ell + \partial_x\theta_m D\partial_x\theta_\ell\right)\,dx,$$
$$\mathbf{C}^M_{ml} = \textstyle\int_{-L/2}^{L/2}\frac{\rho_e\tau(x)^3}{12}\theta_m\theta_\ell\,dx. \tag{7.14}$$

Next, substituting the modal expansions in Eq. (7.7) with the modal functions results in,

$$\sum_{\ell=1}^{N_f} -\partial_x\left[\kappa_s G\tau(x)(\,c_\ell\partial_x w_\ell - d_\ell\theta_\ell\,)\right] - \omega^2\rho_e\tau(x)c_\ell w_\ell(x) + \rho g c_\ell w_\ell(x)$$
$$= \mathrm{i}\rho\omega\varphi_S(x,0) + \mathrm{i}\rho\omega\sum_{\ell=1}^{N_f}c_\ell\varphi_\ell(x,0) \tag{7.15}$$

Next, testing Eq. (7.7) with the modal functions $w_\ell$ results in the following system of equations,

$$\sum_{m=1}^{N_f}\sum_{\ell=1}^{N_f}\int_{-L/2}^{L/2} -w_m\partial_x\left[\kappa_s G\tau(x)(\,c_\ell\partial_x w_\ell - d_\ell\theta_\ell\,)\right]\,dx - \omega^2\int_{-L/2}^{L/2}(w_m\rho_e\tau(x)c_\ell w_\ell)$$
$$-\int_{-L/2}^{L/2}\mathrm{i}\rho\omega c_\ell w_m\varphi_\ell(x,0) + \rho g c_\ell w_m w_\ell(x) = \mathrm{i}\rho\omega\int_{-L/2}^{L/2}w_m\varphi_S(x,0)\,dx \tag{7.16}$$

An integration by parts can be performed at the first integral in the double summation and satisfies the above expression significantly. The produced boundary term $\left[w_m\left[\kappa_s G\tau(x)(\,\partial_x c_\ell w_\ell - d_\ell\theta_\ell\,)\right]_{-L/2}^{L/2}\right.$ will vanish once again as functions $w_\ell$ satisfy the free edge

condition Eq. (2.33), refining Eq. (7.16) into,

$$\begin{aligned}\sum_{m=1}^{N_f}\sum_{\ell=1}^{N_f}\int_{-L/2}^{L/2}\partial_x w_m\left[\kappa_s G\tau(x)(\,c_\ell\partial_x w_\ell - d_\ell\theta_\ell\,)\right]\,dx - \omega^2\int_{-L/2}^{L/2}(w_m\rho_e\tau(x)c_\ell w_\ell)\,dx\\ -\int_{-L/2}^{L/2}(\mathrm{i}\rho\omega c_\ell w_m\varphi_\ell(x,0)\,dx + \rho g c_\ell w_m w_\ell)\,dx = \mathrm{i}\rho\omega\int_{-L/2}^{L/2} w_m\varphi_S(x,0)\,dx\end{aligned} \tag{7.17}$$

And finally in matrix notation and by employing Eq. (7.13) the following system in terms on the unknown $\mathbf{c}_\ell$ is deduced,

$$(\mathbf{A}+\mathbf{B}-\mathbf{C}(\mathbf{B}^M-\omega^2\mathbf{C}^M)^{-1}\mathbf{A}^M)\mathbf{c}_\ell = \mathbf{F}, \tag{7.18}$$

where the matrix coefficients are now given as,

$$\begin{aligned}\mathbf{A} = -\omega^2\textstyle\int_{-L/2}^{L/2}(w_m\rho_e\tau(x)w_\ell)\,dx + \int_{-L/2}^{L/2}(\kappa_s G\tau(x)\partial_x w_m\partial_x w_\ell + \rho g w_m w_\ell(x))\,dx\\ \mathbf{B} = -\textstyle\int_{-L/2}^{L/2}\mathrm{i}\rho\omega c_\ell w_m\varphi_\ell(x,0)\,dx\mathbf{C} = \int_{-L/2}^{L/2}\kappa_s G\tau(x)\partial_x w_m\theta_\ell\,dx,\\ \mathbf{F} = \mathrm{i}\rho\omega\textstyle\int_{-L/2}^{L/2} w_m\varphi_S(x,0)\,dx\end{aligned} \tag{7.19}$$

Solving the system described by Eq. (7.18) retrieves the complex amplitude functions $\mathbf{c}_\ell$. Subsequently, amplitudes $\mathbf{d}_\ell$ are deduced by Eq. (7.18) and can be used to determine the unknown rotation, Eq. (7.9).

A similar approach is followed for the 2D FSDT finite plate case where the equations expressing vertical equilibrium on the upper surface of the coupling region are,

$$\begin{aligned}\partial_{x_1}\left[\kappa_s G\tau\left(\theta_{x_1}+\partial_{x_1}w\right)\right]+\partial_{x_2}\left[\kappa_s G\tau\left(\theta_{x_2}+\partial_{x_2}w\right)\right]\\ +\omega^2\rho_e\tau w = \mathrm{i}\rho\omega\varphi(x,0)-\rho g w,\end{aligned} \tag{7.20}$$

$$\begin{aligned}\partial_{x_1}\left[D(\partial_{x_1}\theta_{x_1}+\nu\partial_{x_2}\theta_{x_2})\right]+\partial_{x_2}\left[D\frac{(1-\nu)}{2}(\partial_{x_2}\theta_{x_1}+\partial_{x_1}\theta_{x_2})\right]\\ -\kappa_s G\tau\left(\theta_{x_1}+\partial_{x_1}w\right)+\omega^2 I_r(\mathbf{x})\theta_{x_1} = 0,\end{aligned} \tag{7.21}$$

$$\begin{aligned}\partial_{x_2}\left[D(\partial_{x_2}\theta_{x_2}+\nu\partial_{x_1}\theta_{x_1})\right]+\partial_{x_1}\left[D\frac{(1-\nu)}{2}(\partial_{x_2}\theta_{x_1}+\partial_{x_1}\theta_{x_2})\right]\\ -\kappa_s G\tau\left(\theta_{x_2}+\partial_{x_2}w\right)+\omega^2 I_r(\mathbf{x})\theta_{x_1} = 0,\end{aligned} \tag{7.22}$$

Working in a similar manner as in the 1D strip the modal expansions of the unknown deflection are rotations are employed noting that it now holds,

$$\theta_{x_1} = \sum_{\ell=1}^{N_f} d_\ell^{(1)}\theta_{1\ell}(\mathbf{x}), \theta_{x_2} = \sum_{\ell=1}^{N_f} d_\ell^{(2)}\theta_{2\ell}(\mathbf{x}). \tag{7.23}$$

Eqs. (7.21) and (7.22) are tested with the computed modal functions $\theta_{1\ell}$ and $\theta_{2\ell}$ respectively, while pressure equilibrium Eq. (7.20) is tested with $w_\ell$.

*Remark* 17. The process, although more involved, is identical to the one followed for the FSDT strip. Notably integration by parts will reveal terms involving rotations across the tangential direction to the free edge that will eventually vanish due to conditions Eqs. (2.24)–(2.26).

The reduced coupled systems link $d_\ell^{(1)}, d_\ell^{(2)}$ and $c_\ell$, and thus reduces Eqs. (7.20)–(7.22) to the following systems of equations in terms of the complex amplitudes,

$$\begin{aligned} \mathbf{A}_1 d_\ell^{(1)} + \mathbf{B}_1 d_\ell^{(2)} + \mathbf{C}_1 \mathbf{c}_\ell &= \mathbf{F} \\ \mathbf{A}_2 d_\ell^{(1)} + \mathbf{B}_2 d_\ell^{(2)} + \mathbf{C}_2 \mathbf{c}_\ell &= 0 \\ \mathbf{A}_3 d_\ell^{(1)} + \mathbf{B}_3 d_\ell^{(2)} + \mathbf{C}_3 \mathbf{c}_\ell &= 0 \end{aligned} \tag{7.24}$$

,

# Part III

# Numerical Results

# Chapter 8

# Numerical Results in the 2D waveguide

Focusing on the hydroelastic problem formulated in the 2D waveguide, the method developed in the previous chapters is investigated in a series of numerical experiments. Moreover, extensive comparisons with results from the literature are presented for validation purposes.

The performance and accuracy of the present method is examined in a series of 2D cases. First, the hydroelastic response of a thin, homogeneous plate and the corresponding wave field transformations in an example configuration featuring an abruptly varying seabed, are considered in order to illustrate the key features of the method in isolation of other homogeneity, i.e. variable thickness. Next, comparisons with published results for different configurations and a range of parameters are carried out. Considered cases involve both Kirchhoff and Mindlin plate models over constant (deep, intermediate and shallow water cases) as well as seabed and thickness variability. Throughout this chapter and for all presented examples, the water density is $\rho_w = 1025\,\mathrm{kg\,m^3}$, unless stated otherwise, and the acceleration of gravity $g = 9.81\,\mathrm{m\,s^2}$.

## 8.1 The case of a uniform, thin plate over arbitrarily varying seabed

The case of a shoaling bathymetric profile is initially considered in order to illustrate the full features of the proposed method. In the following example, the fluid region is defined as $\Omega = [-230\,\mathrm{m}, 230\,\mathrm{m}] \times [-h(x), 0]$ with the bathymetric profile expressed for simplicity as as

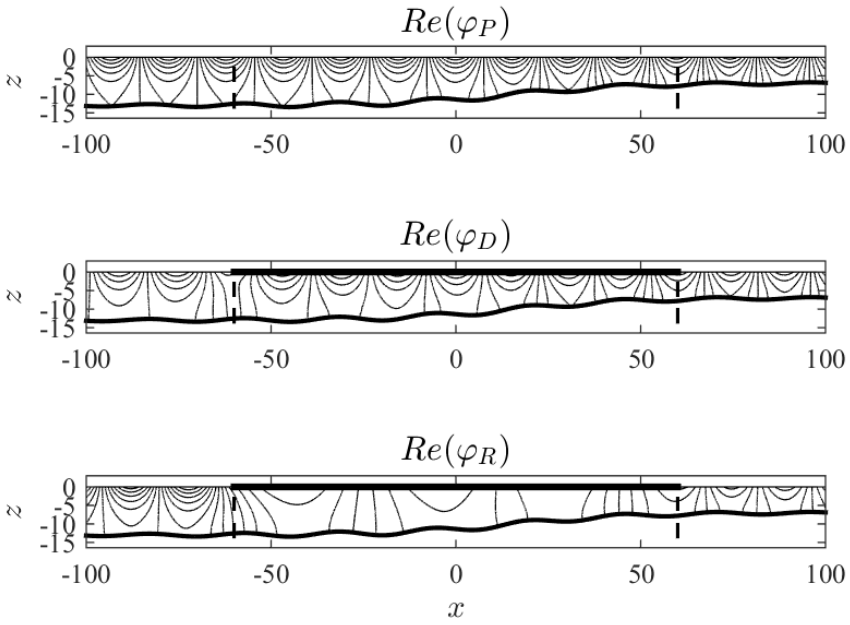


**Figure 8.1** Real part of the solutions to the component propagation (top), diffraction (middle) and radiation problems (bottom)

the superposition $h(x) = g_1(x) + g_2(x)$, with

$$g_1(x) = \frac{(h^- + h^+)}{2} - \frac{(h^- - h^+)}{2} \tanh\left(2\pi\left(x/205 + 0.0014\right) - 0.5\right) \tag{8.1}$$

$$g_2(x) = 0.7 \sin\left(k_b x\right) \exp\left(-10^{-4} x^2\right) \text{ where } k_b = 2\pi/\lambda_b \text{ and } \lambda_b = 25.625\,\text{m} \tag{8.2}$$

The profile corresponds to a corrugated, shoaling region seen in Fig. 8.1. In the above, $h^+ = 13\,\text{m}$ and $h^- = 7\,\text{m}$ correspond to the constant depth data at the left and right half-strips respectively. The homogeneous floating structure is extending in $[-L/2, L/2]$ with $L = 120\,\text{m}$ being the length of the plate. An incident wave field propagating towards the positive x direction with frequency $\omega = 1.4\,\text{s}^{-1}$ is considered to excite the floating structure. Since $k^- h^- = 2.6248$ and $k^+ h^+ = 1.5348$, the set example falls outside the limits of either deep or shallow water wave theory. The thickness of the employed structure is assumed constant at $\tau = 1\,\text{m}$, suggesting a thickness-to-length ratio $\tau/\lambda = 0.0083$ well within the range of application of the Classical Thin Plate theory, allowing the plate to be modeled under the Kirchhoff-Love assumptions. The material properties of the structure are taken as $E = 5\,\text{GPa}$, $\nu = 0.3$ and density $\rho_e = 922.5\,\text{kg}\,\text{m}^3$, corresponding to sea ice (see for example Bennetts et al. (2007); Porter and Porter (2000); Smith and Meylan (2011) and others).

The proposed method, keeping $N_m = N_f = 15$ number of terms in the series expansions Eqs. (1.14) and (1.15) to ensure convergence, is employed for the calculation of the hydrody-

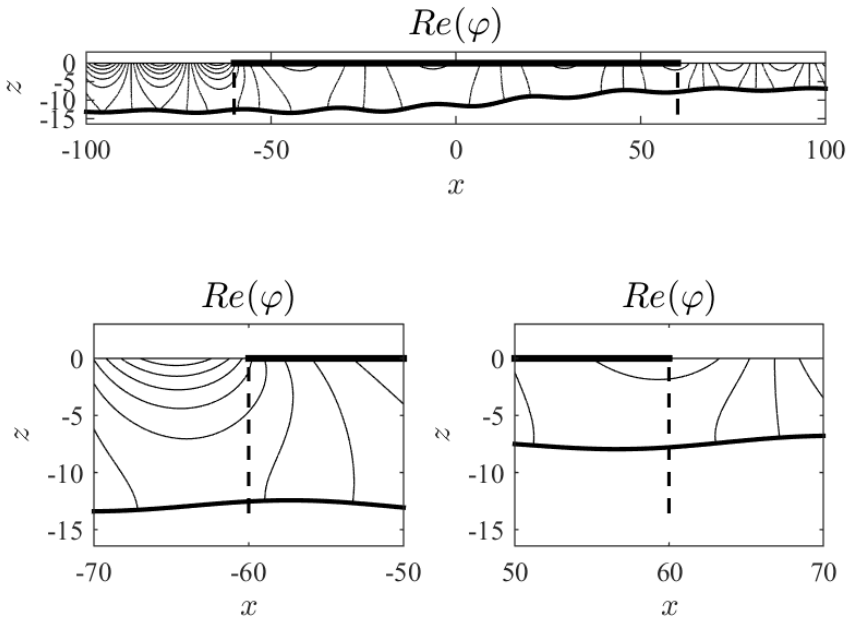


**Figure 8.2** Real part of the total solution (top), fictitious interfaces between subregions (bottom)

namic characteristics of the wave-field and the response of the structure. The latter suggests the employment of 13 evanescent modes in the vertical hydrodynamic expansion, in addition to the propagating and sloping bottom modes and 13 flexural modes in the elastic expansion, in addition to rigid body modes. Linear Lagrange elements are used for the representation of the discrete systems Eqs. (5.3) and (5.17) corresponding to the transmission and radiation-type problem respectively, while a total of 44 elements per mean incident wavelength are employed. Results convergence was assessed in the sense that consecutive mesh refinements rendered negligible residuals. In Fig. 8.1 the equipotential lines, corresponding to the real part of the computed solutions of the component hydrodynamic problems are shown, while in Fig. 8.2, the corresponding plot for the composed total velocity potential is drawn. At the bottom of Fig. 8.1, close-ups of the wave-field solution at the edges of the plate are given. Equipotential lines in the above figures are seen to intersect the bottom normally, satisfying the Neumann condition on the sloping seabed.

Moreover, the matching of the velocity potential and flux on the fictitious interfaces between subregions, depicted by dashed lines, is excellent for radiation-type and total wave-field solutions, as illustrated in Fig. 8.2, suggesting that the weak satisfaction of transmission conditions adequately captures local scattering phenomena at the plate edges and the employed vertical expansion satisfies energy flux conservation across interfaces. Next, the normalized to the wave amplitude modulus of the plate deflection, and the normalized absolute moment and shear force for the given example are plotted in Fig. 8.3. Notably, the satisfaction of the zero

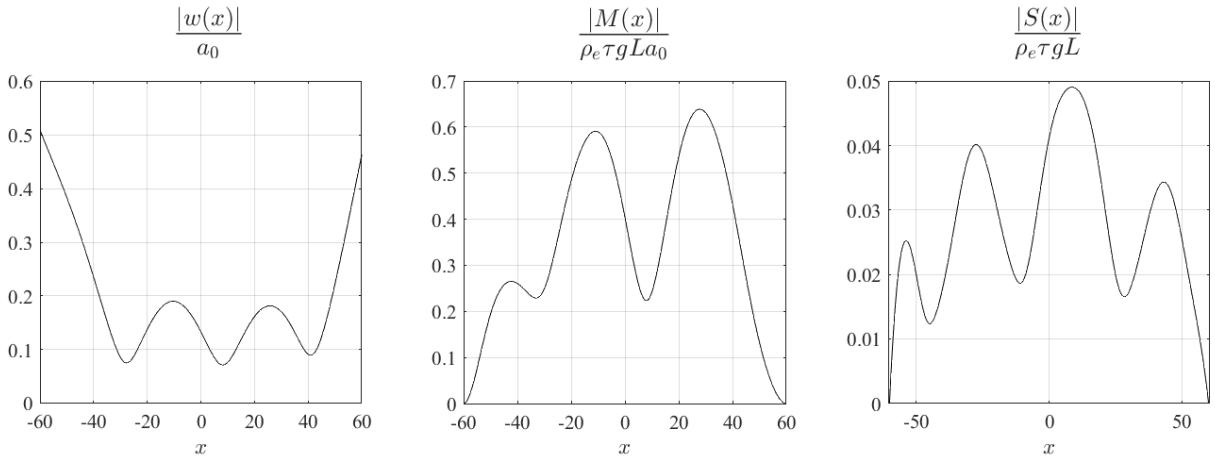


**(i)** Non-dimensionalised moduli of plate deflection (left), bending moment (middle), shear force (right)

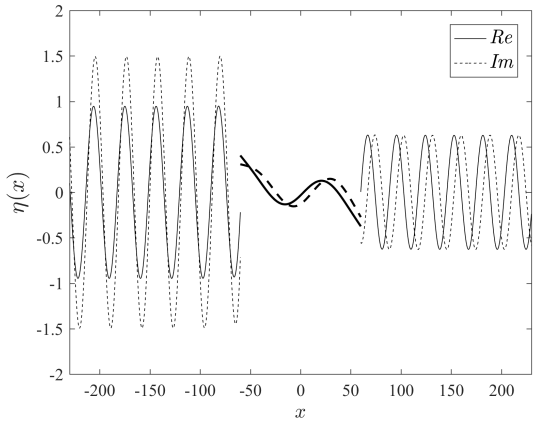


**(ii)** Real and imaginary parts of free surface elevation and plate deflection

**Figure 8.3** Plate response and upper surface elevation

moment and zero shear conditions at the free edges of the plate, observed at Fig. 8.3(i), is *a priori* guaranteed by the employment of the *in vacuo* modes, which is an advantage of the approach. The latter becomes more apparent in the 3D extension of the proposed method, where the satisfaction of plate edge conditions is computationally intensive and not trivial in general geometries.

Finally, in Fig. 8.3(ii) the real and imaginary parts of the solution for the normalized with respect to incident amplitude free surface elevation $\eta(x) = \mathrm{i}\omega g^{-1}\varphi(x,0)\,,\ x \in (\mathrm{x}_1, a_1)\cup(a_2, \mathrm{x}_2)$ and plate deflection $w(x)\,, x \in (a_1, a_2)$ are plotted.

Next, in order to explore the effects of modal truncation in the expansion Eq. (1.14), the computed amplitudes $c_\ell$ are considered for the above example. In Table 1, the first 11 moduli of the computed mode amplitudes $c_\ell$ are presented. For the presented computations, $N_m = 15$

| | $\lvert c_\ell \rvert$ | | | | | | | | | | |
|---|---|---|---|---|---|---|---|---|---|---|---|
| $\ell:/N_f:$ | 1 | 2 | 3 | 4 | 5 | 6 | 7 | 8 | 9 | 10 | 11 |
| 15 | 13.7960 | 41.3947 | 20.6474 | 51.7936 | 23.5340 | 5.9249 | 0.4174 | 0.6211 | 0.0593 | 0.1287 | 0.0165 |
| 20 | 13.7961 | 41.3947 | 20.6474 | 51.7931 | 23.5341 | 5.9247 | 0.4174 | 0.6211 | 0.0593 | 0.1286 | 0.0165 |
| 30 | 13.7961 | 41.395 | 20.6475 | 51.7927 | 23.5339 | 5.9245 | 0.4174 | 0.6210 | 0.0593 | 0.1286 | 0.0165 |

**Table 8.1** Non-dimensional complex amplitudes

vertical modes are employed for the hydrodynamic series expansion while a varying number of flexural modes $N_f = 15, 20, 30$ in the modal expansion is considered. It is evident, that in the present case, fourth mode (2nd flexural mode) is dominant while after the $8^{\text{th}}$ mode the corresponding amplitudes are less than 1% of the maximum mode amplitude $|c_4|$, which is indicative of the rapid convergence of the modal expansion.

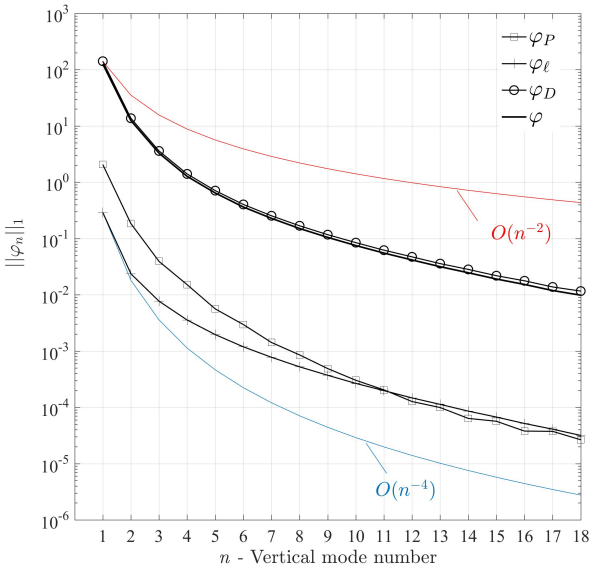


**Figure 8.4** Integrated moduli of the modal amplitude functions for component hydrodynamic solutions vs mode number

Subsequently, in Fig. 8.4, the integrated over the spatial domain moduli of the complex amplitude functions $\|\varphi_n\|_{1,(x_1,x_2)} = \int_{x_1}^{x_2} |\varphi_n(x)|\, dx$ , calculated for the component hydrodynamic problems (incident $\varphi_P$, diffraction $\varphi_D$ and $\ell^{\text{th}}$ radiation $\varphi_\ell$ wave fields) as well as the total solution amplitudes, calculated as $\boldsymbol{\varphi} = \boldsymbol{\varphi}_P + \boldsymbol{\varphi}_D + \sum_{\ell=1}^{N_f} c_\ell \boldsymbol{\varphi}_R$ are comparatively plotted. A total of $N_f = 15$ bending modes were employed in the modal expansion of the plate. The $y$-axis is in logarithmic scale while the $x$-axis shows the increasing number of vertical modes $n$. Notably, the modal amplitude decay rate for the propagating wavefield $\varphi_P$ is $\mathcal{O}n^{-4}$, while the corresponding rates of decay concerning the diffraction solution and the $\ell^{\text{th}}$ radiation potential solution $\varphi_\ell$ appear to be smaller $\mathcal{O}n^{-3+\epsilon}$, $\epsilon < 1$. In the case of the incident wavefield $\varphi_P$ over

an abruptly sloping seabed, the above is in agreement with the findings in Athanassoulis and Belibassakis (1999).

In the aforementioned work, it was shown that the enhanced representation for the wave potential, including the additional sloping bottom mode $Z_{-1}$ features an accelerated rate of convergence $\mathcal{O}n^{-4}$ , compared to the standard representation $\mathcal{O}n^{-2}$ that fails to accurately account for bottom slope effects. The inclusion of the additional mode allows for the consistent satisfaction of the bottom boundary condition, ensuring the absolute and uniform convergence up to the boundaries. The reduced order of decay of the modal amplitudes for the radiation-type wavefields and in extend for the total solution is attributed to the weak satisfaction of the interface conditions.

## 8.2 Numerical Validation of the Methodology

For the validation of the proposed methodology, a series of comparisons with results presented in the literature are performed. For the numerical approximations presented in this section by means of the proposed methodology, $N_m = 15$ modes are kept in the vertical expansion, including the additional sloping bottom mode, while $N_f = 15$ bending modes are kept in the deflection representation.

### 8.2.1 Constant depth

#### Homogenous Thin Plate

The hydroelastic response of a homogeneous thin plate over variable bathymetry is initially compared against the results documented in Belibassakis and Athanassoulis (2005). In the latter work, the consistent coupled mode system, proposed by the authors in an earlier contribution, is extended to account for the hydroelastic problem. The analysis is restricted to homogeneous, thin plates and bathymetric variations that are restricted to the plate-covered region. In the following examples, the plate is assumed to extend infinitely in the $y$-direction, undergoing cylindrical bending under harmonic wave action and the length of the plate is $L = 500\,\mathrm{m}$. In the paper, the plate mass effect is considered negligible and ignored, thus the available data for their analysis are limited to the flexural rigidity of the floating body, $D/\rho_w g = 10^5\,\mathrm{m}^4$. The above premise in unphysical is our case and thus, the above set flexural rigidity is assumed to correspond to a body with constant thickness $\tau = 1.3\,\mathrm{m}$ and material characteristics $E = 5\,\mathrm{GPa}$, $\nu = 0.3$ and density $\rho_e = 922.5\,\mathrm{kg\,m^{-3}}$ following Bennetts et al. (2007). The slenderness of the structure falls well within the limits of the classical plate theory while the material characteristics model sea ice. In the examined scenario, the incoming wave frequency is $\omega = 0.4\,\mathrm{s}$ and the constant depth is $h = 10\,\mathrm{m}$, which reduces the depth-to-incident wavelength ratio to $h/\lambda = 0.066$, approximating shallow wave conditions. Comparisons in terms of the normalized plate deflection to the wave height $|w(x)|/2a_0$ and the modulus of

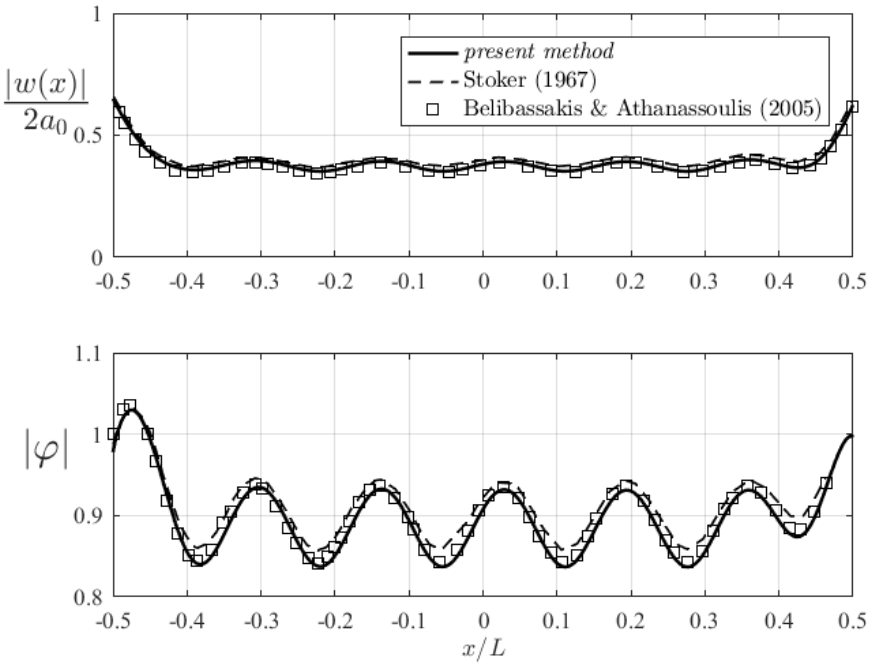


**Figure 8.5** Hydroelastic solution in constant depth and almost shallow water conditions. (a) Normalised deflection to the waveheight (top). (b) Modulus of the velocity potential on the plate. Solid line denotes the present mehtod, dashed line the solution of Stoker's shallow raft model and squared the solution by Belibassakis and Athanassoulis (2005)

the potential on the plate $|\varphi(x, z = 0)|$ are shown in Fig. 8.5. For the discretization of the hydroelastic region, 250 linear Lagrange elements were employed. The above figure illustrates the results of the present method, shown by a solid line, against the hydroelastic CMS solution by Belibassakis and Athanassoulis (2005) and shallow–water thin raft model by Stoker (1967) denoted by a dashed line. The results are found in excellent agreement, verifying the behavior of the proposed method in shallow water conditions. Next, a second case, corresponding to deep water conditions, originally presented in Takagi et al. (2000) is examined. The case explored in was validated against the eigenfunction matching technique by Yoshimoto et al. (1997) and later found in good agreement with the results in Hermans (2003). The examined plate has length $L = 1.4\,\mathrm{m}$ and flexural rigidity $D/\rho_w g = 1.74 \cdot 10^{-3} L^4\,\mathrm{m}^4$, while it floats over constant depth $h = 0.5\,\mathrm{m}$ . The normal incident wave-field has angular frequency $\omega = 4$ m. The plate parameters are chosen as $\tau = 5.2 \cdot 10^{-3}\,\mathrm{m}$, with $E = 5\,\mathrm{Pa}$,$\nu = 0.3$ and density $\rho_e = 922.5\,\mathrm{kg\,m^{-3}}$ to comply with case configuration as discussed in the previous example. In Fig. 8.6, the modulus of the plate deflection normalized with respect to the incident wave height is compared against the results presented in Takagi et al. (2000) denoted with crosses, and once again the results are in very good agreement, indicating that the present method is appropriate for all water-depth conditions. Next, in Fig. 8.7 the proposed method is compared

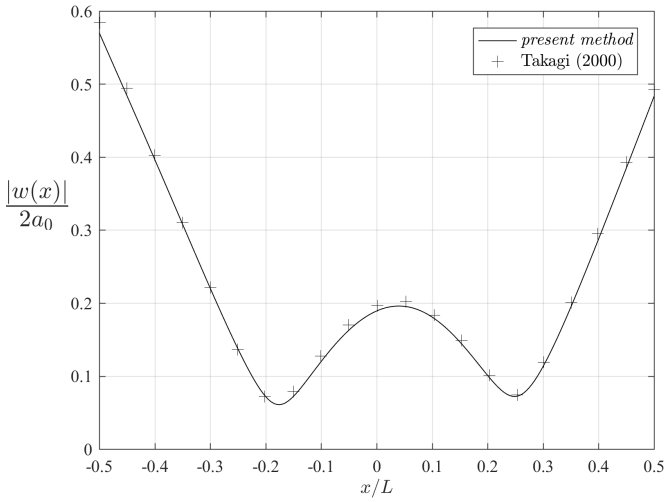


**Figure 8.6** Normalised deflection of floating elastic plate in deep water. Solid line denotes the solution obtained by means of the present method, while crosses denote the solution in Takagi et al. (2000)

against the experimental results published in Wu et al. (1995), and originally presented in Utsunomiya et al. (1995). Check veracity of references here from JFS $\tau = 1.3\,\mathrm{m}$ and material characteristics $E = 5\,\mathrm{GPa}$, $\nu = 0.3$ and density $\rho_e = 922.5\,\mathrm{kg\,m^{-3}}$

The examined homogeneous, thin plate features length $L = 10\,\mathrm{m}$, width $W = 0.5\,\mathrm{m}$, thickness $\tau = 0.038\,\mathrm{m}$ and draft $d = 8.36 \cdot 10^{-3}\,\mathrm{m}$ . The Young's modulus $E = 103\,\mathrm{MPa}$ and the density of the elastic material is $\rho_e = 922.5\,\mathrm{kg\,m^{-3}}$. The constant depth is set to $h = 1.1\,\mathrm{m}$ . In the figure, the normalized plate displacement under three different incident wave periods is illustrated. For $T = 1.429\,\mathrm{s}$ and $T = 0.7\,\mathrm{s}$ the present method, denoted by a continuous line is compared against the converged results obtained by means of the vertical multi-modal approximation, accounting for variable draft, in Bennetts et al. (2007), denoted by a dashed line. Experimental results referenced in Wu et al. (1995) are noted by squares, triangles and circles for periods $T = 2.875\,\mathrm{s}$, $1.429\,\mathrm{s}$ and $T = 0.7\,\mathrm{s}$ respectively. Notably, the geometric characteristics of the given structure suggest that its dynamic response is indeed accurately described by means of the classical thin plate theory, since $\tau/L = 0.0038$. Furthermore even in the higher frequency case, the incident wavelength is considerably larger than the plate thickness ($\tau/\lambda \approx 0.05$) and thus shear deformation effects are rendered negligible. For $T = 1.429\,\mathrm{s}$, the obtained solutions are almost identical while minor deviations of a quantitative nature are observed for the high frequency case. This could be attributed to the fact that the present work does not account for the constant draft. Results are generally found in very good agreement with the results by Bennetts et al. (2007), illustrating the beneficial effects of evanescent mode employment in capturing scattering effects due to the edges of the plate.

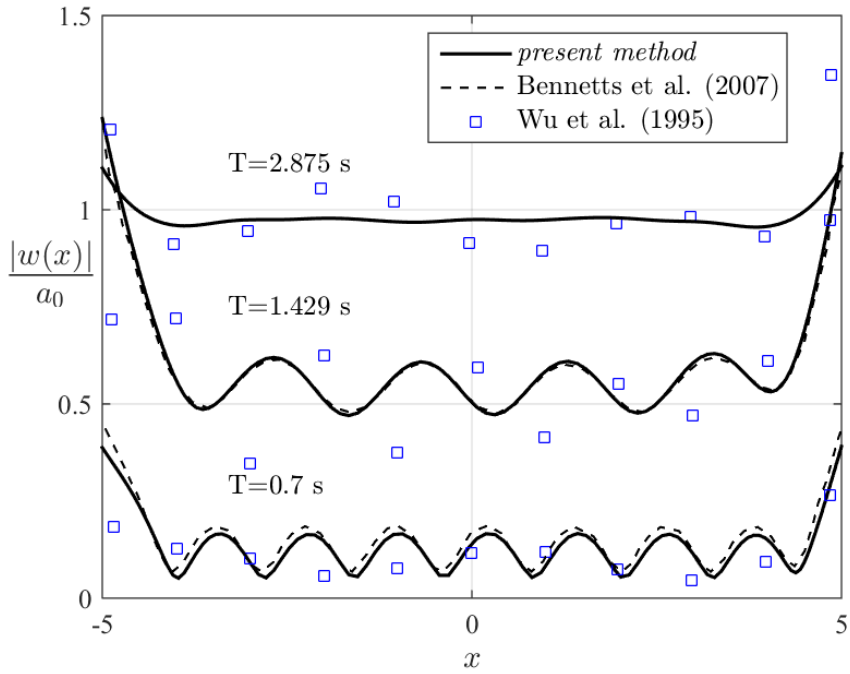


**Figure 8.7** Non-dimensional displacement amplitude for (a) T=2.875 s, (b) T=1.429 s and (c) T=0.7 s. Solid line denotes the solution of the present method while the dashed line indictes the results in Bennetts et al. (2007). Experimental data are denoted by squares.

### Homogeneous thick plate case

In all cases considered to this point, the CPT theory is employed and shear and rotary inertia effects are neglected. Recently, several authors studied the diffraction of surface waves by the presence of floating this elastic plates, e.g., Zhao et al. (2008). In the aforementioned paper, comparisons against the small scale test documented above (Wu et al., 1995) were performed for increasing thickness values, $T = 0.038\,\text{s}$, $0.075\,\text{s}$ and $0.1\,\text{s}$. In Fig. 8.8, the present method employing the Mindlin plate model compared favourably against the results in Zhao et al. (2008), depicted with thinner lines for each thickness values and period $T = 1.429\,\text{s}$. Notably, the dynamic response of the Kirchhoff and Mindlin plate models were almost identical even in the thicker case for $\tau = 0.1\,\text{m}$, where thickness-to-incident wavelength ratio is an order of magnitude smaller than thickness $\tau/\lambda = 0.032$. To illustrate the differences between the two plate models a higher frequency case, for $T = 0.5\,\text{s}$ is considered in Fig. 11. Again, three thickness cases thickness values, $\tau = 0.038\,\text{m}$, $0.075\,\text{m}$ and $0.1\,\text{m}$ were considered for the same plate configuration. In the figure, the non-dimensional deflection and bending moment are calculated for both plate models, resulting to three pairs of curves corresponding to the three thickness values. The pairs are given an increasing number that match increasing thickness values. Solid lines denote the solutions obtained by the thin plate assumption, while the dashed lines indicate Mindlin plate solutions. The thickness-to-incident wavelength ratios, ranging in

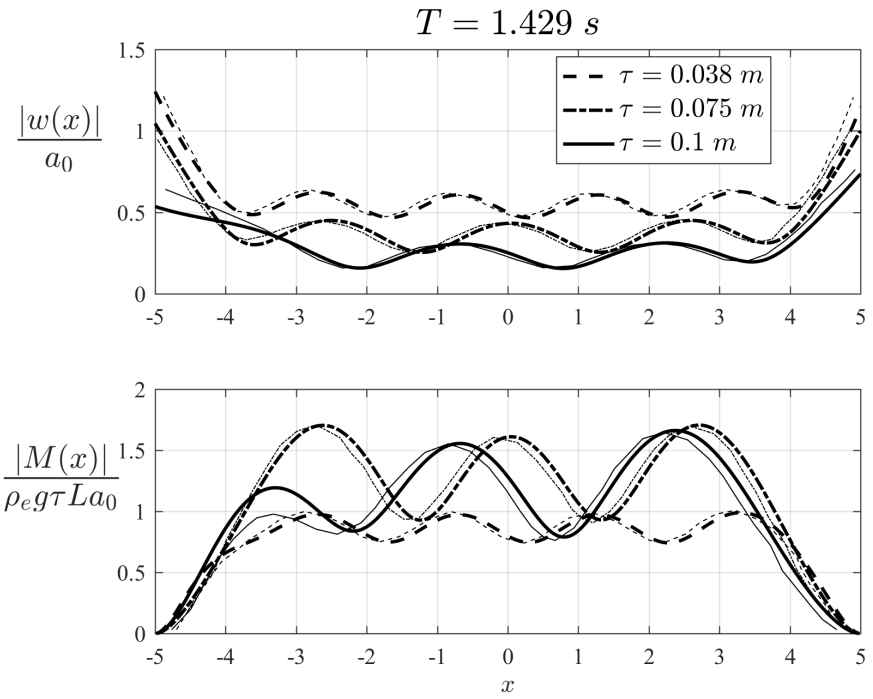


**Figure 8.8** Modulus of the non-dimensionalised deflection and moment for $T = 1.429\,\mathrm{s}$ and different thickness values. Thick lines correspond to results obtained by the present method while thinner lines indicate the results in Zhao et al. (2008)

magnitudes $\tau/\lambda \approx 0.01-0.25$ are comparable to thickness in the examined cases, which justifies thick plate assumptions while the structure remains slender. The plate deflection and bending moment distributions shown in Fig. 8.9, indeed deviate due to the effects of rotary inertia and shear deformation under high frequency excitation.

### Variable Thickness Case

Next, the reflection and transmission coefficients for a floating structure featuring thickness variation along its length are considered. A case considered in Smith and Meylan (2011) is examined. In the aforementioned analysis the results concern the hydroelastic response of a thin ice floe with length $L = 200\,\mathrm{m}$ with set parameters $\rho_e = 922.5\,\mathrm{kg\,m^{-3}}$,$\nu = 0.3$ and fluid density $\rho_w = 1000\,\mathrm{kg\,m^{-3}}$. Concerning the employed Young's modulus the referenced work documents $E = 6\,\mathrm{GPa}$, which corresponds to sea ice, however the provided details are insufficient. Following, Iida and Umazume (2020) that replicated the above case, an unrealistic Young's modulus $\tilde{E} = 6\,\mathrm{GPa}$ is adopted for the structural modeling and deep water conditions are assumed. Two thickness profiles as in Smith and Meylan (2011) $\tau_i = d_0 q_i(x)$ are examined, employing the following distribution functions,

$$q_1(x) = 1 \text{ and } q_2(x) = 0.5 + 0.5\tanh(1.5 - x),\ -100 < x < 100. \tag{8.3}$$

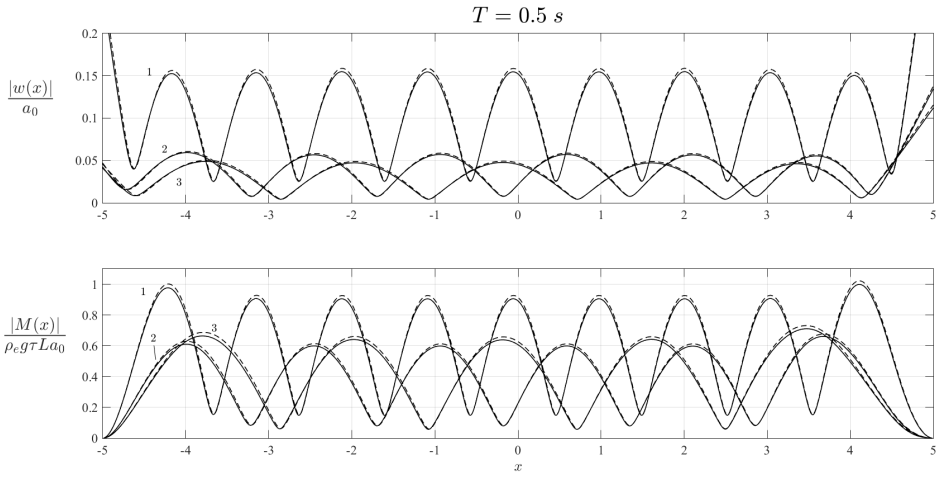


**Figure 8.9** Modulus of the non-dimensionalised deflection and moment for different thickness values. Solid lines correspond to results obtained by the Kirchhoff plate model, while dashed line indicate results by Mindlin for thickness values (1)$\tau = 0.038\,\mathrm{m}$, (2) $0.075\,\mathrm{m}$ and (3) $0.1\,\mathrm{m}$ .

and a range of amplitudes $d_0$. The functions $q_1$ and $q_2$ of Eq. (8.3) correspond to a homogeneous thickness profile and a mollified step function distribution respectively, as seen in Fig. 12. The mean thickness values of $\tau_2$ is equal to corresponding constant thickness $\tau_1$ for varying $d_0$. The reflection coefficient versus a range of wave periods is plotted for four thickness amplitude values $d_0$ corresponding to thickness profiles $\tau_1$ and $\tau_2$. It is observed in Fig.12, that the results by the present method are found to be almost identical with Iida and Umazume (2020). The figure illustrates that qualitative differences between constant and variable thickness profiles become minor as $d_0$ increases, indicating that thickness variations are important for thin plates.

### 8.2.2 Thin Plate Floating over Variable Bathymetry

Next, the variable bathymetry effects are considered. Up to this point, constant seabed cases were considered for validation. In the sequel a series of comparisons with Belibassakis and Athanassoulis (2005) are carried out.

In the following cases, the responses of the floating plate considered in Section 8.2.1, are considered over different bathymetric profiles involving (a) a smooth shoaling (b) and undulating seabed.

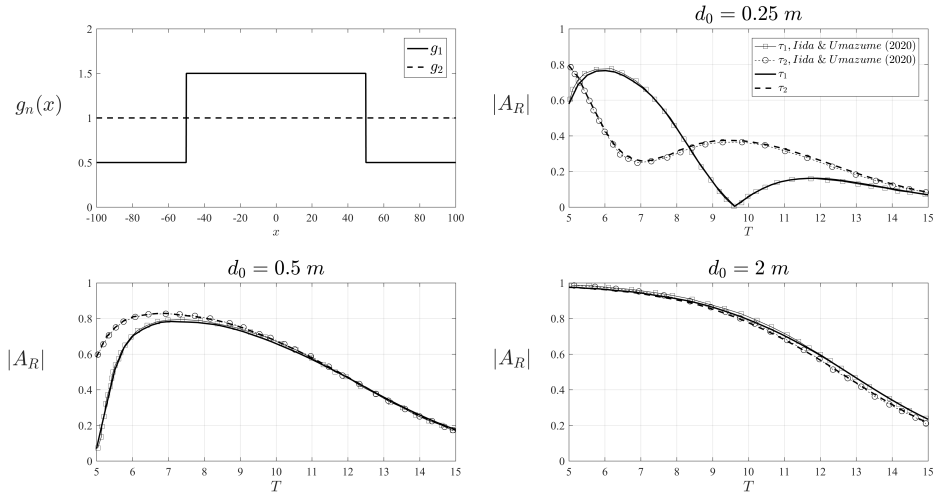


**Figure 8.10** Reflection coefficient vs period for thickness profiles $\tau_1$, $\tau_2$ and different values for $d_0$. The functions $g_i$ are shown in the upper left subplot. The solid and dashed lines correspond to the solution obtained by the present method for the two thickness profiles, while the square solid line and circle dashed line denote the corresponding results in Iida and Masuda 2020)

### Smooth Shoaling

Initially, a bathymetric profile representing a smooth shoal restricted in the hydroelastic region featuring the following depth function is considered,

$$h(x) = \frac{h_1 + h_2}{2} - \frac{h_1 - h_2}{2} \tanh\left(3\pi\left(\frac{x - a_1}{x - a_2} - 0.5\right)\right) \tag{8.4}$$

In Eq. (8.4), $h_1$ and $h_2$ are the constant depth values that correspond to subregions $\omega^j$, $j = 1, 2$. An incident wave angular frequency is $\omega = 0.4\,\mathrm{s}^{-1}$. Two separate cases, with increasingly sloping bathymetry, are considered. The normalized response of a plate floating over a shoaling region with a slope of 3.8% corresponding to $h_1 = 15\,\mathrm{m}$ and $h_1 = 8\,\mathrm{m}$ in Eq. (8.4) and a shoal with a steeper slope 9.4% corresponding to $h_1 = 15\,\mathrm{m}$ and $h_1 = 5\,\mathrm{m}$ are given in Fig. 8.11. The solution by means of the present work is indicated by a solid line, while the results presented in Belibassakis and Athanassoulis (2005) are shown with squares. The two solutions are found in excellent agreement, noting the effectiveness of the method in variable bathymetry.

### Undulating Shoaling

Next, the case of an undulating seabed is examined. The bathymetric profile is described by means of the following depth function,

$$h(x) = 10 - g(x) A_b \sin\left(k_b(x - a_1)\right), \tag{8.5}$$

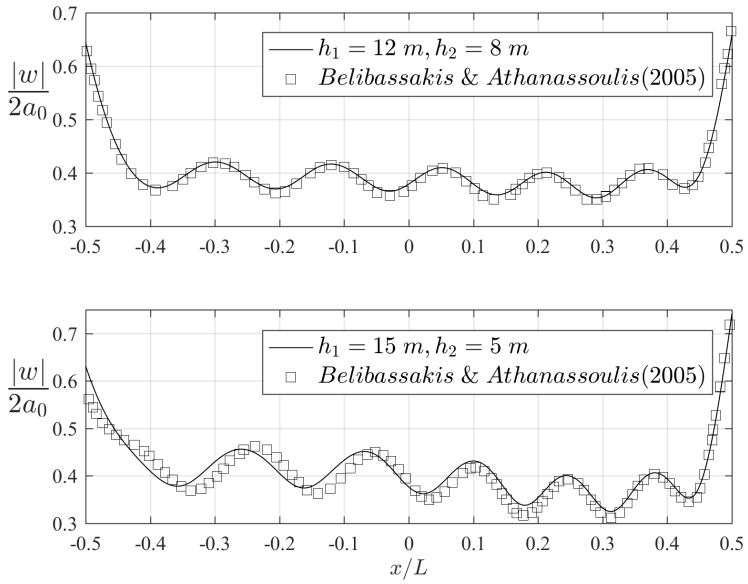


**Figure 8.11** Modulus of the normalised deflection to the waveheight for (top) $h_1 = 15\,\text{m}$ and $h_1 = 8\,\text{m}$, (bottom) $h_1 = 15\,\text{m}$ and $h_1 = 5\,\text{m}$.

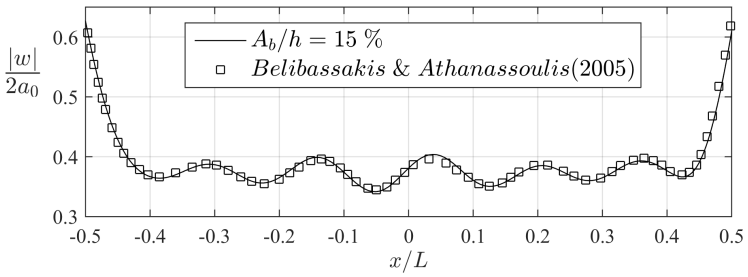


**Figure 8.12** Modulus of the normalised deflection to the waveheight for $A_b/h = 15\%$.

where $k_b = 2\pi/\lambda_b$ is the wavenumber of the seabed disturbance, $\lambda_b = 125\,\text{m}$ is the corresponding wavelength and $A_b$ is the amplitude of undulations. The filtering function is given as,

$$g(x) = \left(1 - \exp\left(-\left(\frac{x - a_1}{\lambda_b}\right)^2\right)\right)\left(1 - \exp\left(-\left(\frac{x - a_2}{\lambda_b}\right)^2\right)\right) \tag{8.6}$$

The undulating profile is again restricted in the hydroelastic region, and disturbances are kept around a mean depth $h = 10\,\text{m}$. The incident wave field angular frequency is kept to $\omega = 0.4\,\text{s}^{-1}$ . In Fig. 8.12 the non-dimensional with respect to the wave height deflection corresponding to a variable seabed profile with $A_b/h = 15\%$ is plotted. The present method solution, drawn with a solid line compares favorably once again, with the results documented in Belibassakis and Athanassoulis (2005).

# Chapter 9

# Numerical Results in the 3D waveguide

A series of 3D cases are explored in the present chapter, illustrating the simulation capabilities of the proposed method.

## 9.1 Homogeneous plate over constant depth

The case of a circular, homogeneous thin plate floating over constant seabed is initially considered. The given case is chosen to illustrate the ability of the FEM-based scheme to straightforwardly capture curved boundaries. In the chosen configuration, plane wave incidence with $T = 1.5\,\mathrm{s}$ over the constant depth $h = 1\,\mathrm{m}$ are assumed. The depth-to-wavelength is reduced to $h/\lambda = 0.299$ suggesting intermediate water depth conditions. The water density is set to $\rho = 1000\,\mathrm{kgm}^{-3}$, while the chosen material properties in this example case are $\rho_e = 922.5\,\mathrm{kgm}^{-3}$, the Poisson's ratio $\nu = 0.3$ and Young's modulus $E = 5\,\mathrm{GPa}$, corresponding to sea ice. The circular floating plate with radius $r = 2\,\mathrm{m}$ is positioned in the centre of the computational region $\Omega = [-10\,\mathrm{m}, 10\,\mathrm{m}] \times [-10\,\mathrm{m}, 10\,\mathrm{m}] \times [-1\,\mathrm{m}, 0]$.

A hybrid mesh, featuring a PML region enclosing the computational domain $\Omega$, as presented in Sections 6.2.1 and 6.2.3 is implemented for the numerical simulation. The non-dimentional layer thickness is kept at $k\theta_l = 10^{-5}$ and discretised with 4 segments. To save computational resources $N_m = 6$ modes are kept in the vertical expansion for the velocity potential, while $N_f = 15$ flexural modes were employed in the modal expansion of the plate deflection. The full 3D solution of the wave field can be constructed as shown in Fig. 9.1. Graphically, Fig. 9.1 is comprised by a series of $(x_1 - z)$ sections superimposed along the $x_2$ direction, illustrating the vertical structure of the solution and creating a 3D representation. The real part of the total solution on the upper surface $z = 0$ is shown in Fig. 9.2(i). In Fig. 9.2(ii) the corresponding modulus of induced plate deflection under wave action is plotted. The symmetric configuration of the chosen example and the comparable incident wavelength and plate diameter justify the

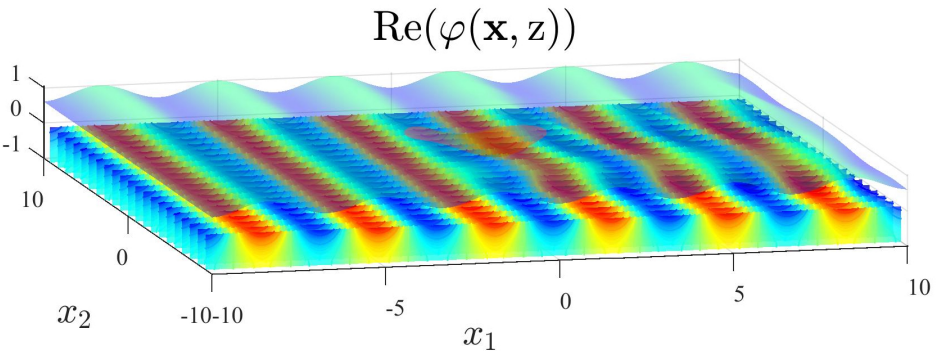


**Figure 9.1** Illustration of the 3D wave field solution in $\Omega$

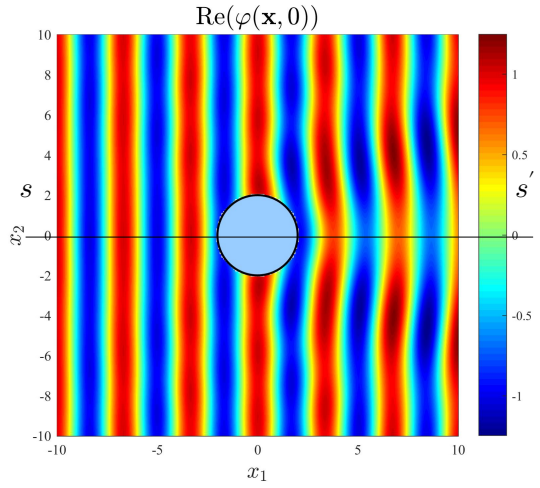


**(i)** Real part of the total velocity potential.

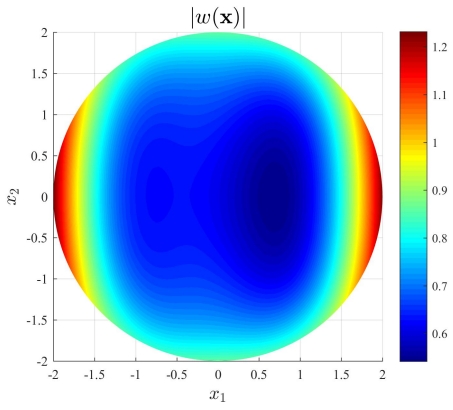


**(ii)** Modulus of plate deflection

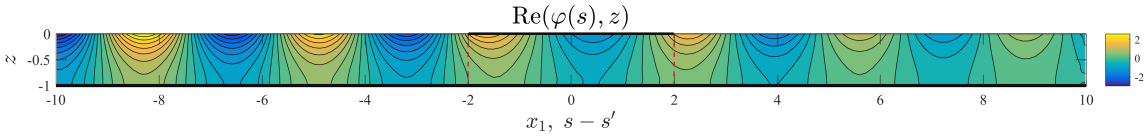


**(iii)** Vertical section $s - s'$

**Figure 9.2** Real part of the total wave field solution $\varphi$ for the case of a circular plate with radius $r = 2\,\mathrm{m}$, $T = 1.5\,\mathrm{s}$

calculated response. To demonstrate the solution matching between free-surface ($\Omega_1$) and constrained subregion ($\Omega_2$), the total wave field on the vertical cross-section $s - s'$ and $y = 0$ is shown (see Fig. 9.2(i)). Excellent potential matching across the interface (depicted with red dashed lines) is demonstrated with the employment of $N_m = 6$ modes on the vertical hydrodynamic expansion. Furthermore, the vertical structure of the solution is shown to satisfy the condition on the flat seabed, while the upwave and downwave regions to the plate correspond with the results shown in Fig. 9.2(i). The decomposed radiation $\varphi_R(\mathbf{x}, 0)$ and diffracted $\varphi_D(\mathbf{x}, 0)$ solutions on the upper surface are also shown in Fig. 9.3 respectively. The

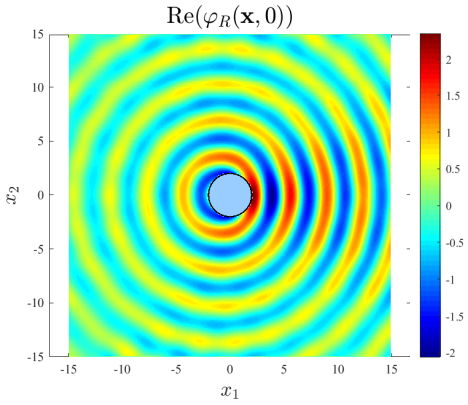


**(i)** Real part of $\varphi_R(\mathbf{x},0)$

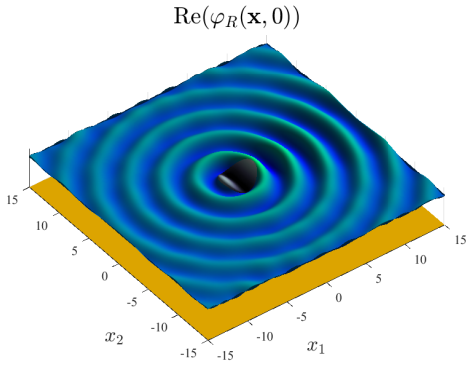


**(ii)** 3D representation of the upper surface solution

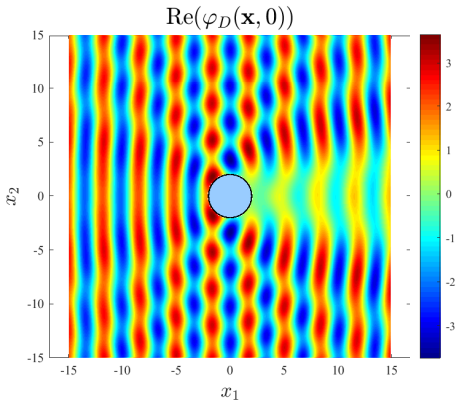


**(iii)** Real part of $\varphi_D(\mathbf{x},0)$

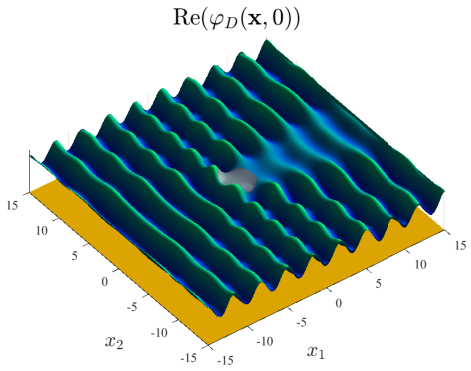


**(iv)** 3D representation of the upper surface solution

**Figure 9.3** Real part of the radiation $\varphi_R$ and diffracted wave field $\varphi_D$ solutions for the case of a circular plate with radius for the case of a circular plate with radius $r = 2\,\mathrm{m}$, $T = 1.5\,\mathrm{s}$

diffracted solution pattern features a zone of shielding in the downwave region to the structure as well as a moderately amplified upwave front showing signs of reflection.

Next, the case of an L-shaped thin plate, floating over a flat seabed is chosen to display the versatility of the proposed method. The L shape of the plate generates concave points for both fluid and hydroelastic subdomains and is often employed as a benchmark case for restrictive geometries. The same material properties, depth and excitation frequency are employed in this second example. The total, radiated and diffracted wave field solutions are given in Fig. 9.4. In Fig. 9.4(i) the subtle downwave pattern illustrates the compliant response of the structure. In Figs. 9.4(iii) and 9.4(iv) and Figs. 9.4(v) and 9.4(vi) the rich decomposed solutions due to the complex geometry of the structure are shown.

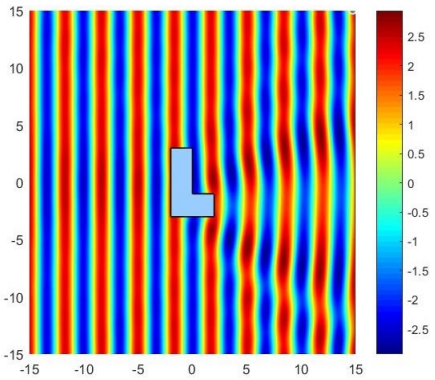

**(i)** Real part of $\varphi(\mathbf{x}, 0)$

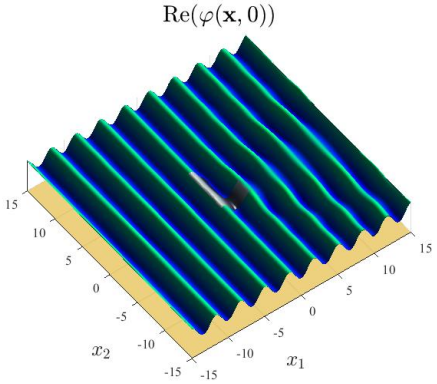


**(ii)** 3D representation of the upper surface solution

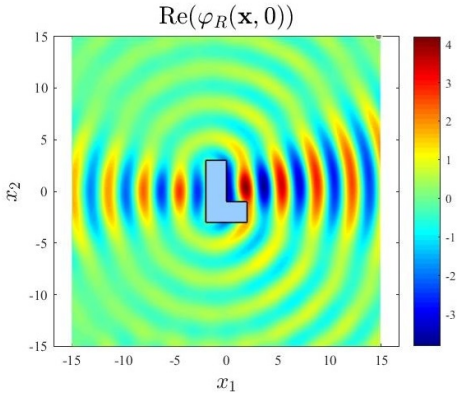


**(iii)** Real part of $\varphi_R(\mathbf{x}, 0)$

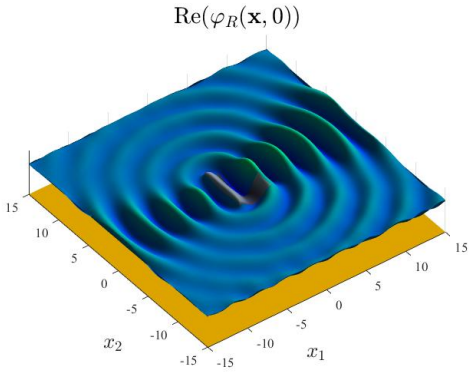


**(iv)** 3D representation of the upper surface radiation solution

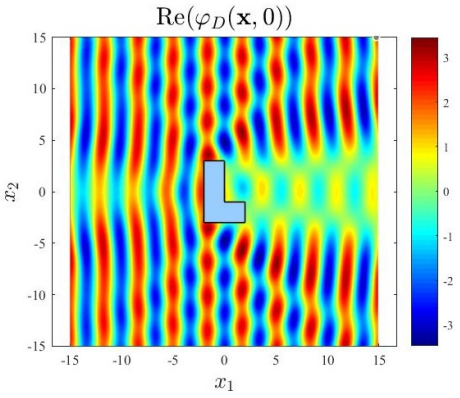


**(v)** Real part of $\varphi_D(\mathbf{x}, 0)$

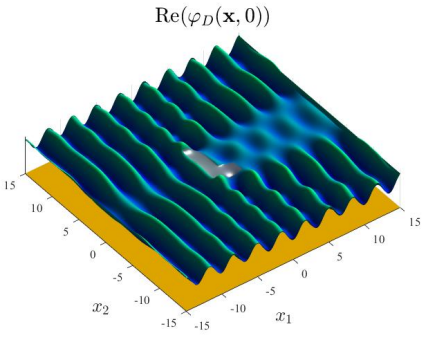


**(vi)** 3D representation of the upper surface diffraction solution

**Figure 9.4** Real part of the wave field solutions for an L-shaped plate and $T = 1.5\,\mathrm{s}$

## 9.2 Homogeneous plate over variable depth

In this section, the case of a homogeneous rectangular plate over a shoaling seabed, introduced in Gerostathis et al. (2016) is considered. The shoaling bathymetry is described once again byEq. (8.4) with the local depth at the regions of incidence and transmission are set to $h_1 = 15\,\mathrm{m}$ and $h_2 = 5\,\mathrm{m}$ respectively. Plane wave incidence, $T = 15\,\mathrm{s}$ on a rectangular thin plate of dimensions $250\,\mathrm{m} \times 140\,\mathrm{m}$ is examined. The material properties of the homogeneous plate are chosen so as to keep the flexural rigidity in accordance with the example found in the literature, $D/\rho g = 10^5\,\mathrm{m}^4$ and $m = \omega^2\tau\rho_e/(\rho g) = 0.005$. The latter choices correspond to $E = 5\,\mathrm{GPa}$ $\rho_e = 220.3\,\mathrm{kgm}^{-3}$ and $\tau = 1.2\,\mathrm{m}$. The total solution on the upper surface is once again shown in Fig. 9.5. A distinct diffraction pattern in the downwave region is observed. The wave characteristics are found generally in good agreement with the case shown in Gerostathis et al. (2016) but the structure appears to be significantly more compliant. The latter is attributed to a potentially poor choice of dimensional parameters in the present calculations or the coarse computational mesh. Notably, the employed irregular mesh resulted in about half a million *dofs* for each hydrodynamic subproblem. Calculations in this chapter are kept to the above standard.

Subsequently, motivated by the previous observation and in order to further investigate the effects of bending rigidity on the structural hydroelastic response along with the total wave field solution, three cases of increasing Young's moduli are explored, namely $E = 5\,\mathrm{MPa}$, $9\,\mathrm{GPa}$, $210\,\mathrm{GPa}$. In the context of the present dimensional analysis, the latter values correspond to a flexible cork material, sea ice and structural steel respectively. For the first case material density is set to $\rho_e = 220.3\,\mathrm{kgm}^{-3}$. For sea ice the value is set $\rho_e = 922.5\,\mathrm{kgm}^{-3}$ as previously discussed , while the same value is employed for steel. This nonphysical assumption is employed to maintain the buoyant action of the structure. It is stressed here that the aim of the investigation

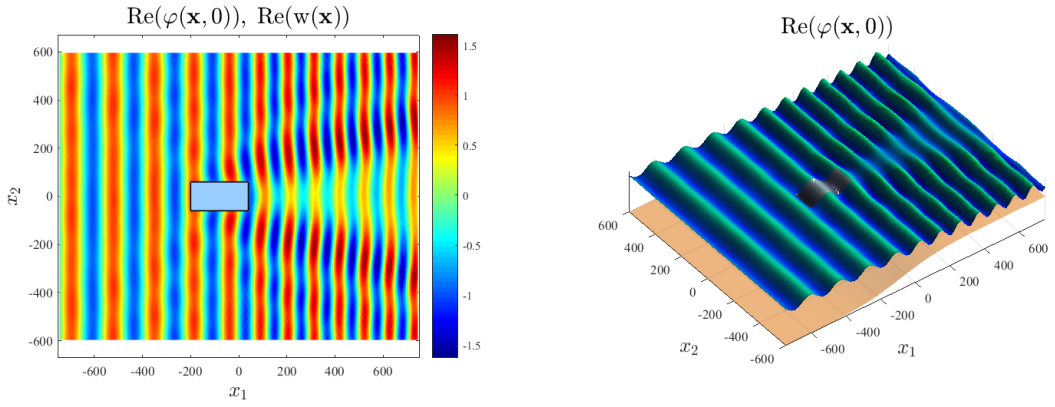


**(i)** Real part of $\varphi(\mathbf{x}, 0)$

**(ii)** 3D representation of the upper surface solution

**Figure 9.5** Real part of the total wave field solution $\varphi(\mathbf{x}, 0)$ for the case of a rectangular plate and $T = 15\,\mathrm{s}$

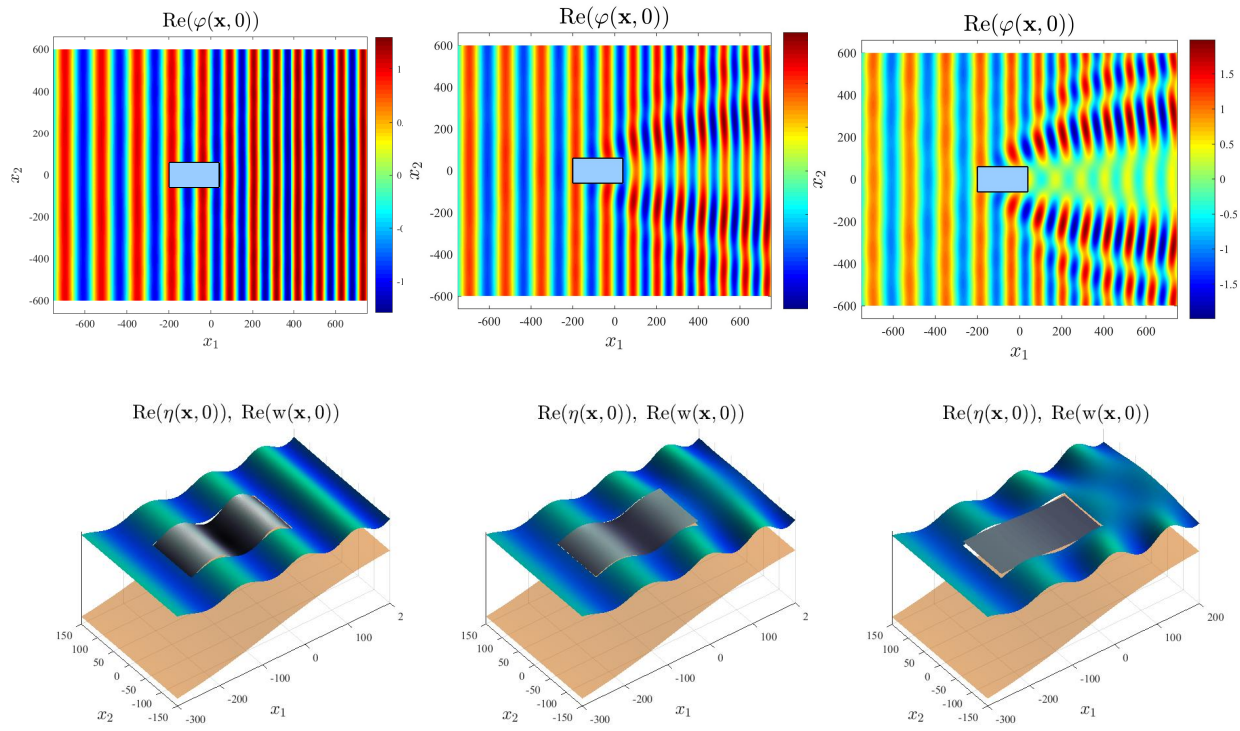


**(i)** $E = 5\,\text{MPa}$ **(ii)** $E = 9\,\text{GPa}$ **(iii)** $E = 210\,\text{GPa}$

**Figure 9.6** Real part of $\varphi(\mathbf{x}, 0)$, upper surface elevation $\eta(\mathbf{x})$ and deflection $w(\mathbf{x})$for three stiffness values

is to assess extreme cases on the flexibility spectrum. The real part of the total wave field solutions in each explored case is plotted in Fig. 9.6. The sloping bathymetry of the previous example is used. In Section 9.2 it is observed that the incident wavetrain to the extremely compliant structure remains undisturbed. In the shoaling region the wavelength is shown to decrease. The upper surface elevation $\eta(\mathbf{x})$ and plate deflection $w(\mathbf{x})$ for the corresponding cases are also plotted. It is seen in Fig. 9.6(i) that the upper surface elevation and deflection almost match showing the extremely compliant mode of the flexible structure. The second case with geophysical significance is depicted in Section 9.2. The subtle diffraction pattern and intense plate flexure are in accordance with examples in the previous subsection. In this case, Fig. 9.6(ii), the interaction between plate response and surface elevation are shown to interact and generate the diffracted pattern at the downwave region.

Similarly, the rich downwave structure in the stiffer case Section 9.2 is due to the intense coupled interaction phenomena, further illustrated in Fig. 9.6(iii) where the subtle response of the stiffer structure has a profound impact on the wave field (downwave structure). A comparative illustration of the induced plate deflections are shown in Fig. 9.7. From the extremely flexible (i) to the stiffer case (iii), the responses are gradually attenuated. In the first case the upwave edge of the plate follows surface elevation while the increased response on

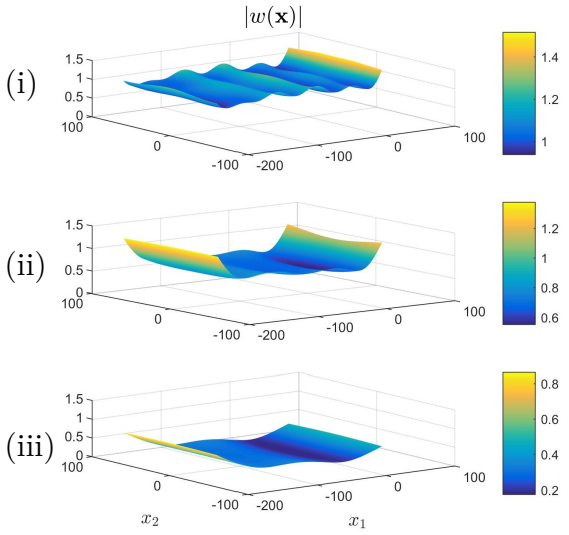


**Figure 9.7** Modulus of plate deflection for (i) $E = 5\,\mathrm{MPa}$, (ii) $E = 9\,\mathrm{GPa}$, (iii) $E = 210\,\mathrm{GPa}$.

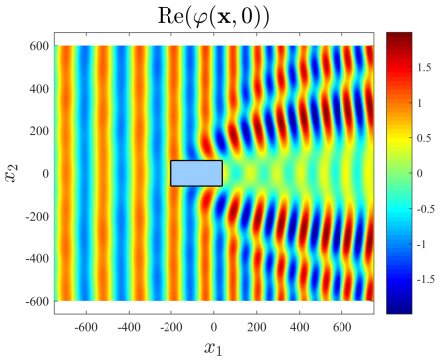


**(i)** $\theta = 0^\circ$

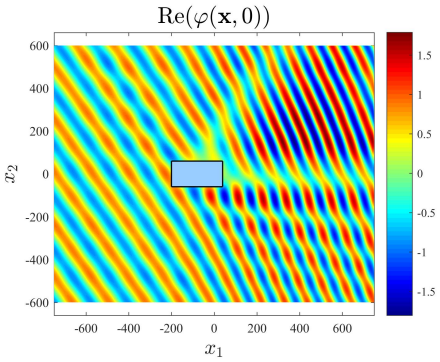


**(ii)** $\theta = 45^\circ$

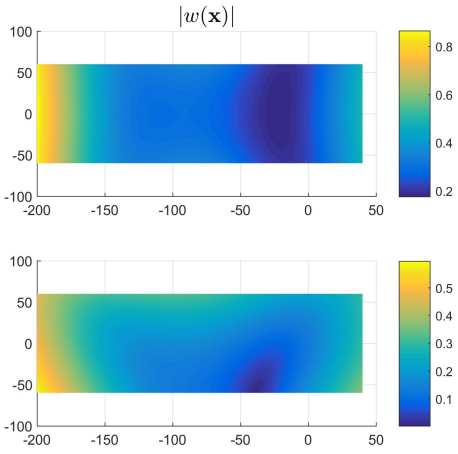


**(iii)** Modulus of deflection for $\theta = 0^\circ$ (up) and $\theta = 45^\circ$ (down)

**Figure 9.8** Oblique wave incidence, $\theta = 0^\circ$ (reference), $\theta = 45^\circ$

the downwave edge is justified by local wave amplitude increase. For the sea ice case, the plate response on the upwave front is greater with the overall response being reduced compared to the extremely flexible case. For the stiffer case response appears attenuated with the maximum deflection appearing at the upwave front.

Finally, oblique wave incidence is examined for a rectangular plate of the same geometry to further exhibit the potential of the proposed method to model 3D effects. For illustration purposes the case of a very stiff structure, as explored in the prequel is used. The same sloping seabed profile is employed to calculate the hydroelastic response of the structure and wave field transformations with $\theta = 45^{\circ}$ angle of incidence. Results, are plotted in Fig. 9.8. The total solutions for the cases of $x_1-$parallel plane wave and oblique incidence are shown in Figs. 9.8(i) and 9.8(ii), while the effects on plate response in Fig. 9.8(iii).

# Part IV

# Time Domain Methods

# Chapter 10

# Shallow depth approximation

This final chapter is dedicated to time domain finite element schemes, targeting shallow water environment. The research work is briefly outlined while selected journal publications are included for the reader's reference.

The transient hydroelastic response of an inhomogeneous thin, elastic structure under long wave excitation is analysed by means of the finite element method. The analysis is restricted in the 2D ocean strip while the structure is assumed to extend indefinitely in the direction normal to wave incidence, thus performing cylindrical bending. The simple model is used for the simulation of the generated kinematic and stress fields of the structure, when the latter interacts with a long wave. The explored FEM scheme is able to treat the full equations for the hydrodynamics and allow for non-linearity in the structure by employing Gao's beam model (Gao, 1996) to account for moderately large deflections and strains.

Initially, the governing equations of fluid and elastic motions, coupled through pressure equilibrium on the section of the fluid surface occupied by the structure are considered. Domain partitioning dictates the creation of two free-surface regions, denoted as $\Omega_i, i = 1, 2$ and $\Omega_0, i = 1, 2$ while the region of hydroelastic coupling is $\Omega_0$.

For the hydrodynamics, the shallow water equations for long wave propagation are considered in free-surface regions $\Omega_i, i = 1, 2$,

$$\partial_t u + u\partial_x u + g\partial_x \eta = 0, \tag{10.1}$$

$$\partial_t \eta + \partial_x \left((b(x) + \eta)u\right) = 0 \tag{10.2}$$

By assuming a velocity potential function $u = \partial_x \phi$, Eq. (10.1) can be combined in a single evolution equation in terms of potential $\phi$. In the region of hydroelastic coupling $\Omega_0$, the

following equations hold,

$$\rho_p \tau \partial_t^2 \eta - \mathrm{I}_r \partial_t^2 \partial_x^2 \eta + \tilde{D} \partial_x^2 \eta - s\left(\partial_x^2 \eta\right) \partial_x^2 \eta + \rho_w g(\eta + \partial_t \phi) + \frac{\rho_w}{2}\left(\partial_x \phi\right)^2) = -q(x;t) \tag{10.3}$$

$$\partial_t \eta + \partial_x\left((b(x) + \eta)\partial_x \phi\right) = 0 \tag{10.4}$$

In Eq. (10.3), $I_r = \rho_p \tau^3/12$ is the rotary inertia per width and $\tilde{D} = E\tau^3(1-\nu)(1+\nu)^{-1}(1-2\nu)^{-1}/12$ is the flexural rigidity per width of the model. Compared to the classical thin strip the above model incorporates the effects of rotary inertia and the nonlinear term stemming from considering the moderately large deflection of a thin beam, when non-negligible stress variation in the lateral direction is considered. In addition, the non-linear pressure coupling term $\frac{1}{2}\rho_w(\partial_x \phi)^2$ which is significant when velocity becomes large is included. By excluding the nonlinear terms and neglecting the rotary inertia in Eq. (10.3), the thin strip model corresponding to the Euler-Bernoulli under plane strain assumptions is deduced. Similarly, by neglecting the nonlinear terms and employing the wave small amplitude assumption reduces Eq. (10.1) to the linearised shallow water equations. To derive higher order FEM schemes for the coupled problem in 1D, the weak forms of the systems of equations in each subregion are derived. The weight functions $v \in H^2(\Omega_0)$, that multiplies Eq. (10.3), and functions $w_0 \in H^1(\Omega_0)$and $w_i \in H^1(\Omega_i)$ for Eq. (10.4) and Eq. (10.1) are defined respectively. Next, special hydroelastic elements are considered for discretization, featuring $C^1$ approximation for the plate deflection and $C^0$ approximation for the velocity potential. Hence, the *dofs* in $\Omega_0$ include $\eta$, $\partial_x \eta$ and $\phi$, while only $\phi$ is unknown in $\Omega_i, i = 1, 2$. Interelement connectivity ensures the continuity for the potential function on the fictitious interface.

The specially constructed element incorporates cubic Hermite-shape functions for the approximation of the beam deflection/upper surface elevation (notably $\eta = w$ in $\Omega_0$) and the strip slope, while quadratic Lagrange-shape functions are employed for the the approximation of $\phi$ in the middle region. In the free fluid regions Lagrange elements are used.

Upon discretisation, the following dynamic nonlinear system of equations is expressed in terms of the vector $\mathbf{u}$ of global unknowns,

$$\mathbf{M}\partial_t^2 \mathbf{u} + \mathbf{C}(\mathbf{u})\partial_t \mathbf{u} + \mathbf{K}(\mathbf{u})\mathbf{u} = 0, \tag{10.5}$$

supplemented by appropriate initial conditions. For the fully linear case (in both the elastic response and hydrodynamic modelling) the dependence of the matrices on the solution is eliminated. The implicit Crank-Nicolson time marching method in conjunction with Newton-Raphson iteration scheme is subsequently used for the solution of Eq. (10.5). In post-processing, the obtained solutions are used to derive the stress state of the elastic body.

Notably, the derived schemes can be employed in a number of applications in (a) ice shelf research and (b) marine technology. In the sequel, contributions in scientific journals focusing on the above are included instead of an in-depth analysis of the developed schemes.

## 10.1 Publications in scientific journals

The following research contributions are included in this last section of the thesis to illustrate notable applications of the time-domain hydroelastic FEM schemes, which were breifly delineated in the prequel. The referenced work focuses on the account of inhomogeneity effects, like variable bathymetry for the hydrodynamic modelling, and material and geometric inhomogeneity for the elastic body.

1. Papathanasiou, T. K., Karperaki, A. E., Theotokoglou, E. E., and Belibassakis, K. A. (2015b). Hydroelastic analysis of ice shelves under long wave excitation. Nat. Hazards Earth Syst. Sci., 15(8):1851–1857, https://doi.org/10.5194/nhess-15-1851-2015.

2. Karperaki, A. (2015). FEM Hydroelastic Models with Application to the Nonlinear Response of Large Floating Bodies in Shallow Wave Conditions. *Procedia Computer Science*, 66:122–131, https://doi.org/10.1016/j.procs.2015.11.015.

3. Karperaki, A., Belibassakis, K., and Papathanasiou, T. (2016). Time-domain, shallow-water hydroelastic analysis of VLFS elastically connected to the seabed.*Marine Structures*, 48:33-51, ttps://doi.org/10.1016/j.marstruc.2016.04.002.

In the first publication 1, the hydroelastic FEM are applied in polar research. Motivated by the 2011 Sulzberger Ice Shelf (SIS) calving event and its correlation with the Honshu Tsunami, the SIS stable configuration is studied. In the fully, linear regime the extreme values of the bending moment distribution in both space and time are examined. Finally, the location of these extrema is investigated for different values of ice shelf thickness and tsunami wave length are studied. In the latter, efforts are focused in the shallow water limit, while an initial attempt to account for intermediate water made.

The second contribution 2, considers non-linear effects in both the hydrodynamic and structural modelling by means of the non-linear shallow water equations and the Gao beam in the 1D setting. The effects of the incorporated nonlineariry are assessed by means of a numerical example featuring an elevation pulse of increasing steepness.

Finally, in contribution 3 an application in marine engineering is considered. In the linear setting, the thin raft is equipped with linear connectors to the seabed resembled as dash-pot configurations. The work attempts to assess the response mitigation and wave extraction capabilities of such configurations under long wave excitation.

Nat. Hazards Earth Syst. Sci., 15, 1851–1857, 2015
www.nat-hazards-earth-syst-sci.net/15/1851/2015/
doi:10.5194/nhess-15-1851-2015


Natural Hazards and Earth System Sciences
Open Access

# Hydroelastic analysis of ice shelves under long wave excitation

**T. K. Papathanasiou**[1,a], **A. E. Karperaki**[2], **E. E. Theotokoglou**[3], **and K. A. Belibassakis**[2]

[1]Department of Civil Engineering and Surveying & Geoinformatics Engineering, Technological Educational Institute of Athens, Athens, Greece
[2]School of Naval Architecture and Marine Engineering, National Technical University of Athens, Zografou Campus, Athens, Greece
[3]Department of Mechanics, School of Applied Mathematical and Physical Science, National Technical University of Athens, Zografou Campus, Athens, Greece
[a]now at: DICAM, University of Trento, via Mesiano 77, 38123 Trento, Italy

*Correspondence to:* A. E. Karperaki (karperaki.ang@gmail.com)

Received: 10 March 2015 – Published in Nat. Hazards Earth Syst. Sci. Discuss.: 5 May 2015
Revised: 29 July 2015 – Accepted: 5 August 2015 – Published: 19 August 2015

**Abstract.** The transient hydroelastic response of an ice shelf under long wave excitation is analysed by means of the finite element method. The simple model, presented in this work, is used for the simulation of the generated kinematic and stress fields in an ice shelf, when the latter interacts with a tsunami wave. The ice shelf, being of large length compared to its thickness, is modelled as an elastic Euler-Bernoulli beam, constrained at the grounding line. The hydrodynamic field is represented by the linearised shallow water equations. The numerical solution is based on the development of a special hydroelastic finite element for the system of governing of equations. Motivated by the 2011 Sulzberger Ice Shelf (SIS) calving event and its correlation with the Honshu Tsunami, the SIS stable configuration is studied. The extreme values of the bending moment distribution in both space and time are examined. Finally, the location of these extrema is investigated for different values of ice shelf thickness and tsunami wave length.

## 1 Introduction

The catastrophic impact of climate change on the Antarctic Peninsula is examined in the works of Scambos et al. (2003) and Skvarca et al. (1999), where attempts to identify the mechanisms of climate-induced, ice shelf disintegration are made. Ice shelf stability is being re-evaluated as wave trains are becoming rougher and elevated temperatures lead to the further weakening of ice formations (Young et al., 2011). In fact, the question of whether ocean wave forcing acts as a collapse triggering mechanism is thoroughly explored in the literature. In particular, gravity wave forcing is depicted as a major cause of rift propagation within an ice shelf, preceding breakup events (Bromirski and Stephen, 2012). Additionally, the effects of infra-gravity waves and intense storm activity are also considered crucial for ice shelf stability (Bromirski et al., 2010).

The present contribution is motivated by the calving event triggered by the Honshu earthquake-generated tsunami, in March 2011. Observational data showed that the Tsunami generated by the aforementioned earthquake in Japan reached the Sulzberger Ice Shelf in Antarctica and caused the formation of two icebergs, the largest being the size of Manhattan island (Brunt et al., 2011). It is evident that the oscillatory flexural bending, induced by wave excitation, is a primary mechanism for ice shelf and ice tongue calving. Ice-tsunami wave interaction is also manifested in the run-up stage, when drifting ice formations are swept by the incoming long wave. The Tohoku Tsunami exhibited the rare feature of transporting large ice masses, causing significant disruptions on the Kuril Islands shoreline as documented in Kaistrenko et al. (2013).

Due to their structural characteristics, namely their negligible bending rigidity and large horizontal dimension, the dynamic response of ice shelves when interacting with the ocean wave field can be effectively modelled as an initial–boundary value problem of hydroelasticity. Hydroelastic analysis is also applied for the study of ice floes sub-

jected to ocean forcing (see Squire, 2007). Under the above considerations, ice shelves can be modelled as constrained semi-infinite plates floating over a water region with either zero or non-zero draft (see Sergienko, 2010). Related to ice shelf modelling, a recent work of Bhattacharjee and Guedes Soares (2012) focuses on the frequency domain problem of a floating semi-infinite plate in the vicinity of a vertical wall. A variety of plate edge conditions are examined, including a free, a fixed and a pinned condition at the vertical wall interface. Brocklehurst et al. (2010) present an analytical solution to the problem of a clamped semi-infinite, homogeneous, elastic plate over a constant bathymetry region. Tkacheva (2013) employs an eigenmode expansion for the solution of a fixed plate on a vertical wall under regular wave loading.

The majority of studies consider the case of harmonic wave excitation, which enables the calculation of the floating body response in the frequency domain. In this case, a common line of work is the modal expansion technique, where the elastic deformation is deduced by the superposition of distinct modes of motion (Belibassakis and Athanassoulis, 2005). The hydrodynamic forces are treated primarily through the employment of the Green function method or the eigenfunction expansion matching method. A number of studies have focused on transient analysis of elastic floating bodies, allowing for non-harmonic wave forcing and time-dependant loads on the body. These attempts incorporate direct time integration schemes, Fourier transforms, modal expansion techniques and other methods (Meylan and Sturova, 2009; Sturova, 2009; Watanabe et al., 1998). For a non-uniform elastic plate floating on shallow waters of variable depth, Papathanasiou et al. (2015) developed a higher-order finite element for the time domain solution of the hydroelastic problem composed of a freely floating or semi-fixed body, while the non-linear transient response is examined in Sturova et al. (2010) by means of a spectral–finite difference method.

In the present contribution, the previous work of the authors on higher order FE schemes (i.e. Papathanasiou et al., 2015) will be applied in the hydroelastic analysis of ice-shelves under long-wave excitation. In Sect. 2 the physical domain and the governing equations are presented. The variational formulation of the previously defined initial boundary value problem is discussed in Sect. 3. In Sect. 4 a case study, with parameters resembling that of the Sulzberger Ice shelf, is analyzed by means of the proposed methodology. The temporal distributions of the maximum and minimum bending moment values, along with their corresponding location along the semi-fixed floating body are given. Finally, a parametric analysis regarding the location of the occurred extreme bending moment values is performed for different ice shelf thickness and initial disturbance wavelength values.

## 2 Physical domain geometry and governing equations

The ice shelf is represented by an elastic, heterogeneous, thin plate with a fixed edge, extending infinitely at the $y$ direction (vertical to the page). The plate of horizontal length $L$, rests on a layer of inviscid, incompressible fluid over an impermeable bottom. Assuming shallow water conditions, the long wave approximation (i.e. wavelength much greater than water depth) can be employed. The last assumption allows for dimensionality reduction, resulting in a 1-D system of equations, since now the $z$ component of the fluid velocity is considered negligible. The domain is divided into regions $S_0 \equiv (0,\, L)$ and $S_1 \equiv (L,\, \infty)$, with the hydroelastic coupling taking place at the former (Papathanasiou et al., 2015). In $S_0$, the plate deflection coincides with the water upper surface elevation $\eta(x,\, t)$. The fluid velocity potential in the two regions is denoted as $\varphi_0$ and $\varphi_1$ respectively. In order to account for the draft of the plate, the variable bathymetry function $b(x) = H(x) - d(x)$, where $B(x)$ is the water depth and $d(x) = \tau(x)\,\rho_\mathrm{i}/\rho_\mathrm{w}$ the draft of the plate, $\tau(x)$ being the plate thickness, is defined. The ice and water density are $\rho_\mathrm{i}$ and $\rho_\mathrm{w}$, respectively. The flexural rigidity of the plate is given by $D(x) = E\,\tau^3/12(1-\upsilon^2)$, with $E$ being the Young's Modulus of ice and $\upsilon$ the Poisson's ratio. The mass per unit length of the plate is denoted by $m(x) = \rho_\mathrm{i}\,\tau$. After introducing the non-dimensional variables $\widetilde{x} = x/L$, $\widetilde{\eta} = \eta/L$, $\widetilde{t} = t\sqrt{g\,L^{-1}}$, $\widetilde{\varphi_0} = \varphi_0\, g^{-1/2}\, L^{-3/2}$, $\widetilde{\varphi_1} = \varphi_1\, g^{-1/2}\, L^{-3/2}$ and dropping tildes, the governing system of differential equations is reduced to (see also Sturova, 2009),

$$M\ddot{\eta} + (K\eta_{xx})_{xx} + \eta + \dot{\varphi}_0 = 0, \quad x \in S_0 \tag{1}$$

$$\dot{\eta} + (B\varphi_{0x})_x = 0, \quad x \in S_0, \tag{2}$$

$$\ddot{\varphi}_1 - (B\varphi_{1x})_x = 0, \quad x \in S_1, \tag{3}$$

where a superimposed dot denotes differentiation with respect to time while an index following the a function denotes differentiation with respect to the spatial variable. In addition, the coefficients appearing in the above equations are defined as

$$K(x) = D(x)/\rho_\mathrm{w} g L^4, \quad M(x) = m(x)/\rho_\mathrm{w} L,$$
$$B(x) = b(x)/L.$$

The bending moment and shear force along the shelf are given by the expressions $M_\mathrm{b} = K\,\eta_{xx}$ and $V = (K\,\eta_{xx})_x$, respectively.

### 2.1 Stress distribution within the ice beam

In agreement with the Euler–Bernoulli beam model, the normal stress varies linearly along the $z$ direction. The maximum normal stress value at any given cross section is

$$\sigma_{xx}^{\max} = \frac{M_\mathrm{b}}{K}|z|_{\max} = |z|_{\max}\eta_{xx}. \tag{4}$$

The shear stress distribution, as derived from equilibrium relations, varies quadratically along the vertical direction. Maximum shear stress, located at the neutral fibre is,

$$\sigma_{xz}^{\max} = \frac{3}{2}\frac{V}{\tau/L} = \frac{3L}{2}\frac{K_x\eta_{xx} + K\eta_{xxx}}{\tau}. \tag{5}$$

The above system of equations is supplemented with boundary, interface and initial conditions. At the fixed end, simulating the ice shelf grounding line, the deflection and slope are set to zero. At the free edge of the plate, representing the ice shelf tip facing the ocean, zero bending moment and shear force is imposed. These conditions read

$$\eta(0,t) = \eta_x(0,t) = M_{\mathrm{b}}(1,t) = V(1,t) = 0. \tag{6}$$

The water velocity is assumed zero underneath the grounding line and thus the velocity potential gradient vanishes,

$$\varphi_{0x}(0,t) = 0. \tag{7}$$

At the interface between $S_0$ and $S_1$, assuming energy and mass conservation, the following matching conditions are derived (Stoker, 1957; Sturova, 2009):

$$\begin{aligned} B(1^-)\varphi_{0x}\left(1^-,t\right) &= B\left(1^+\right)\varphi_{1x}\left(1^+,t\right) \text{ and} \\ \dot{\varphi_0}\left(1^-,t\right) &= \dot{\varphi_1}\left(1^+,t\right). \end{aligned} \tag{8}$$

The ice shelf is assumed to be initially at rest, while an incoming long wave transverses region $S_1$ and reaches the free edge of the shelf. The initial boundary value problem formulation is thus completed with the following conditions,

$$\eta(x,0) = \dot{\eta}(x,0) = \varphi_{0x}(x,0) = 0, \quad x \in S_0 \text{ and} \tag{9a}$$

$$\varphi_{1x}(x,0) = 0, \quad \dot{\varphi_1}(x,0) = -F(x), \quad x \in S_1. \tag{9b}$$

In the last of Eq. (9b), $F(x)$ denotes the free surface elevation caused by the Tsunami wave at an initial time, at an area distant to the ice shelf edge.

## 3 Finite elements – variational formulation of the governing equations

In order to derive the variational formulation of the above problem, Eqs. (1)–(3) are multiplied by the weight functions $\nu$, $-w_0$ and $w_1$, respectively. Integration by parts yields

$$\begin{aligned} &\int_0^1 M\nu\ddot{\eta}\mathrm{d}x + \int_0^1 K\nu_{xx}\eta_{xx}\mathrm{d}x + \int_0^1 \nu\eta\mathrm{d}x + \int_0^1 \nu\dot{\varphi_0}\mathrm{d}x \\ &\quad + \left[\nu(K\eta_{xx})_x\right]_0^1 + \left[\nu_x K\eta_{xx}\right]_0^1 = 0, \end{aligned} \tag{10}$$

$$-\int_0^1 w_0\ddot{\eta}\mathrm{d}x - \left[Bw_0\varphi_{0x}\right]_0^1 + \int_0^1 Bw_{0x}\varphi_{0x}\mathrm{d}x = 0, \tag{11}$$

$$\int_1^\infty w_1\ddot{\varphi_1}\mathrm{d}x - \left[Bw_1\varphi_{1x}\right]_1^\infty + \int_1^\infty Bw_{1x}\varphi_{1x}\mathrm{d}x = 0. \tag{12}$$

Using the conditions described in Eqs. (6)–(8), and adding Eqs. (10)–(12) the equivalent semi-discrete variational problem is formulated as Papathanasiou et al. (2015).

Find $\eta$, $\varphi_0$ and $\varphi_1$, such that for every $\nu$, $w_0$ and $w_1$ at any given moment in time it holds

$$\begin{aligned} &\int_0^1 M\ddot{\eta}^h\nu^h\mathrm{d}x + \int_0^1 \nu^h\dot{\varphi_0}^h\mathrm{d}x - \int_0^1 w_0^h\ddot{\eta}^h\mathrm{d}x + \int_1^\infty w_1^h\ddot{\varphi_1}^h\mathrm{d}x \\ &\quad + a\left(\eta^h,\nu^h\right) + b_0\left(w_0^h,\varphi_0^h\right) + b_1\left(w_1^h,\varphi_1^h\right) = 0, \end{aligned} \tag{13}$$

where

$$a\left(\eta^h,\nu^h\right) = \int_0^1 \left(K\nu_{xx}^h\eta_{xx}^h + \nu^h\eta^h\right)\mathrm{d}x,$$

$$b_0\left(w_0^h,\varphi_0^h\right) = \int_0^1 Bw_{0x}^h\varphi_{0x}^h\mathrm{d}x,$$

and

$$b_1\left(w_0^h,\varphi_0^h\right) = \int_1^\infty Bw_{1x}^h\varphi_{1x}^h\mathrm{d}x,$$

while superscript $h$ denotes spatially discrete quantities.

A special hydroelastic element is developed and employed for the solution of Eq. (13). The reader is directed to the previous work by Papathanasiou et al. (2015) for more details concerning the proposed finite element scheme. The interpolation degree selected features 5th order Hermite polynomials for the beam deflection/upper surface elevation in the hydroelastic region and 4th order Lagrange polynomials for the approximation of the water velocity potential. Hence, within each element, $\eta(xt)$ and $\varphi_0(x,\,t)$ are approximated by $\eta^h = \sum_{i=1}^{6}\eta^i(t)\,H_i(x)$, $\varphi_0^h = \sum_{i=1}^{5}\varphi_0^i(t)\,L_i(x)$. Domain $S_1$ is discretized only in region $[1,\,R]$, where the positive constant $R \gg 1$ is selected large enough so that any disturbance propagating inside $S_1$ does not reach point $R$ within the time interval of interest. Fourth order Lagrange shape functions are used for the interpolation of the velocity potential $\varphi_1$. By substituting the above approximate solutions into Eq. (13) and letting the weight functions $\nu$ assume the form of the Hermite $C^1$ shape functions while $w_0$ and $w_1$ are substituted by the Lagrange $C^0$ shape functions, the resulting system is derived in the form, $\mathbf{M}\ddot{\boldsymbol{u}} + \mathbf{C}\dot{\boldsymbol{u}} + \mathbf{K}\boldsymbol{u} = 0$, with the vector of unknowns being $\boldsymbol{u} = [\eta\ \ \eta_x\ \ \varphi_0\ \ \varphi_1]^T$.

## 4 Results

In the present section, the simplistic, mechanical model described above will be employed for the calculation of the hydroelastic response of the Sulzberger Ice shelf under long wave forcing. The SIS is simulated by a semi-fixed plate of 100 km in length. For the employed bathymetric profile, mean depth values were used. In Brunt et al. (2011) it is mentioned that the water column depth in front of the ice-shelf is 150 m, while it increases to 800 m within 100 km from the ice shelf front. Thus, the ocean depth under the ice shelf is assumed to be 150 m, while a mildly sloping bottom is considered over a distance of 100 km from the edge of the ice shelf (see Fig. 1). The water depth increases from 150 m, at $x = 1$ to 800 m at $x = 2$ (Brunt et al., 2011). The initial, bell-shaped free-surface elevation considered in the following examples is

$$\eta_0 = A \exp\left(-x^{-\mu(x_0+w)^2} - x^{-\mu(x-x_0+w)(x-x_0-w)}\right), \quad (14)$$

where $A$ represents the amplitude, $x_0$ the origin location, $w$ the half-wavelength and $\mu$ a smoothness parameter controlling the steepness of the initial pulse. Finally, the material constants selected are as follows: ice shelf density $\rho_i = 922.5\,\mathrm{kg\,m^{-3}}$, water density $\rho_w = 1025\,\mathrm{kg\,m^{-3}}$, Young's modulus $E = 5 \times 10^9$ Pa and Poisson's ratio $v = 0.3$ (see also Sturova, 2009). The acceleration of gravity is $g = 10\,\mathrm{m\,s^{-2}}$. In the following analysis 400 hydroelastic elements have been used, while the number of elements in region $S_1$ is selected such that the element size is the same for both regions $S_0$ and $S_1$. Numerical experiments have shown that this discretization ensures convergence, as any further refinement induces virtually no variation of the results. Finally, the Newmark method has been employed for time integration. The non-dimensional time interval $T = 70$ (corresponding to 7000 s) is considered.

At first, the effects of an initial pulse with $A = 0.5$ m, $\mu = 50 \times 10^5\,\mathrm{m^{-2}}$ and $w = 8000$ m are considered. In Fig. 1, a visual representation of the given pulse propagation is plotted. The bell-shaped disturbance is split into two waves travelling in opposite directions. The pulse propagating to the left (towards the negative $x$ axis) is partially reflected when reaching the bathymetric variation at $x = 2$. As the wave propagates over decreasing depth, its amplitude increases, while the velocity decreases. The velocity reduction is evident in the curved trajectory path for $1 \le x \le 2$, as shown in Fig. 1. At $x = 1$, the wave impacts the ice shelf free edge, initiating the propagation of the hydroelastic wave while it is partially reflected. The hydroelastic wave, featuring dispersive characteristics, is fully reflected at the grounding line (fixed end, $x = 0$), at $t \approx 67$. The dispersive nature of the hydroelastic pulse can also be seen in Figs. 2 and 3, manifested as the formation of smaller disturbances preceding the main elevation wave. These disturbances reach the grounding line at earlier times than the main pulse and lead to an increase of

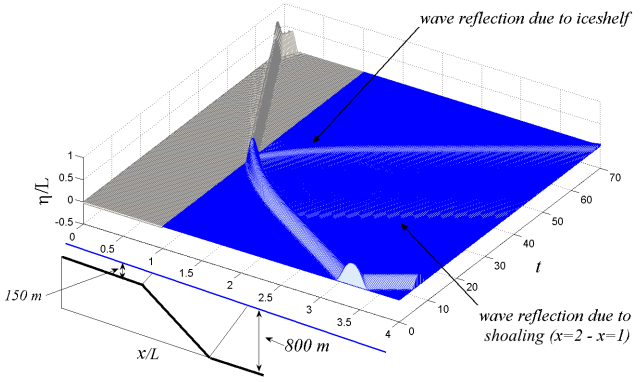


**Figure 1.** Space-Time plot of the bell-shaped pulse propagation. The bathymetric profile is shown in a schematic below. All dimensions are normalized with respect to the plate length $L = 100$ km.

the bending moment locally. This phenomenon is displayed in the maximum and minimum bending moment time profiles (Figs. 2 and 3) as spikes, located at $x = 0$ and appearing in the time interval from $t \approx 55$ to $t \approx 65$.

The present analysis aims to provide some first and simple means for the estimation of long wave impact on floating, slender formations and their response, as a first step towards the hydroelastic modelling of ice shelves. As illustrated in Fig. 1, phenomena, such as wave reflection, hydroelastic dispersion, bending moment variation are well reproduced. In order to investigate the generated stress field within the floating body, the bending moment distribution is examined. Bending moment distributions are directly linked to maximum normal stress values. In particular, for notched or pre-cracked specimens it is usually those normal stresses that mostly influence crack initiation and propagation. The latter phenomena are crucial when a pre-existing crack happens to be inside a tensile zone of large magnitude.

Typically, for the bending of thin beams, the normal stresses due to bending are dominant and as a first approach, shear stresses may be neglected. In Figs. 2 and 3 the maximum and minimum bending moment temporal and spatial distributions are shown. For the maximum bending moment, the temporal distribution is shown in a thick red line, while the location of the corresponding values along the ice shelf is given by the thin black line (Fig. 2). When at rest, the maximum bending moment is zero in absence of flexural effects. Immediately after impact, $t \approx 30$ the maximum bending moment is seen to increase. The location of the maximum bending moment value is found to follow the main pulse towards the fixed end. At $t = 34$, the entire pulse has passed underneath the floating cantilever, causing an increase in maximum bending moment. At the same time, the location of the maximum value for the bending moment is shifted back near the free edge. This is due to the fact that the entire wavelength of the initial pulse has passed underneath the floating cantilever, causing the tip to bend again as it recovers

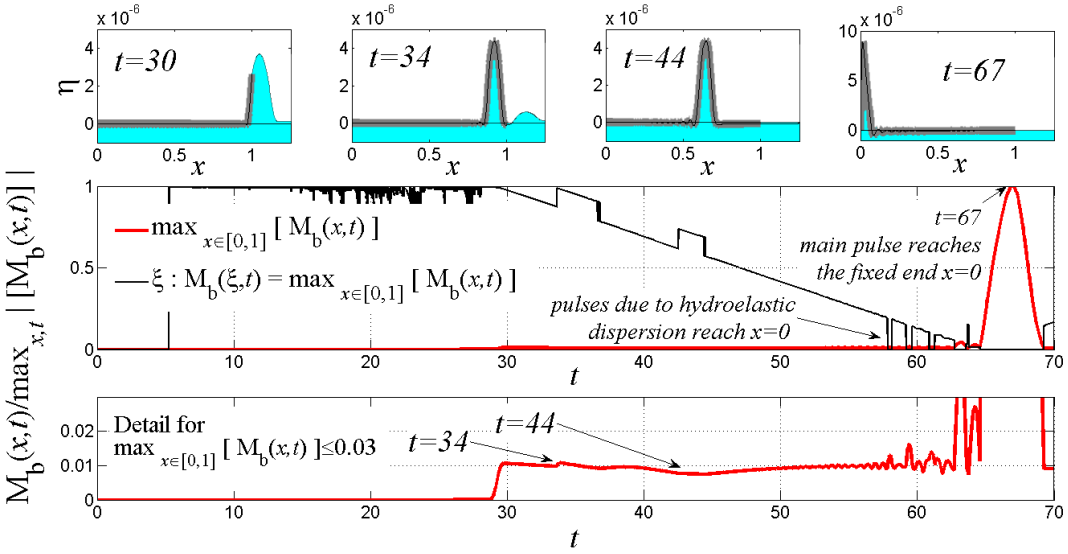


**Figure 2.** Maximum bending moment temporal profile (red thick line) and location of corresponding values along the floating cantilever (black line). A detailed figure of the profile after the wave impact is presented, along with representative snapshots of the deformed ice shelf.

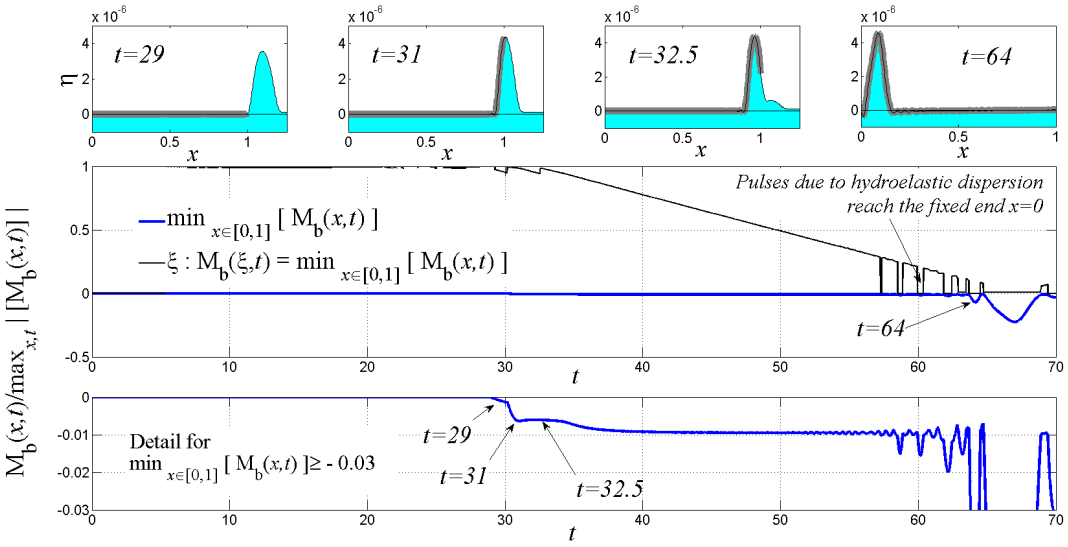


**Figure 3.** Minimum bending moment temporal profile (blue thick line) and location of corresponding values along the floating cantilever (black line). A detailed figure of the profile after the wave impact is presented, along with representative snapshots of the deformed ice shelf.

to the initial undeformed state. At $t = 44$ the location of the maximum bending moment value is shifted towards the ice shelf tip once again. The above can be attributed to flexural effects taking place at the right side of the propagating disturbance. As the hydroelastic wave propagates away from the free edge, the tip is restored to its original position causing additional flexing in the interior of the cantilever. Due to the fact that, in the present work, the grounding line is simplistically modelled as a fixed boundary, the global bending moment extrema are found at the fixed edge, at the time of reflection $t = 67$. Prior to full reflection, a series of spikes in the maximum bending moment distribution are caused by the dispersed hydroelastic waves reaching the fixed edge before the main pulse.

As shown in Fig. 3, the minimum bending moment intensifies until the entire pulse wavelength has passed under the floating cantilever, at which point the minimum bending moment value remains virtually constant up to the arrival of the dispersed wave train at the fixed edge.

Notably, the notion that the pulse will reach the fixed end is rather unrealistic. The induced flexural effects will cause the bending failure of the semi-fixed floating body long before the hydroelastic pulse arrives at the grounding line. As seen in Figs. 2 and 3, the maximum and minimum bending

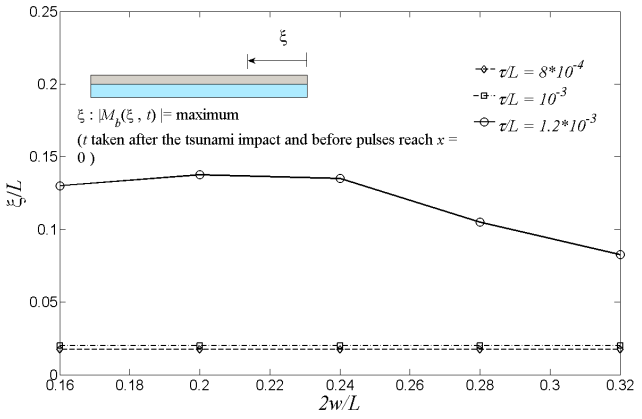


**Figure 4.** Location of extreme bending moment along the semi-fixed floating body for various values of thickness and initial disturbance wavelength. Variable $\xi$ measures the distance of the point of occurrence of the extreme value from the free edge.

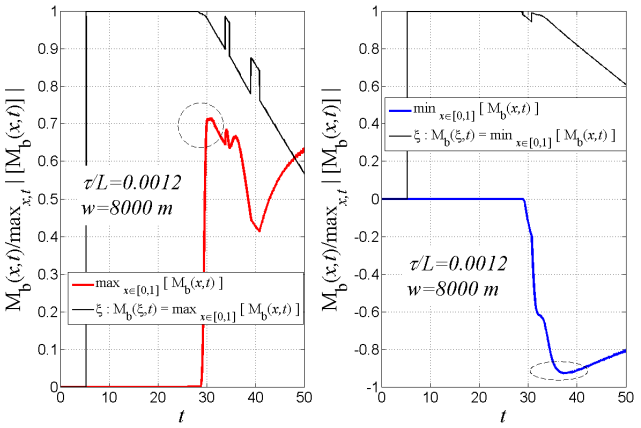


**Figure 5.** Plot of maximum and minimum bending moment value distributions for $w = 8000$ m and $\tau/L = 0.0012$. Extreme bending moment value is negative, during the entry phase, for an ice shelf thickness value of 120 m.

moment values reach a plateau approximately after the full disturbance passes underneath the ice shelf. Considering the effects before the hydroelastic wave train reaches the grounding line, namely for short times after the long wave impact, the corresponding location of the given extreme bending moment value along the ice shelf may be linked to both ice shelf thickness and initial disturbance form. Figure 4 displays a parametric study of the extreme bending moment value location for different ice shelf thickness and tsunami wavelength values. Variable $\xi$ denotes the distance from the free edge up to the location of the extreme value along the semi-fixed floating body $x = 1$. In all cases, the extreme bending moment values have been considered in a time interval excluding the effects of the fixed end forcing ($t \geq 50$). In that manner, Fig. 4 demonstrates the location of extreme bending moments for the phase during which the main pulse enters the region of hydroelastic interaction. As can be seen in the aforementioned figure, the location of the extreme bending moment is relatively insensitive to variations of the wavelength. For thickness values of 80 and 100 m, this location is found to be at about 2 % of the ice shelf length (2 km into the 100 km long ice shelf), calculated from the free edge. The above results are found in agreement with the work of Squire (1993), where the breakup of shore fast ice, modelled as a semi-infinite, thin floating plate, is investigated in the frequency domain. Furthermore, as thickness increases, the location of extreme values seems to shift towards the interior of the ice shelf. For a thickness of 120 m, location $\xi$ is placed at approximately 10 % of the ice shelf length and features a slight variation with increasing initial disturbance wavelength. However, this variation is very small when compared to the total length of the beam. Another interesting feature is that in this last case (120 m thickness) the maximum absolute value found corresponds to negative values of the bending moment (see Fig. 5), whereas for thickness values of 80 and 100 m the maximum absolute bending moment values are found to be positive (sagging moments). This feature explains the different shape of the 120 m curve in Fig. 4, when compared to the curves corresponding to 80 and 100 m, which closely resemble one another. The fact that in the case of 120 m the extreme bending moment values are negative might be attributed to the beam thickness being very large compared to the water depth under the ice shelf. Finally, these results are strongly dependent on the form of the incoming wave, in the sense that if another wave profile instead of an elevation pulse is chosen, the bending moment fields will be of a different nature.

## 5 Conclusions

In the present work, the transient hydroelastic response of a semi-fixed floating cantilever, resembling an ice shelf, is studied by means of a higher order finite element scheme. The simple model derived above is able to provide valuable information regarding the kinematic and stress fields induced by long wave forcing on an ice shelf. An illustrative case study is presented with parameters selected so as to approximately simulate the Sulzberger Ice Shelf topology and the relevant calving event conditions, initiated by the 2011 Honshu Tsunami. Bending moment profiles, as generated by a long wavelength elevation pulse, are studied and critical points of the induced stress field are located. During the wave entry in the hydroelasticity dominated region, the locations of extreme bending moments is found to be relatively insensitive to the excitation wavelength for given ice shelf thickness values. Important extensions of the present study include 3-D hydroelastic interaction, as well as the investigation nonlinearity effects of both in the hydrodynamic model and in the elastic subregion. Finally, the study of tsunami-ice interaction in the run-up stage constitutes another possible

future research direction in the context of the present model applications.

*Acknowledgements.* The present work has been supported by the project HYDELFS funded by the Operational Program "Education and Lifelong Learning" of the National Strategic Reference Framework (NSRF 2007-2013) -Research Funding Program ARHIMEDES-III: Investing in knowledge society through the European Social Fund. In particular, author Theodosios K. Papathanasiou acknowledges support from the aforementioned program for the period from 6 September 2012 to 30 September 2014.

Edited by: I. Didenkulova
Reviewed by: E. Pelinovsky and another anonymous referee

## References

Belibassakis, K. A. and Athanassoulis, G. A.: A coupled-mode model for the hydroelastic analysis of large floating bodies over variable bathymetry regions, J. Fluid Mech., 531, 221–249, 2005.

Bhattacharjee, J. and Guedes Soares, C.: Flexural gravity wave over a floating ice sheet near a vertical wall, J. Eng. Math., 75, 29–48, 2012.

Brocklehurst, P., Korobkin, A. A., and Părău, E. I.: Interaction of hydro-elastic waves with a vertical wall, J. Eng. Math., 68, 215–231, 2010.

Bromirski, P. D. and Stephen, R. A.: Response of the Ross Ice shelf, Antarctica, to ocean-gravity wave forcing, Ann. Glaciol., 53, 163–172, 2012.

Bromirski, P. D., Sergienko, O. V., and MacAyeal, D. R.: Transoceanic infragravity waves impacting Antarctic ice shelves, Geophys. Res. Lett., 37, L02502, doi:10.1029/2009GL041488, 2010.

Brunt, K. M., Okal, E. A., and MacAyeal, D. R.: Antarctic ice shelf calving triggered by the Honsu (Japan) Earthquake and tsunami, March 2011, J. Glaciol., 57, 785–788, 2011.

Kaistrenko, V., Razjigaeva, N., Kharlamov, A., and Shishkin, A.: Manifestation of the 2011 Great Tohoku Tsunami on the Coast of the Kuril Islands: A Tsunami with Ice, Pure Appl. Geophys., 170, 1103–1114, 2013.

Meylan, M. H. and Sturova, I. V.: Time-dependent motion of a two-dimensional floating elastic plate, J. Fluid Struct., 25, 445–460, 2009.

Papathanasiou, T. K., Karperaki, A., Theotokoglou, E. E., and Belibassakis, K. A.: A higher order FEM for time-domain hydroelastic analysis of large floating bodies in an inhomogeneous shallow water environment, P. Roy. Soc. A, 471, 20140643, doi:10.1098/rspa.2014.0643, 2015.

Scambos, T., Hulbe, C., and Fahnestock, M.: Climate-Induced ice shelf disintegration in the Antarctic Peninsula, in: Antarctic Peninsula Climate Variability: Historical and Paleoenvironmental Perspectives, edited by: Domack, E., Levente, A., Burnet, A., Bindschadler, R., Convey, P., and Kirby, M., American Geophysical Union, Washington, D.C., 79–92, doi:10.1029/AR079p0079, 2003.

Sergienko, O. V.: Elastic response of floating glacier ice to impact of long-period ocean waves, J. Geophys. Res., 115, F04028, doi:10.1029/2010JF001721, 2010.

Skvarca, P., Rack, W., Rott, H., and Ibarzábal y Donángelo, T.: Climatic trend, retreat and disintegration of ice shelves on the Antarctic Peninsula: an overview, Polar Res., 18, 151–157, 1999.

Squire, V. A.: The breakup of shore-fast ice, Cold Reg. Sci. Technol., 21, 211–218, 1993.

Squire, V. A.: Of ocean waves and sea-ice revisited, Cold Reg. Sci. Technol., 49, 110–133, 2007.

Stoker, J.: Water Waves: The mathematical Theory with Applications, Wiley-Interscience, New York, 1957.

Sturova, I. V.: Time-dependent response of a heterogeneous elastic plate floating on shallow water of variable depth, J. Fluid Mech., 637, 305–325, 2009.

Sturova, I. V., Korobkin, A. A., Fedotova, Z. I., Chubarov, L. B., and Komarov, V. A.: Nonlinear dynamics of non-uniform elastic plate floating on shallow water of variable depth, Proceedings of the 5th International Conference on Hydroelasticity, Southampton, UK, 2010.

Tkacheva, L. A.: Interaction of surface and flexural gravity waves in ice cover with a vertical wall, J. Appl. Mech. Tech. Phys., 54, 651–661, 2013.

Watanabe, E., Utsunomiya, T., and Tanigaki, S.: A transient response analysis of a very large floating structure by finite element method, Struct. Eng. Earthq. Eng., 15, 155–163, 1998.

Young, I. R., Zieger, S., and Bahanin, V.: Global Trends in Wind Speed and Wave Height, Science, 332, 451–455, 2011.

Procedia Computer Science

Volume 66, 2015, Pages 122–131

YSC 2015. 4th International Young Scientists Conference on Computational Science

# FEM hydroelastic models with application to the nonlinear response of large floating bodies in shallow wave conditions

Angeliki E. Karperaki[1]

[1]*School of Naval Architecture and Marine Engineering, National Technical University of Athens, Athens, Greece*

*karperaki.ang@gmail.com*

**Abstract**

A higher order finite element scheme is presented for the study of the transient hydroelastic response of a floating, thin, nonlinear strip in shallow wave conditions. First, nonlinear effects are introduced only in the elasticity model, where large deflections and non-negligible normal stress variation in the lateral direction are assumed. The nonlinear beam is initially coupled with the linearized and subsequently with the full nonlinear Shallow Water equations, introducing nonlinearity in both the hydrodynamics and the elasticity model. The effects of the incorporated nonlinear effects are assessed through a numerical example featuring an elevation pulse of increasing steepness.

*Keywords:* transient hydroelasticity, large floating bodies, Shallow Water Equations, Galerkin FEM, nonlinear floating elastic strip

## 1 Introduction

The study of the hydroelastic interaction between ocean waves and large floating bodies is highly relevant to both marine engineering and polar science (Squire, 2008) . Geophysical formations and pontoon-type Very Large Floating Structures (or VLFS) exhibit large horizontal dimensions compared to thickness. Due to their slenderness, hydroelastic effects are dominant over rigid body motion (Wang, Watanabe, & Utsunomiya, 2008). The majority of works on hydroelasticity consider the response of a thin, floating body in the frequency domain where eigenfunction expansion methods, Galerkin schemes and Green functions have been used (Chen, Wu, Cui, & Juncher Jensen, 2006). In order to account for irregular forcing however, transient analysis tools, like direct time integration schemes and Fourier transforms need to be employed. Some contributions in the study of the transient hydroelastic response of a floating strip include those of Papathanasiou *et al*. (2015 (a)), (2015 (b)) and Sturova *et al*. (2010). In the literature, floating bodies are most commonly modeled as thin plates under the Kirchhoff-Love assumptions ( (Meylan & Squire, 1994), (Sturova, A., Fedotova, Chubarov, & Komarov, 2010),

 Selection and peer-review under responsibility of the Scientific Programme Committee of YSC 2015


doi:10.1016/j.procs.2015.11.015

(Papathanasiou T. , Karperaki, Theotokoglou, & Belibassakis, 2015 (b))). However, several attempts have been made to include higher order elasticity models like the Reissner-Mindlin or the Von Karman plates (Chen, Juncher Jensen, Cui, & Fu, 2003). For the hydrodynamic modeling, small amplitude wave theory is most commonly used. Special attention is paid in shallow water models, since a variety of engineering applications positions floating structures nearshore, making shallow and variable bathymetry effects crucial. For the hydroelastic response of large floating bodies over general bathymetry, modelled as thin elastic plates, a coupled-mode system has been derived in Belibassakis and Athanassoulis in (2005) and Belibassakis and Athanassoulis (2006). This method is based on a local vertical expansion of the wave potential in terms of hydroelastic eigenmodes, extending earlier approaches for the propagation of water waves in variable bathymetry regions (Athanassoulis & Belibassakis, 1999).

Several attempts have been made to study the dynamic response of floating plates within the scope of shallow water models; notably in Sturova *et al*. (2010) the linear plate is coupled with two Boussinesq-type models, and the Green-Naghdi equations, while in Hegarty and Squire (2004) nonlinear models are developed for the study of the hydroealstic interaction between large amplitude ocean waves and a thin ice floe. In this latter work, nonlinear terms are introduced in both the equations for the fluid and the plate model.

In the present contribution, the finite element method is employed for the solution of the transient 1D hydroelastic problem over variable, shallow bathymetry. At first, nonlinear effects are incorporated in the simplified elasticity model, while the linearized shallow water equations are employed for the hydrodynamic modeling. Considering large deflections and non-negligible lateral stress variation, the nonlinear beam introduced by Gao (1996), is considered. Next, nonlinearity is also incorporated in the hydrodynamic modeling through the employment of the full Shallow Water equations. The derived nonlinear models are compared against the Euler-Bernoulli floating beam model presented in Papathanasiou *et al*. (2015 (b))

In Sect. 2, after presenting the governing equations and the aforementioned nonlinear models, the corresponding initial-boundary value (IBV) hydroelastic problems are defined. Subsequently, in Sect. 3 the variational equivalent of the IBV problems will be derived, while the higher-order finite element scheme used for the solution of these problems is presented. In Sect. 4 the solutions given by the nonlinear models are examined in a numerical example featuring variable bathymetry. Different excitation steepness values are considered in order to examine the dominance of the incorporated nonlinear terms.

# 2 Governing Equations

In the present section the mathematical formulation of the 1D hydroelastic model is presented. Consider a layer of inviscid and irrotational fluid of density $\rho_w$ , confined in the domain $\Omega$ (see Figure 1) in the $xz$ plane. The domain is decomposed into three regions, namely $\Omega_1 \equiv (-\infty,0)$ , $\Omega_0 \equiv (0,L)$ and $\Omega_2 \equiv (L,\infty)$ , where $L$ is the length of the strip. Due to the fluid assumptions, a velocity potential function $\phi$ can be defined as $u = \partial_x \phi$ where $u$ denotes the horizontal fluid velocity. The floating plate is assumed to extend infinitely in the $y$ direction, vertical to the page, corresponding to a beam under normal incident wave loading. The beam deflection and the fluid upper surface elevation are assumed to coincide at all times. Additionally, the floating strip features uniform thickness $\tau$ and density $\rho_e$ .The bathymetry function is given as $b(x) = h(x) - d$ , where $h(x)$ is the local depth and $d = \rho_w^{-1}\rho_e\tau$ is the plate draft, which is non-zero only at the region of the hydroelastic coupling. At the free water surface regions, the Shallow Water Equations (SWE) are considered,

$$\partial_t u + u\partial_x u + g\partial_x \eta = 0, \tag{1}$$

$$\partial_t \eta + \partial_x \left( [b(x) + \eta] \partial_x \phi \right) = 0 \tag{2}$$

With the added assumption of small steepness waves, the linearised Shallow Water Equations (LSWE) are straightforwardly derived by excluding the nonlinear terms in Eqs. (1) and (2). In the hydroelasticity dominated region the coupling is accomplished through the dynamic pressure applied at the floating strip, given by

$$p = \rho_w g\eta + \rho_w \partial_t \phi + \frac{\rho_w}{2} \left( \partial_x \phi \right)^2 \tag{3}$$

For the floating body, the nonlinear elastic beam model introduced by Gao (Gao, 1996) will be examined in the following analysis, while the floating Euler-Bernoulli beam (EB) will provide a linear benchmark solution. In the classical beam theory, the deflection of a thin, elastic and homogeneous floating body under vertical loading, denoted by $q(x,t)$ ,and pressure forcing given by the linearized Eq. (3), is given by

$$m\partial_t^2 \eta + D\partial_x^4 \eta + \rho_w g\eta + \rho_w \partial_t \phi = -q(x,t) \tag{4}$$

The fully linear EB-LSW model, presented in Papathanasiou *et al*. (2015 (b)) will provide the basis for the assessment of the incorporated nonlineariaty. The first term (LHS) in Eq. (4) accounts for inertial effects, where $m$ is the mass per unit length of the floating body, while the second term accounts for flexural effects and $D$ denotes the bending rigidity of the beam. The Gao beam (GB) model (Gao, 1996) accounts for moderately large deflections, where the deflection is assumed to be of the same order of magnitude as the strip slenderness ratio $\tau/L$ , and non-negligible normal stress variation in the lateral (axial) direction. In GB, with zero axial loading present, the deflection of the floating beam over shallow water is given by,

$$m\partial_t^2 \eta - I_r \partial_t^2 \partial_x^2 \eta + D\partial_x^4 \eta - s(\partial_x \eta)^2 \partial_x^2 \eta + \rho_w g\eta + \rho_w \partial_t \phi + \frac{\rho_w}{2} \left( \partial_x \phi \right)^2 = -q(x,t) \tag{5}$$

In addition to the inertial and bending rigidity terms, which are similar to EB, rotary inertia effects are accounted through the term $-I_r \partial_t^2 \partial_x^2 \eta$ , where $I_r$ is the rotary stiffness coefficient. The nonlinear term $-s(\partial_x \eta)^2 \partial_x^2 \eta$ , with $s = 3E\tau(1-\nu^2)^{-1}/2$ , is a product of the large deflection assumption, where up to second order strain terms are kept in the Green-St. Venant strain tensor.

## 2.1 Initial Boundary Value problems

In the following section, the IBV problems of a freely-floating nonlinear strip, interacting with a surface wave propagating in a shallow water environment, modeled first by the linearized and then by the full shallow water equations, are formulated.

The horizontal velocity vanishes at infinity, hence it holds

$$\partial_x \phi_1 (|x| \to \infty, t) = \partial_x \phi_2 (|x| \to \infty, t) = 0 \tag{6}$$

The unconstrained floating body configuration results in vanishing conditions for the shear stress and bending moments at the beam edges,

$$M_b(0,t) = V(0,t) = M_b(1,t) = V(1,t) = 0 \; t \in (0,T] \tag{7}$$

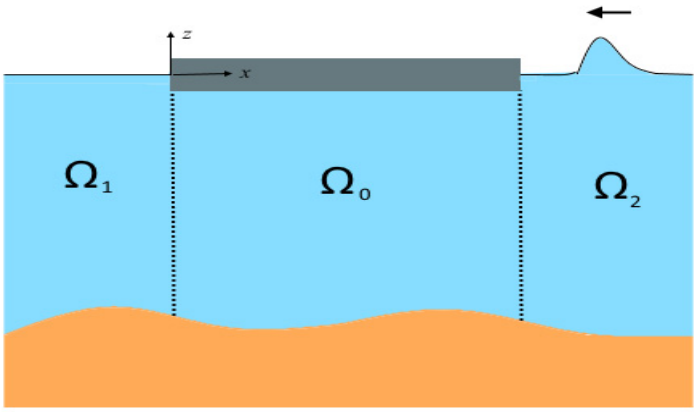


**Figure 1** 1D hydroelastic domain configuration

Introducing the non-dimensional quantities $\tilde{x}=L^{-1}x$ , $\tilde{t}=g^{1/2}L^{-1/2}t$ , $\tilde{\eta}=L^{-1}\eta$ and $\tilde{\phi}=g^{-1/2}L^{-3/2}\phi$, and considering the corresponding non dimensional forms of the equations (1)-(5), two IBVPs can be defined. The problem defined by the weekly nonlinear GB-LSW model is given as,

$$\partial_t^2\phi_1-\partial_x\left(B(x)\partial_x\phi_1\right)=0 \quad \text{in } \Omega_1\,, \tag{8}$$

$$M\varepsilon\partial_t^2\eta_0-I_R\varepsilon^3\partial_t^2\partial_x^2\eta_0+\varepsilon^3K\partial_x^4\eta_0-\varepsilon S(\partial_x\eta_0)^2\partial_x^2\eta_0 +\eta_0+\partial_t\phi_0+=Q(x,t) \tag{9a}$$

$$\partial_t\eta+\partial_x\left(B(x)\partial_x\phi_0\right)=0 \quad \text{in } \Omega_0\,, \tag{9b}$$

$$\partial_t^2\phi_2-\partial_x\left(B(x)\partial_x\phi_2\right)=0 \text{ in } \Omega_2\,. \tag{10}$$

with $\eta_i=-\partial_t\phi_i$, $i=1,2$, $M=\rho_e/\rho_w$, $B(x)=L^{-1}b(x)$, $\varepsilon=\tau/L\ll 1$ and $Q(x,t)=-q(x,t)\left(\rho_w gL\right)^{-1}$.

At the interfaces, appropriate mass and momentum conservation conditions are expressed as

$$B(0^-)\partial_x\phi_1\big|_{x=0^-}=B(0^+)\partial_x\phi_0\big|_{x=0^+}\,,\ \partial_t\phi_1\big|_{x=0^-}=\partial_t\phi_0\big|_{x=0^+}\,,\ t\in(0,T] \tag{11a}$$

$$B(1^-)\partial_x\phi_0\big|_{x=1^-}=B(1^+)\partial_x\phi_2\big|_{x=1^+}\,,\ \partial_t\phi_0\big|_{x=1^-}=\partial_t\phi_2\big|_{x=1^+}\ t\in(0,T] \tag{11b}$$

Finally, the GB-SW hydroelastic model, where nonlinear terms are included in both hydrodynamic and elasticity models constitutes the following IBV problem,

$$\partial_t^2\phi_1+2^{-1}\partial_t\left(\partial_x\phi_1\right)^2-\partial_x\left(B(x)\partial_x\phi_1\right)+\frac{1}{2}\partial_x\left(\partial_x\phi_1\right)^3+\partial_x\left(\partial_t\phi_1\partial_x\phi_1\right)=0\,,\ \text{in } \Omega_1 \tag{12}$$

$$M\varepsilon\partial_t^2\eta_0-I_R\varepsilon^3\partial_t^2\partial_x^2\eta_0+\varepsilon^3K\partial_x^4\eta_0-\varepsilon S(\partial_x\eta_0)^2\partial_x^2\eta_0 +\eta_0+\partial_t\phi_0+\frac{1}{2}\left(\partial_x\phi_0\right)^2=Q(x,t) \tag{13a}$$

$$\partial_t\eta+\partial_x\left([B(x)+\eta_0]\partial_x\phi_0\right)=0\ \text{, in } \Omega_0\,, \tag{13b}$$

$$\partial_t^2\phi_2+\frac{1}{2}\partial_t\left(\partial_x\phi_2\right)^2-\partial_x\left(B(x)\partial_x\phi_2\right)+\frac{1}{2}\partial_x\left(\partial_x\phi_2\right)^3+\partial_x\left(\partial_t\phi_2\partial_x\phi_2\right)=0\text{ , in }\Omega_2\text{ .} \tag{14}$$

with $\eta_i=-\partial_t\phi_i-\frac{1}{2}\left(\partial_x\phi_i\right)^2$ , $i=1,2$ , $I_R=\frac{\rho_e}{12\rho_w}$ , $S=\frac{3E}{2(1-v^2)\rho_w gL}$ and $K=\frac{E(1-v)}{12(1+v)(1-2v)\rho_w gL}$ .

The interface conditions (11) are reformulated as

$$\left(B(0^-)+\eta_1(0^-,t)\right)\partial_x\phi_1\big|_{x=0^-}=\left(B(0^+)+\eta_0(0^+,t)\right)\partial_x\phi_0\big|_{x=0^+}\ \ \partial_t\phi_1\big|_{x=0^-}=\partial_t\phi_0\big|_{x=0^+} \tag{15a}$$

$$\left(B(1^-)+\eta_0(1^-,t)\right)\partial_x\phi_0\big|_{x=1^-}=\left(B(1^+)+\eta_2(1^+,t)\right)\partial_x\phi_2\big|_{x=1^+}\ \ \partial_t\phi_0\big|_{x=1^-}=\partial_t\phi_2\big|_{x=1^+} \tag{15b}$$

Initially the plate and fluid are assumed to be at rest while an upper surface elevation is imposed at the right half strip, corresponding to the following initial conditions

$$\eta_0(x,0)=\phi_0(x,0)=0\text{ in }\Omega_0\text{ , }\ \phi_1(x,0)=\partial_t\phi_1(x,0)=0\ \text{ in }\Omega_1\text{ and}$$

$$\phi_2(x,0)=0,\partial_t\phi_2(x,0)=-G(x)\text{ in }\Omega_2 \tag{16}$$

where $G(x)$ is an upper surface elevation imposed in subregion $\Omega_2$ .

# 3 Variational formulation

In the present section, the equivalent variational formulations of the IBVPs defined previously will be presented. First, the systems of Eqs. (8) - (10) and (12)-(14) are multiplied by the weight functions $w_1\in H^1(\Omega_1)$ , $v\in H^2(\Omega_0)$ and $w_2\in H^1(\Omega_2)$ accordingly. Then, performing integration by parts, adding the corresponding equations and applying the appropriate interface and farfield conditions, yields the following variational problem,

*Find* $\eta_0$ *and* $\phi_i$ , $i=0,1,2$ , *such that for every* $w_i\in H^1(\Omega_i)$ , $i=0,1,2$ *and* $v\in H^2(\Omega_0)$ *it is*

$$\begin{aligned}
&\int_{-\infty}^{0}\left[w_1\partial_t^2\phi_1+\lambda w_1\partial_x\phi_1\partial_{tx}^2\phi_1+\partial_x w_1B(x)\partial_x\phi_1-\frac{\lambda}{2}\partial_x w_1\left(\partial_x\phi_1\right)^3-\lambda\partial_x w_1\partial_t\phi_1\partial_x\phi_1\right]dx\\
&+\int_0^1\left[M\varepsilon v\partial_t^2\eta_0+I_R\varepsilon^3\mu\partial_x v\partial_t^2\partial_x\eta_0+\varepsilon^3K\partial_x^2v\partial_x^2\eta_0+\frac{\varepsilon S\mu}{3}\partial_x v(\partial_x\eta_0)^3\right]dx\\
&+\int_0^1\left[v\eta_0+v\partial_t\phi_0+\frac{\mu}{2}v\left(\partial_x\phi_0\right)^2-w_0\partial_t\eta_0+\partial_x w_0[B(x)+\lambda\eta_0]\partial_x\phi_0\right]dx\\
&+\int_1^{+\infty}\left[w_2\partial_t^2\phi_2+\lambda w_2\partial_x\phi_2\partial_{tx}^2\phi_2+\partial_x w_2B(x)\partial_x\phi_2-\frac{\lambda}{2}\partial_x w_2\left(\partial_x\phi_2\right)^3-\lambda\partial_x w_2\partial_t\phi_2\partial_x\phi_2\right]dx\\
&=\int_0^1vQ(x,t)dx,\quad \mu,\lambda=0,1
\end{aligned} \tag{17}$$

*and* $(\phi_1(x,0),w_1)_1=(\phi_0(x,0),w_0)_0=(\phi_2(x,0),w_2)_2=0$ , $(\eta_0(x,0),w_0)_0=(\partial_t\varphi_1(x,0),w_1)_1=0$ , $\left(\partial_t\phi_2(x,0),w_2\right)_2=-\left(G(x),w_2\right)_2$ , with $(\ ,\ )_i$ , $i=0,1,2$ being the $L^2$ -inner product in region $\Omega_i$ .

Setting $\lambda = 0$ and $\mu = 1$ retrieves the variational formulation of the GB-LSW IBV problem, while setting $\lambda = 1$ and $\mu = 1$ results in the variational equivalent of the GB-SWE IBV problem. Notably, setting $\lambda = 0$ $\mu = 0$, Eq. (17) reduces to the variational equivalent of the linear hydroelastic problem formulated by means of the EB-LSW model.

## 3.1 Finite element formulation

Next, the finite element method will be employed for the numerical solution of the variational problem described by Eq. (17). The velocity potential of the free water surface regions are approximated by quadratic Lagrange elements while a special, 5-node element is introduced for the hydroelasticity dominated region. The reader is directed to the work of Papathanasiou *et al*. (2015 (b)) for a more in depth analysis. The hydroelastic element incorporates 5th order Hermite polynomials for the interpolation of the beam deflection/upper surface elevation in the middle region and 4th order Lagrange polynomials for the interpolation of the velocity potential. Hence the approximate solutions are taken as, $\eta^h = \sum_{i=1}^{6} H_i(x)\eta_i^h(t)$ for the middle region and $\varphi_j^h = \sum_{i=1}^{5} L_i(x)\varphi_{ij}^h(t)$, $j = 1,2$ for the free water surface regions. A second order system of ordinary differential equation is derived when the approximate solutions are substituted into a discretized Eq. (17). In the weakly nonlinear GB-LSW model case, the system is given as $\mathbf{M}\ddot{u} + \mathbf{C}\dot{u} + \mathbf{K}(u)u = 0$, where $u$ is the vector of the nodal unknowns, while a system of the form $\mathbf{M}\ddot{u} + \mathbf{C}(u)\dot{u} + \mathbf{K}(u)u = 0$ is produced by the GB-SW model. After setting $\dot{u} = y$ and taking $\mathbf{z} = [u \ y]^{\mathrm{T}}$, the previous is reduced to the first order system of nonlinear equations, $\mathbf{A}\dot{z} + \mathbf{B}(z)z = 0$. This last equation is integrated in time using a Crank-Nicolson time marching scheme.

# 4 Numerical Results

In the present section, the three hydroelastic models are compared in a numerical example featuring variable bathymetry (see Figure 2). An incoming elevation pulse, typical in long wave modeling (Tadepalli & Synolakis, 1996), provides the initial excitation. Since the scope of the present work is to give a preliminary assessment of the accounted nonlinear effects, a single slenderness ratio $\varepsilon = \tau / L$ for the floating body is investigated .The wavelength for both examined excitation scenarios is set at $W = 300m$ and the amplitude is taken as $A = 0.4$ and $0.8m$, thus the examined wave steepness ratios are set to $A/W = 0.0013$ and $0.0027$.

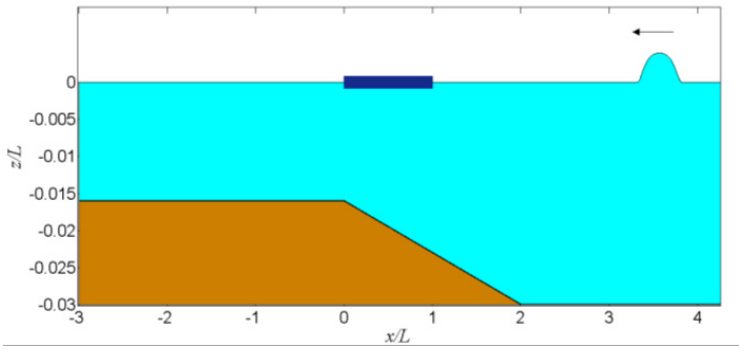


**Figure 2** Numerical example configuration

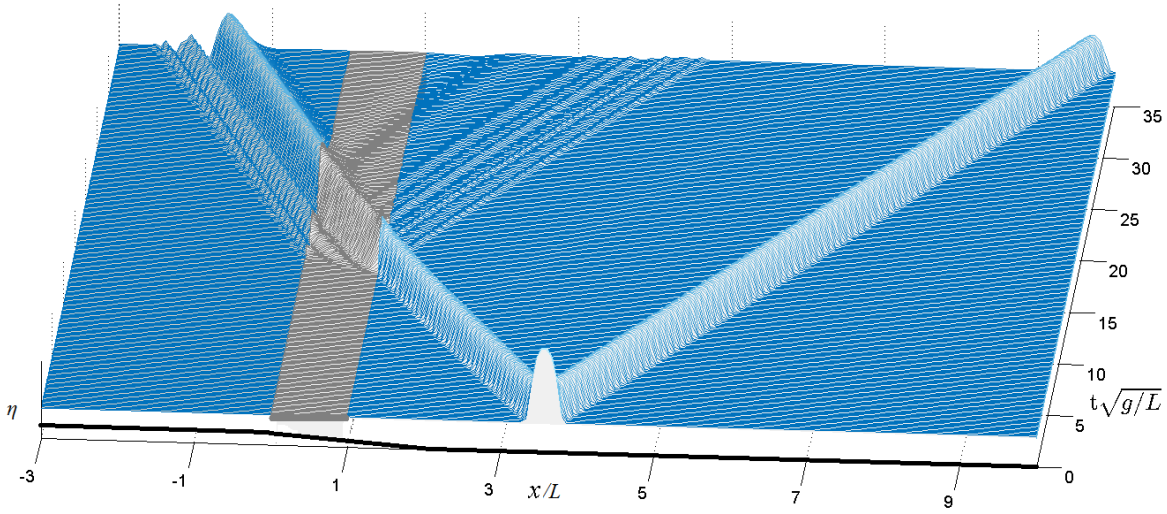


**Figure 3** Space time plot of the elevation pulse propagation

The incoming forcing initially transverses over a flat bottom, set at a depth of 15 m, until it reaches a shoaling region where the depth is assumed to decrease linearly to 8 m, where it is kept constant (Figure 2). The strip is assumed to be floating over the shoaling region. The uniform thickness of the body is set at $\tau = 3m$, while its length was taken as $L = 500m$, resulting in a slenderness ratio of $\varepsilon = 0.006$. Finally, the material constants selected are; density $\rho_e = 922.5\ kg/m^3$, water density $\rho_w = 1025\ kg/m^3$, Young's modulus $E = 5 \cdot 10^9\ Pa$ and Poisson's ratio $\nu = 0.3$.

For the given analysis, 150 special hydroelastic elements and 10000 time steps were employed for the approximation of the middle region and the calculation of the transient strip response. In Figure 3 a space time plot illustrating the propagation of the imposed upper surface elevation in $\Omega_2$ is shown. The initial pulse in split into two propagating waves, travelling in opposite directions. As the wave travelling towards the negative x-axis reaches the shoaling region it is partially reflected. When the wave impacts the free edge of the floating strip, the hydroelastic pulse begins to propagate showing dispersive characteristics. A reflected wave back propagating in $\Omega_2$ is formed at impact.

In Figure 4 and Figure 5 , the solutions obtained by means of the fully linear (EB-LSW) and the two non-linear models are compared. The comparison is shown at three distinct moments in time representing the phases of wave impact, hydroelastic wave propagation and wave exit from the middle region. On the left column of the figures, the calculated strip responses are shown, while on the right the corresponding deviations from the linear model solution are presented. It is observed that the nonlinearity introduced by the GB-LSW is rather weak, since the strip response is essentially reduced to the EB-LSW solution for the examined excitation scenarios. The deviation between the GB-LSW and the EB-LSW models is kept under 10% in both cases. Moreover, the deviation increase with increasing excitation steepness is minimal. This is attributed to the fact that the floating strip is considered thin in this case. Since, $\varepsilon \ll 1$, the rotary inertia and nonlinear terms of the Gao beam model are rather weak (see Eq 9(a)) and the solution is reduced to the one calculated by the classical thin beam theory. The limitations posed by the linear model would become evident with increasing dimensionless parameter $\varepsilon$. On the other hand, the deviations between the GB-SW and the EB-LSW solutions seem to increase proportionally with excitation steepness. In Figure 4 the maximum deviation is seen to exceed 20 % while in Figure 5 it exceeds 40%. Hence, the nonlinearity introduced in the hydrodynamic modeling is dominant over the nonlinear effects incorporated by the large deflections assumption of the strip model.

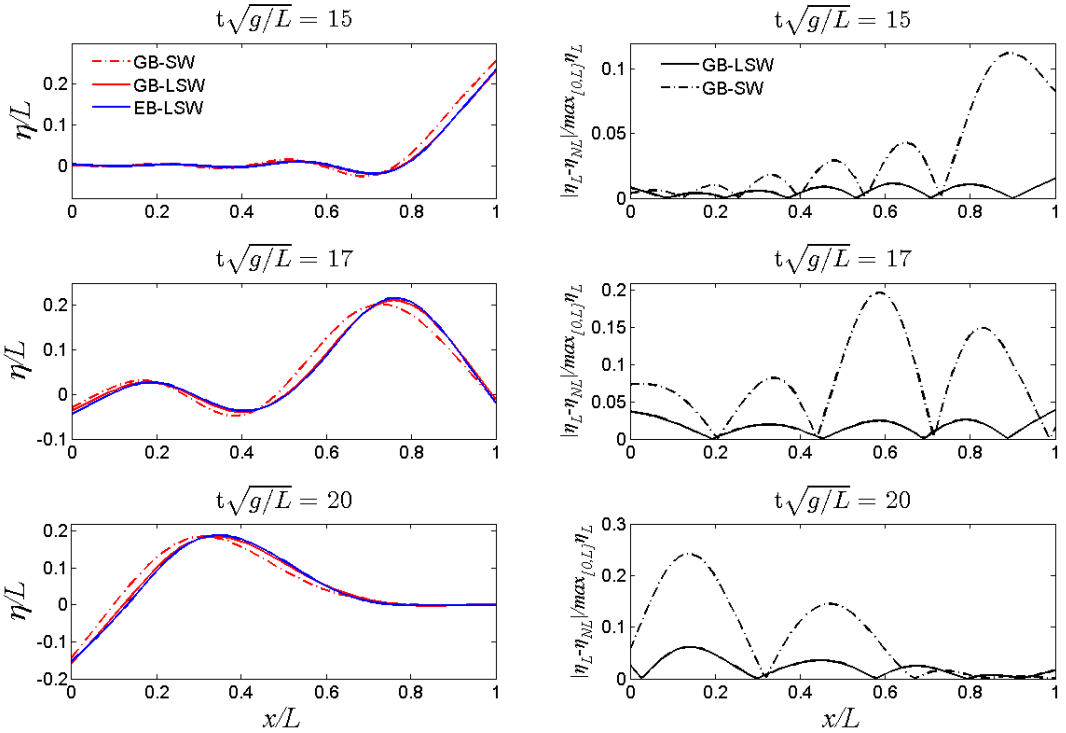


**Figure 4 (Left)**Strip response at given moments in time, calculated by the EB-LSW , GB-LSW and GB-SW models for an elevation pulse with a steepness ratio of 0.0013 .**(Right)** Deviations between the calculated solutions by the GB-LSW and GB-SW models and the fully linear EB-LSW model.

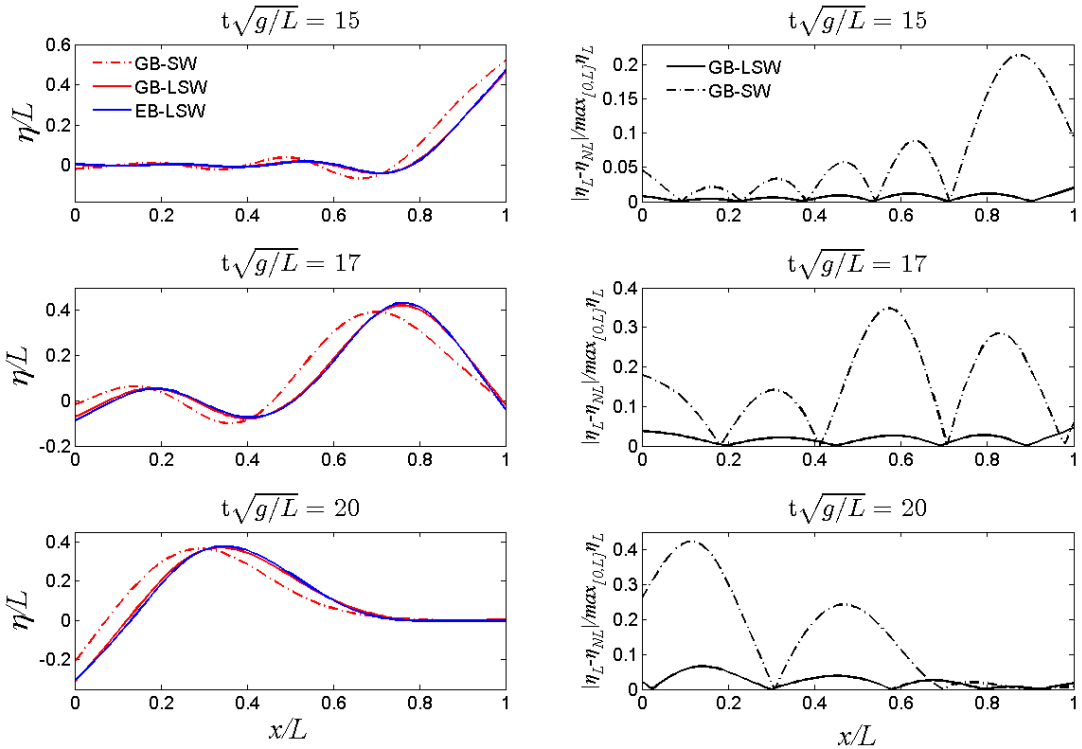


**Figure 5** (**Left**)Strip response at given moments in time, calculated by the EB-LSW , GB-LSW and GB-SW models for an elevation pulse with a steepness ratio of 0.0027 .(. **(Right)** Deviations between the calculated solutions by the GB-LSW and GB-SW models and the fully linear EB-LSW model.

# 5 Conclusions

In this contribution, a higher-order finite element scheme is employed for the solution of the 1D hydroelastic problem of a floating nonlinear strip in shallow water conditions. Two nonlinear hydroelastic models were considered. The Gao nonlinear beam is initially coupled with the linearized shallow water equations (GB-LSW model) and subsequently with the full nonlinear equations (GB-SW mode). The variational equivalent of the defined IBV problems were solved by mains a special 5-node hydroelastic element, featuring $5^{th}$ order Hermite polynomials for the interpolation of the upper surface elevation/strip deflection in the middle region, and $4^{th}$ order Lagrange polynomials for the interpolation of the velocity potential function in the same region. The higher-order finite element scheme was first applied in the solution of the hydroelastic problem of a floating, linear, elastic strip under the classical beam theory assumptions in Papathanasiou *et al*. (2015 (b)) and is now extended to nonlinear strip modeling.

In the present work, the nonlinear effects incorporated by the GB-LSW and GB-SW models were examined for a given floating body slenderness ratio and varying excitation steepness. When compared with the aforementioned linear model, the deviation between the calculated GB-SW and EB-LSW model solutions increases proportionally with increasing initial excitation steepness. In the case of the GB-LSW, the obtained strip responses under the examined excitations were essentially reduced to the ones calculated by the fully linear model, with the deviation between the solutions being kept under 10%. Hence, the nonlinearity in the hydrodynamic equations appeared to be dominant over the nonlinear effects introduced by the large deflections assumption in the strip model, for the examined non-dimensional slenderness parameter $\varepsilon$ .

The present contribution is a first step in the implementation of higher-order finite element schemes in the solution of the hydroelastic problem with incorporated nonlinearity. Although the presented results give a clear indication of the strength of the accounted nonlinear effects, further investigation is required in order to establish the range of validity for the presented nonlinear hydroelastic models. Possible future extensions include the study of higher order shallow water wave and plate models in a general bathymetry.

# Acknowledgements

The author gratefully acknowledges Prof K. A. Belibassakis and Dr T. K. Papathanasiou for their valuable suggestions and constructive comments on the present work.

# References

Athanassoulis, G. A., & Belibassakis, K. A. (1999). A consistent couple-mode theory for the propagations of small-amplitude water waves over variable bathymetry. *J. Fluid Mech., 389*, 275-301.

Belibassakis, K. A., & Athanassoulis, G. A. (2005). A coupled-mode model for the hydroelastic analysis of large floatng bodies over bathymetry regions. *J. Fluid Mech., 531*(221-249).

Belibassakis, K. A., & Athanassoulis, G. A. (2006). A coupled-mode technique for weakly non-liner wave interaction with large floating bodies lying over variable bathymetry regions. *App. Ocean Res., 28*, 59-76.

Chen, X. J., Juncher Jensen, J., Cui, W. C., & Fu, S. X. (2003). Hydroelasticity of a floating plate in multidirectional waves. *Ocean Eng., 30*(15), 1997-2017.

Chen, X. J., Wu, Y. S., Cui, W. C., & Juncher Jensen, J. (2006). Review of hydroelasticity theories for global response of marine structures. *Ocean Eng*.(33), 439-457.

Gao, D. Y. (1996). Nonlinear beam theory with applications to contact problems and variational approaches. *Mech. Res. Commun*, 11-17.

Hegarty, G. M., & Squire, V. A. (2004). On Modelling the Interaction of Large Amplitude Waves with a Solitary Floe. *Proceedings of the Fourteenth International Offshore and Polar Engineering Conference*. Toulon, France.

Meylan, M. H., & Squire, V. A. (1994). The response of ice floes to ocean waves. *J. Geophys. Res., 99*, 891-900.

Papathanasiou, T. K., Karperaki, A. E., Theotokoglou, E. E., & Belibassakis, K. A. (2015 (a)). Hydroelastic analysis of ice shaleves under long wave excitation. *Nat. Hazards Earth Syst. Sci., 15*, 1-7.

Papathanasiou, T., Karperaki, A., Theotokoglou, E. E., & Belibassakis, K. A. (2015 (b)). A higher order FEM for time-domain hydroelastic analysis of large floating structures in an inhomogeneouw shallow water environment. *Proc. R. Soc. A, 471*.

Squire, V. A. (2008). Synergies between VLFS Hydroelasticity and Sea Ice Research. *Int. J. Offshore Polar Eng., 18*(3), 1-13.

Sturova, I. V., A., K. A., Fedotova, Z. I., Chubarov, L. B., & Komarov, V. A. (2010). Nonlinear dynamics of non-uniform elastic plate floating on shallow water of variable depth. *5th International Comnference on Hydroelasticity*. Southampton, UK.

Tadepalli, S., & Synolakis, K. (1996). Model for the leading waves of tsunamis. *Phys. Rev. Lett., 77*, 2141-2144.

Wang, C. M., Watanabe, E., & Utsunomiya, T. (2008). *Very large floating structures*. London: Taylor and Francis.

Marine Structures 48 (2016) 33–51

Contents lists available at ScienceDirect

Marine Structures

journal homepage: www.elsevier.com/locate/marstruc

# Time-domain, shallow-water hydroelastic analysis of VLFS elastically connected to the seabed

A.E. Karperaki [a, *], K.A. Belibassakis [a], T.K. Papathanasiou [b, 1]

[a] School of Naval Architecture and Marine Engineering, National Technical University of Athens, Iroon Polytechniou St. 9, Zografou Campus, 15773 Athens, Greece

[b] Department of Mechanics, School of Applied Mathematical and Physical Science, National Technical University of Athens, Iroon Polytechniou St. 9, Zografou Campus, 15773 Athens, Greece

ARTICLE INFO

*Article history:*
Received 2 July 2015
Received in revised form 7 April 2016
Accepted 21 April 2016

*Keywords:*
VLFS
Transient hydroelastic analysis
Variable bathymetry
Shallow water
FEM

ABSTRACT

In order to ensure the safe operation of a VLFS, a combination of mooring, breakwater and other motion reducing systems is employed. In the present work, the transient hydroelastic response of a floating, thin elastic plate, elastically connected to the seabed, is examined. The plate is modelled as an Euler-Bernoulli strip, while the linearized shallow water equations are used for the hydrodynamic modelling. Elastic connectors are approximated by a series of simple spring-dashpot systems positioned along the strip. A higher order finite element scheme is employed for the calculation of the hydroelastic response of the strip-connector configuration over the shallow bathymetry. After the definition of the initial-boundary value problem, its variational form is derived and discussed. Next, on the basis of the aforementioned formulation, an energy balance expression is obtained. The effect of variable bathymetry on the response of a two connector-strip system is examined by means of three seabed profiles featuring a flat bottom, an upslope and a downslope environment. For the flat bottom case, the strip response mitigating effect exerted by the employment of two and three elastic connectors is considered. Finally, by means of the derived energy balance equation, the energy exchange is monitored, providing a valuable insight into the transient phenomena that take place in the studied configurations.



## 1. Introduction

In the past decades, due to the advances in marine technology, the hydroelastic response of Very Large Floating Structures (VLFSs) has received great scientific attention. Population densification in coastal areas, along with the increasing work load in major ports, has led to costly land reclamation solutions in order to accommodate the need for commercial space, necessary for industrial growth [1]. Compared to expanding industrial zones inland or resulting to environmentally hostile and costly land reclamation solutions, the employment of VLFS as operational docks constitutes an attractive alternative. Pontoon type VLFSs are essentially floating plates of large horizontal dimensions resting on the water surface [2]. With horizontal dimensions stretching from tens to hundreds of meters, VLFSs provide extended floor span, highly

* Corresponding author.
*E-mail addresses:* karperaki.ang@gmail.com (A.E. Karperaki), kbel@fluid.mech.ntua.gr (K.A. Belibassakis), t.papathanasiou@unitn.it (T.K. Papathanasiou).
[1] Now at: DICAM, University of Trento, via Mesiano 77, 38123 Trento, Italy.

http://dx.doi.org/10.1016/j.marstruc.2016.04.002
0951-8339/

desirable for various applications ranging from storage, docking and military operation platforms to recreational facilities and floating airport and helicopter bases [1,2]. Moreover, the ability to moor the structures at safe distances from the shore makes them suitable for the accommodation of socially sensitive facilities, such as power and sewage treatment plants [1–5].

The large length to thickness ratio of VLFSs makes elastic deformation dominant under ocean wave action. Hence, the extensive study and comprehension of hydroelastic effects is essential in the development of robust VLFSs' design codes. Due to their small rigidity, pontoon type VLFSs are most commonly modelled as thin, elastic, floating plates of either negligible or non-negligible draft. Commonly the classical Kirchhoff plate theory is used for the approximation of the strip deflection [6,7], while some works consider higher −order [8] and nonlinear strip [9] theories.

Most tools developed for the study of hydroelastic effects employ either frequency domain or time-domain techniques. Frequency domain tools employ Galerkin schemes [7], Green function methods [10] and eigenfunction expansion approaches [11]. However, the treatment and analysis of transient phenomena, characterised by steep wave fronts, and strong nonlinearity effects, requires time domain methods. Analysis tools in the time domain include direct integration schemes [12,13] and Fourier transform techniques [14,15]. Considering long wave excitation, Sturova [16] developed an eigenfunction expansion technique for the calculation of the hydroelastic response of thin heterogeneous plates. In the same line of work, Papathanasiou et al. [17] proposed a higher order finite element scheme for the solution of the initial-boundary value hydroelastic problem of a thin plate floating over mildly sloped bathymetry in shallow water conditions.

Pontoon type VLFSs are suitable for calm waters and are usually moored nearshore. The proximity to coastal areas and the large horizontal dimensions make variable bathymetry effects important. In [18] the effects of a sloping sea bed are considered, while a fast−multipole method is developed in [19] to account for variable bathymetry. Belibassakis & Athanassoulis [20] have developed a coupled mode method for the calculation of the hydroelastic response of a floating, thin plate over general bathymetry, which is recently extended to 3D by Gerostathis et al. [21].

In order to avoid drift off and reduce vibration effects of a VLFS, a combination of mooring, breakwater and other motion reducing systems is employed [1–3]. The choice of the response mitigating system is dictated by the allowable displacement values for the given configuration. Negata [22] and Seto & Ochi [23] showed that the motion of a floating plate surrounded by bottom-founded breakwaters is considerably reduced in the case of incoming long waves. Numerical studies have confirmed that the gravity type breakwater system is highly effective in reducing both drift forces on the floating structure and its hydroelastic response [24,25].

On the other hand, bottom-founded breakwaters have a profound environmental impact, as they disrupt ocean currents, and costly construction. Alternative breakwater systems, like the box-like floating breakwater [3], have been proposed as eco-friendly alternatives. The need to mitigate the hydroelastic response of floating bodies has also led to the development of auxiliary structural elements acting as motion reducing mechanisms. Such devices, attached at the free edges of the floating structure, are able to dissipate the incoming wave energy and achieve the necessary hydroelastic response mitigation. The devices range from submerged vertical or horizontal plates [26,27], acting as reflectors, to air cushions [28]. In order to derive the optimal configuration for a given structure and environmental conditions, computationally intensive, parametric studies must be carried out. Khabakhpasheva & Korobkin [29] underline the need for a simple model able to capture the effect of the motion reducing device on the dynamic response of the structure. In the same work, the response mitigating effect of an elastic spring, connecting one of the free edges of the floating strip to the seabed, is studied among other systems. Finally, Karmakar & Guedes Soares [30] study the scattering of gravity waves by a moored elastic strip, floating over shallow bathymetry, in the frequency domain. In Ref. [30] a thorough analysis of the vertical strip deflection, bending moment, strain shear force and spatial distribution for moored configurations under harmonic excitation is presented.

In the present work, the time-domain hydroelastic response of a thin, elastic, floating plate, elastically connected to the sea bed, is examined. The plate is modelled as an Euler-Bernoulli strip, while the linearized shallow water equations are used for the hydrodynamic modelling. The main novelty of the present contribution, compared to the previous work carried out by the authors [17], lays on the inclusion of multiple elastic connectors in the developed shallow-water, time-domain model. The elastic connectors are represented by simple spring-dashpot systems distributed along the structure. The present study also considers the effect of the number, arrangement, stiffness and damping coefficients of the connectors on the resulting transient hydroelastic response of the strip-connector configuration, floating over shallow waters. The investigation finds important applications in a number of fields, such as the design of mooring systems [30], the vibration reduction of a floating structure [31] and wave energy harvesting [32]. The numerical solution is calculated by means of a higher order finite element scheme.

In Section 2, the initial-boundary value problem is formulated. Next, in Section 3 the variational form of the above problem is given. Subsequently, the energy balance expression is derived from the variational form, while the employed finite element scheme is briefly introduced. Finally, in Section 4 a series of numerical results is presented. In order to explore the effects of bathymetry, three seabed profiles are defined. Namely, a flat bottom, an upslope and a downslope environment were considered. For the flat bottom case, the response reducing effects of elastic strip configurations employing two and three connectors, are studied and compared against the freely floating case. Strip deflection and bending moment distributions in given time instances are plotted for various elastic connector parameters. Finally, the energy exchange within the system is monitored by means of the energy balance expression, providing a valuable insight into the physical phenomenon and the effectiveness of the studied configurations.

## 2. Governing equations

In this section, the hydroelastic problem of a thin, floating, strip that is elastically connected to the seabed is presented. Shallow-water conditions are assumed in the following analysis. The general formulation of the above problem, for a freely-floating elastic strip, has already been presented in Sturova [16] and Papathanasiou et al. [17]. In the present contribution, the strip is assumed to be elastically connected to the bottom boundary, at both edges, while additional $N-1$ elastic connectors are distributed along the strip length (see Fig. 1). A Cartesian coordinate system is introduced. The horizontal axis $x$ coincides with the mean water level, while the vertical axis $z$ is pointed upwards. The plate extends infinitely in the direction vertical to the page, hence allowing the treatment of the floating body configuration in the $xz$ plane.

The upper surface elevation is denoted by $\eta(x,t)$. The thin, elastic strip of length $L$, thickness $\tau(x)$ and density $\rho_p$ is resting over a layer of water with density $\rho_w$. The fluid layer is contained in the domain $\Omega$:$(-\infty < x < \infty,\ -b < z < \eta)$, where the depth function is given by $b(x) = h(x) - d(x)$, with $h(x)$ being the depth measured up to the mean water level and $d(x) = \tau(x)\rho_p/\rho_w$ the plate draft. The horizontal extent of the domain is decomposed into subregion $S_0$:$0 < x < L$, where the hydroelastic coupling takes place, and the free fluid surface subregions, $S_1$:$(-\infty,0]$ and $S_2$:$[L,-\infty)$. In the middle region $S_0$, the plate deflection and the free surface elevation coincide. The velocity potential functions, defined in each sub domain, are denoted as $\varphi_i$, $i = 0,1,2$ respectively. Assuming a thin body, the Euler-Bernoulli beam theory can be employed for the approximation of the floating strip hydroelastic response. The resulting system of equations, valid in $\Omega$, becomes

$$m(x)\partial_{tt}\eta + \partial_{xx}[D(x)\partial_{xx}\eta] + \rho_w g\eta + \rho_w \partial_t \varphi_0 = \sum_{n=2}^{N} \delta(x - x_n)(k_n\eta + c_n\partial_t\eta),\ x \in S_0, \tag{1}$$

$$\partial_t\eta + \partial_x[b(x)\partial_x\varphi_0] = 0,\ x \in S_0, \tag{2}$$

$$\partial_{tt}\varphi_1 - g\partial_x[b(x)\partial_x\varphi_1] = 0,\ x \in S_1, \tag{3}$$

$$\partial_{tt}\varphi_2 - g\partial_x(b(x)\partial_x\varphi_2) = 0,\ x \in S_2, \tag{4}$$

where $g$ is the acceleration of gravity and $m(x) = \rho_p\tau(x)$ is the plate mass per unit length. The Dirac function is denoted by $\delta$. The flexural rigidity of the plate is $D(x) = E\tau(x)^3/12(1-\nu^2)$, with $E$ being the Young's modulus, $\nu$ the Poisson's ratio of the plate material. Furthermore, it is assumed that $t/L \ll 1$ in order to comply with the Kirchhoff thin plate theory. Finally, the strip is connected with the seabed, at $x_n$ horizontal locations, by elastic connectors with stiffness $k_n$, and damping coefficients $c_n$ for $n = 1,\ldots,N+1$, represented by simple spring-dashpot systems. Eq. (1) accounts for the deflection of the elastic strip, according to the Kirchhoff plate theory assumptions, resting on a fluid layer described by the linearized shallow water equations. The present model incorporates inertial and flexural effects by means of the terms $m(x)\partial_{tt}\eta$ and $\partial_{xx}[D(x)\partial_{xx}\eta]$, respectively. The classical thin plate model is augmented by the hydroelastic coupling terms $\rho_w g\eta$ and $\rho_w\partial_t\varphi_0$, rising from the linearized dynamic condition at the upper surface boundary of the middle region$S_0$.

The forcing term in the right hand side of Eq. (1) accounts for the collective restoring effect of the elastic connectors distributed along the strip length ($n = 2,\ldots,N$), excluding edge connectors. Notably, the restoring effect of the connectors positioned at the free edges of the strip is accounted by the imposed non-zero shear force boundary conditions at the strip edges and is thus not included in the aforementioned forcing term. Moreover, Eq. (2) expresses mass conservation in the water region, under the plate, while Eqs. (3) and (4) are derived through a simple algebraic manipulation of the linearized shallow water equations, modelling long wave propagation in the free water surface subregions $S_i$, $i = 1,2$. For the given

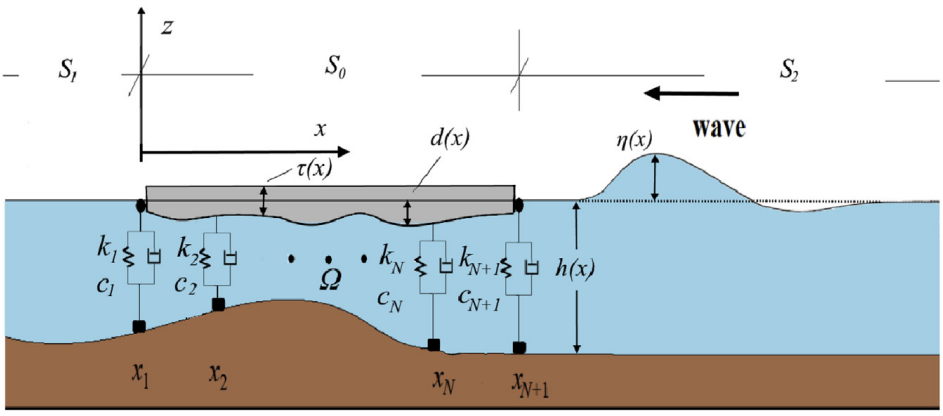


**Fig. 1.** A floating elastic strip with multiple elastic connectors along its length.

subregions, it holds that $\eta_i = -g^{-1}\partial_t\varphi_i$, $i = 1,2$ [16]. Hence, the upper surface elevation in the halfstrips is directly derived from the corresponding velocity potential functions.

The system of Eqs. (1)–(4) is supplemented by the following conditions at infinity,

$$\partial_x\varphi_1(x\to-\infty,t) = 0 \text{ and } \partial_x\varphi_2(x\to\infty,t) = 0. \tag{5}$$

implying quiescence in the far field. At the interfaces between subregions mass and energy conservation is assumed, yielding the following matching conditions,

$$b(0^-)\partial_x\varphi_1(0^-,t) = b(0^+)\partial_x\varphi_0(0^+,t) \text{ and } b(L^+)\partial_x\varphi_2(L^+,t) = b(L^-)\partial_x\varphi_0(L^-,t),$$

$$\partial_x\varphi_1(0^-,t) = \partial_x\varphi_0(0^+,t) \text{ and } \partial_x\varphi_0(L^-,t) = \partial_x\varphi_2(L^+,t).$$

At the free strip edges, located at $x = 0$ and $x = L$, zero-moment and non-zero shear force conditions are imposed,

$$D(0)\partial_{xx}\eta = 0 \text{ and } D(0)\partial_{xxx}\eta = -k_1\eta - c_1\partial_t\eta \text{ at } x = 0,$$

$$D(L)\partial_{xx}\eta = 0 \text{ and } D(L)\partial_{xxx}\eta = k_{N+1}\eta + c_{N+1}\partial_t\eta \text{ at } x = L.$$

Initially, at $t = 0$, the plate is at rest, while a free water surface disturbance, denoted by $S(x)$, begins to propagate in subregion $S_2$. Thus, the conditions that complete the initial-boundary value problem are given as

$$\eta(x,0) = \partial_t\eta(x,0) = \partial_x\varphi_0 = 0 \text{ for } x\in S_0,\ \varphi_1 = \partial_t\varphi_1 = 0 \text{ for } x\in S_1 \text{ and } \varphi_2 = 0, \partial_t\varphi_2 = -S(x) \text{ for } x\in S_2.$$

Using the following nondimensional variables $\tilde{x} = xL^{-1}$, $\tilde{\eta} = \eta L^{-1}$, $\tilde{t} = g^{1/2}L^{-1/2}t$, $\tilde{\varphi}_i = g^{-1/2}L^{-3/2}\varphi_i$, for $i = 0,1,2$, the initial-boundary value problem under consideration is rewritten (after dropping tildes)

$$M(x)\partial_{tt}\eta + \partial_{xx}[K(x)\partial_{xx}\eta] + \eta + \partial_t\varphi_0 = \sum_{n=2}^{N}\delta(x-x_n)\left(\widehat{k}_n\eta + \widehat{c}_n\partial_t\eta\right),\ x\in S_0, \tag{6}$$

$$\partial_t\eta + \partial_x[B(x)\partial_x\varphi_0] = 0,\ x\in S_0, \tag{7}$$

$$\partial_{tt}\varphi_1 - \partial_x[B(x)\partial_x\varphi_1] = 0,\ x\in S_1, \tag{8}$$

$$\partial_{tt}\varphi_2 - \partial_x[B(x)\partial_x\varphi_2] = 0,\ x\in S_2, \tag{9}$$

where the following nondimensional quantities are involved,

$$M(x) = m(x)\rho_w^{-1}L^{-1},\ K(x) = D(x)\rho_w^{-1}g^{-1}L^{-4} \text{ and } B(x) = b(x)L^{-1}.$$

The corresponding interface conditions become

$$B\left(0^-\right)\partial_x\varphi_1\left(0^-,t\right) = B\left(0^+\right)\partial_x\varphi_0\left(0^+,t\right),\ B\left(1^-\right)\partial_x\varphi_0\left(1^-,t\right) = B\left(1^+\right)\partial_x\varphi_2\left(1^+,t\right), \tag{10}$$

and

$$\partial_t\varphi_1(1^-,t) = \partial_t\varphi_0(1^+,t),\ \partial_t\varphi_0(1^-,t) = \partial_t\varphi_2(1^+,t), \tag{11}$$

while the nondimensional boundary conditions read as follows

$$K(0)\partial_{xx}\eta = 0 \text{ and } K(0)\partial_{xxx}\eta = -\widehat{k}_1\eta(0,t) - \widehat{c}_1\partial_t\eta(0,t) \text{ at } x = 0, \tag{12}$$

$$K(1)\partial_{xx}\eta = 0 \text{ and } K(1)\partial_{xxx}\eta = \widehat{k}_{N+1}\eta(1,t) + \widehat{c}_{N+1}\partial_t\eta(1,t) \text{ at } x = 1. \tag{13}$$

In the above equations $\widehat{k}_n = k_n(\rho_w g)^{-1}$ and $\widehat{c}_n = c_n g^{1/2}L^{-1/2}(\rho_w g)^{-1}$, for $n = 1,2,\ldots,N+1$, are the nondimensional connector stiffness and damping coefficients. For simplicity in presentation, the hat notation is omitted in the following analysis.

## 3. Variational formulation

The variational form of the previously defined transient hydroelastic problem is derived and discussed in the present section. For the derivation of the variational formulation of the problem the same standard process is followed as in Papathanasiou et al. [17]. The reader is directed to the given work for a more detailed account. Concisely, it is mentioned that Eqs.

(6)–(9) are multiplied by the weight functions $v \in H^2(S_0)$, $-w_0 \in H^1(S_0)$, $w_1 \in H^1(S_1)$, and $w_2 \in H^1(S_2)$, respectively (where $H$ denotes the Sobolev spaces in the corresponding intervals). After performing integration by parts and adding the resulting equations, the following variational problem is defined,

Find $\eta(x,t)$, $\varphi_0(x,t)$, $\varphi_1(x,t)$ and $\varphi_2(x,t)$ such that for every $v \in H^2(S_0)$, $-w_0 \in H^1(S_0)$ , $w_1 \in H^1(S_1)$ and $w_2 \in H^1(S_2)$ it holds that

$$\int_0^1 M v \partial_{tt}\eta dx + \int_0^1 v\partial_t\varphi_0 dx - \int_0^1 w_0\partial_t\eta dx + \int_{-\infty}^0 w_1\partial_{tt}\varphi_1 dx + \int_1^\infty w_2\partial_{tt}\varphi_2 dx + \\ + a(\eta,v) + b_0(\varphi_0,w_0) + b_1(\varphi_1,w_1) + b_2(\varphi_2,w_2) + q(\eta,v) + c(\partial_t\eta,v) = 0, \tag{14}$$

where the bilinear functionals are given by

$$q(\eta,v) = \sum_{n=1}^{N+1} v(x_n)k_n\eta(x_n,t) \tag{15a}$$

and

$$c(\partial_t\eta,v) = \sum_{n=1}^{N+1} v(x_n)c_n\partial_t\eta(x_n,t), \tag{15b}$$

while as defined in [17],

$$a(\eta,v) = \int_0^1 (K\partial_{xx}v\partial_{xx}\eta + v\eta)dx, \tag{15c}$$

$$b_0(\varphi_0,w_0) = \int_0^1 \partial_x w_0 B\partial_x\varphi_0 dx, \tag{15d}$$

$$b_1(\varphi_1,w_1) = \int_{-\infty}^0 \partial_x w_1 B\partial_x\varphi_1 dx, \tag{15e}$$

$$b_2(\varphi_2,w_2) = \int_1^\infty \partial_x w_2 B\partial_x\varphi_2 dx. \tag{15f}$$

### 3.1. Energy balance considerations

Following [17], an energy balance equation is derived from the variational formulation Eq. (14). The above result is subsequently used in order to study the energy exchange between the defined subregions in the presence of nonconservative restoring forces.

In order to derive the energy conservation principle, we set $v = \partial_t\eta$, $w_0 = \partial_t\varphi_0$, $w_1 = \partial_t\varphi_1$ and $w_2 = \partial_t\varphi_2$ in Eq. (14). The substitution is valid under sufficient regularity assumptions for the weak solution and the definition of the weight functions given above. Hence, Eq. (14) is transformed into the following

$$\frac{1}{2}\frac{d}{dt}\left[\int_0^1 M(\partial_t\eta)^2 dx + \int_{-\infty}^0 (\partial_t\varphi_1)^2 dx + \int_1^\infty (\partial_t\varphi_2)^2 dx + a(\eta,\eta) + b_0(\varphi_0,\varphi_0) + \right. \\ \left. + b_1(\varphi_1,\varphi_1) + b_2(\varphi_2,\varphi_2) + q(\eta,\eta) + 2\int_0^t c(\partial_s\eta,\partial_s\eta)dt\right] = 0, \tag{16}$$

where, Eq. (15a, b) take the form

$$q(\eta,\partial_t\eta)=\frac{1}{2}\frac{d}{dt}\sum_{n=1}^{N+1}k_n\eta^2(x_n,t)=\frac{1}{2}\frac{d}{dt}q(\eta,\eta) \tag{17a}$$

and

$$c(\partial_t\eta,\partial_t\eta)=\sum_{n=1}^{N+1}c_n[\partial_t\eta(x_n,t)]^2, \tag{17b}$$

while, after substitution, the functionals of Eq. (15c-f) are rewritten as in [17].

In Eqs. (16) and (17b) $s$ denotes a dummy variable. Eq. (16) expresses the energy conservation principle for the studied system. The quantity $E(t)$

$$\begin{aligned}E(t)=&\int_0^1 M(\partial_t\eta)^2dx+\int_{-\infty}^0(\partial_t\varphi_1)^2dx+\int_1^\infty(\partial_t\varphi_2)^2dx+a(\eta,\eta)+b_0(\varphi_0,\varphi_0)+\\&+b_1(\varphi_1,\varphi_1)+b_2(\varphi_2,\varphi_2)+q(\eta,\eta)+2\int_0^t c(\partial_s\eta,\partial_s\eta)dt,\end{aligned} \tag{18}$$

i.e. the quantity in the brackets in the left-hand side of Eq. (16) should remain constant in time, and equal the energy provided by the initial free surface disturbance, $E(t)=E(0)$ for every $0\le t\le T$. The above energy balance equation provides a valuable tool in the study of the hydroelastic wave propagation in the defined strip-connector system. When the excitation reaches the strip, the strain and kinetic energy of the plate will increase and eventually vanish as the wave exits the structure and a state of rest is reached. The study of the initial excitation energy ($E(0)$) conversion, as the pulse propagates in $S_0$, in correlation with the configuration material and geometry parameters, is indicative of the elastic connector effects on the strip response. Following that line of thought, it is interesting to examine the quantities appearing in the energy balance equation (18). In the free water surface subregions $S_i$, $i=1,2$ the total energy is defined as the sum of the kinetic and potential energy of the water column given respectively as,

$$E_{K2}(t)=\frac{1}{2}\int_1^\infty(\partial_t\varphi_2)^2dx \text{ and } E_{P2}(t)=\frac{1}{2}\int_1^\infty B(\partial_x\varphi_2)^2dx, \text{ for } S_2, \tag{19}$$

$$E_{K1}(t)=\frac{1}{2}\int_{-\infty}^0(\partial_t\varphi_1)^2dx \text{ and } E_{P1}(t)=\frac{1}{2}\int_{-\infty}^0 B(\partial_x\varphi_1)^2dx, \text{ for } S_1. \tag{20}$$

Additionally, the kinetic and strain energy of the strip are given by the following terms,

$$E_K(t)=\frac{1}{2}\int_0^1 M\partial_t\eta^2dx \tag{21a}$$

and

$$E_S(t)=\frac{1}{2}\int_0^1 K(\partial_{xx}\eta)^2dx. \tag{21b}$$

The total fluid energy in the subregion $S_0$ is given as follows,

$$E_P(t)=\frac{1}{2}\int_0^1\left[B(\partial_x\varphi_0)^2+\eta^2\right]dx. \tag{22}$$

The quantity of Eq. (22) consists of the kinetic fluid energy in the middle subregion and the potential energy due to elastic strip deflection. Furthermore, the elastic potential energy of the employed $N+1$ connectors is given by

$$W(t) = \frac{1}{2}\sum_{n=1}^{N+1} k_n \eta^2(x_n, t), \tag{23}$$

while the energy dissipation due to connector damping is expressed as

$$C(t) = \sum_{n=1}^{N+1} \int_0^t c_n [\partial_s \eta(x_n, s)]^2 ds. \tag{24}$$

Integrating Eq. (18) with respect to time from $t = 0$ to $t = T$, and using the fact that $E(t) = E_0$, the following holds

$$\int_0^T E(t)dt = E_0 T, \tag{25}$$

where $E_0$ is the initial excitation energy, expressed as the sum of potential and kinetic energy of the water column, provided by the imposed free surface disturbance $S(x)$ in the right halfstrip $S_2$. Eq. (25) is written in a more convenient form as,

$$\sum_{l=1}^{2}(\overline{E}_{K_l} + \overline{E}_{P_l}) + \overline{E}_K + \overline{E}_S + \overline{E}_P + \overline{W} + 2\overline{C} = 1\,. \tag{26}$$

In Eq. (26) the following definitions are used for the time averaged energy quantities,$\overline{E}_X = \frac{1}{E_0 T}\int_0^T E_X(t)dt$, where subscript x is interchanged to denote the kinetic, strain and potential energies in the respective subregions. Additionally, $\overline{W} = \frac{1}{E_0 T}\int_0^T W(t)dt$ and $\overline{C} = \frac{1}{E_0 T}\int_0^T C(t)dt$.

### 3.2. Finite element formulation

For the numerical solution of the equivalent variational problem (Eq. (14)), domain $\Omega$ is discretized and the unknown fields are approximated by means of the higher order finite element scheme developed in [17]. The discrete approximate solutions of the variational problem are given as,

$$\eta^h = \sum_{i=1}^{6} H_i(x)\eta_i^h(t) \;\text{ and }\; \varphi_j^h = \sum_{i=1}^{5} L_i(x)\varphi_{ij}^h(t),\; j = 0, 1, 2.$$

Substituting the above into the discretized variation problem defined by Eq. (14) results in a second order system of the form $\mathbf{M}\partial_{tt}u + \mathbf{C}\partial_t u + \mathbf{K}u = 0$, where vector $u$ contains the nodal unknowns $\eta_j^h, \varphi_{1j}^h, \varphi_{2j}^h$ and $\varphi_{0j}^h$ with $j$ now being a global node index. Subsequently, a Newmark time integration scheme (see [17]) is employed in order to calculate the solution.

## 4. Numerical results

In this section, a series of numerical results are presented using the physical parameters employed in the experiments described in Wu et al. [33]. In the aforementioned work the length of the strip model was $L = 10$ m, its thickness $\tau = 0.038$ m and the material elastic modulus $E = 103$ MPa. Moreover, the strip material density was $\rho_p = 220$ kg/m$^3$, and thus, its draft amounted to $d = 0.084$ m The experiment was performed in water depth of l.1 m, using incident wave heights of 5, 10 and

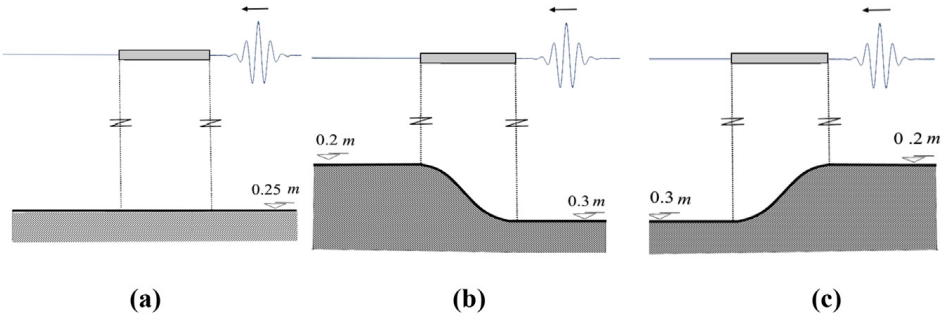


**Fig. 2.** (a) Flat bottom profile, (b) upslope and (c) downslope bathymetric profiles, with a mean bottom slope of 1%.

20 mm and wave periods ranging from 0.5 to 3 s, corresponding to deep and intermediate water depth conditions, respectively.

In order to comply with the shallow water assumption in the present work, the above physical data are used for calculations with a reduced water depth of $h = 0.25$ m (in nondimensional terms $h = 0.025$), as shown in Fig. 2(1). Moreover, in order to illustrate the effects of variable bathymetry, two additional depth profiles, shown in Fig. 2(b) and (c) have been considered, corresponding to an upslope and a downslope environment with a mean bottom slope of 1%. For the excitation $S(x)$ an incident wavepacket, with central wavelength $\lambda_0 = 4.5$ m (in nondimensional terms $\lambda_0 = 0.45$) and small amplitude $A = 0.0076$ m, was considered in the following analysis. The imposed upper surface disturbance is described by,

$$\eta(x,0) = A f_R(x - x_0; R)\cos(2\pi x/\lambda_0) \tag{27}$$

where $f_R$ is a symmetric envelope of bandwidth $R$ with respect to $x_0$, which is the initial position of the wavepacket.

In the following section, Section 4.1, a validation of the proposed methodology will be presented by comparing it against the analytical solution for the time harmonic responses of an elastic, floating structure. Comparisons are made for a strip employing an elastic connector at the upwave end of the structure and floating over constant shallow depth. Next, the effect of multiple connectors on the elastic responses will be studied in the time domain. Both a constant depth (Section 4.2) and two mildly sloped bottom environments (Section 4.3) will be considered.

### 4.1. Validation against analytic solution for harmonic responses in constant depth

For the case of thin, floating, elastic structures, in shallow water conditions and constant depth, the following 'shallow-wave equation of a freely floating board' derived by Stoker [[34], Sec. 10.13, Eq. 10.13.74],

$$KB^2 \frac{d^6\psi(x)}{dx^6} + \left(1 - M\omega^2\right)B^2\frac{d^2\psi(x)}{dx^2} + \mu\psi(x) = 0, \tag{28a}$$

$$\eta(x) = -\frac{iB}{\omega}\frac{d^2\psi(x)}{dx^2} \tag{28b}$$

is used. The above model refers to the linear harmonic responses of the structure. In the above expressions, the quantities $K$, $M$ and $B$ correspond to the nondimensional plate stiffness, plate mass and depth function (as defined in Sect. 2), while $\mu = \omega^2 B$ is the frequency parameter. The nondimensional frequency $\omega = \Omega L/g^{1/2}$ is used, where $\Omega$ is the angular frequency. Variables $\psi(x)$, $\eta(x)$ denote the complex amplitudes of the potential and the flexural deflection in the middle region $S_0$,

$$\varphi_0(x,t) = \mathrm{Re}(\psi(x)\exp(-i\omega t)), \quad \eta(x,t) = \mathrm{Re}(\eta(x)\exp(-i\omega t)). \tag{29}$$

The dispersion relation of Eq. (28a) is

$$\mu B = K\kappa_n^6 B^2 + \left(1 - M\omega^2\right)\kappa_n^2 B^2, \tag{30}$$

and its roots $\{\pm\kappa_n,\ n = 0,1,2\}$, the hydroelastic wavenumbers, are symmetrically distributed on the complex plane. The first root $\kappa_0$, is real and positive while roots $\kappa_1$,$\kappa_2$ have opposite real parts and equal positive imaginary parts. The solution of Eq. (28) a-b is given by (see also Belibassakis & Athanassoulis [20], Sec5.3]):

$$\varphi(x) = \sum_{n=0}^{n=2} \alpha_n \exp(i\kappa_n x) + \beta_n \exp(-i\kappa_n x). \tag{31}$$

Similarly, in the free water surface subregions $S_i$, $i = 1,2$, the harmonic solution of Eqs. (3) and (4) is given by

$$\psi_1(x) = K_T \exp(-i\kappa_1^w x), \quad \psi_2(x) = \exp(-i\kappa_2^w x) + K_R \exp(i\kappa_2^w x), \tag{32}$$

where $\psi_i(x)$ denote the corresponding complex wave potentials, $K_T$ is the transmission coefficient of waves in $S_1$ and $K_R$ is the reflection coefficient of waves backscattered in $S_2$, respectively. The wavenumbers $\kappa_i^w$ in the water subregions $S_i$, $i = 1,2$ are estimated by the asymptotic form of the water-wave dispersion relation in shallow conditions

$$k_i = \sqrt{\mu_i}/B_i, \ \ i = 1,2. \tag{33}$$

Finally, the coefficients $\alpha_n$,$\beta_n$ of Eq. (31), are easily determined from the boundary conditions Eqs. 12–14, at $x = 0$ and $x = 1$. These boundary conditions are expressed in terms of $\psi(x)$ through Eq. (28b), in conjunction with the following end conditions

$$\frac{d\psi}{dx} + i\kappa_1^w \psi = 0, \text{at } x = 0, \quad \text{and} \quad \frac{d\psi}{dx} - i\kappa_2^w \psi = -2i\kappa_2^w \exp(-i\kappa_2^w), \quad \text{at } x = 1. \tag{34}$$

They provide the matching of the complex wave potential $\psi(x)$ at the interfaces between the three subregions.

In order to calculate the harmonic responses of the hydroelastic system by means of the proposed time-domain method, a very broad ramp function $f_R$, containing a multiple number of wavelengths, is used. A comparison against the analytical solution is presented in Fig. 3 for a frequency parameter $\mu = 0.117$, corresponding to nondimensional depth $B = 0.025$ and central wavelength $\lambda = 0.45$ m (nondimensional $\lambda = 0.045$), and thus ensuring shallow wave conditions.

More specifically, in Fig. 3 the harmonic responses of the freely floating board with an elastic connector located at its right end, at $x = 1$, are shown. Results are calculated by the analytical solution of Stoker's model and by the presented FEM for a various connector stiffness coefficients $k$ and zero damping are plotted. These stiffness values include the freely floating case, corresponding to $k = 0$, with increasing $k = 0.01$, 0.1, and 1 as shown in the figure. The proposed method solutions are found to be in good agreement with the analytical solution, for all values of the examined connector stiffness. The small deviations are attributed to the approximation of the harmonic response of the structure by means of the presented transient methodology.

Furthermore, in Fig. 3, it can be seen that for a very stiff connector ($k = 1$), the elastic deflection of the structure at the upwave connected end (at $x = 1$) almost vanishes. The above fact leads to the conclusion that the wave induced vibration of the elastic structure, in the vicinity of the elastic connector, becomes weaker (and eventually vanishes) with increasing connector stiffness. We note here that this finding is in contradiction with the corresponding results reported by Cunbao et al. (2007) [31], although the latter studies are not directly comparable since they refer to intermediate and deep water conditions.

### 4.2. Constant depth environment

The constant depth profile, illustrated in Fig. 2(a) is initially examined. The horizontal domain is appropriately truncated, and the present system is integrated up to the time ensuring that no reflections from the computational domain boundaries are backscattered, contaminating the numerical solution ($T = 76$). For the calculation of the plate response, 200 hydroelastic elements were employed, along with 8000 timesteps. Initially, the freely floating strip response is examined. A series of snapshots, showing the propagation of the initial disturbance, is presented in Fig. 4, for the freely floating case, i.e. $k_n = c_n = 0$, $n = 1,2,\ldots,N+1$. For illustration purposes the nondimensional upper surface elevation is plotted ten times larger in the given figure. The initial excitation (Eq. (28)) with $f_R(x) = \exp(\alpha(x - x_0)^2)$, where $\alpha = 11.5$ and $x_0 = 9.3$, modelling a narrow band pulse, is used in the calculations. The pulse is split into two waveforms traveling in opposite directions at constant speed (Fig. 4(b)). As the two waveforms are not dispersive, their forms remain unaltered while traversing the truncated water region $S_2(x > 1)$ In Fig. 4(c) the waveform propagating towards the negative $x$ axis, is seen to approach the free

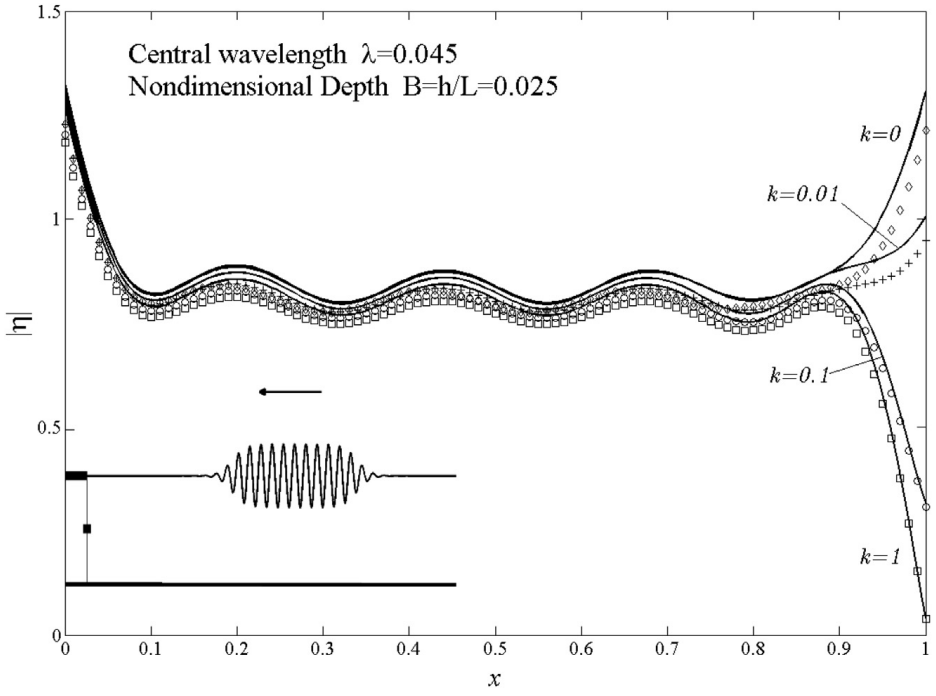


**Fig. 3.** Harmonic responses of a thin elastic plate in constant depth and shallow water conditions, with an elastic connector of stiffness $k$ located at $x = 1$. The analytical solution is represented by solid lines, while the FEM solution is denoted by diamonds ($k = 0$), stars ($k = 0.01$), circles ($k = 0.1$), and squares ($k = 1$).

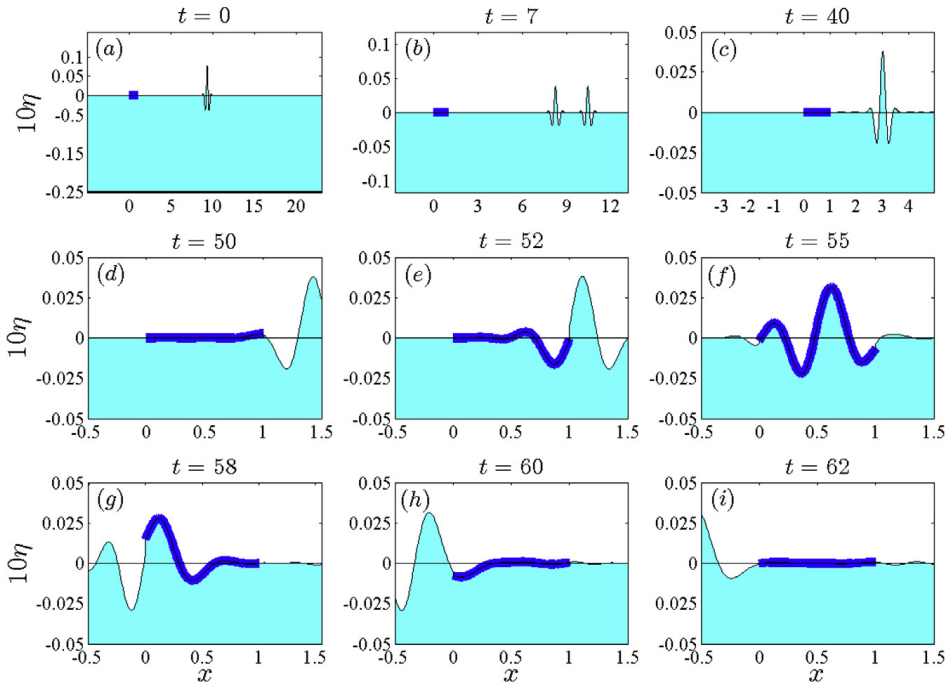


**Fig. 4.** Snapshots of the wavepacket propagation in domain $\Omega$ for the case of a constant depth profile (a). Note that for illustration purposes the nondimensional free-surface elevation and the plate deflection are multiplied by 10.

edge of the elastic strip at $x=1$. Subsequently, after wave impact, the propagation of the hydroelastic pulse is plotted in Fig. 4(d)–(h). The incident wave is partially reflected, backpropagating in the right subregion $S_2(x>1)$,

and partially transmitted in the left truncated subregion $S_1(x<0)$, as seen in Fig. 4(h). The structure eventually approaches a state of rest in Fig. 4(i). Next, the effect of the employed elastic connectors on the hydroelastic response of the strip is investigated for the same environment and incident wave. In the following analysis two and three elastic connector-strip configurations with $k_n=k,\ c_n=c,$ where $n=1,2$ for the former case and $n=1,2,3$ for the later, are considered. In Fig. 5 the deflection of a strip featuring two elastic connectors positioned at the free ends ($x=0$ and $x=1$), is plotted for an extended range of characteristic nondimensional stiffness values $k=\{1\ \ 0.1\ \ 0.01\}$, and zero damping, i.e. $c=0$. Calculated results are

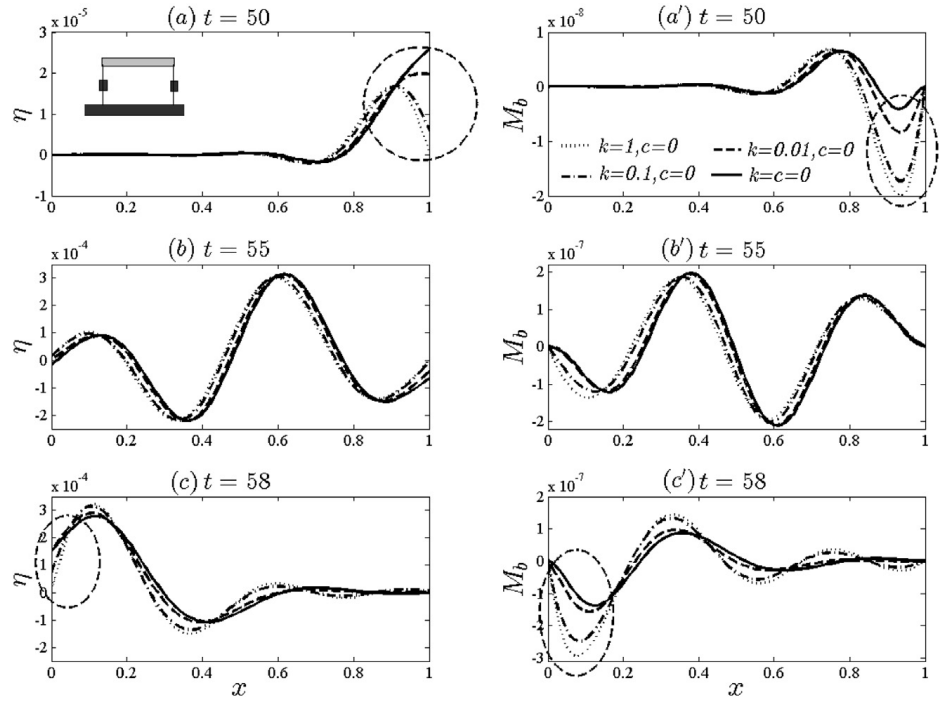


**Fig. 5.** Nondimensional strip deflection (left subplots) and bending moment $M_b=K\eta_{xx}$, (right subplots) distribution for several connector stiffness values and zero damping. Two connector configuration for bathymetric profile (a).

compared against the freely floating case response. The deflection of the elastic strip for different elastic connector stiffness values is shown at three distinct instances in time, representing the phases of wave entry in the middle subregion $S_0(0<x<1)$, the hydroelastic pulse propagation and the transmission into the downwave subregion $S_1(x<0)$. The nondimensional bending moment distributions along the elastic strip are also presented for the same time instances.

It is observed that during the wave entry phase, increasing the connector stiffness, reduces the deflection, and increases the bending moment values in the vicinity of the strip end ($x=1$), as indicated by the dashed circles in Fig. 5(a) and (a′). Compared to the freely floating response at the given moment in time ($t=50$), setting $k=0.01$, 0.1 and $k=1$ reduces the maximum absolute strip deflection by 22.8%, 34.8% and 35.5%, respectively. On the other hand, the calculated maximum absolute bending moments substantially increase with increasing connector stiffness, at the vicinity of the free edge, reaching an intensification of over 200% for $k=1$. This can be attributed to the local restriction imposed on the elastic motion of the strip by the connector at $x=1$. Next, in the hydroelastic pulse propagation phase, examined in Fig. 5(b) and (b′), the maximum deflection reductions achieved by the employment of the edge connectors reaches 0.25%, 3% and 4.85% for $k=0.01$,0.1 and $k=1$ respectively. The calculated, maximum bending moment at $t=55$, also appears reduced by 0.4%, 5% and 8.2% for the corresponding stiffness coefficient values.

During the wave transmission phase, increasing connector stiffness results in larger moduli of deflections and bending moments, in the vicinity of the downwave end of the structure, as indicated by the dashed circles in Fig. 5(c) and (c′). Particularly, for $k=0.01$, 0.1 and $k=1$ maximum absolute deflection increases by 4.31%, 13.45% and 15.9%, respectively.

The imposed restriction on strip deflection is magnified with increasing connector stiffness, causing the flexural response of the strip to intensify locally at the strip edges during wave impact and hydroelastic pulse transmission. The latter has a profound effect on both the flexural deflection of the structure and the induced bending moment profiles. Examining the overall responses in time, the maximum absolute deflection was significantly reduced by 29.26% for $k=0.1$ while the maximum absolute bending moment of the elastic strip is increased by 35.4%, compared to the freely floating case. The overall maximum absolute deflection was also effectively mitigated by setting $k=0.01$ (22.36%) and $k=1$ (27.49%). However, increasing connector stiffness led to magnification of the maximum absolute bending moment, by 0.21%, 35.4% and 62.47% for increasing stiffness coefficients. The previous observation suggests that deflection mitigation through connector stiffening might lead to undesirable, excessive stresses due to flexural motion.

In Fig. 6 a system with three elastic connectors is examined. The previous configuration is enhanced by a third connector, positioned at the middle of the elastic strip ($x=0.5$). At wave entry, shown in Fig. 6(a), the deflection appears to be reduced by 35.5% for $k=1$, compared to the freely floating case, while bending moment intensification is observed in Fig. 6(a′) in the vicinity of the strip upwave edge (depicted once again by the dashed circle). In Fig. 6(b) (at $t=55$) the strip deflection, once again compared with the freely floating case, increases by 1.1%, 11%, and 30.1%, for $k=0.01$, 0.1 and $k=1$, respectively. At the same instance, the calculated maximum absolute bending moment also appears to be magnified, as shown in 6(b′). This is attributed to the overstiffening of the system due to the presence of the middle elastic connector. The kink in bending moment distribution observed in Fig. 6(b′) for $k=1$, at the middle of the floating strip, is indicative of the induced, excessive local stresses due to bending, attributed to the imposed restriction on deflection. At $t=58$, (Fig. 6(c)) the deflection almost

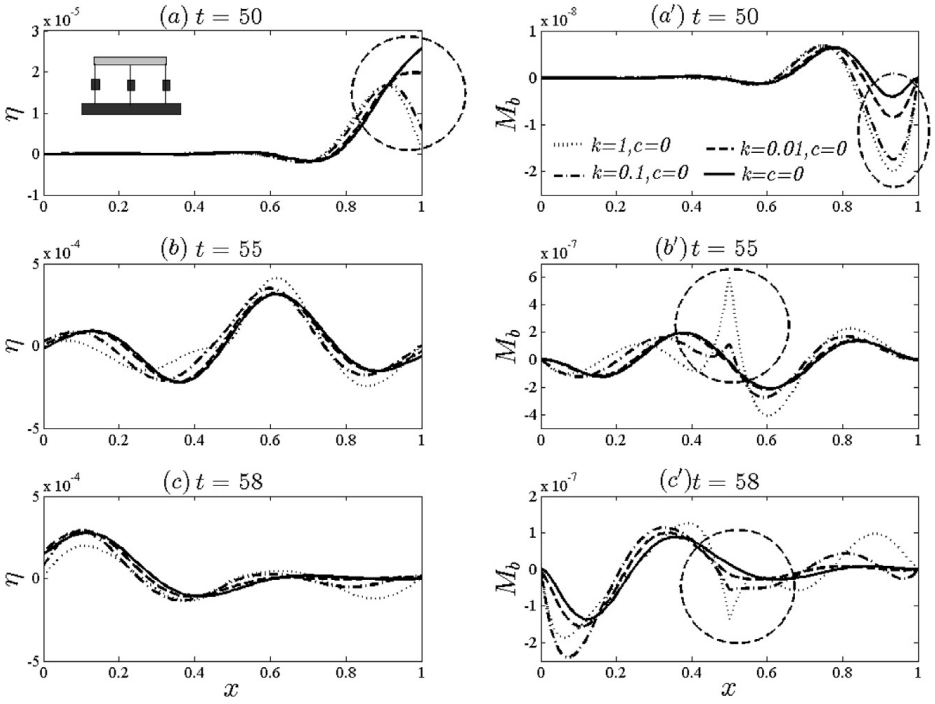


**Fig. 6.** Same as Fig. 5 for the three connector-strip configuration.

vanishes for $k = 1$, showing a reduction of 29% compared to the freely floating case. Maximum overall deflection reduction (over time) is achieved for $k = 0.01$ (by 22.32%) when compared with the free strip response. On the other hand, overall maximum, absolute bending moment is increased by 180%, 35% and 2% for stiffness coefficients $k = 1, 0.1$ and $k = 0.01$. Hence it is deduced that the intensity of flexural effects, i.e. induced maximum bending moment values, rise with increasing connector stiffness for both examined configurations when compared with the freely floating case.

Next, the combined stiffness and damping effects of the elastic connectors on the hydroelastic response of the studied system, in constant depth, are studied. To this purpose, the resulting maximum absolute deflection and maximum absolute bending moment values are calculated. The same set of damping coefficients $c = \{1, 0.1, 0.01, 0\}$ and an extended interval of stiffness coefficient values $0 < k < 10$ are used. Notably, the above interval selection includes the values of interest for practical applications. In Figs. 7 and 8 the maximum absolute deflection and the maximum absolute bending moment distributions are

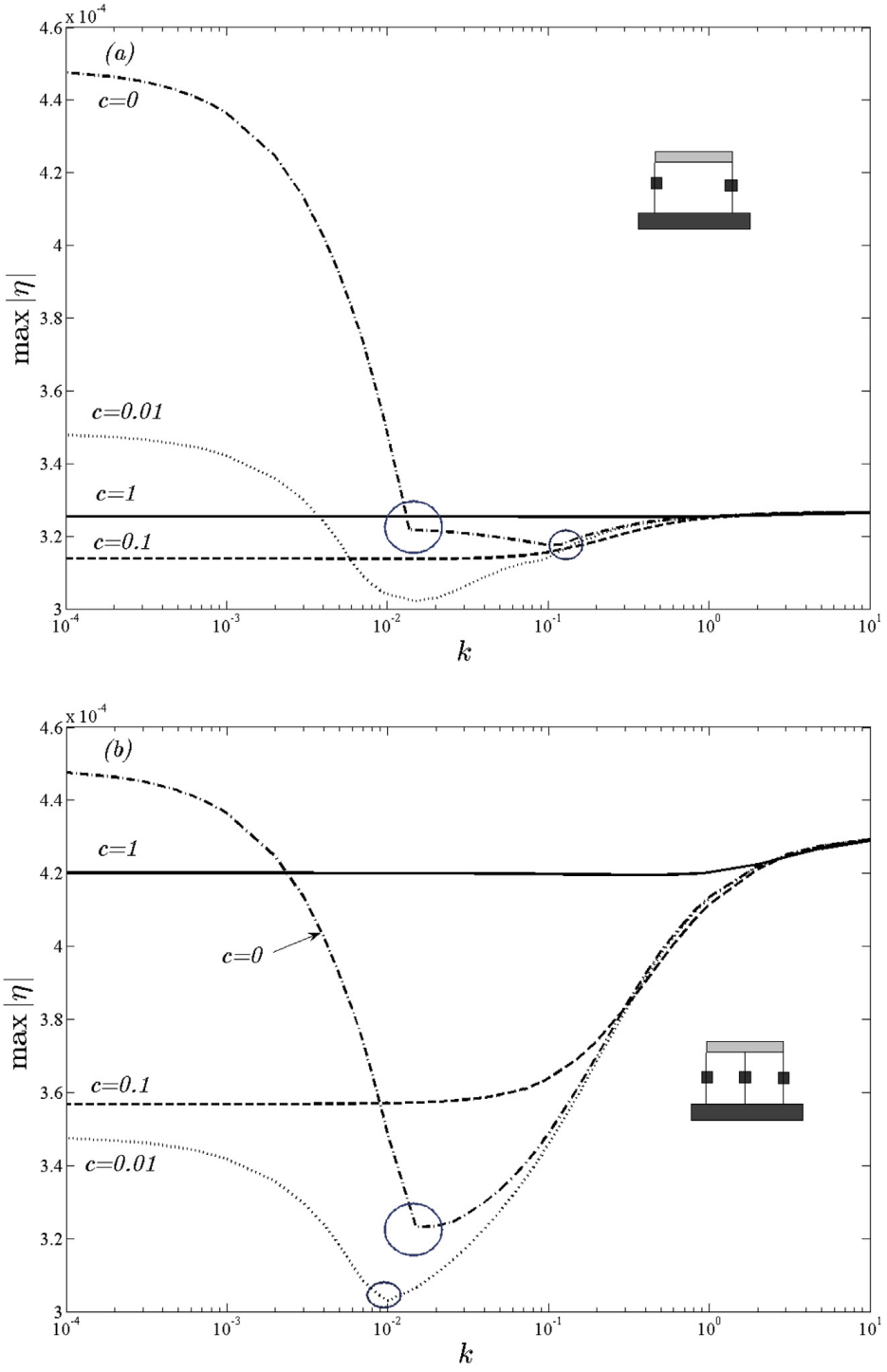


**Fig. 7.** Semi-log plot of the maximum absolute deflection: (a) two edge connectors, (b) three connectors.

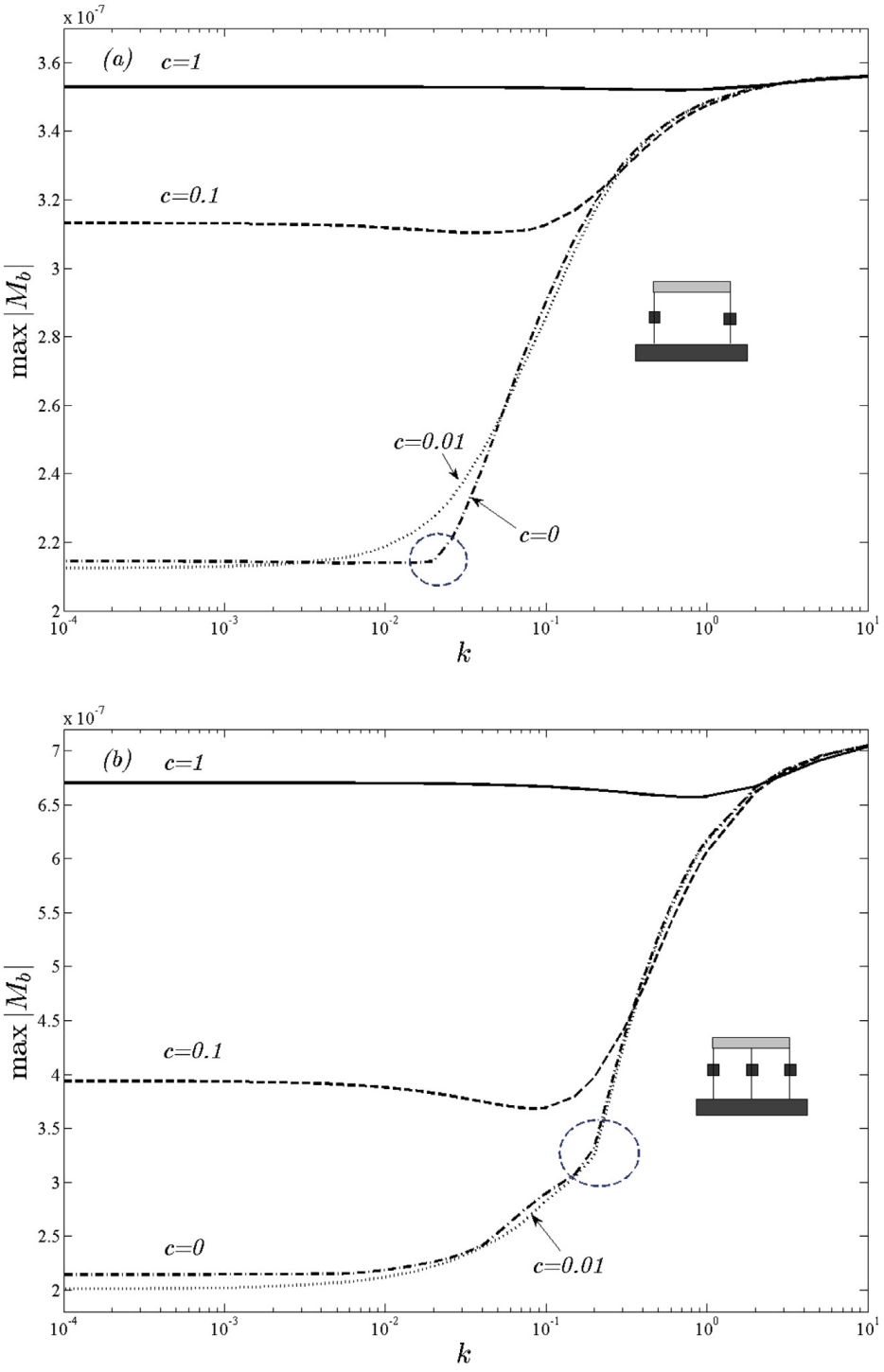


**Fig. 8.** Semi-log plot of the maximum absolute bending moment: (a) two edge connectors, (b) three connectors.

presented for both examined configurations featuring two and three connectors. As expected, the calculated maximum absolute deflection corresponds to the undamped case, i.e. $c = 0$, and small stiffness coefficient values (Fig. 7 a, b).

It is noted that for large stiffness coefficient values, the maximum absolute deflection is practically independent of the studied damping parameter values. Additionally, it is observed in Fig. 7 (a) and (b), that the optimal damping parameter, minimizing the maximum absolute deflection, is generally dependent on the stiffness of the connectors. In the overdamped case ($c = 1$) the above correlation appears weaker. Thus, it is deduced that it is possible to achieve minimization of the flexural deflections of a given configuration, for certain stiffness and damping coefficients ($c = 0.01$ and $k$~$10^{-2}$ in the considered examples), by means of the proposed methodology.

For the same example, in Fig. 8, it is shown that the maximum (absolute) bending moment, calculated for the three-connector configuration (Fig. 8(b)) is larger than the obtained value for the two-connector strip configuration,

examined in Fig. 8(a). The above is attributed to the system overstiffening due to the presence of the added middle connector.

Furthermore, as the stiffness coefficients $k$, become very large, the maximum calculated (absolute) bending moment does not depend on the damping coefficient. This phenomenon is illustrated by the plateau areas depicted in both Fig. 8(a) and (b). Finally, the observable points of inflection in Figs. 7 and 8, noted by the circled areas, are associated with abrupt changes in the location of the maxima values along the strip.

In order to gain a better understanding of the energy exchange between subregions, during the hydroelastic pulse excitation and propagation, the various terms composing the total energy of the system are studied. An illustration of the energy balance, expressed by Eq. (19), is shown in Fig. 9 for the case of a two-connector configuration, with $k = c = 0.01$. The total energy of the system, including the dissipated energy due to connector damping effects, is denoted by the solid black line, and remains constant in time. The energy of the water column in subdomain $S_2(x > 1)$ decreases after the moment of wave impact. After the excitation of the floating strip, the hydroelastic pulse begins to propagate in the middle region. Concurrently, the sum of the strain, kinetic and potential energy of the strip increases until a state of rest is reached and the quantities vanish after the full transmission of the pulse into the left halfstrip. Although the elastic connector energy $W(t)$ vanishes, the dissipated energy due to connector damping, represented by quantity $C(t)$, remains constant in time after the strip reaches a state of rest once again. Hence, the total connector energy $W(t) + 2C(t)$, increases after wave impact and remains constant after wave transmission into $S_1(x < 0)$. Finally, as the wave train enters the left half strip, the sum of the kinetic and potential energy of the water column in this region increases until full wave transmission in $S_2(x > 1)$ is achieved.

Next, a correlation between the energy quantities, defined in Sect. 3.1, and the elastic connector parameters is examined for the studied thin, elastic strip, employing two and three connectors and floating over the constant depth profile (a). Notably, the minimisation of the strip kinetic energy is important for the design of hydroelastic response mitigating devices and systems. In addition, structural safety and robust design would be translated in strip strain energy minimisation, while efficient wave energy harvest into dissipative energy maximisation. To this aim, the correlation between the energy quantities and the elastic connector parameters is further investigated in Figs. 10 and 11, for the defined strip-connector configurations. In Figs. 10(a) and 11(a) the elastic spring energy averaged in time, $\overline{W}$ is examined for a range of spring coefficient values. As expected, when the connector stiffness is small, less elastic energy is stored, while on the other hand, as the system is over stiffened the strip deflection is restricted, resulting again in smaller potential energy sums. Additionally, the elastic spring energy is found to increase with decreasing damping parameters in both cases.

Naturally, increasing the damping parameter results in a larger restoring force term which minimizes deflection. Finally, the near resonance conditions concerning the entire system for a given elastic strip are dependent on both connector stiffness and damping coefficients and is clearly depicted by the maxima of the $\overline{W}$-curves concerning the elastic connector energy. The damping energy is associated with the oscillatory speed of the strip (see Eq. (25)). In both cases, featuring two and three connectors, overstiffening results in vanishing damping energy, regardless of the damping

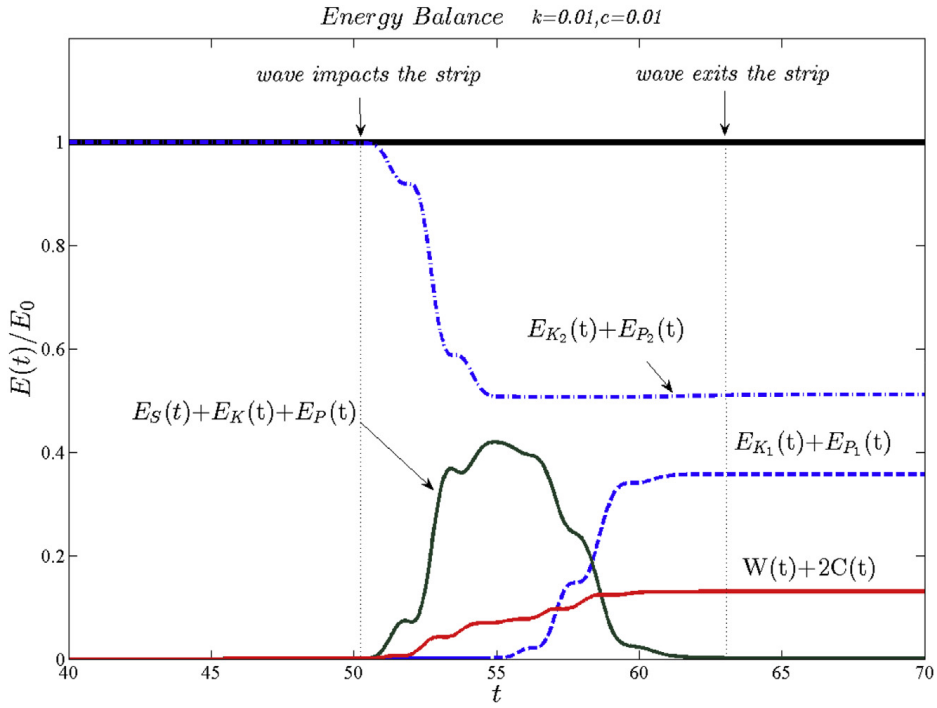


**Fig. 9.** The energy balance for a two connector configuration with $k = c = 0.01$.

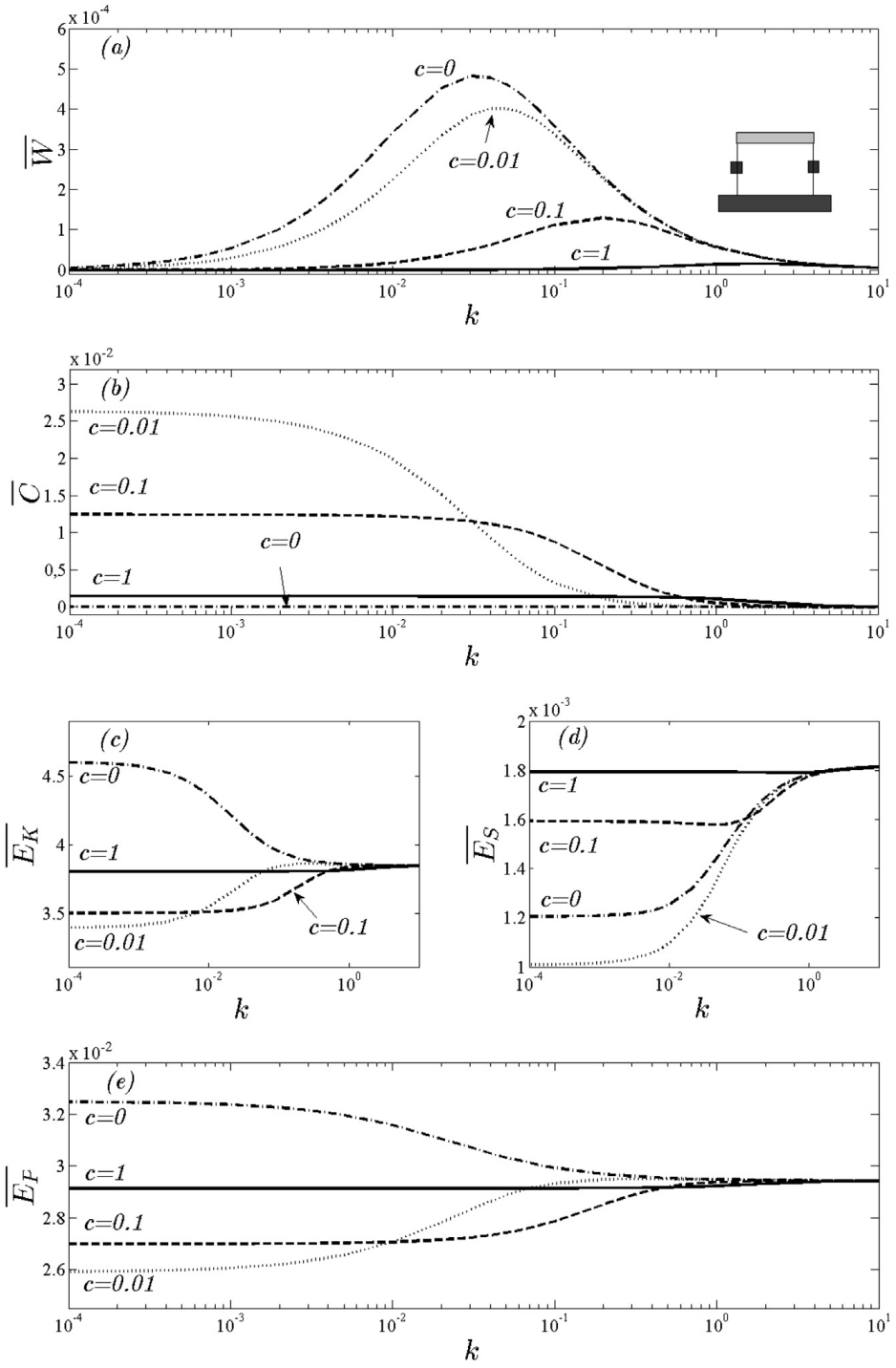


**Fig. 10.** Semi-log plot of the averaged energy quantities for the two-connector case. Connector parameters (a) elastic $\overline{\boldsymbol{W}}$ and (b) damping$\overline{\boldsymbol{C}}$. Elastic strip energy parameters (c) kinetic energy$\overline{\boldsymbol{E}}_{\boldsymbol{K}}$, (d) strain energy $\overline{\boldsymbol{E}}_{\boldsymbol{S}}$ and (e) potential energy $\overline{\boldsymbol{E}}_{\boldsymbol{P}}$.

parameter. The previous fact is straightforward, since in the presented 1-D hydroelastic system, the intensification of the restoring force on the strip results in energy reflection back in the free surface region. This fact essentially leads to less energy sums being transmitted into the middle subregion $S_0(0<x<1)$. Additionally, it is observed in Figs. 10(b) and 11(b) that for a given configuration and connector stiffness parameter, there exist specific values of the damping coefficient for which dissipated energy is maximized. This is expected to have an important effect on the kinetic energy of the elastic strip$\overline{E}_K$. The kinetic energy is presented in 10 (c) and 11(c) for a combination of stiffness and damping coefficients for the two and three connector configuration, respectively. Maximum kinetic energy is obtained when the restoring force is minimal, hence for $c=0$ and $k\sim10^{-4}$. Since the kinetic energy of the strip is also a function of oscillatory motion speed (see Eq. (22a)), minimization is achieved for the damping parameter values maximizing energy dissipation, as previously described.

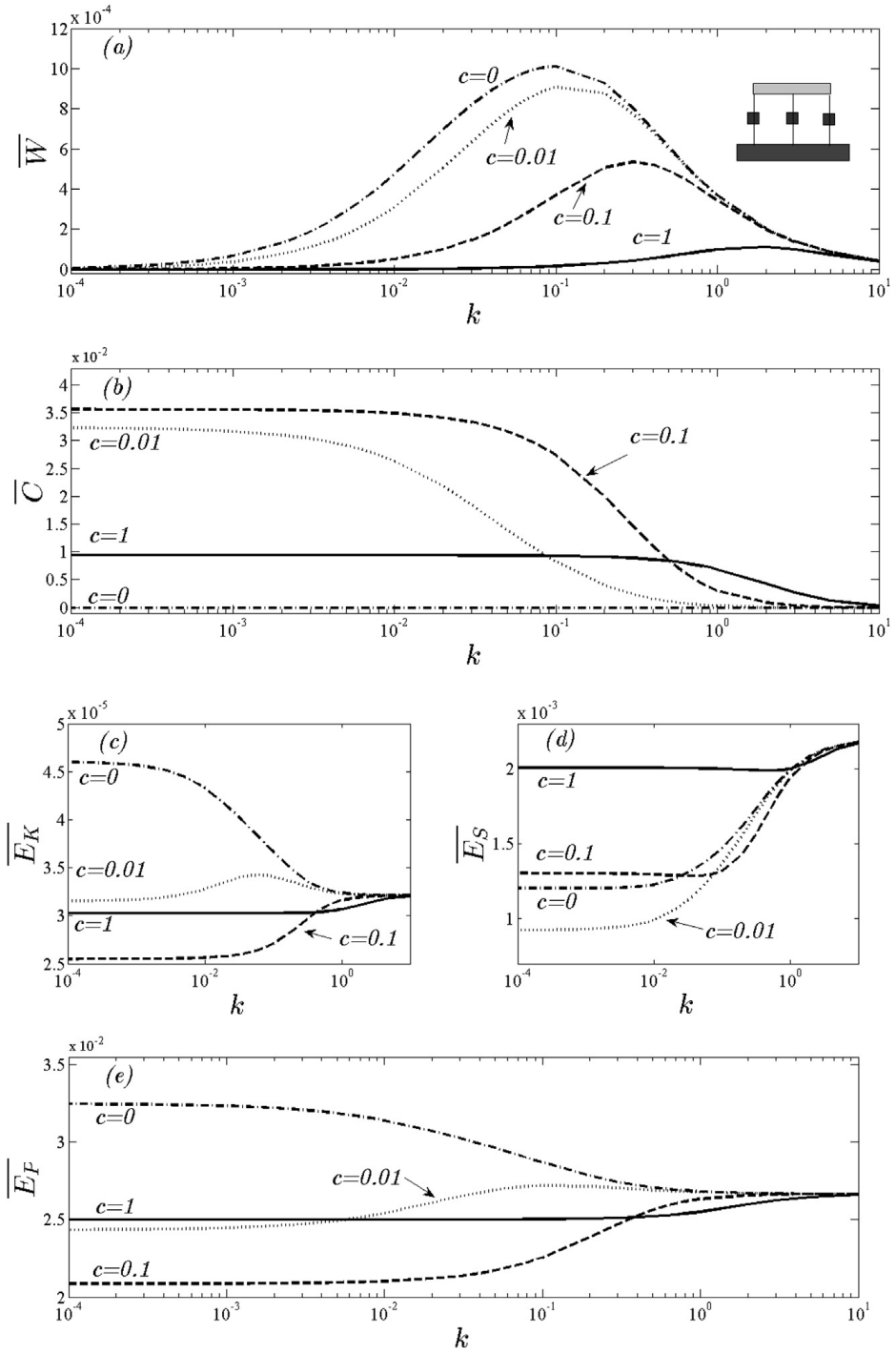


**Fig. 11.** Same as Fig. 10 for the three connector-strip configuration.

The averaged strain energy$\overline{E}_S$, which expresses the amount of flexural deformation undergone by the strip (defined by Eq. (29b)), is examined in Figs. 10(d) and 11(d). It is observed in both cases that the minimum strain energy, for low values of stiffness, is obtained for damping coefficient value $c$ between 0 and 0.01. This is compatible with the fact that the maximum absolute bending moment, as seen in Fig. 8(a) and (b), is minimal for the same values in both examined strip-connector configurations. Notably, the strain energy of the strip, in both cases, becomes larger with increasing stiffness coefficients which correlates with previous observations for the bending moment, illustrated in Fig. 8. Finally, the total energy $\overline{E}_P$ in the middle subregion is depicted in 10(e) and 11(e). Since the elastic strip deflection is generally very small, the energy sum expressed by $\overline{E}_P$ is dominated by the kinetic energy of the water column in the middle region ($S_0$) and resembles the kinetic strip energy plotted in Figs. 10(c) and 11(c).

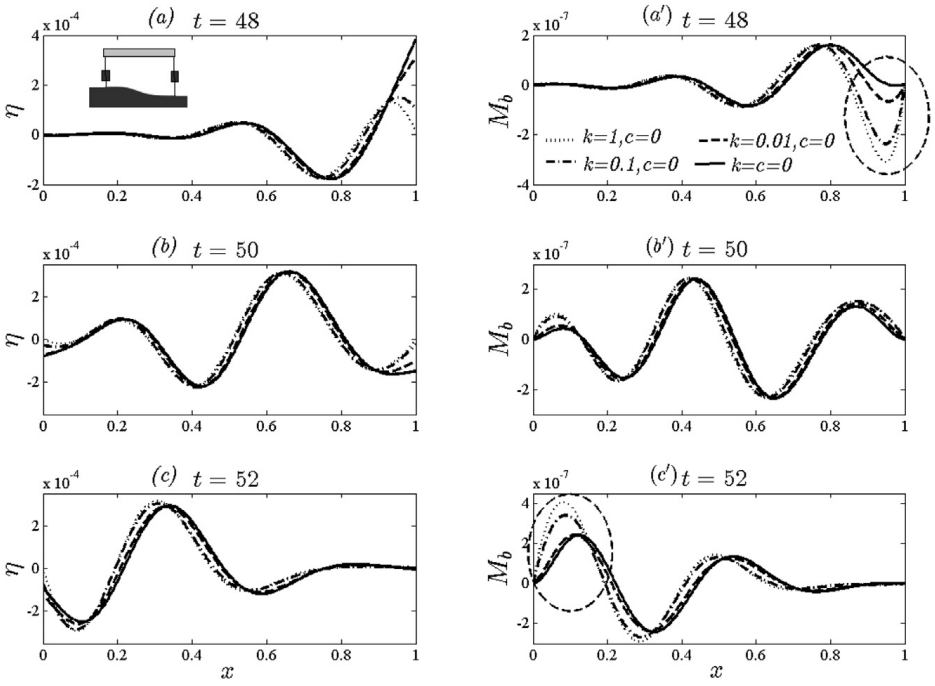


**Fig. 12.** Nondimensional strip deflection (left subplots) and bending moment $M_b = K\eta_{xx}$, (right subplots) distribution for several connector stiffness values and zero damping. Two connector-strip configuration for bathymetric profile (b).

### 4.3. Sloping bottom profiles (b) and (c)

Variable bathymetric effects, as previously mentioned, are an important consideration in nearshore and coastal marine structure design. The proposed computational tool, able to account for a variable seabed, could be found useful in the study of bathymetric effects on the hydroelastic response of a floating strip with elastic connectors. In this section, numerical results are presented and discussed for the two variable seabed profiles corresponding to an upslope (b) and a downslope (c) environment (see Fig. 2).

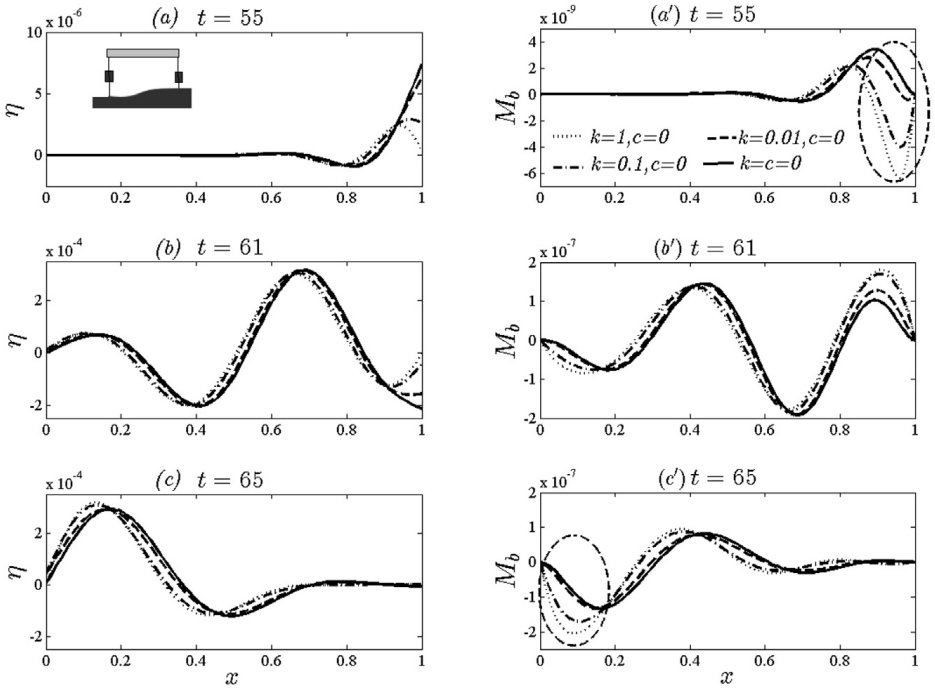


**Fig. 13.** Same as in Fig. 12 but for the downslope environment (c).

More specifically, in Figs. 12 and 13, the strip responses and bending moment distributions for the two connector-strip configuration are plotted at three distinct time instances for profiles (b) and (c) respectively. Curves corresponding to various connector stiffness parameter values are presented, while zero damping effects are considered. In accordance with previous observations (see Fig. 5), it is established that increasing connector stiffness, results in larger maximum absolute bending moment values. The above leads to increased normal stresses induced by flexural motion, but to an overall reduced hydroelastic response compared to the freely floating case, for both profiles of variable bathymetry.

In the case of the upslope environment, it is observed in Fig. 12(a) that at the wave entry phase ($t=48$), the maximum absolute strip deflection appears reduced by 19.24%, 54.5% and 55% for $k=0.01$, 0.1 and 0.1 respectively, compared to the freely floating case. Marginal response reduction is achieved at $t=50$ (Fig. 12(b)), reaching 0.12%, 1.95% and 3.34% for $k=0.01$, 0.1, when compared to the freely floating case. At the wave exit phase, the maximum absolute strip deflection is only slightly reduced by 1.1% for $k=0.01$, while it increases by 3.85% and 8% for $k=0.1$ and $k=1$. The overall (over time) maximum absolute deflection is reduced by 22.36% 29.45% and 28.23% for $k=0.01, 0.1$ and 1. In Fig. 12(c), absolute maximum deflection increased by 3.85% and 8% for $k=0.1, 1$, while marginal reduction of 1.19% is achieved for $k=0.01$. The above findings are in agreement with previous observations for the constant depth case (see Fig. 5).

The corresponding bending moment distributions, presented in Fig. 12(a′)–(c′), exhibit intensification of flexural effects in the vicinity of the strip edges during wave entry and exit (denoted by the dashed circles in Fig. 12(a′)–(c′)), which was also observed in the constant depth case. However, maximum absolute bending moment intensification is reduced compared to the constant depth profile calculations, reaching 48.2% and 93.7% for $k=0.1$ and 1 at wave entry (i.e. Fig. 12(a′)), while a slight decrease of 0.39% compared to the freely floating case, calculated for bathymetric profile (b), is achieved for $k=0.01$. At wave propagation phase $t=50$ (i.e. Fig. 12(b′)), maximum absolute bending is slightly increased by 1.16%, 2.32% and 1.15% for increasing stiffness. This can be attributed to the fact that the propagating pulse becomes steeper with decreasing depth (profile b), causing an intensification of flexural effects. During the wave exit phase bending moment intensification is observed (i.e. Fig. 12(c′)), with maximum increase reaching 66% for $k=1$ compared to the freely floating case.

Finally, the hydroelastic responses of the two connector-strip configuration floating over the downslope bathymetric profile (c) are examined in Fig. 13. Overall maximum strip deflection is once again reduced by 22.35%, 29.08 and 27.68% for increasing connector stiffness values. Moreover, bending moment intensification is observed at the vicinity of employed connectors at wave entry and transmission phases (i.e. Fig. 13(a′)–(b′)). Hence, bathymetric effects appear to have minimal impact on the hydroelastic response of the examined configurations.

Increasing the connectors' damping parameter, while keeping the stiffness value constant was also found to reduce the strip elastic motion. Examining the bending moment distributions for the varying damping analysis it was observed that bending moment is magnified in the vicinity of the free edges during wave entry and exit. This were the case for both considered profiles. Hence, the inclusion of dampers in the elastic connector design might have an undesirable intensification effect in the induced stresses on the strip. In conclusion, the design of an efficient elastic connector configuration constitutes a multi-parametric optimization problem. The proposed methodology is able to provide useful information concerning the vibration reduction of the structure and support the design of efficient mooring systems.

## 5. Conclusions

The time-domain hydroelastic response of a thin, floating strip, elastically connected to the seabed, is examined in the present work. Based on the variational formulation of the initial-boundary value problem in shallow water conditions, an energy balance equation is derived, while a higher-order finite element scheme is implemented for the numerical solution. Results for various strip-connector configurations of interest, illustrating the response reducing effects of the employed connectors, are presented. In addition to the flat bottom case, two variable bathymetric profiles (an upslope and a downslope environment) were studied. Numerical results were obtained for the cases of two strip-connector configurations. The first configuration employs two elastic connectors, positioned at the free strip ends, while the second features an additional connector located at the middle of the structure. The study of the aforementioned configurations reveals that response mitigation is possible through the increase the number and the stiffness of the employed connectors. However, deflection mitigation through connector stiffening is associated with excessive maximum bending moment values, at the vicinity of the connector locations along the strip. Hence, overstiffening can be correlated with undesirable bending induced local stresses. Moreover, optimal damping coefficient for the minimization of the maximum absolute defection and bending moment is found to be generally depended on connector stiffness. In conclusion, the design of an efficient elastic connector-strip configuration constitutes a multi-parametric optimization problem. The proposed methodology is able to provide useful information concerning the vibration reduction of the structure and support the design of efficient motion mitigating systems. Future research will focus on the treatment of the 3D problem and intermediate water depth effects. Finally, the investigation of weak nonlinearity is of equal importance. An initial investigation in the latter direction has been presented in Karperaki et al. [35].

## Acknowledgements

The present work has been supported by the project HYDELFS funded by the Operational Program “Education and Lifelong Learning” of the National Strategic Reference Framework (NSRF 2007–2013) -Research Funding Program ARHIMEDES-III:

Investing in knowledge society through the European Social Fund. In particular, author Theodosios K. Papathanasiou acknowledges support from the aforementioned program for the period from 6/9/2012 to 30/09/2014.

## References

[1] Wang CM, Watanabe E, Utsunomiya T. Very large floating structures. London, UK: Taylor and Francis; 2008.
[2] Watanabe E, Utsunomiya T, Wang CM. Hydroelastic analysis of pontoon-type VLFS: a literature survey. Eng Struct 2004;2004(26):245–56.
[3] Wang CM, Tay ZY. Very large floating structures: applications, research and development. Procedia Eng 2011;14:62–72.
[4] Chen XJ, Wu YS, Cui WC, Juncher Jensen J. Review of hydroelasticity theories for global response of marine structures. Ocean Eng 2006;33:439–57.
[5] Ohmatsu S. Overview: research on wave loading and responses of VLFS. Mar Struct 2005;18:149–68.
[6] Ertekin CR, Kim JW, Yoshida K, Mansour AE, editors. Very large floating structures (parts I,II) Mar Struct; 2000. Vol. 13 No. 4,5 and 2001; Vol 14 No. 1,2.
[7] Kashiwagi MA. B-spline Galerkin scheme for calculating the hydroelastic response of a very large floating structure waves. J Mar Sci Tech 1998;3:37–49.
[8] Wang CM, Xiang Y, Utsunomiya T, Watanabe E. Evaluation of modal stress resultants in freely vibrating plates. Int J Solids Struct 2001;38:6525–58.
[9] Chen XJ, Jensen JJ, Cui WC, Fu SX. Hydroelasticity of a floating plate in multidirectional waves. Ocean Eng 2003;30:1997–2017.
[10] Eatock Taylor R, Ohkusu M. Green functions for hydroelastic analysis of vibrating freefreebeams and plates. Appl Ocean Res 2000;22:295–314.
[11] Kim JW, Ertekin RC. An eigenfunction-expansion method for predicting hydro-elastic behaviour of a shallow-draft VLFS. In: Proceedings of the 2nd international conference on hydroelastic marine technology, Fukuoka, Japan; 1998.
[12] Watanabe E, Utsunomiya T, Tanigaki S. A transient response analysis of a very large floating structure by finite element method. Struct Eng Earthq Eng 1998;15:155–63.
[13] Watanabe E, Utsunomiya T. Transient response analysis of a VLFS at airplane landing. In: Proceedings of the international workshop on very large floating structures, Hayama, Japan; 1996. p. 243–7.
[14] Kashiwagi MA. time-domain mode-expansion method for calculating transient elastic responses of a pontoon-type VLFS. J Mar Sci Technol 2000;5:89–100.
[15] Montiel F, Bennets LG, Squire VA. The transient response of floating elastic plates to wavemaker forcing in two dimensions. J Fluid Struct 2012;28:416–33.
[16] Sturova IV. Time-dependent response of a heterogeneous elastic plate floating on shallow water of variable depth. J Fluid Mech 2009;637:305–25.
[17] Papathanasiou TK, Karperaki A, Theotokoglou EE, Belibassakis KA. A higher order FEM for time-domain hydroelastic analysis of large floating bodies in an inhomogeneous shallow water environment. Proc R Soc A 2014;471:20140643.
[18] Sun H, Cui WC, Liu YZ, Liao SJ. Hydroelastic response analysis of mat-like VLFS over a plane slope in head seas. China Ocean Eng 2003;17:315–26.
[19] Utsunomiya T, Watanabe E, Nishimura N. Fast multipole algorithm for wave diffraction/radiation problems and its application to VLFS in variable water depth and topography. In: Proceedings of the 20th international conference on offshore mechanics and arctic engineering; 2001. p. 1–7.
[20] Belibassakis KA, Athanassoulis GA. A coupled mode model for the hydroelastic analysis of large floating bodies over variable bathymetry regions. J Fluid Mech 2005;531:221–49.
[21] Gerostathis Th P, Belibassakis KA, Athanassoulis GA. 3D hydroelastic analysis of very large floating bodies over variable bathymetry regions. J. Ocean Eng. Mar. Energy 2016. http://dx.doi.org/10.1007/s40722-016-0046-6.
[22] Nagata S, Yoshida H, Fujita T, Isshiki H. Reduction of the motion of and elastic floating plate in waves by breakwaters. In: Proceedings of the 2nd international conference on hydroelasticity in marine technology, Fukuoka, Japan; 1998. p. 229–38.
[23] Seto H, Ochi M. A hybrid element approach to hydroelastic behavior of a very large floating structure in regular wave. In: Proceedings of the 2nd international conference on hydroelasticity in marine technology, Fukuoka, Japan; 1998. p. 185–94.
[24] Utsunomiya T, Watanabe E, Nakamua N. Analysis of drift force on VLFS by the near-field approach. In: Proceedings of the 11th offshore & polar engineering conference, Stavanger, Norway; 2001. p. 217–21.
[25] Ohmatsu S. Numerical calculation method of hydroelastic response of a pontoon-type VLFS close to a breakwater. In: Proceedings of the 3rd international workshop VLFS, Honolulu, Hawaii; 1999. p. 805–11.
[26] Ohta H, Torii T, Hayashi N, Watanabe E, Utsunomiya T, Sekita K, et al. Effect of attachment of a horizontal/vertical plate on the wave response of a VLFS. In: Proceedings of the 3rd international workshop VLFS, Honolulu, Hawaii; 1999; 1999. p. 265–74.
[27] Watanabe E, Utsunomiya T, Kuramoto M, Ohta H, Torii T, Hayashi N. Wave response analysis of VLFS with an attached submerged plate. In: Proceedings of the 12th international conference in ocean polar engineering, Kyushu, Japan; 2002; 2002. p. 319–26.
[28] van Kessel JLF, Pinkster JA. The effect of aircushion division on the motions of large floating structures. In: The proceedings of the 26th international conference on offshore mechanics and arctic engineering, san Diego, USA; 2007. p. 677–86.
[29] Khabakhpasheva TI, Korobkin AA. Hydroelastic behaviour of compound floating plate in waves. J Eng Math 2002;44:21–40.
[30] Karmakar D, Guedes Soares C. Scattering of gravity waves by a moored finite floating elastic plate. Appl Ocean Res 2012;2012(34):135–49.
[31] Cunbao Z, Jiazhong Z, Wenhu H. Vibration reduction of floating elastic plates in water waves. Mar Struct 2007;20:71–99.
[32] Korobkin AA, Khabakhpasheva TI. Wave power absorbers at floating platform. In: 25th int. Workshop on water waves and floating bodies, Harbin, China; May 2012. p. 9–12. http://www.iwwwfb.org.
[33] Wu C, Watanabe E, Utsunomiya T. An eigenfunction expansion-matching method for analyzing the wave-induced responses of an elastic floating plate. Appl. Ocean Res. 1995;17:301–10.
[34] Stoker JJ. Water waves: the mathematical theory with applications interscience. 1957.
[35] Karperaki AE, Belibassakis KA, Papathanasiou TK, Markolefas SI. Higher-order FEM for nonlinear hydroelastic analysis of a floating elastic strip is shallow-water conditions. In: VI international conference on computational methods for coupled problems in science and engineering, Venice, Italy; 2015. 1110–1022.

# Conclusion and Future Research Direction

The primary objective of the present thesis is the investigation of hydroelastic phenomena in an inhomogeneous ocean setting. The conducted study led to different approaches targeting frequency domain (which consists the bulk of the work presented in Parts I-III of the present), and time domain analyses (delineated in Part IV). The main points and contributions are summarised below,

In the *frequency domain*, the proposed methodology treats the hydroelastic interaction of small amplitude incident waves with inhomogeneous plates of negligible draft floating over regions characterized by variable bathymetry. Moreover, the method allows for the treatment of thin to moderately thick plates modelled by the Kirchhoff (CPT) and Minldin's (FSDT) respectively. The wave field decomposition into diffraction and radiation components along with a modal expansion for the plate deflection, employing the *in vacuo* flexural modes are principal features of the work as seen in Chapter 1. The latter allows for the full decoupling of structural mechanics to wavefield transformations generating a series of hydrodynamic sub-problems which are formulated in terms of solely kinematic considerations Chapter 1. For the component hydrodynamic problems, a weighted residuals approach is subsequently followed for the derivation of suitable weak formulations for FEM implementation. For radiation-type problems the weighted residuals approach in conjunction with a Lagrange multiplier formulation was followed to derive a series of saddle-point problems. The aim of the latter approach was to weakly satisfy the continuity requirement across the fictitious sub-domain interface boundary and alleviate the complexity of constructing suitable FEM spaces (Chapter 3) with integrated essential conditions. Next, the dimensionality reduction of the derived weak formulations was sought by means of an enhanced vertical representation for the wave potential, augmented by the sloping bottom mode, originally proposed in Athanassoulis and Belibassakis (1999) for the consistent treatment of sloping topography (Chapter 4). Finally, the FEM is employed for the treatment of the reduced weak hydrodynamic problems in 1D and 2D, while the pressure condition on the plate-covered part of the fluid surface is imposed by means of Galerkin's method, as presented in Chapters 5 and 7 respectively. Furthermore, towards a monolithic approach, the free vibration problem of the inhomogeneous plates was treated by the FEM in

1D and 2D, employing the same discretization for the domain of interest. Finally, in search of appropriate closure conditions a PML-FEM scheme featuring unbounded absorbing functions was implemented (Chapter 6).

In the 2D setting modelling a floating plate strip interacting with a range independent waveguide, the proposed method is validated against a series of numerical cases, featuring a range of configurations, and experimental data documented in the literature exhibiting excellent performance (Chapter 8). The direct extension of the method to 3D illustrated the capability of the proposed method to treat inhomogeneity and general geometries while achieving computational savings.

A major advantage of the proposed method is that it carries no simplifying assumptions for the vertical structure of the wave-field or the bathymetric slope of the examined waveguide. The characteristics of the wave-field, as well as the bending moment and shear force distributions of the structure, can be recovered either straightforwardly or by trivial post-processing. Moreover, due to the treatment of the weak problem formulation, the smoothness requirement on the depth function, documented in Belibassakis and Athanassoulis (2005) is relaxed, enabling the treatment of more general profiles, while the numerical scheme remains rapidly convergent. Regarding the structural modelling, the method is able to account for both material and geometric inhomogeneity, while first order shear effects and rotary inertia, relevant in high-frequency excitation scenarios, are also taken into account by means of the FSDT. Moreover, despite the augmented discretised system, the constrained formulation allows for the employment of conventional trial spaces, and the final discretization is performed with Lagrange elements. A major advantage of the present method is its versatility to treat general bathymetry and structural shape. Finally, the method immediately allows for the structural modelling by means of higher-order plate theories with minimal reformulation.

Several directions for future research can be outlined. In the sequel these are prioritised as follows,

- ☐ Enhance the validation of the method in 3D. In the 2D setting all features of the proposed methodology are extensively validated against both experimental and numerical results published in the literature. The same was proven non-trivial for the 3D case. Verification of 3D bathymetric effects can be achieved be considering published experimental results.

- ☐ Extend and implement the proposed method in the study of interesting technological and physical features. The method can be straightforwardly extended to treat multi-body configurations in the general 3D setting. Minimal reformulation would allow for the consideration of technological features, like the treatment of multiple connected flexible bodies (Ren et al., 2019; Zhang and Lu, 2018). Moreover the method can be extended for modelling the hydroelastic interactions of 3D bodies in polynya (Li et al., 2020). Finally, the method can be extended to treat the effects of elastic medium porosity. Porous structures are implemented in energy dissipation applications relevant to ocean

engineering. The recent works of Meylan et al. (2017), Zheng et al. (2020) and Koley (2020) document the integration of porosity effects in established methods of floating hydroelasticity by incorporating Darcy's law on the boundary conditions of the wetted surface of the structure.

- ☐ Incorporate finite draft effects. The assumption of shallow draft leads to the generation of geometrically conforming interfaces. From a numerical point of view, deviating from the latter would require the employment of 'mortar' methods in the weak formulation of radiation-type sub-problems. A stabilisation approach for the corresponding discrete saddle-point problems will recover the method's consistency (Barbosa and Hughes, 1991; Burman, 2014).

- ☐ Extend and incorporate the developed tools for nonlinear analysis in the context of Stokes theory following the work of Belibassakis and Athanassoulis (2002). In this case, nonlinearity should also be introduced in the modelling of structural motion to account for large deflections in accordance with the hydrodynamic assumption of greater wave amplitude.

- ☐ Explore the parallelisation potential of the computational method. The employed decomposition into subproblems and the developed FEM-based numerical schemes allow for parallel computations, an alternative that promises accelerated runtime that has not been exploited in the present version of the numerical tool.

- ☐ Numerical investigation of discrete *inf-sup* conditions for the formulated saddle point problems. To ensure the numerical stability of the method, the proposed FEM spaces pair for the primary variable and the Lagrange multiplier functions must be shown to satisfy the discrete Babuska-Brezzi conditions.

# Bibliography


Abarbanel, S. and Gottlieb, D. (1997). A Mathematical Analysis of the PML Method. *Journal of Computational Physics*, 134(2):357–363.

Aranha, J. A., Mei, C. C., and Yue, D. K. P. (1979). Some properties of a hybrid element method for water waves. *International Journal for Numerical Methods in Engineering*, 14(11):1627–1641.

Athanassoulis, G. A. and Belibassakis, K. A. (1999). A consistent coupled-mode theory for the propagation of small-amplitude water waves over variable bathymetry regions. *Journal of Fluid Mechanics*, 389:275–301.

Athanassoulis, M. A. and Belibassakis, K. (2009). A novel coupled-mode theory with application to hydroelastic analysis of thick, non-uniform floating bodies over general bathymetry. *Proceedings of the Institution of Mechanical Engineers Part M: Journal of Engineering for the Maritime Environment*, 223(3):419–438.

Bai, J. K. and Yeung, R. (1974). Numerical Solution to free surface flow problems. In *10th Symposium of Naval Hydrodynamics 24-28 June, Cambridge, Massachusetts*.

Bai, K. J. (1972). A Variational Method in potential flows with a free surface. Technical Report AD-755 465.

Barbosa, H. J. and Hughes, T. J. (1991). The finite element method with Lagrange multipliers on the boundary: circumventing the Babuška-Brezzi condition. *Computer Methods in Applied Mechanics and Engineering*, 85(1):109–128.

Batoz, J. L. (1980). A STUDY OF THREE-NODE TRIANGULAR PLATE BENDING ELEMENTS. 15(January):1771–1812.

Batoz, J. L. and Lardeur, P. (1989). A discrete shear triangular nine D.O.F. element for the analysis of thick to very thin plates. *International Journal for Numerical Methods in Engineering*, 28(3):533–560.

Belibassakis, K. and Athanassoulis, G. (2009). Hydroelasticity in marine technology. In *The Fifth International Conference on Hydroelasticity in Marine Technology*, Southampton.

Belibassakis, K. A. and Athanassoulis, G. A. (2002). Extension of second-order Stokes theory to variable bathymetry. *Journal of Fluid Mechanics*, 464:35–80.

Belibassakis, K. A. and Athanassoulis, G. A. (2005). A coupled-mode model for the hydroelastic analysis of large floating bodies over variable bathymetry regions. *Journal of Fluid Mechanics*, 531:221–249.

Belibassakis, K. A. and Athanassoulis, G. A. (2006). A coupled-mode technique for weakly nonlinear wave interaction with large floating structures lying over variable bathymetry regions. *Applied Ocean Research*, 28(1):59–76.

Belibassakis, K. A., Athanassoulis, G. A., and Gerostathis, T. P. (2001). A coupled-mode model for the refraction-diffraction of linear waves over steep three-dimensional bathymetry. *Applied Ocean Research*, 23(6):319–336.

Belibassakis, K. A., Gerostathis, T. P., and Athanassoulis, G. A. (2011). A coupled-mode model for water wave scattering by horizontal, non-homogeneous current in general bottom topography. *Applied Ocean Research*, 33(4):384–397.

Bennetts, L. G., Biggs, N. R., and Porter, D. (2007). A multi-mode approximation to wave scattering by ice sheets of varying thickness. *Journal of Fluid Mechanics*, 579:413–443.

Berenger, J. P. (1994). A perfectly matched layer for the absorption of electromagnetic waves. *Journal of Computational Physics*, 114(2):185–200.

Berkhoff, J. C., Booy, N., and Radder, A. C. (1982). Verification of numerical wave propagation models for simple harmonic linear water waves. *Coastal Engineering*, 6(3):255–279.

Bermúdez, A., Hervella-Nieto, L., Prieto, A., and Rodríguez, R. (2004). Une PML exacte et bornée pour l'équation de Helmholtz. *Comptes Rendus Mathematique*, 339(11):803–808.

Bermúdez, A., Hervella-Nieto, L., Prieto, A., and Rodríguez, R. (2006). Optimal perfectly matched layers for time harmonic acoustic scattering problems. *Preprint*, (March 2006).

Bermúdez, A., Hervella-Nieto, L., Prieto, A., and Rodríguez, R. (2007). An optimal perfectly matched layer with unbounded absorbing function for time-harmonic acoustic scattering problems. *Journal of Computational Physics*, 223(2):469–488.

Bermúdez, A., Hervella-Nieto, L., Prieto, A., and Rodríguez, R. (2010). Perfectly Matched Layers for time-harmonic second order elliptic problems. *Archives of Computational Methods in Engineering*, 17(1):77–107.

Bermúdez, A., Hervella-Nieto, L., and Rodríguez, R. (2001). Finite element computation of the vibrations of a plate-fluid system with interface damping. *Computer Methods in Applied Mechanics and Engineering*, 190(24-25):3021–3038.

Bhat, R. B. (1985). Naural frequencies of rectangular plates using characteristic orthogonal polynomials in Rayleigh-Ritz method. *Journal of Sound and Vibration*, 102(4):493–499.

Bishop, R. E. and Price, W. G. (1976). On the relationship between "dry modes" and "wet modes" in the theory of ship response. *Journal of Sound and Vibration*, 45(2):157–164.

Booij, N. (1983). A note on the accuracy of the mild-slope equation. *Coastal Engineering*, 7(3):191–203.

Brekhovskikh, L. M. and Lysanov, Y. P. (1982). *Fundamentals of Ocean Acoustics*. Berlin, Heidelberg.

Brezzi, F. and Fortin, M., editors (1991). *Mixed and Hybrid Finite Element Methods*. New York, NY.

Bromirski, P. D. and Stephen, R. A. (2012). Response of the ross ice shelf, antarctica, to ocean gravity-wave forcing. *Annals of Glaciology*, 53(60):163–172.

Brunt, K. M., Okal, E. A., and Macayeal, D. R. (2011). Antarctic ice-shelf calving triggered by the Honshu (Japan) earthquake and tsunami, March 2011. *Journal of Glaciology*, 57(205):785–788.

Burman, E. (2014). Projection stabilization of Lagrange multipliers for the imposition of constraints on interfaces and boundaries. *Numerical Methods for Partial Differential Equations*, 30(2):567–592.

Chai, Y., Li, W., Gong, Z., and Li, T. (2016). Hybrid smoothed finite element method for two-dimensional underwater acoustic scattering problems. *Ocean Engineering*, 116:129–141.

Chamberlain, P. G. and Porter, D. (1995). Decomposition methods for wave scattering by topography with application to ripple beds. *Wave Motion*, 22(2):201–214.

Chen, X. J., Jensen, J. J., Cui, W. C., and Fu, S. X. (2003). Hydroelasticity of a floating plate in multidirectional waves. *Ocean Engineering*, 30(15):1997–2017.

Cheng, Y., Ji, C., Zhai, G., and Oleg, G. (2017). Fully nonlinear numerical investigation on hydroelastic responses of floating elastic plate over variable depth sea-bottom. *Marine Structures*, 55:37–61.

Cimpeanu, R., Martinsson, A., and Heil, M. (2015). A parameter-free perfectly matched layer formulaton for the finite-element-based solution f the Helmholtz equation. *Journal of Computational Physics*, 296:329–347.

Collino, F. and Monk, P. B. (1998). Optimizing the perfectly matched layer. *Computer Methods in Applied Mechanics and Engineering*, 164(1-2):157–171.

Dai, J., Wang, C. M., Utsunomiya, T., and Duan, W. (2018). Review of recent research and developments on floating breakwaters.

Ding, J., Tian, C., sheng Wu, Y., feng Wang, X., long Liu, X., and Zhang, K. (2019). A simplified method to estimate the hydroelastic responses of VLFS in the inhomogeneous waves. *Ocean Engineering*, 172(December 2018):434–445.

Ding, J., Tian, C., sheng Wu, Y., wei Li, Z., jie Ling, H., and zhou Ma, X. (2017). Hydroelastic analysis and model tests of a single module VLFS deployed near islands and reefs. *Ocean Engineering*, 144:224–234.

Dingenmanns, W. M. (1997). Practical aspects of linear wave propagation models. pages 399–433.

Ertekin, R. C. and Xia, D. (2014). Hydroelastic response of a floating runway to cnoidal waves. *Physics of Fluids*, 26(2):27101.

Faltinsen, O. M. (2015). Hydrodynamics of marine and offshore structures.

Finlayson, B. A. (2013). The Method of Weighted Residuals and Variational Principles. *The Method of Weighted Residuals and Variational Principles*.

Finlayson, B. A. and Scriven, L. E. (1967). On the search for variational principles. *International Journal of Heat and Mass Transfer*, 10(6):799–821.

Fox, C. and Squire, V. A. (1991). Coupling between the ocean and an ice shelf. *Annals of Glaciology*, 15:101–108.

Fung, Y., Tong, P., and Bechtel, S. (2003). *Classical and Computational Solid Mechanics*, volume 56.

Gao, D. Y. (1996). Nonlinear Elastic Beam Theory with Application in Contact Problems and Variational Approaches. *Mechanics Research Communications*, 23(1):11–17.

Gerostathis, T. P., Belibassakis, · . K. A., Athanassoulis, · . G. A., Belibassakis, K. A., and Athanassoulis, G. A. (2016). 3D hydroelastic analysis of very large floating bodies over variable bathymetry regions. *Journal of Ocean Engineering and Marine Energy*, 2(2):159–175.

Givoli, D. (1991). Non-reflecting boundary conditions. *Journal of Computational Physics*, 94(1):1–29.

Givoli, D. (1992). *Numerical Methods for Problems in Infinite Domains*. Elsevier Science Ltd.

Givoli, D. (2004). High-order local non-reflecting boundary conditions: A review. *Wave Motion*, 39(4):319–326.

Guo, X., Wang, B., Mei, C. C., and Liu, H. (2017). Scattering of periodic surface waves by pile-group supported platform. *Ocean Engineering*, 146:46–58.

Harari, I. and Albocher, U. (2006). Studies of FE/PML for exterior problems of time-harmonic elastic waves. *Computer Methods in Applied Mechanics and Engineering*, 195(29-32):3854–3879.

Hegarty, G. M. and Squire, V. A. (2004). On modelling the interaction of large amplitude waves with a solitary floe. In *Proceedings of the International Offshore and Polar Engineering Conference*, pages 845–850. OnePetro.

Hegarty, G. M. and Squire, V. A. (2008). A boundary-integral method for the interaction of large-amplitude ocean waves with a compliant floating raft such as a sea-ice floe. *Journal of Engineering Mathematics*, 62(4):355–372.

Hermans, A. J. (2003). The ray method for the deflection of a floating flexible platform in short waves. *Journal of Fluids and Structures*, 17(4):593–602.

Huang, L., Ren, K., Li, M., Tuković, Ž., Cardiff, P., and Thomas, G. (2019). Fluid-structure interaction of a large ice sheet in waves. *Ocean Engineering*, 182:102–111.

Hughes, T. J. R. (2000). *The Finite Element Method: Linear Static and Dynamic Finite ELement Analysis*.

Iida, T. and Umazume, K. (2020). Wave response of segmented floating plate and validation of its homogenized solution. *Applied Ocean Research*, 97(February):102083.

Ilyas, M., Meylan, M. H., Lamichhane, B., and Bennetts, L. G. (2018). Time-domain and modal response of ice shelves to wave forcing using the finite element method. *Journal of Fluids and Structures*, 80:113–131.

Jensen, F. B., Kuperman, W. A., Porter, M. B., and Schmidt, H. (2011). *Computational Ocean Acoustics*. Springer New York.

Jiao, J., Yu, H., Chen, C., and Ren, H. (2019). Time-domain numerical and segmented model experimental study on ship hydroelastic responses and whipping loads in harsh irregular seaways. *Ocean Engineering*, 185:59–81.

Kalyanaraman, B., Meylan, M. H., Bennetts, L. G., and Lamichhane, B. P. (2020). A coupled fluid-elasticity model for the wave forcing of an ice-shelf. *Journal of Fluids and Structures*, 97:103074.

Kantorovich, L. V. and Krylov, V. I. (1960). *Approximate Methods of Higher Analysis*. Interscience Pub., New York, 4th ed. edition.

Karperaki, A., Belibassakis, K., and Papathanasiou, T. (2016). Time-domain, shallow-water hydroelastic analysis of VLFS elastically connected to the seabed. *Marine Structures*, 48.

Karperaki, A. E. and Belibassakis, K. A. (2021). Hydroelastic analysis of Very Large Floating Structures in variable bathymetry regions by multi-modal expansions and FEM. *Journal of Fluids and Structures*, 102:103236.

Karperaki, A. E., Papathanasiou, T. K., and Belibassakis, K. A. (2019). An optimized, parameter-free PML-FEM for wave scattering problems in the ocean and coastal environment. *Ocean Engineering*, 179:307–324.

Kashiwagi, M. (1998). A B-spline Galerkin scheme for calculating the hydroelastic response of a very large floating structure in waves. *Journal of Marine Science and Technology*, 3(1):37–49.

Kashiwagi, M. (2000). Research on hydroelastic responses of VLFS: Recent progress and future work. *International Journal of Offshore and Polar Engineering*, 10(2):81–90.

Kim, K. H., Bang, J. S., Kim, J. H., Kim, Y., Kim, S. J., and Kim, Y. (2013). Fully coupled BEM-FEM analysis for ship hydroelasticity in waves. *Marine Structures*, 33:71–99.

Kirby, J. T. and Dalrymple, R. A. (1984). Verification of a parabolic equation for propagation of weakly-nonlinear waves. *Coastal Engineering*, 8(3):219–232.

Kirby, J. T. and Dalrymple, R. A. (1986). An approximate model for nonlinear dispersion in monochromatic wave propagation models. *Coastal Engineering*, 9(6):545–561.

Koley, S. (2020). Water wave scattering by floating flexible porous plate over variable bathymetry regions. *Ocean Engineering*, 214:107686.

Korobkin, A., Părău, E. I., and Vanden-Broeck, J. M. (2011). The mathematical challenges and modelling of hydroelasticity.

Kyoung, J. H., Hong, S. Y., Kim, B. W., and Cho, S. K. (2005). Hydroelastic response of a very large floating structure over a variable bottom topography. *Ocean Engineering*, 32(17-18):2040–2052.

Lamas-Pardo, M., Iglesias, G., and Carral, L. (2015). A review of Very Large Floating Structures (VLFS) for coastal and offshore uses.

Lassas, M. and Somersalo, E. (1998). On the Existence and Convergence of the Solution of PML Equations. *Computing (Vienna/New York)*, 60(3):229–241.

Leissa, A. W. (1973). The free vibration of rectangular plates. *Journal of Sound and Vibration*, 31(3):257–293.

Li, Z. F., Shi, Y. Y., and Wu, G. X. (2020). A hybrid method for linearized wave radiation and diffraction problem by a three dimensional floating structure in a polynya. *Journal of Computational Physics*, 412:109445.

Liu, X., Wang, X., and Xu, S. (2020). A DMM-EMM-RSM hybrid technique on two-dimensional frequency-domain hydroelasticity of floating structures over variable bathymetry. *Ocean Engineering*, 201:107135.

Martin, P. A. (2006). *Multiple Scattering: Interaction of Time-Harmonic Waves with N Obstacles*. Cambridge Univerity Press.

Massel, S. R. (1993). Extended refraction-diffraction equation for surface waves. *Coastal Engineering*, 19(1-2):97–126.

Mei, C. C. and Chen, H. S. (1976). A hybrid element method for steady linearized free-surface flows. *International Journal for Numerical Methods in Engineering*, 10(5):1153–1175.

Mei, C. C., Stiassnie, M., and Yue, D. K. P. (2005). *Theory and Applications of Ocean Surface Waves: Part 1: Linear Aspects . Advanced series on Ocean engineering -23*, volume 23. World Scientific.

Meylan, M. H., Bennetts, L. G., and Peter, M. A. (2017). Water-wave scattering and energy dissipation by a floating porous elastic plate in three dimensions. *Wave Motion*, 70:240–250.

Mikhlin, S. G. (1964). *Variational Methods in Mathematical Physics*. Pergamon Press, New York,.

Miles, J. W. and Chamberlain, P. G. (1998). Topographical scattering of gravity waves. *Journal of Fluid Mechanics*, 361:175–188.

Mindlin, R. D. (1951). Influence of Rotatory Inertia and Shear on Flexural Motions of Isotropic, Elastic Plates. *Journal of Applied Mechanics*, 18:31–38.

Modesto, D., Fernández-Méndez, S., and Antonio Huerta, P. E. (2016). Elliptic harbor wave model with perfectly matched layer and exterior bathymetry effects. *Journal of Waterway, Port, Coastal and Ocean Engineering*, 142(5).

Modesto, D., Zlotnik, S., and Huerta, A. (2015). Proper generalized decomposition for parameterized Helmholtz problems in heterogeneous and unbounded domains: Application to harbor agitation. *Computer Methods in Applied Mechanics and Engineering*, 295:127–149.

Navon, I. M., Neta, B., and Hussaini, M. Y. (2004). A perfectly matched layer approach to the linearized shallow water equations models. *Monthly Weather Review*, 132(6):1369–1378.

Newman, J. N. (1994). Wave effects on deformable bodies. *Applied Ocean Research*, 16(1):47–59.

Nguyen, H. P., Wang, C. M., Flocard, F., and Pedroso, D. M. (2019). Extracting energy while reducing hydroelastic responses of VLFS using a modular raft wec-type attachment. *Applied Ocean Research*, 84(September 2018):302–316.

Norrie, D. H. and Vries, G. D. (1980). The Finite Element Method. *Mathematics in Science and Engineering*, 146(C):311–324.

Ohmatsu, S. (2005). Overview: Research on wave loading and responses of VLFS. *Marine Structures*, 18(2):149–168.

Oliveira, F. S. B. F. (2004). Assessment of open boundary conditions on the elliptic formulation of the mild-slope equation. *Ocean Engineering*, 31(11-12):1567–1576.

Oñate, E. (2010). *Structural analysis with the finite element method: linear statics: v.1: Basis and solids*, volume 47.

Oosterhout, G. M., van der Hoogt, P. J., and Spiering, R. M. (1995). Accurate calculation methods for natural frequencies of plates with special attention to the higher modes. *Journal of Sound and Vibration*, 183(1):33–47.

Oskooi, A. F., Zhang, L., Avniel, Y., and Johnson, S. G. (2008). The failure of perfectly matched layers, and towards their redemption by adiabatic absorbers. *Optics Express*, 16(15):11376.

Panchang, V. G., Pearce, B. R., Wei, G., and Cushman-Roisin, B. (1991). Solution of the mild-slope wave problem by iteration. *Applied Ocean Research*, 13(4):187–199.

Papathanasiou, T., Karperaki, A., Theotokoglou, E., and Belibassakis, K. (2015a). A higher order FEM for time-domain hydroelastic analysis of large floating bodies in an inhomogeneous shallow water environment. *Proceedings of the Royal Society A: Mathematical, Physical and Engineering Sciences*, 471(2173).

Papathanasiou, T. K. and Belibassakis, K. A. (2018). Resonances of enclosed shallow water basins with slender floating elastic bodies. *Journal of Fluids and Structures*, 82:538–558.

Papathanasiou, T. K., Karperaki, A. E., and Belibassakis, K. A. (2019). On the resonant hydroelastic behaviour of ice shelves. *Ocean Modelling*, 133(October 2018):11–26.

Papathanasiou, T. K., Karperaki, A. E., Theotokoglou, E. E., and Belibassakis, K. A. (2015b). Hydroelastic analysis of ice shelves under long wave excitation. *Natural Hazards and Earth System Sciences*, 15(8):1851–1857.

Peterson, K., Bochev, P., and Kuberry, P. (2019). Explicit synchronous partitioned algorithms for interface problems based on Lagrange multipliers. *Computers and Mathematics with Applications*, 78(2):459–482.

Porter, D. and Porter, R. (2004). Approximations to wave scattering by an ice sheet of variable thickness over undulating bed topography. *Journal of Fluid Mechanics*, 509(509):145–179.

Porter, R. and Porter, D. (2000). Water wave scattering by a step of arbitrary profile. *Journal of Fluid Mechanics*, 411:131–164.

Praveen, K. M., Karmakar, &. D., Soares, &. C. G., Karmakar, D., and Soares, C. G. (2019). Influence of Support Conditions on the Hydroelastic Behaviour of Floating Thick Elastic Plate. *Journal of Marine Science and Application*.

Praveen, K. M. and Karmakar, D. (2019). Wave transformation due to floating elastic thick plate over changing bottom topography. In *Lecture Notes in Civil Engineering*, volume 23, pages 417–430. Springer.

Qi, Q. and Geers, T. L. (1998). Evaluation of the Perfectly Matched Layer for Computational Acoustics. *Journal of Computational Physics*, 139(1):166–183.

Rabinovich, D., Givoli, D., and Bécache, E. (2010). Comparison of high-order absorbing boundary conditions and perfectly matched layers in the frequency domain. *International Journal for Numerical Methods in Biomedical Engineering*, 26(10):1351–1369.

Radder, A. C. and Dingemans, M. W. (1985). Canonical equations for almost periodic, weakly nonlinear gravity waves. *Wave Motion*, 7(5):473–485.

Rappaport, C. M. (1995). Perfectly Matched Absorbing Boundary Conditions Based on Anisotropic Lossy Mapping of Space. *IEEE Microwave and Guided Wave Letters*, 5(3):90–92.

Reddy, J. N. (2006). *Theory and Analysis of Elastic Plates and Shells*, volume (5)2. CRC Press.

Ren, N., Zhang, C., Magee, A. R., Hellan, Ø., Dai, J., and Ang, K. K. (2019). Hydrodynamic analysis of a modular multi-purpose floating structure system with different outermost connector types. *Ocean Engineering*, 176:158–168.

Senjanović, I., Hadžić, N., Vladimir, N., and Cho, D. S. (2014). Natural vibrations of thick circular plate based on the modified Mindlin theory. *Archives of Mechanics*, 66(6):389–409.

Singer, I. and Turkel, E. (2004). A perfectly matched layer for the Helmholtz equation in a semi-infinite strip. *Journal of Computational Physics*, 201(2):439–465.

Smith, M. J. and Meylan, M. H. (2011). Wave scattering by an ice floe of variable thickness. *Cold Regions Science and Technology*, 67(1-2):24–30.

Squire, V. A. (2008). Synergies between VLFS hydroelasticity and sea-ice research. *Proceedings of the International Offshore and Polar Engineering Conference*, 8:1–13.

Squire, V. A. (2018). A fresh look at how ocean waves and sea ice interact. *Philosophical Transactions of the Royal Society A: Mathematical, Physical and Engineering Sciences*, 376(2129).

Stoker, J. J. (1967). *Water Waves*. John Wiley & Sons, Inc., Hoboken, NJ, USA.

Sturova, I. V., Korobkin, A. A., Fedotova, K. A., Chubarov, L. B., and Komarov, V. A. (2009). Nonlinear dynamics of non-uniform elastic plate floating on shallow water of variable depth. In Temarel, P. and Hirdaris, S. E., editors, *Hydroelasticity in Marine Technology*, Southampton. University of Southampton, UK.

Sun, Z., Korobkin, A., Sui, X. P., and Zhi, Z. (2021). A semi-analytical model of hydroelastic slamming. *Journal of Fluids and Structures*, 101:103200.

Sydenstricker, R. M., Landau, L., and Marques, A. (1995). PSEUDOCONSISTENT LOAD VECTOR AND MASS MATRIX. *Communications in Numerical Methods in Engineering*, 11:317–330.

Takagi, K., Shimada, K., and Ikebuchi, T. (2000). Anti-motion device for a very large floating structure. *Marine Structures*, 13(4-5):421–436.

Taylor, R. E. and Eatock Taylor, R. (2007). Hydroelastic analysis of plates and some approximations. *Journal of Engineering Mathematics*, 58(1-4):267–278.

Taylor, R. E. and Waite, J. B. (1978). The dynamics of offshore structures evaluated by boundary integral techniques. *International Journal for Numerical Methods in Engineering*, 13(1):73–92.

Timoshenko, S. and Woinowsky-Krieger, S. (1959). Theory of plates and shells.

Toselli, A. and Widlund, O. (2005). *Domain Decomposition Methods — Algorithms and Theory*, volume 34.

Tsay, T.-K. and Liu, P. L.-f. (1983). A finite element model for wave refraction and diffraction. *Applied Ocean Research*, 5(1):30–37.

Turkel, E. and Yefet, A. (1998). Absorbing PML boundary layers for wave-like equations. *Applied Numerical Mathematics*, 27(4):533–557.

Utsunomiya, T., Watanabe, E., Wu, C., Hayashi, N., Nakai, K., and Sekita, K. (1995). Wave response analysis of a flexible floating structure by be-fe combination method. In *Proceedings of the International Offshore and Polar Engineering Conference*, volume 1995-June, pages 400–405. International Society of Offshore and Polar Engineers.

Wang, C. M. and Tay, Z. Y. (2011). Very large floating structures: Applications, research and development. *Procedia Engineering*, 14:62–72.

Wang, C. M., Watanabe, E., and Utsunomiya, T. (2006). *Very large floating structures*, volume 2.

Washizu, K. (1975). *Variational methods in elasticity and plasticity*. Pergamon Press Ltd, second edition.

Watanabe, E., Wang, C. M., Utsunomiya, T., and Moan, T. (2004). CORE Report No. 2004-02 VERY LARGE FLOATING STRUCTURES: APPLICATIONS, ANALYSIS AND DESIGN. Technical report, Centre for Offshore Research and Engineering, NUS.

Wu, C., Watanabe, E., and Utsunomiya, T. (1995). An eigenfunction expansion-matching method for analyzing the wave-induced responses of an elastic floating plate. *Applied Ocean Research*, 17(5):301–310.

Xia, D., Ertekin, R. C., and Kim, J. W. (2004). Nonlinear hydroelastic response of a two-dimensional mat-type VLFS by the green-naghdi theory. In *Proceedings of the International Conference on Offshore Mechanics and Arctic Engineering - OMAE*, volume 3, pages 823–832. American Society of Mechanical Engineers Digital Collection.

Yoshimoto, H., Ohmatsu, S., Hoshino, K., and Ikebuchi, T. (1997). Slamming load on a very large floating structure with shallow draft. *Journal of Marine Science and Technology*, 2(3):163–172.

Young, I. R., Zieger, S., and Babanin, A. V. (2011). Global trends in wind speed and wave height. *Science*, 332(6028):451–455.

Zhang, X. and Lu, D. (2018). An extension of a discrete-module-beam-bending-based hydroelasticity method for a flexible structure with complex geometric features. *Ocean Engineering*, 163:22–28.

Zhao, C., Hu, C., Wei, Y., Zhang, J., and Huang, W. (2008). Diffraction of surface waves by floating elastic plates. *Journal of Fluids and Structures*, 24(2):231–249.

Zheng, S., Meylan, M. H., Fan, L., Greaves, D., and Iglesias, G. (2020). Wave scattering by a floating porous elastic plate of arbitrary shape: A semi-analytical study. *Journal of Fluids and Structures*, 92:102827.

Zienkiewicz, O. and Taylor, R. (2005). *The finite element method*. 6 edition.

# Appendix A

# Plate element

The lock-free Discrete Shear Triangle (DST) for thick plates and its degeneration to thin plates, the Discrete Shear Triangle (DKT) proposed in Batoz and Lardeur (1989) are considered. The characteristics of the DST are summarised below :

- Deflection and rotations are independently approximated with a $C^0$ underlying continuity requirement springing from the Mindlin formulation
- The potential energy is expressed as the sum of the bending and shear energies.
- The kinematic requirement expressed at Eq. (2.15), is imposed discretely at the mid-point of each edge, $k = 4, 5, 6$. Setting

For sign compatibility it is set $\theta_{x_1} = -\beta_{x_2}$, $\theta_{x_2} = \beta_{x_1}$ for the rotations. Moving towards more technical details for the DST its is noted that the total rotations $\beta_{x_1}, \beta_{x_2}$ are approximated by quadratic Lagrange shape functions within the element thus,

$$\beta_{x_j}(\mathbf{x}) = \sum_{i=1}^{6} L_i(\mathbf{x})\beta^i_{x_j}, \text{ for } j = 1, 2. \tag{A .1}$$

with $\beta^i_{x_j}$ being the nodal values for rotations at the corners $i = 1, 2, 3$ and mid-side points $i = 4, 5, 6$. Simultaneously, the added assumption that rotations vary linearly along element edges results in,

$$\beta_n|_k = 0.5\,\beta_n|_i + 0.5\,\beta_n|_j, \text{for } k = 4, 5, 6 \text{ and } (i, j) = (2, 3), (3, 1), (1, 2). \tag{A .2}$$

The above relations along with the discrete satisfaction of the kinematic consideration Eq. (2.15) on the edge mid-points, consistent with FSDT theory,

$$(\partial_s w)|_k + (\partial_s \beta)|_k = F(\beta_{x_1}, \beta_{x_2}) \text{ for } k = 4, 5, 6 \tag{A .3}$$

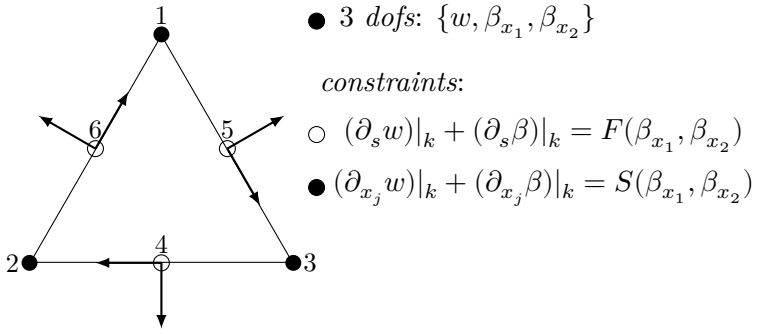


**Figure A .1** Discrete Shear Triangle-DST

leads to the following expressions involving the 9 element *dofs* contained in vector $\mathbf{U} = \left[w^{(1)} \quad \beta_{x_1}^{(1)} \quad \beta_{x_2}^{(1)} \quad w^{(2)} \quad \beta_{x_1}^{(2)} \quad \beta_{x_2}^{(2)} \quad \beta_{x_2}^{(2)} \quad w^{(3)} \quad \beta_{x_1}^{(3)} \quad \beta_{x_2}^{(3)}\right]$.

$$\begin{aligned} \beta_{x_1} &= \mathbf{H_{x_1}} \mathbf{U} \\ \beta_{x_2} &= \mathbf{H_{x_2}} \mathbf{U} \end{aligned} \tag{A .4}$$

To derive the expressions $\mathbf{H_{x_1}}$ and $\mathbf{H_{x_2}}$ we begin from examining $F(\beta_{x_1}, \beta_{x_2})$ in Eq. (A .3).

Exploiting moment equilibrium relations for the plate cross section expressions for the shear strains are derived,

$$\begin{aligned} M_{x_1,x_1} + M_{x_1x_2,x_1} - T_{x_1} = 0 \rightarrow \gamma_{x_1z} = 1/(k_s G\tau) M_{x_1,x_1} + M_{x_1x_2,x_1} \\ M_{x_1x_2,x_2} + M_{x_2,x_2} - T_{x_2} = 0 \rightarrow \gamma_{x_2z} = 1/(k_s G\tau) M_{x_1x_2,x_2} + M_{x_2,x_2} \end{aligned} \tag{A .5}$$

Thus the discrete constraints on the vertices and midnodes, a direct expression of Eq. (2.15), are written as,

$$\begin{aligned} \gamma_{x_1z} = F_{x_1} = \partial_{x_1} w + \beta_{x_1} \\ \gamma_{x_2z} = F_{x_2} = \partial_{x_2} w + \beta_{x_2} \end{aligned} \tag{A .6}$$

For the isotropic case it is deduced that,

$$\begin{aligned} F_{x_1} = D/(k_s G\tau) \left( \partial_{x_1x_1}\beta_{x_1} + \nu \partial_{x_1x_2}\beta_{x_2} + \frac{1-\nu}{2}(\partial_{x_2x_2}\beta_{x_1} + \partial_{x_1x_2}\beta_{x_2}) \right) \\ F_{x_2} = D/(k_s G\tau) \left( \partial_{x_2x_2}\beta_{x_2} + \nu \partial_{x_1x_2}\beta_{x_1} + \frac{1-\nu}{2}(\partial_{x_1x_1}\beta_{x_2} + \partial_{x_1x_2}\beta_{x_1}) \right). \end{aligned} \tag{A .7}$$

Now considering the cubic approximation for the rotations Eq. (A .1) results in the following,

$$\begin{aligned} F_{x_1} = D/(k_s G\tau) \Bigg( \sum_{i=1} \partial_{x_1x_1} L_i(\xi,\eta)\beta_{x_1}^{(i)} + \nu \partial_{x_1x_2} L_i(\xi,\eta)\beta_{x_2}^{(i)} \\ + \frac{1-\nu}{2}(\partial_{x_2x_2} L_i(\xi,\eta)\beta_{x_1}^{(i)} + \partial_{x_1x_2} L_i(\xi,\eta)\beta_{x_2}^{(i)}) \Bigg) \\ , F_{x_2} = D/(k_s G\tau) \Bigg( \sum_{i=1} \partial_{x_2x_2} L_i(\xi,\eta)\beta_{x_2}^{(i)} + \nu \partial_{x_1x_2} L_i(\xi,\eta)\beta_{x_1}^{(i)} \\ + \frac{1-\nu}{2}(\partial_{x_1x_1} L_i(\xi,\eta)\beta_{x_2}^{(i)} + \partial_{x_1x_2} L_i(\xi,\eta)\beta_{x_1}^{(i)}) \Bigg) \end{aligned} \tag{A .8}$$

The above suggest that Eq. (A .8) can be in turn written as,

$$\begin{aligned} F_{x_1} &= \sum_{i=1} a_1(i)\beta_{x_1}^{(i)} + a_2(i)\beta_{x_2}^{(i)} \\ F_{x_2} &= \sum_{i=1} b_1(i)\beta_{x_1}^{(i)} + b_2(i)\beta_{x_2}^{(i)} \end{aligned} \tag{A .9}$$

with the coefficients $a_1, a_2$ and $b_1, b_2$ given as functions of material parameters and Lagrangian shape functions.

$$\begin{aligned} a_1(i) &= \tfrac{E\tau^2}{12(1-\nu)^2\kappa_s G}\left(\partial_{x_1x_1}L_i + \tfrac{1-\nu}{2}\partial_{x_2x_2}L_i\right), \\ a_2(i) &= \tfrac{E\tau^2}{12(1-\nu)^2\kappa_s G}\left(\nu\partial_{x_1x_2}L_i + \tfrac{1-\nu}{2}\partial_{x_1x_2}L_i\right), \\ b_1(i) &= \tfrac{E\tau^2}{12(1-\nu)^2\kappa_s G}\left(\nu\partial_{x_1x_2}L_i + \tfrac{1-\nu}{2}\partial_{x_1x_2}L_i\right), \\ b_2(i) &= \tfrac{E\tau^2}{12(1-\nu)^2\kappa_s G}\left(\partial_{x_2x_2}L_i + \tfrac{1-\nu}{2}\partial_{x_1x_1}L_i\right). \end{aligned} \tag{A .10}$$

Along each triangle side $(ij)$ with length $l_{ij}$ the following transformations hold,

$$\begin{bmatrix} \beta_n \\ \beta_S \end{bmatrix} = \begin{bmatrix} C_k & S_k \\ -S_k & C_k \end{bmatrix} \begin{bmatrix} \beta_{x1} \\ \beta_{x2} \end{bmatrix} \tag{A .11}$$

with $C_k = \frac{x_2^j - x_2^i}{l_{ij}}$ and $S_k = \frac{x_1^j - x_1^i}{l_{ij}}$ are the directional cosine and sine of the given element edge. Employing th above transformation the rotations can be shifted to the $(n, s)$ frame and vice versa. Along with the assumption of linear variation along an edge Eq. (A .2) results in the following refined expressions for Eq. (A .9),

$$\begin{aligned} F_{x_1} &= \sum_{i=1}^{3} a_1'(i)\beta_{x_1}^{(i)} + a_2'(i)\beta_{x_2}^{(i)} + \sum_{k=4}^{6} a_s'\beta_s^{(k)} \\ F_{x_2} &= \sum_{i=1}^{3} b_1'(i)\beta_{x_1}^{(i)} + b_2'(i)\beta_{x_2}^{(i)} + \sum_{k=4}^{6} b_s'\beta_s^{(k)} \end{aligned} \tag{A .12}$$

Next, the constraints along the edge mid-nodes $k = 4, 5, 6$ read,

$$\partial_s w|_k + \beta_s|_k = -C_k F_{x_1} + S_k F_{x_2} \tag{A .13}$$

Moreover the assumption of Hermite interpolation for the deflection $w(s)$ along the edges which translates into,

$$\partial_s w|_k = -1.5/l_{ij}(w^{(i)} - w^{(j)}) - 0.25\ \partial_s w|_i - 0.25\partial_s w\ |_j \tag{A .14}$$

By means of **??** and Eq. (A .14) new expressions can be derived for $\beta_s|_k$ at the mid points,

$$\begin{aligned}\beta_s|_k = 1.5/l_{ij}(w^{(i)} - w^{(j)}) + 1.5C_k F_{x_2} - 1.5S_k F_{x_1} - 0.25C_k\beta_{x_2}^{(i)} \\ +0.25S_k\beta_{x_1}^{(j)} - 0.25C_k\beta_{x_2}^{(j)} + 0.25C_k\beta_{x_1}^{(j)}\end{aligned} \tag{A .15}$$

Substituting the expressions Eq. (A .12) into Eq. (A .15) results in the following,

$$\mathbf{A}\boldsymbol{\beta_s}|_k = \mathbf{X}_k, \tag{A .16}$$

with matrix $\mathbf{A}$ given below,

$$\begin{bmatrix} 1 - 1.5C_4 b_s'(4) + 1.5C_4 a_s'(4) & -1.5C_4 b_s'(5) + 1.5S_4 a_s'(5) & -1.5C_4 b_s'(6) + 1.5S_4 a_s'(6) \\ 1.5C_5 b_s'(4) + 1.5C_5 a_s'(4) & 1 - 1.5C_5 b_s'(5) + 1.5S_5 a_s'(5) & -1.5C_5 b_s'(6) + 1.5S_5 a_s'(6) \\ -1.5C_6 b_s'(4) + 1.5C_6 a_s'(4) & -1.5C_6 b_s'(5) + 1.5S_6 a_s'(5) & 1 - 1.5C_6 b_s'(6) + 1.5S_6 a_s'(6) \end{bmatrix}$$

The elements of the vector on the right hand side of Eq. (A .16) are reduced to,

$$\begin{aligned}X_k = 1.5/l_{ij}(w^{(i)} - w^{(j)}) + 1.5C_k\left(\sum_{i=1}^{3} b_{x_1}'\beta_{x_1}^{(i)} + \sum_{i=1}^{3} b_{x_2}'\beta_{x_2}^{(i)}\right) - 1.5S_k\left(\sum_{i=1}^{3} a_{x_1}'\beta_{x_1}^{(i)} + \sum_{i=1}^{3} a_{x_2}'\beta_{x_2}^{(i)}\right) \\ -0.25C_4\beta_{x_2}^{(i)} + 0.25S_4\beta_{x_2}^{(i)} - 0.25C_4\beta_{x_2}^{(j)} + 0.25S_4\beta_{x_2}^{(j)}\end{aligned} \tag{A .17}$$

Alternatively, $\mathbf{X}_k = \mathbf{L}\mathbf{U}$. Solving Eq. (A .16) for $\boldsymbol{\beta_s}$,

$$\boldsymbol{\beta_s} = \mathbf{H}_s\mathbf{U} \tag{A .18}$$

with $\mathbf{H}_s = \mathbf{A}^{-1}\mathbf{L}$. Returning to Eq. (A .12) and substituting the above,

$$\begin{aligned}F_{x_1} &= \sum_{i=1}^{3} a_1'(i)\beta_{x_1}^{(i)} + a_2'(i)\beta_{x_2}^{(i)} + \sum_{k=4}^{6} a_s'(k)\mathbf{H}_s\mathbf{U}, \\ F_{x_2} &= \sum_{i=1}^{3} b_1'(i)\beta_{x_1}^{(i)} + b_2'(i)\beta_{x_2}^{(i)} + \sum_{k=4}^{6} b_s'(k)\mathbf{H}_s\mathbf{U}.\end{aligned} \tag{A .19}$$

Equation (A .19) can be written in matrix form as,

$$\begin{bmatrix} F_{x_1} \\ F_{x_2} \end{bmatrix} = \begin{Bmatrix} \mathbf{FX_1} \\ \mathbf{FX_2} \end{Bmatrix} \mathbf{U} \tag{A .20}$$

Based on the above, returning to Eq. (A .4), the arrays $\mathbf{H_{x_1}}, \mathbf{H_{x_1}}$ expressing the rotations in terms of the element unknowns are,

$$\begin{aligned}
H_{x_1}(1) &= -L_4 S_4 H_{s_4}(1) - L_5 S_5 H_{s_5}(1) - L_6 S_6 H_{s_6}(1) \\
H_{x_1}(2) &= L_1 + 0.5 C_5^2 L_5 + 0.5 C_6^2 L_6 - N_4 S_4 H_{S_4}(2) - N_5 S_5 H_{S_5}(2) - N_6 S_6 H_{S_6}(2) \\
H_{x_1}(3) &= 0.5 C_5 S_5 L_5 + 0.5 C_6 S_6 L_6 - L_4 S_4 H_{S_4}(3) - L_5 S_5 H_{S_5}(3) - L_6 S_6 H_{S_6}(3) \\
H_{x_1}(4) &= -L_4 S_4 H_{s_4}(4) - L_5 S_5 H_{s_5}(4) - L_6 S_6 H_{s_6}(4) \\
H_{x_1}(5) &= L_2 + 0.5 C_4^2 L_4 + 0.5 C_6^2 L_6 - L_4 S_4 H_{S_4}(5) - L_5 S_5 H_{S_5}(5) - L_6 S_6 H_{S_6}(5) \\
H_{x_1}(6) &= 0.5 C_4 S_4 L_4 + 0.5 C_6 S_6 L_6 - L_4 S_4 H_{S_4}(6) - L_5 S_5 H_{S_5}(6) - L_6 S_6 H_{S_6}(6) \\
H_{x_1}(7) &= -L_4 S_4 H_{s_4}(7) - L_5 S_5 H_{s_5}(7) - L_6 S_6 H_{s_6}(7) \\
H_{x_1}(8) &= L_3 + 0.5 C_5^2 L_5 + 0.5 C_4^2 L_4 - L_4 S_4 H_{S_4}(8) - L_5 S_5 H_{S_5}(85) - L_6 S_6 H_{S_6}(8) \\
H_{x_1}(9) &= 0.5 C_5 S_5 L_5 + 0.5 C_4 S_4 L_4 - L_4 S_4 H_{S_4}(9) - L_5 S_5 H_{S_5}(9) - L_6 S_6 H_{S_6}(9)
\end{aligned}$$

and,

$$\begin{aligned}
H_{x_2}(1) &= L_4 C_4 H_{s_4}(1) + L_5 C_5 H_{s_5}(1) + L_6 C_6 H_{s_6}(1) \\
H_{x_2}(2) &= 0.5 C_5 S_5 L_5 + 0.5 C_6 S_6 L_6 + L_4 S_4 H_{s_4}(2) + L_5 S_5 H_{s_5}(2) + L_6 S_6 H_{S_6}(2) \\
H_{x_2}(3) &= L_1 + 0.5 S_5^2 L_5 + 0.5 S_6^2 L_6 + N_4 C_4 H_{s_4}(3) + N_5 C_5 H_{s_5}(3) + N_6 C_6 H_{S_6}(3) \\
H_{x_2}(4) &= L_4 C_4 H_{s_4}(4) + L_5 C_5 H_{s_5}(4) + L_6 C_6 H_{s_6}(4) \\
H_{x_2}(5) &= 0.5 C_4 S_4 L_4 + 0.5 C_6 S_6 L_6 + L_4 S_4 H_{s_4}(5) + L_5 S_5 H_{s_5}(5) + L_6 S_6 H_{s_6}(5) \\
H_{x_2}(6) &= L_2 + 0.5 S_4^2 L_4 + 0.5 S_6^2 L_6 + L_4 C_4 H_{s_4}(6) + L_5 C_5 H_{s_5}(6) + L_6 C_6 H_{s_6}(6) \\
H_{x_2}(7) &= L_4 C_4 H_{s_4}(7) + L_5 C_5 H_{s_5}(7) + L_6 C_6 H_{s_6}(7) \\
H_{x_2}(8) &= 0.5 C_5 S_5 L_5 + 0.5 C_4 S_4 L_4 + L_4 C_4 H_{s_4}(8) + L_5 C_5 H_{s_5}(8) + L_6 C_6 H_{s_6}(8) \\
H_{x_2}(9) &= L_3 + 0.5 S_5^2 L_5 + 0.5 S_4^2 L_4 - L_4 C_4 H_{s_4}(9) - L_5 C_5 H_{s_5}(9) - L_6 C_6 H_{s_6}(9)
\end{aligned}$$

The curvatures can now be computed as,

$$\boldsymbol{\chi} = \begin{bmatrix} \partial_{x_1}\beta_{x_1} & \partial_{x_2}\beta_{x_2} & \partial_{x_2}\beta_{x_1} + \partial_{x_1}\beta_{x_2} \end{bmatrix}^{\mathsf{T}} = \mathbf{B_b U} \tag{A .21}$$

with $\mathbf{B_b} = \begin{bmatrix} \partial_{x_1}\mathbf{H_{x_1}} \\ \partial_{x_2}\mathbf{H_{x_2}} \\ \partial_{x_2}\mathbf{H_{x_1}} + \partial_{x_1}\mathbf{H_{x_2}} \end{bmatrix}$.

The shear strains are written as,

$$\boldsymbol{\gamma} = \begin{bmatrix} \gamma_{x_1 z} & \gamma_{x_2 z} \end{bmatrix}^{\mathsf{T}} = \mathbf{B}_s \mathbf{U} \tag{A .22}$$

The $k^{\text{th}}$element stiffness matrix is

$$\mathbf{k} = \mathbf{k}_b + \mathbf{k}_s, \text{ with} \tag{A .23}$$

$$\mathbf{k}_b = \int_K \mathbf{B_b}^{\mathsf{T}} \mathbf{D}_b \mathbf{B_b} \, dA \text{ and} \tag{A .24}$$

$$\mathbf{k}_s = \int_K \mathbf{B_b}^{\mathsf{T}} \mathbf{D}_b \mathbf{B_b} \, dA \tag{A .25}$$

# Appendix B

# Perfectly Matched Layer

Analytical solutions for the exterior Helmholtz problem in (a) $\mathbb{R}^2$ and (b) the infinite strip are employed in the calculation of convergence results for the PML-FEM scheme introduced in Chapter 6.

Analytical outgoing solutions are given for reference below. In particular, the scattered wavefield solutions due to the circular inclusion are provided for the case of an incident plane wave, and an incident wavefield generated by a point source located at a distance from the centre of the circular scatterer. For the scattering problem in the infinite strip, with homogeneous Neumann conditions on the planar boundaries, a semi-analytical solution is devised by means of a rapidly convergent normal mode series expansion.

### (a) Exterior Helmholtz problem in $\mathbb{R}^2$

The scattered wavefield by a circular inclusion with surface $S$ and radius $a$, is obtained as the solution to the exterior Helmholtz problem with constant parameter $k$ in the 2D plane $\Omega = \{\mathbf{x} \in \mathbb{R}^2 : r = (x_1^2 + x_2^2)^{1/2} > a\}$

$$\nabla^2 \varphi_s + k^2 \varphi_s, \text{in}\Omega. \tag{B .1}$$

$$\text{with } \alpha \partial_n \varphi_s + \beta \varphi_s = -(\alpha \partial_n \varphi_i + \beta \varphi_i) \text{ on } S. \tag{B .2}$$

$$\text{and } \lim_{|r| \to \infty} |r|(\partial_{|r|} \varphi_s - \mathrm{i}k\varphi_s) = 0. \tag{B .3}$$

General Robin type condition on the inclusion surface is assumed along with radiation conditions at infinity. The incident wavefield data on the scatterer surface, $f$ are known.The representation of the solution is given by means of Hankel functions of the first kind and $m$ order as in ,

$$\varphi_s(r, \theta) = \sum_{m=0}^{\infty} A_m \cos(m\theta) H_m^{(1)}(kr) \tag{B .4}$$

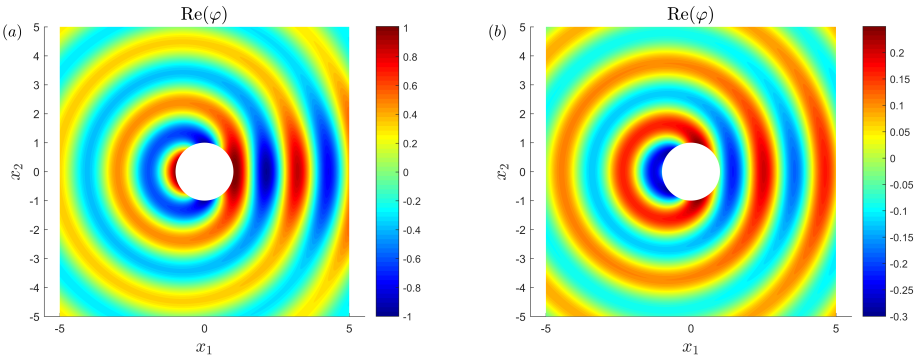


**(i)** Plane wave incidence. **(ii)** Wavefield generated by a source

**Figure B .1** Analytical solutions for $ka = 1$ and an imposed Dirichlet condition on the scatterer

Coefficients $A_m$ are dependent on the imposed boundary condition scatterer surface $S$ and the incident wavefield. For the case of plane wave incidence (see Fig. B .1) the analytical solution of the scattered field assuming an acoustically soft and hard boundary respectively, are given by,

$$A_m = -e_m \mathrm{i}^m \frac{J_m(ka)}{H_m^{(1)}(ka)} \text{ and } A_m = -e_m \mathrm{i}^m \frac{J_m(ka)'}{H_m^{(1)}(ka)'} \tag{B .5}$$

where $e_m$ denotes the Jacobi symbol. In the case of an incident wavefield generated by an acoustic source located at a distance $s$ from the centre of the circular scatterer the corresponding coefficients are (Martin, 2006),

$$A_m = -e_m (-1)^m \frac{H_m^{(1)}(ks) J_m(ka)}{H_m^{(1)}(ka)} \text{ and } A_m = -e_m \frac{H_m^{(1)}(ka) J_m(ka)'}{H_m^{(1)}(ka)'} \tag{B .6}$$

## (b) Analytical solution in a planar waveguide

Next, a scattering field in an infinite strip resembling a waveguide with planar boundaries is generated to be used as reference data outside a circular inclusion. The domain is composed of an infinite strip confined in $\Omega_s = \{x_1 \in \mathbb{R}^2, x_2 \in (-h, 0)\}$. The Helmholtz equation defined in $\Omega' = \Omega_s \; S_i$, while boundary condition Eq. (B .2) holds on the surface of the scatterer. Homogeneous Neumann boundary conditions are applied on both upper and bottom planar boundaries. Hence it holds,

$$\nabla^2 \varphi_s + k^2 \varphi_s, \text{ in} \Omega', \tag{B .7}$$

$$\text{with } \alpha \partial_n \varphi_s + \beta \varphi_s = -(\alpha \partial_n \varphi_i + \beta \varphi_i) \text{ on } S. \tag{B .8}$$

$$\text{and } \partial_{x_2} \varphi_s(x_1, 0) = \partial_{x_2} \varphi_s(x_1, -h). \tag{B .9}$$

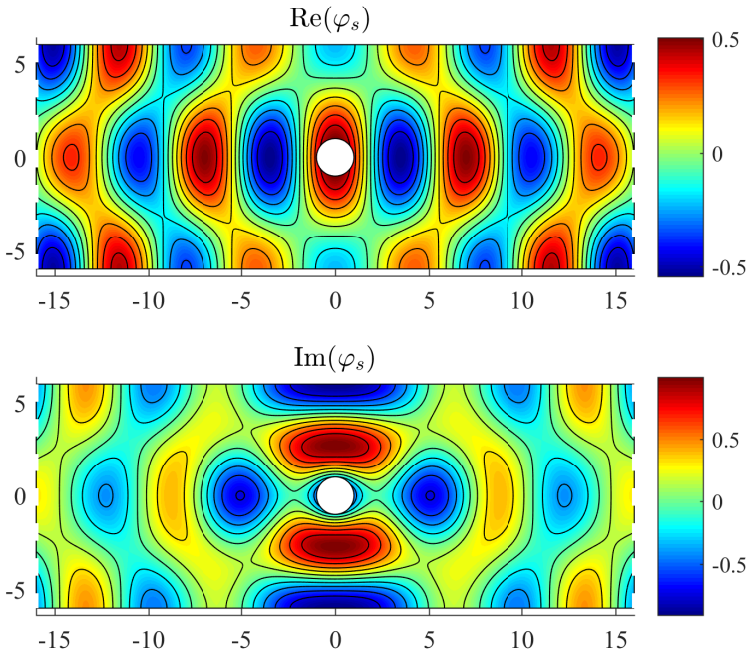


**Figure B .2** Scattering in a simple waveguide in the absence of inclusions with the method of image

Tha above problem must assume outgoing solutions at the lateral open boundaries. Analytical solutions corresponding to a radiating field in homogeneous waveguides with planar boundaries, in the absence of inclusions, can be easily constructed by the method of multiple images (see Brekhovskikh and Lysanov (1982); Jensen et al. (2011)). For simplicity, the field emitted by an infinite series of $2m$ mirror sources positioned along the $x_2-$ axis at $h$ intervals, defined as follows,

$$\varphi_s(\mathbf{x}) = \sum_{m=-\infty}^{\infty} H_0^{(1)}(kr_m),\ r_m = \sqrt{x_1^2 + (x_2 - mh)^2}. \tag{B .10}$$

The produced radiating wavefield satisfies the imposed homogeneous Neumann conditions on the waveguide planar boundaries. However, it is known that the series Eq. (B .10) is slowly convergent, hence an alternative representation can be obtained by separation of variables in the form of a normal mode series (Jensen et al., 2011) where the wavefield potential is given as a sum of eigenfunctions for the infinite strip $\Omega_s$.

$$\varphi_s(\mathbf{x}) = 2\sum_{m=0}^{\infty} \tilde{Y}_n(x_2), \tilde{Y}_n(x_2^s) \frac{\exp(\mathrm{i}k_{x_1})|x_1 - x_1^s|}{k_{x_1}^n}. \tag{B .11}$$

with the horizontal and vertical wavenumbers given as, $k_{x_1}^n = \sqrt{k^2 - k_{x_2}^n}$ and $k_{x_2}^n = n\pi/h$.The functions $\tilde{Y}_n(x_2)/\left\|\tilde{Y}_n\right\|$, represent the normalised vertical structure of the modes.

The vertical modes, corresponding to eigenvalues $k_{x_2}^n$ are chosen as $\tilde{Y}_n = \cos(k_{x_2}(x_2 + h/2))$ in order to satisfy the planar boundary conditions. The latter series can be truncated, keeping the propagating and a number of evanescent modes sufficient for rapid convergence in the whole region outside a ball in the vicinity of the fictitious source, i.e. $kr_0 > \epsilon$. Indicative plots of the waveguide solution are shown in Fig. B .2 with imposed Neumann Conditions on the planar boundaries, for $ka = 1$ and $kh = 12$.

# Angeliki E. Karperaki

**PhD Candidate**
National Technical University of Athens

## Contact Information

**Address:** School of Naval Architecture and Marine Engineering, National Technical University of Athens, Zografos, 15773, Athens, Greece
**E-mail:** akarperaki@mail.ntua.gr

## Education

**2014-Present** — **National Technical University of Athens (NTUA)**,
School of Marine Engineering and Naval Architecture

- PhD Candidate, Department of Naval and Marine Hydrodynamics.

**Thesis Title:**
"Hydroelastic interaction between water waves and large floating bodies in an inhomogeneous ocean environment"
Academic advisor: Prof. Kostas Belibassakis.

**2012-2014** — **National Technical University of Athens (NTUA)**

- MSc in *Computational Mechanics*

**2010-2011** — **Edinburgh Napier University**

- MSc in *Construction Project Management*

**2009-2010** — **University of Edinburgh/University of Glasgow**

- MSc in *Structural Engineering and Mechanics*

**2006-2009** — **University of Bradford**

- BEng in *Civil and Structural Engineering* (2.1)

## Research Interests and Expertise

- Wave propagation in inhomogeneous regions, water waves, hydroelasticity, hydroacoustics
- Mathematical Modelling, computational mechanics, Finite Element Method
- Structural Mechanics

## Publications in Peer-reviewed Journals

- **A. E. Karperaki** and K. A. Belibassakis, "Hydroelastic analysis of Very Large Floating Structures in variable bathymetry regions by multi-modal expansions and FEM", *J. Fluids and Structures* 102, 103236, 2021.
- F. Karathanasi, **A. E. Karperaki**, T. Gerostathis, K. Belibassakis, "Offshore-to-Nearshore Transformation of Wave Conditions and Directional Extremes with Application to Port Resonances in the Bay of Sitia-Crete", *Atmosphere* 11, 280, 2020.
- D. E. Anevlavi, E. S. Filippas, **A. E. Karperaki**, K. A. Belibassakis, "A Non-Linear BEM–FEM Coupled Scheme for the Performance of Flexible Flapping-Foil Thrusters", *J. Mar. Sci. Eng.* 8, 56, 2020.
- **A. E. Karperaki**, T. K. Papathanasiou, K. A. Belibassakis, "An optimized, parameter-free PML-FEM for wave scattering problems in the ocean and coastal environment", *Ocean Engineering*, 179, 307-324, 2019.
- T. K. Papathanasiou, **A. E. Karperaki**, K. A. Belibassakis, "On the resonant hydroelastic behaviour of ice shelves", *Ocean Modelling*, 133, 11-26, 2019.

- **A. E. Karperaki**, K. A. Belibassakis and T. K. Papathanasiou, "Time-domain, shallow water hydroelastic analysis of VLFS elastically connected to the seabed", *Marine Struct.*, 48, 33-51, 2017.
- T. K. Papathanasiou, **A. E. Karperaki,** E. E. Theotokogkou and K. A. Belibassakis, "Hydroelastic analysis of ice shelves under long wave excitation", *Nat. Hazards Earth Syst. Sci.*, 15, 1851–1857, 2015.
- T. K. Papathanasiou, **A. Karperaki**, E. E. Theotokogkou and K. A. Belibassakis, "A higher order FEM for time-domain hydroelastic analysis of large floating bodies in an inhomogeneous shallow water environment", *Proc. R. Soc. Lond. A*, 471, 20140643, 2014.

## Publications in Conference Proceedings

- T. K. Papathanasiou, **A. E. Karperaki** and K. A. Belibassakis,"Finite element simulation of long wave impact on floating breakwaters with variable thickness", IOP Conf. Ser.: Mater. Sci. Eng. 276, 012022, 2017.
- **A. E. Karperaki**, T. K. Papathanasiou and K. A. Belibassakis, "A coupled-mode system for the near-trapping of water waves in the presence of variable bathymetry", 11th HSTAM International Congress on Mechanics, Athens, Greece, May 27-30, 2016.
- T. K. Papathanasiou, **A. E. Karperaki** and K. A. Belibassakis, "An efficient Coupled-Mode/FEM Numerical Method for Linear Wave Propagation Over 3D Variable Bathymetry domains", 26th ISOPE International Ocean and Polar Engineering Conference, Rhodes, Greece, June 26-July 2, 2016.
- **A. E. Karperaki,** K. A. Belibassakis, T. K. Papathanasiou, S. I. Markolefas , "Hydroelastic analysis of VLFS, elastically connected to the seabed in shallow wave conditions", International Conference 'Science in Technology' SCinTE 2015, Athens, Greece, November 5-7, 2015.
- **A. E. Karperaki**, K. A. Belibassakis, T. K. Papathanasiou, "Propagation of acoustic-gravity waves in inhomogeneous ocean environment generated by sea bottom deformation", 8th GRACM International Congress on Computational Mechanics, Volos, Greece, July 12-15, 2015.
- **A. E. Karperaki**, K. A. Belibassakis, T. K. Papathanasiou, S. I. Markolefas, "Higher-order FEM for nonlinear hydroelastic analysis of a floating elastic strip in shallow-water conditions", VI International Conference on Coupled Problems in Science and Engineering (COUPLED PROBLEMS 2015), B. Schrefler, E. Onate and M. Papadrakakis (Eds.), San Servolo, Venice, Italy, May 18-20 2015.
- K. A. Belibassakis, G. A. Athnanassoulis, **A. E. Karperaki**, T. K. Papathanasiou, "Propagation of acoustic-gravity waves in inhomogeneous ocean environment based on modal expansions and hp-FEM", VI International Conference on Coupled Problems in Science and Engineering (COUPLED PROBLEMS 2015), B. Schrefler, E. Onate and M. Papadrakakis (Eds.), San Servolo, Venice, Italy, May 18-20 2015.
- T. K. Papathanasiou, **A. E. Karperaki**, E. E. Theotokoglou and K. A. Belibassakis, "Hydroelastic analysis of ice shelves under long wave excitation", European Geosciences Union general assembly Vienna, Austria, 27 April-2 May, 2014.

## Participation in Funded Research Projects

- Participation in EU /Greek government, co - funded research program ARCHIMIDES III (T.E.I. of ATHENS) – "Hydroelastic response of large floating structures and arbitrarily shaped bodies in an environment of varying 3D bathymetry". Technological Educational Institute of Athens, contract from 21/10/2014 to 30/6/2015 (part time).

## Teaching Experience

Teaching assistant in courses coordinated by the Schools of Naval Architecture and Marine Engineering and Chemical Engineering of NTUA

| | |
|---|---|
| 2016-2019 | **Waves in the Ocean Environment** (mathematical treatment of linear acoustic and water wave propagation in the ocean waveguide) |
| 2016-2017 | **Error estimation and adaptive techniques** in finite element method |